PROBING COLLOIDAL FORCES

WITH SURFACE COLLISIONS

A Thesis

by

Xin Wu, B.Sc. Fudan University (Shanghai, China)

Submitted to

the Faculty of Graduate Studies and Research

of McGill University in partial fulfillment of the requirements

for the degree of Doctor of Philosophy

Department of Chemistry

McGill University

Montreal, Quebec, CANADA

March 1996

ISBN 0-612-19786-7

ABSTRACT

The principal objectives of this thesis are to introduce a new method, colloidal particle scattering (CPS), to measure colloidal and surface forces, and to demonstrate various applications of this method. CPS determines particle-particle interaction forces through creating particle collisions and extracting the interaction forces from the degree of asymmetry of the collision trajectories. Since the force to deflect a micron-sized particle is much smaller than that to deform a macroscopic spring or cantilever used in a commercial force apparatus, this new technique increases the resolution of force determination by four orders of magnitude.

Based on the CPS principles, we have built a force apparatus called "microcollider". It successfully determined the van der Waals forces and the electrostatic force between two 5 μm latex spheres at different salt concentrations. A "hairy" latex model was introduced to explain the measured van der Waals forces which are weaker than those predicted by theory assuming smooth latex surfaces. This is consistent with other experimental findings about the surfaces of latex particles.

A similar "hairy" model was applied to determine the adsorption layer thicknesses of two triblock copolymers adsorbed on latex particles. The results show that the configuration of the buoy block composed of polyethylene oxide (PEO) is more extended than a random PEO coil, which agrees with theoretical predictions. Moreover, excellent quantitative agreement between the adsorption layer thicknesses determined by CPS and other methods has been found.

Dynamic steric interactions between two high molecular weight PEO adlayers have also been studied. Both the elastic modulus and the adsorption layer thickness were determined. The results show that a thick layer has a lower elastic modulus than a thin one composed of the same polymer. This implies that an extended loop/tail structure in a thick layer is less stiff than a flat compact one in a thin layer, which is consistent with theory.

In addition, the microcollider can accurately determine particle-wall interactions as well. A rather weak electrokinetic lift force was measured. The results are in good agreement with the solutions rigorously derived from two new theories.

RÉSUMÉ

Cette thèse vise à présenter une nouvelle méthode, *colloidal particle scattering* (CPS), et ses applications pour mesurer les forces colloïdales et les forces de surface. Par la méthode du CPS, nous pouvons provoquer des collisions entre deux particules afin d'obtenir les forces d'interaction par l'analyse de l'asymétrie des trajectoires. La force requise pour dévier la trajectoire d'une particule de quelque micromètres est beaucoup plus petite que celle requise pour déformer un ressort macroscopique, utilisé dans un appareil commercial. Le CPS permet donc une résolution de quatre ordres de grandeur supérieur.

Nous avons construit un appareil appelé "*microcollider*" à partir des principes du CPS. Cet instrument nous a permis de mesurer les forces de van der Waals et la force électrostatique entre deux particules de latex de cinq micromètres, et à des concentrations de sel différents. Un modèle de particule de latex "velu" fut introduit. Les forces de van der Waals expérimentales, qui sont plus faible que celles prédites par la théorie basée sur l'hypothèse de particules à surface lisse, ont pu être expliquées.

Un modèle similaire fut utilisé pour mesurer l'épaisseur de la couche de deux copolymères tribloc adsorbé sur les particules de latex. Les résultats indiquent que la configuration du bloc de bouée composé de l'oxyde de polyéthylène (OPE) est plus étendue qu'une pelote du polymère, comme le prédit la théorie. D'ailleurs, les épaisseurs de la couche obtenus des expériences du CPS sont d'accord avec la littérature.

L'interaction stérique dynamique entre deux couches de OPE adsorbées sur les particules de latex, fut aussi étudiée. Le module d'élasticité et l'épaisseur de la couche furent

déterminés. Les résultats indiquent qu'une couche épaisse a un module d'élasticité plus bas qu'une couche mince. Cela implique que la structure "boucle et queue" d'une couche épaisse, est moins rigide que celle d'une structure plate et compacte d'une couche mince. Cette conclusion a été vérifiée par la théorie.

En plus, le *microcollider* est capable de mesurer l'interaction entre une particule et une surface. Une très faible force appelée "force ascensionnelle électrocinétique" fut déterminé. Les résultats sont en accord avec les solutions des deux nouvelles théories.

ACKNOWLEDGMENTS

My most sincere gratitude to

Prof. T. G. M. van de Ven

for his valuable guidance and continual encouragement as the director of this research project, and also for his trust and friendship as my mentor.

My special appreciation and thanks to

Dr. P. Warszynski

for his patient assistance, insightful discussion and trustful friendship. Without his contribution and support at the early stages of this project, today's success would not be possible.

My warmest thanks to Dr. T. Dabros, Dr. J. Petlicki, Dr. G. Garnier and Dr. B.Alince for their advice and help.

I would also like to thank Dr. Mungai Kamiti, Dr. Marco Polverari, Dr. Zheming Xia, Dr. Maher Al-Jabari, Alain Carignan, Claudia Fernandez, Ondrej Drabek, Alois Vanerek, Craig Murphy, Chris Sauve and all other students and staffs at the center and the department who offered great help and made my stay at McGill an enjoyable experience.

My sincere acknowledgment goes to Mr. Fred Kluck for his patience and help in the design and making of the microcollider parts, and also to Ms. A. McGuinness, Ms. P. A. McCaffrey and Ms. S. Shaieb for their friendship and help.

Finally, I wish to express my deepest gratefulness and love to my parents, Tingman Wu and Tingen Sun for their encouragement, support and love throughout my school years, and to my uncle and aunts, Tingyuan Sun, Lynn Drapeau and Tingmao Sun for their support.

GUIDELINES CONCERNING THESIS PREPARATION

In accordance with the regulations concerning the submission of thesis, we reproduce the following:

"Candidates have the options of including, as part of the thesis, the text of one or more papers submitted or to be submitted for publication, or the clearly-duplicated text of one or more published papers. These texts must be bound as an integral part of the thesis.

If this option is chosen, **connecting texts that provide logical bridges between the different papers are mandatory.** The thesis must be written in such a way that it is more than a mere collection of manuscripts; in other words, results of a series of papers must be integrated.

The thesis must still conform to all other requirements of the "Guidelines for Thesis Preparation". **The thesis must include:** A Table of Contents, an abstract in English and French, an introduction which clearly states the rationale and objectives of the study, a comprehensive review of the literature, a final conclusion and summary, and a thorough bibliography or reference list.

Additional material must be provided where appropriate (e.g. in appendices) and in sufficient detail to allow a clear and precise judgement to be made of the importance and originality of the research reported in the thesis.

In the case of manuscripts co-authored by the candidate and others, **the candidate is required to make an explicit statement in the thesis as to who contributed to such work and to what extent.** Supervisors must attest to the accuracy of such statements at the

doctoral oral defense. Since the task of the examiners is made more difficult in these cases, it is in the candidate's interest to make perfectly clear the responsibilities of all the authors of the co-authored papers."

This is done on pages 10-12 of this thesis.

TABLE OF CONTENTS

CHAPTER 3 CHARACTERIZATION OF HAIRY LATEX PARTICLES WITH COLLOIDAL PARTICLE SCATTERING

CHAPTER 4 RETARDED VAN DER WAALS FORCES BETWEEN TRIBLOCK-COATED LATEX SPHERES

CHAPTER 5 DYNAMIC INTERACTIONS BETWEEN POLYETHYLENE OXIDE LAYERS ADSORBED ON LATEX BEADS

CHAPTER 6 ELECTROKINETIC LIFT:

OBSERVATIONS AND COMPARISONS WITH THEORIES

CHAPTER 7 GENERAL CONCLUSIONS

APPENDIX AN OPERATIONAL MANUAL OF THE MICROCOLLIDER

LIST OF FIGURES

CHAPTER 3

CHAPTER 4

CHAPTER 5

CHAPTER 6

CHAPTER 7

APPENDIX

LIST OF TABLES

LIST OF SYMBOLS

Symbol	Definition
A	Hamaker constant
Ad	dimensionless parameter of Hamaker constant
A_i	any parameter in a force equation
Al	dimensionless parameter of retardation wavelength
a	particle radius
a_1 , a_2	readings from a Starrett displacement meter
B	a parameter in the electrostatic force equation
b	an adjustable parameter in an empirical expression of the lift force
C	salt concentration
C_{add}	amount of added polymer scaled by the total surface area of particles
C_b	number of blobs per unit volume
C_H	parameter in the general form of the equation of van der Waals forces
c	speed of light
c'	an adjustable parameter in an empirical expression of the lift force
Dl	dimensionless parameter of surface potential
D_s	average diffusion coefficient of all ionic species
$D_{x,z}$	diffusion coefficient of the particle in two directions perpendicular to the flow
D_1 , D_2	diffusion coefficients of two positive and negative ionic species

$\mathbf{E}$	electric field
E	elastic modulus
E_m	electrophoretic mobility
F	generalized force on a particle
F	interaction force
F_I	steric force in the interpenetration region
F_{I+C}	steric force in the interpenetration-plus-compression region
F_{coll}	colloidal force
F_{elas}	elastic force
F_{elec}	electrostatic force
F_{hydr}	hydrodynamic force
F_{int}	interaction force, referred to colloidal force in this thesis
F_{lift}	electrokinetic lift force
F_{net}	net value of all forces except drag force
F_{vdw}	van der Waals forces
f_i	external force on particle surface
f_{perm}	a factor related to the permeability of a polymer layer
$f_\perp$	deviation factor
G	shear rate
g	gravitational acceleration constant
H	dimensionless separation distance between particle and wall
h	separation distance between two shear planes on particle surfaces

	or separation distance between particle and wall in Chapter 6
h_c	separation distance between two solid core surfaces
h_d	"denting" thickness
h_m	separation distance at the secondary energy minimum
h_{min}	minimum approach distance
h_w	dimensionless separation distance between two polymer surfaces
$\bar{h}$	dimensionless separation distance between two particles
$\mathbf{I}$	unit tensor
i	index number
J	number of experimental trajectories
j	index number
K	solution conductivity
k	Boltzmann constant
L_d	drainage layer thickness
L_h	latex hairy layer thickness
L_i	impenetrable layer thickness
L_m	distance between two lines marked on the video monitor
L_p	penetrable layer thickness
L_s	polymer adsorption layer thickness
$\mathbf{M}$	mobility tensor
m	number of subunits
N	number of force parameters

N_A	Avogadro's constant
N_e	average interval between entanglement or attachment points
n_∞	salt concentration in the bulk
O	Oseen tensor
Pe	Peclet number
Pe^*	effective Peclet number in terms of lift force calculation
p	pressure of fluid
p_h	dimensionless parameter of separation distance scaled by retardation wavelength
p'	an adjustable parameter in an empirical expression of the lift force
R	inverse mobility tensor
r	position vector of the moving particle
r_{eff}	time ratio of effective shearing
r_n	a parameter in the equation of van der Waals forces according to the Lifshitz theory
r_s	radial scattering distance
r_{th}	distance from the origin to a theoretical final position in a scattering diagram
T	temperature
t	time
t_{eff}	total effective shearing time
t_{end}	ending time of shearing

t_i	external torque on particle surface
	or effective shearing time in one cycle in Chapter 6
t_m	time for a particle to travel the distance L_m
t_{shear}	total shearing time
t_0	starting time of shearing
$\mathbf{U}$	generalized particle velocity
u	particle velocity
u_{gap}	translational velocity of the bottom of the particle
u_{gr}	normal particle velocity in the absence of the lift force
u_i	translational velocity of a particle in x, y or z-direction
u_{lift}	normal particle velocity under the lift force
$u_\perp$	normal particle velocity
V	interaction energy
V_{elas}	elastic energy
$\overline{V}_1$	molar volume of solvent
$\overline{V}_2$	molar volume of polymer
$\mathbf{v}$	fluid velocity
$\mathbf{v}^0$	undisturbed fluid velocity
$\mathbf{x}$	vector to any point in space
x_i	x-coordinate of the initial position of the moving particle
x_f	x-coordinate of the experimental final position of the moving particle
$\mathbf{y}$	vector to any point on particle surface

z	z-coordinate of a particle (or particle depth)
ze	ionic charge
Z_f^{exp}	a complex number representing the experimental final position
Z_f^{th}	a complex number representing the theoretical final position
Z_i	a complex number representing the initial position
z_i	z-coordinate of the initial position of the moving particle
z_f	z-coordinate of the experimental final position of the moving particle
γ_0	a parameter in the electrostatic force equation
ΔG	error in shear rate
Δr	distance from the initial position to the theoretical final position on a scattering diagram
Δt	time measurement error
Δu	error in particle velocity
ΔZ_f^{exp}	error of the experimental final position
$\Delta\theta$	deviation of the experimental scattering angle from the theoretical one
$\Delta_{x,z}^{Br}$	error caused by Brownian motion
ϵ , ϵ_2	permittivity of the medium
ϵ_0	permittivity of vacuum
ϵ_1 , ϵ_3	permittivity of two interacting particles
ζ	zeta-potential of a particle (or a wall if it is equal)
ζ_a	zeta-potential of a particle
ζ_w	zeta-potential of a wall

θ	one of the polar coordinates
θ_s	scattering angle
κ	reciprocal Debye length
λ	retardation wavelength
μ	fluid viscosity
ν	segment number on a polymer chain
ξ_n	a discrete set of frequencies
ρ_f	fluid density
ρ_p	particle density
σ	stress tensor
τ	dimensionless Debye length
ϕ	one of the polar coordinates
χ^2	a parameter indicating the goodness-of-fit
χ_1	Flory-Huggins interaction parameter
ψ_0	surface potential on a particle
Ω	angular velocity of a particle
ω_i	angular velocity of a particle in x, y or z-direction

CHAPTER 1

INTRODUCTION

BACKGROUND AND THESIS TOPICS

Suspension stability and the rheological behavior of various colloidal systems are governed by colloidal forces. Generalized as surface forces, they include electrostatic, van der Waals, steric, hydrophilic/hydrophobic and adhesion forces (1). Their active ranges are determined by the nature of the forces and the conditions of a system. Since colloidal particle surfaces are usually not smooth, only the long-range interactions (significant up to several or tens of nanometers depending on particle size) plus the short-range steric interaction are the determining factors for properties of colloidal systems. Therefore, the study of these long-range forces and the steric force becomes the main topic of this thesis.

Generally speaking, electrostatic and van der Waals forces are long-range interactions. They were extensively studied in theory more than five decades ago. The combination of these two forces forms the backbone of the famous DLVO theory (2):

$$F_{coll} = F_{elec} + F_{vdw} \quad . \qquad [1.1]$$

where F_{coll} is colloidal (or surface) force and F_{elec} and F_{vdw} are electrostatic and van der Waals forces respectively. Electrostatic forces can be calculated from the Gouy-Chapman theory which solves the Poisson-Boltzmann equation analytically and gives the expression for sphere-sphere interactions in a symmetrical electrolyte solution using the Derjaguin approximation (3):

$$F_{elec} = 32\pi\epsilon\kappa a \tanh^2\left(\frac{ze\psi_0}{4kT}\right)\left(\frac{kT}{ze}\right)^2 e^{-\kappa h} \quad , \qquad [1.2]$$

where a is the particle radius, ϵ is the permittivity of the medium, κ is the reciprocal Debye length, k is the Boltzmann constant, T is the temperature, ze is the ionic charge, h is the separation distance between the two shear planes on the particle surfaces and ψ_0 is the surface potential on this shear plane.

Long-range van der Waals interactions originate from short-range van der Waals forces between atoms consisting colloidal particles. The force between two equal-sized spheres can be expressed in a general form:

$$F_{vdw} = \frac{C_H a}{12 h_c^2} \quad , \qquad [1.3]$$

where h_c is defined as the separation distance between two solid core surfaces. Obviously, for bare and smooth particles, $h_c = h$ (to be discussed later). In terms of the Lifshitz theory, C_H can be expressed as (3),

$$C_H = \frac{3kT}{2} \sum_{n=0}^{\infty} \left(\frac{\epsilon_1 - \epsilon_2}{\epsilon_1 + \epsilon_2} \right) \left(\frac{\epsilon_3 - \epsilon_2}{\epsilon_3 + \epsilon_2} \right) (1 + r_n) e^{-r_n} \quad , \qquad [1.4]$$

where ϵ_1 and ϵ_3 are the permittivities of the two particles, ϵ_2 is the permittivity of the medium, and

$$r_n = \frac{2 h_c \epsilon_2^{1/2} \xi_n}{c} \quad , \qquad [1.5]$$

in which c is the speed of light and ξ_n is a discrete set of frequencies.

Alternatively, a simpler Hamaker's approach can be applied assuming the force is additive and nonretarded. In that case, C_H in Eq. [1.3] equals A, the Hamaker constant. However, when h_c is larger than a few nanometers, retardation effect caused by the time delay for an electromagnetic signal to travel between the gap becomes significant. A modified expression proposed by Schenkel and Kitchener (4) takes this effect into account:

$$C_H = Af(p_h)$$

$$\text{where} \quad f(p_h) = \frac{1 + 3.54p_h}{(1 + 1.77p_h)^2} \qquad \text{when } p_h < 1; \qquad [1.6]$$

$$\text{and} \quad f(p_h) = \frac{0.98}{p_h} - \frac{0.434}{p_h^2} + \frac{0.067}{p_h^3} \qquad \text{when } p_h > 1.$$

in which $p_h = 2\pi h_c/\lambda$, λ being the retardation wavelength. In colloid science, the combination of Eqs. [1.3] and [1.6] is usually preferred because of its simplicity.

Both electrostatic and van der Waals forces have been experimentally determined with surface force apparatus (SFA) (5,6), atomic force microscopes (AFM) (7-9) and total internal reflection microscopes (TIRM) (10,11). These measured forces are mainly between two macroscopic surfaces or between one colloidal particle and one macroscopic surface. Although they are not really colloidal forces, they usually reveal the same trends. The interactions between two 2 μm latex spheres were also determined with an AFM (12). However, for SFA and AFM measurements, most of the information about the interaction forces is obtained from the steep rising part of the energy barrier, so the attractive van der Waals forces are usually overwhelmed by the repulsive electrostatic force. This severely affects the accuracy of determined van der Waals forces. An alternative way to measure van

der Waals forces between colloidal particles is to study the rate of particle coagulation and calculate the Hamaker constant from the critical coagulation concentration (13,14). The results are subject to large errors but are within the same order of magnitude as the theoretical Hamaker constant. Because of the practical importance of van der Waals interactions, two thesis chapters (Chapters 3 and 4) have been devoted to the determination of this force and a much higher accuracy (±10% errors) has been achieved with a new experimental method (to be discussed later). When particles are coated with a thin adsorption layer, instead of Eq. [1.3], a more complicated equation with an apparent Hamaker constant as a function of layer thickness, L_a and separation distance, h, should be used. The subsequent change in van der Waals forces is called the Vold effect (15,16). In this thesis, the van der Waals interactions between two layers are neglected, so the complicated equation reduces to Eq. [1.3]. Obviously in this equation, $h_c = h + 2L_a$. As will be shown in Chapters 3 and 4, both A and L_a can be determined by using Eq. [1.3].

Hydrophilic/hydrophobic and adhesion forces are short-range interactions. Exceptions were reported for the hydrophobic force which was observed acting between non-charged fluorocarbon surfaces at a distance of 80-90 nm (17). However, this force diminishes dramatically between charged surfaces (18), which are usually encountered in an aqueous colloidal system, so the study of long-range hydrophobic forces will not be emphasized in this thesis.

The steric force is a very short-range force which only acts on two overlapping polymer layers. Because its magnitude increases dramatically as two layers overlap, steric interaction overwhelms any other forces when it is present. Steric forces under "static"

conditions can be described by a mixing mechanism which was developed by Fischer (19) and Napper (20). It predicts that when two polymer layers are brought into contact, the polymer chains start to interpenetrate each other and eventually compress each other when the separation distance between the two core surfaces is less than the layer thickness. The resulting repulsive force can be calculated from the change in free energy. If the segment density is assumed constant, the steric forces in the regimes of interpenetration (or mixing) and interpenetration plus compression are (20),

$$F_I = 4\pi akT\frac{\overline{V}_2^2\nu^2}{\overline{V}_1 N_A}(0.5 - \chi_1)\left(\frac{1}{L_s} - \frac{h_c}{2L_s^2}\right) \quad \text{when } L_s \le h_c \le 2L_s \text{ ;}$$

$$F_{I+C} = 4\pi akT\frac{\overline{V}_2^2\nu^2}{\overline{V}_1 N_A}(0.5 - \chi_1)\left(\frac{1.5}{h_c} - \frac{1}{L_s}\right) + 2\pi akT\nu\ln\left(\frac{L_s}{h_c}\right) \quad \text{when } h_c \le L_s \text{ ,} \qquad [1.7]$$

where $\overline{V}_1$ and $\overline{V}_2$ are molar volume of solvent and polymer respectively, ν is the segment number on polymer chains attached to unit surface area, N_A is the Avogadro's constant and χ_1 is the Flory-Huggins interaction parameter.

When the time scale for polymer chain relaxation is longer than the time of contact, polymer layers probably resemble an elastic gel, i.e. they "dent" rather than "mix". Under this dynamic condition, the elastic force resulting from the compression can be described by Jäckel's theory (21):

$$F_{elas} = \frac{4\sqrt{2}}{3}Eh_d^{\frac{3}{2}}(a + L_s)^{\frac{1}{2}} \quad , \qquad [1.8]$$

where E is the elastic modulus of the polymer layer and h_d is the "denting" thickness of one layer.

Similar to electrostatic forces, steric interactions under "static" conditions have been extensively studied with SFAs (22,23), AFMs (24) and recently with a scanning probe microscope (25,26). A steep increase in the repulsive force was observed as two surfaces approach each other, the same trend as predicted by theories. By constrast, very few studies on dynamic interactions between polymer layers have ever been reported. Israelachivili *et al.* observed these dynamic interactions with a SFA operating at a vibration frequency of 200 Hz (27). Higher frequencies (~300 kHz) have been generated with an AFM operating at a tapping mode (28). However, the tapping mode was designed to eliminate the lateral shear force causing sample degradation, and it has yet to be applied in the study of dynamic steric interactions. Since these dynamic interactions are frequently encountered in high-shear systems, it is of imperative importance to model and determine them. In Chapter 5 of this thesis, a new experimental method (see below) has been used to study these interactions between two polyethylene oxide layers adsorbed on latex particles.

Because of various limitations of current surface force measurement techniques mentioned above, a new method, colloidal particle scattering (CPS), was developed in our research group to accurately determine colloidal forces. Instead of determining forces with soft springs or cantilevers, we use colloidal particles both as research objects and probes. It is known that during a particle collision in a linear shear flow, colloidal forces make collision trajectories asymmetrical (3), so it is possible to determine the forces by studying this asymmetry. Based on this idea, the first apparatus, a "traveling microtube", was built more

than two decades ago to measure electrostatic, van der Waals (29,30) and "static" steric forces (30,31). Because of the high sensitivity of collision trajectories to the interaction forces, the resolution of force measurement is typically 3-4 orders of magnitude higher than that from a SFA or an AFM. This high sensitivity is only rivaled by a TIRM which, however, is limited to measure particle-wall interactions. The traveling microtube generates particle collisions in a 200 μm-diameter glass tube by passing latex suspensions through it. Locally near a particle, the Poiseuille flow resembles a simple shear flow. Two particles located on two neighboring layers will collide because of their different velocities. However, since collisions occur randomly in the tube, it is difficult to track and record them at the right moment. Usually it takes more than one day to record one single collision in which the particles approach one another sufficiently close to observe the colloidal forces. This inefficiency seriously limits the application of the traveling microtube in the study of colloidal forces. Recently a new setup was designed to solve this problem. Particle collisions are generated in the vicinity of a glass wall to which one latex sphere is attached. Another sphere which is mobile and close to the wall can be manipulated to collide with the stationary sphere by a wall shear flow (32). This instrument was called "surface collision apparatus" in ref. (33) because collisions only occur near a glass surface. Compared with the traveling microtube, it has several advantages: better illumination of the colliding particles; a well-defined geometry which makes accurate determination of particle coordinates possible; and most importantly, better control of the collisions. The collisions in this instrument are artificially generated rather than passively observed, similar to a "supercollider" used in elementary particle research. This greatly increases the efficiency of collision recording (>200 collisions

per day). Likewise, we call it a "microcollider" and this name will be used throughout the thesis. Another advantage of this instrument is that unlike the reference particle in a traveling microtube, the stationary particle in the microcollider does not rotate with the mobile one during a collision, so a sliding motion occurs which greatly decreases the time of contact between two specific spots on particle surfaces. This enables us to study dynamic steric interactions at a relatively low shear rate (~4 s^{-1}). The details of this technique will be discussed in Chapter 2. Since the invention of the microcollider, traveling microtube experiments have been discontinued in our lab. Hence, in this thesis, unless indicated otherwise, the CPS method implies the use of the microcollider.

The microcollider can also be used to study particle-wall interactions with the same sensitivity and accuracy. In that case, a mobile particle near a wall is monitored and the interaction forces can be calculated from the vertical displacement (or change in depth) of that particle. This method of force measurement has been demonstrated in Chapter 6 in which an electrokinetic lift force was determined. The results helped us develop and verify a new electrokinetic theory which describes high-Peclet number systems more precisely than any other theories.

PUBLICATIONS, CREDITS AND THESIS OUTLINE

- Chapter 2 "Colloidal Particle Scattering: A New Method to Measure Surface Forces"

  T.G.M. van de Ven, P. Warszynski, X. Wu, and T. Dabros, *Langmuir* **10**, 3046 (1994).

This chapter gives a review of different methods to measure surface forces, an introduction to colloidal particle scattering and a detailed description of the microcollider. The preliminary results of the surface potential of latex particles and the Hamaker constant of polystyrene in water are also included.

In this chapter, Dr. van de Ven initiated the research. He and Dr. Dabros provided theoretical guidance. Dr. Warszynski wrote a calculation program according to their hydrodynamic theory to invert the trajectory equation, set up the hardware of the microcollider and developed the alignment techniques. The author finalized the hardware, developed the controling and image analysis software and data processing procedures. The experiments were performed by Dr. Warszynski and the author.

- Chapter 3 "Characterization of Hairy Latex Particles with Colloidal Particle Scattering"

  X. Wu and T.G.M. van de Ven, submitted to *Langmuir*.

This chapter gives the first application of CPS on commercial 5 μm sulfate latex beads which usually have a rough and hairy surface. The van der Waals forces between these particles modeled by Eqs. [1.3] and [1.6] were determined. The model yielded the hairy layer thickness and the Hamaker constant as the best-fit parameters. An improved data selection procedure was also proposed.

In this chapter, the author did all the experimental work and Dr. van de Ven provided theoretical guidance; the same applied to Chapters 4 and 5.

- Chapter 4 "Retarded van der Waals Forces between Triblock-Coated Latex Spheres"

  X. Wu and T.G.M. van de Ven, submitted to *Langmuir*.

  A similar model as in Chapter 3 was used to measure the adsorption layer thickness of two commercial triblock copolymers. The Hamaker constant and retardation wavelength of polystyrene in water were also determined.

- Chapter 5 "Dynamic Interactions between Polyethylene Oxide Layers Adsorbed on Latex Beads"

  X. Wu and T.G.M. van de Ven, submitted to *J. Colloid Interface Sci.*

  In this chapter, the dynamic interactions between polymer layers were modeled by Eq. [1.8]. It yielded the elastic modulus and the polymer layer thickness as the best-fit parameters.

- Chapter 6 "Electrokinetic Lift: Observations and Comparisons with Theories"

  X. Wu, P. Warszynski, and T.G.M. van de Ven, *J. Colloid Interface Sci.* in press.

  A vertical drifting of a charged latex particle under the electrokinetic lift force was observed and recorded with the microcollider. The force-distance curve was then determined. It disagrees with previous theories which neglect the main contribution to the lift force. The results of two new theories which give a correct analysis of the lift force are quoted and their predictions are consistent with the experimental findings.

In this chapter, the author did most of the experimental work and developed the data processing procedures. Dr. Warszynski did part of the lab work, developed a new electrokinetic theory and wrote a computer program to obtain the numerical solutions. Dr. van de Ven provided theoretical guidance.

- Chapter 7 General Conclusions

This chapter summarizes various applications of CPS and proposes some new areas for future research.

- Appendix: An Operational Manual of the Microcollider

This appendix gives detailed operational procedures of CPS experiments as well as the instructions of various software and programs to process data. Black-and-white photos are included for better illustration.

The microcollider is a state-of-the-art instrument. It owes its success to the collaborative effort of several talented researchers. For this reason, throughout the thesis the word "we" is used to reflect this teamwork effort. Chapters 2 - 6 have been written in the form of a regular publication. Modifications are only brought in to unify the symbols and formats and to bridge different chapters.

REFERENCES

1. Israelachvili, J. N., "Intermolecular and Surface Forces." Academic Press, London 1985, p.111.
2. Israelachvili, J. N., and Ninham, B. W., *J. Colloid Interface Sci.* **58,** 14 (1977).
3. van de Ven, T. G. M., "Colloidal Hydrodynamics." Academic Press, London 1989, p.26, 39 and 363.
4. Schenkel, J. H., and Kitchener, J. A., *Trans. Faraday Soc.* **56,** 161 (1960).
5. Israelachvili, J. N., and Adams, G. E., *J. Chem. Soc. Faraday Trans. 1* **74,** 975 (1978).
6. Pashley, R. M., *J. Colloid Interface Sci.* **83,** 531 (1981).
7. Ducker, W. A., Senden, T. J., and Pashley, R. M. *Nature* **353,** 239 (1991).
8. Butt, H. -J., *Biophys. J.* **60,** 1438 (1991).
9. Hartmann, U., *Phys. Rev. B* **43,** 2404 (1991).
10. Prieve, D. C., and Frej, N. A., *Langmuir* **6,** 396 (1990).
11. Flicker, S. G., Tipa, J. L., and Bike, S. G., *J. Colloid Interface Sci.* **158,** 317 (1993).
12. Li, Y. Q., Tao, N. J., Garcia, A. A., and Lindsay, S. M., *Langmuir* **9,** 637 (1993).
13. Reerink, H., and Overbeek, J. Th. G., *Discuss. Faraday Soc.* **18,** 74 (1954).
14. Ottewill, R. H., and Shaw, J. N., *Discuss. Faraday Soc.* **42,** 154 (1966).
15. Vold, M. J., *J. Colloid Sci.* **16,** 1 (1961).
16. Osmond, D. W. J., Vincent, B., and Waite, F. A., *J. Colloid Interface Sci.* **42,** 262 (1973).

17. Claesson, P. M., and Christenson, H. K., *J. Phys. Chem.* **92,** 1650 (1988).

18. Israelachvili, J. N., and Pashley, R. M., *J. Colloid Interface Sci.* **98,** 500 (1984).

19. Fischer, E. W., *Kolloid Z.* **160,** 120 (1958).

20. Napper, D. H., *J. Colloid Interface Sci.* **58,** 390 (1977).

21. Jäckel, K., *Kolloid Z. Z. Polym.* **197,** 143 (1964).

22. Israelachvili, J. N., Tandon, R. K., and White, L. R., *J. Colloid Interface Sci.* **78,** 430 (1980).

23. Klein, J., and Luckham, P. F., *Macromolecules* **17,** 1041 (1984).

24. Rutland, M. W., and Senden, T. J., *Langmuir* **9,** 412 (1993).

25. Evans, E., Ritchie, K., and Merkel, R., *Biophys. J.* **68,** 2580 (1995).

26. Evans, E., private communication.

27. Israelachvili, J. N., Kott, S. J., and Fetters, L. J., *J. Polym. Sci.: Part B: Polym. Phys.* **27,** 489 (1989).

28. Zhong, Q., Inniss, D., Kjoller, K., and Elings, V. B., *Surface Sci.* **290,** L688 (1993).

29. Takamura, K., Goldsmith, H. L., and Mason, S. G., *J. Colloid Interface Sci.* **82,** 175 (1981).

30. Takamura, K., Goldsmith, H. L., and Mason, S. G., *J. Colloid Interface Sci.* **82,** 190 (1981).

31. de Witt, J. A., and van de Ven, T. G. M., *J. Colloid Interface Sci.* **151,** 118 (1992).

32. Dabros, T., and van de Ven, T. G. M., *J. Colloid Interface Sci.* **149,** 493 (1992).

33. van de Ven, T. G. M., Warszynski, P., X. Wu, and Dabros, T., *Langmuir* **10,** 3046 (1994) (Chapter 2 of this thesis).

CHAPTER 2

COLLOIDAL PARTICLE SCATTERING:

A NEW METHOD TO MEASURE

SURFACE FORCES

OBJECTIVES

In the previous chapter, we have stated the importance of determining various colloidal forces and the limitation of current commercial force apparatus. In this chapter, we are to introduce a new method to measure colloidal forces. The preliminary experimental results will demonstrate its ultra-high sensitivity and accuracy.

ABSTRACT

A new method to determine colloidal forces is presented. It is based on observing the changes in two-particle collision trajectories in a linear shear flow and inverting the trajectory equations describing such collisions. In the absence of colloidal forces and under low Reynolds number conditions, collisions are symmetric and reversible. When colloidal forces are acting between the particles, this symmetry is broken and the degree of asymmetry is a measure of the magnitude of colloidal forces.

From a sufficiently large number of experimentally observed collision trajectories we can determine the colloidal forces by a minimization method, assuming some relationship between the interaction force and interparticle distance. This relationship can either be taken from theory, e.g., classical DLVO theory, or be represented by a general function of interparticle distance with adjustable parameters which can be determined from the best fit between theory and experiment. From Monte Carlo simulations it has been found that the number of collisions required for a reliable determination of the colloidal force-distance relationship is about 25.

Some experiments have been done with a "microcollider" which we describe in detail. The results for latex particles in mixtures of glycerol-water and D_2O-water show that the method is capable of detecting forces that are 3-4 orders of magnitude smaller than those measured by a conventional surface force apparatus or by an atomic force microscope. A minimization analysis of data obtained previously with the traveling microtube apparatus is also presented.

INTRODUCTION

Determination of interaction forces between particles is a fundamental problem in colloid science as the way the force varies with interparticle distance determines various properties of a colloidal system. By adding electrolytes, neutral polymers or polyelectrolytes to a suspension or letting them adsorb on particle surfaces, one can change the interaction forces between particles and thus change the stability or the rheological behavior of the system.

The most direct method of determining interaction forces was developed by Israelachvili and Tabor (1). The method is based on the measurement of the interaction forces between crossed macroscopic mica cylinders which can be accurately positioned within a separation distance from a fraction of a nanometer to 1 μm. The distance is obtained from the interference pattern of laser light, and the force is calculated from the compression of the spring to which one of the cylinders is attached. The experimental apparatus, usually called "surface force apparatus" (SFA), is now commercially available and many results for interaction forces in various systems have been published (2). However, there are some drawbacks of this method: (i) Although the distances between interacting surfaces are in the range typically encountered in colloidal systems, measurement is possible only for macroscopic mica surfaces and not for real colloidal particles; (ii) a SFA is not sensitive enough to measure the force close to the secondary energy minimum, which is often the most crucial part for a colloidal system; (iii) Usually only the static forces, i.e., forces with a characteristic time longer then a second, can be measured, whereas the characteristic time for

Brownian collision of 1 μm particles is of the order of 10^{-4}-10^{-3} s. The dynamic forces acting between particles during a collision can be very different from static ones. The hysteresis observed in some experiments (3) measuring interaction forces between two polymer surfaces may be attributed to the influence of the relaxation of polymer conformation on the measured force. Recent technical improvement allows a vibrational motion of one of the surfaces and thus enable a SFA to measure dynamic forces (4). However, the piezoelectric bimorph does not improve the sensitivity of measurement, and the vibrational frequency is limited by the natural frequency of the bimorph which is in the order of 100 Hz.

Another widely used instrument to measure surface forces is atomic force microscope (AFM) (5). It measures forces either between a standard AFM tip of the microscope probe (usually a Si_3N_4 crystal) and a macroscopic surface (6,7), or between a colloidal particle glued to the end of the cantilever and the surface (8,9). Recently, an attempt has been made to measure forces between two latex particles (10). Depending on the operating mode of an AFM, one can measure either static or dynamic forces with a contact mode or tapping mode respectively. The sensitivity of an AFM is limited by the spring constant of its cantilever and the accuracy of the cantilever deflection measurement. For a typical spring constant of the order of 0.1 N/m and a deflection of 0.1 nm, one can measure a force of the order of 10^{-11} N. Like a SFA, this force is 3-4 orders of magnitude larger than the interaction force around a secondary energy minimum. At a tapping mode, the force detection capability is even lower because the spring constant is usually two orders of magnitude higher.

Other direct force measurement methods are the micropipet method (11), the osmotic stress method (12) and the osmotic pressure method (13). All of them measure static

equilibrium forces. The micropipet method does not give any interaction force-distance relationships. It only measures the surface affinity at one separation distance. Furthermore, it is limited to membrane systems. The osmotic stress method is limited to the study of multilayer materials. Neither of them can be applied to study any commonly used polymers or colloids. The osmotic pressure method actually measures the interaction forces between latex particles, but the force profile depends on the assumed crystal model which is not exactly the same as that in a real concentrated latex suspension containing both ordered and disordered structures. Therefore, the interpretation of the results is open to discussion.

It is also possible to obtain the interaction forces indirectly by correlating experimentally obtained coagulation rates with theoretical predictions. In that case, however, reliable results can only be obtained for monodisperse particles, provided that the initial concentration of particles is known. The same restrictions apply to the method of determining the interaction forces from deposition experiments (14). The latter method has the advantage that deposition rates can be visually measured, so the results are more reliable than those from coagulation experiments. Deposition rates can later be correlated to theoretical predictions to give the interaction forces. Limitations of the method are discussed in ref. (15).

Some other methods involve finding the interaction energy profile for a particle near an interface and then calculating the force by differentiation. This can be achieved by using evanescent wave spectroscopy techniques to find the concentration profile of colloidal particles at an interface, which, in case of dilute suspensions, is related to the interaction energy by the Boltzmann distribution (16). Another method involves studying the Brownian motion of particles near an interface (17-19). From the amplitude of Brownian displacements

in the neighborhood of the secondary minimum, one can find the shape of the interaction energy profile. These two methods indeed measure forces in the most important region of a force-distance profile, but they are limited to measuring the static interactions between a particle and a surface only.

The energy-distance relationship can also, in principle, be calculated from the pair correlation function which can be calculated from the structure factor obtained from static light scattering experiments (20). Because of the complication of the model and calculation procedures, only limited success has been achieved (21).

In this paper we present a new method of force measurement which we call colloidal particle scattering (CPS). The method is analogous to elementary particle (e.g. electrons) scattering which can be used to evaluate the interactions between elementary particles by studying the distribution of impact parameters and deflection angles of collisions. However, elementary particle scattering cannot really quantitatively determine the particle-particle interactions because the exact trajectory of each collision is unknown. CPS does not have such a limitation. Every individual collision trajectory is accurately measured. In different collisions, e.g. a head-on collision or a grazing collision, particles "sample" different regions of the interaction force profile, and obtaining a sufficient number of different collisions allows one to determine the full force profile. The procedure of obtaining the force profile from collisions with the CPS method is called trajectory inversion. The inversion is done by assuming some functional force-distance relationship with several adjustable parameters, and fitting them by matching the calculated trajectories and the experimental trajectories using a least squares method. Brownian motion of particles and experimental errors may cause

deviations in particle trajectories. To obtain a reliable fit, the number of collision trajectories should well exceed the number of parameters to be fitted. A Monte-Carlo simulation of the experiment has been done to determine the minimum number of collisions required to invert the trajectory equation at a given level of experimental error.

The CPS method has the advantage that interaction forces are measured between real colloidal particles instead of macroscopic surfaces. Dynamic forces can be easily determined since the measurement is done with moving particles. The relative approach velocity of a particle is around 10 μm/s, equivalent to the maximum velocity that can be achieved by a SFA operating in a dynamic mode. The approach velocity of CPS can be even higher if a high-speed video system is used. Moreover, the CPS method is far more sensitive than SFA and AFM methods. It can detect forces which correspond to interaction energies of several kT. With this capability, it can determine the force-distance relationship around a secondary energy minimum accurately.

To illustrate the usefulness of our trajectory inversion technique used in CPS, we include some reanalysis of the collision data obtained previously with the traveling microtube apparatus (22,23). That apparatus is based on the same idea as CPS, but with it one cannot easily observe enough collisions in a single experiment to invert the trajectory equation reliably.

In this chapter we present a new experimental setup, "microcollider", to replace the traveling microtube. It is based on microscopic observations of the relative motion of two colloidal particles. One particle is attached to a surface and the other one moves along the surface in a wall shear flow to collide with the stationary one. With this apparatus it is

possible to create a sufficiently large number of collisions between two particles. The collision trajectories are analyzed by an image processing board. The interaction force between the particles is calculated with the trajectory inversion technique mentioned above. Some preliminary results show that the force-distance profile can be accurately determined by this method.

BASIC PRINCIPLES

1. Inversion of trajectory equation

The principle of the method is illustrated in Figs. 2.1 and 2.2. One latex particle is stuck to a surface and another one moves towards it in a wall shear flow. The origin of the coordinate system is placed on the surface right below the center of the stationary particle. If the Brownian motion of the particles is neglected, the trajectory equation of the moving particle is, in general, given by:

$$\frac{d\mathbf{r}}{dt} = \mathbf{M}\cdot(\mathbf{F}_{hydr} + \mathbf{F}_{int}) \qquad [2.1]$$

where $\mathbf{r}$ is the position vector of the moving particle, t is the time, $\mathbf{M}$ is the mobility tensor, $\mathbf{F}_{hydr}$ is the hydrodynamic force and $\mathbf{F}_{int}$ is the interaction force between two particles which consists of several contributions such as van der Waals forces, electric double-layer forces, steric forces, electroviscous forces, etc.

The mobility matrix and hydrodynamic force are generally a function of the particle coordinates which can be found from the solution of the Navier-Stokes equation. Since in

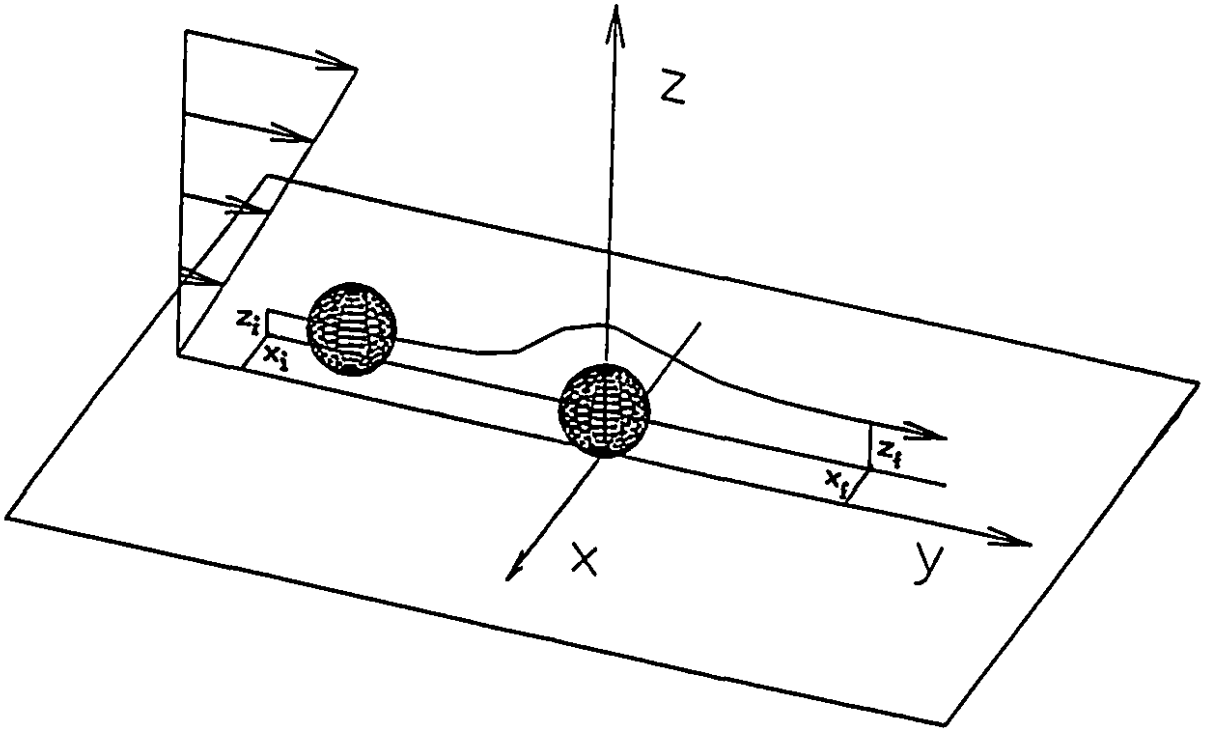

Fig. 2.1 Illustration of a colloidal particle collision. The particle in the center is stuck to the wall. A second particle is moving toward it to undergo a collision. The collision trajectory, illustrated by the curve with an arrow at the end, can be represented by the initial position (x_i, z_i) of the moving particle before the collision and the final position (x_f, z_f) of the particle after the collision.

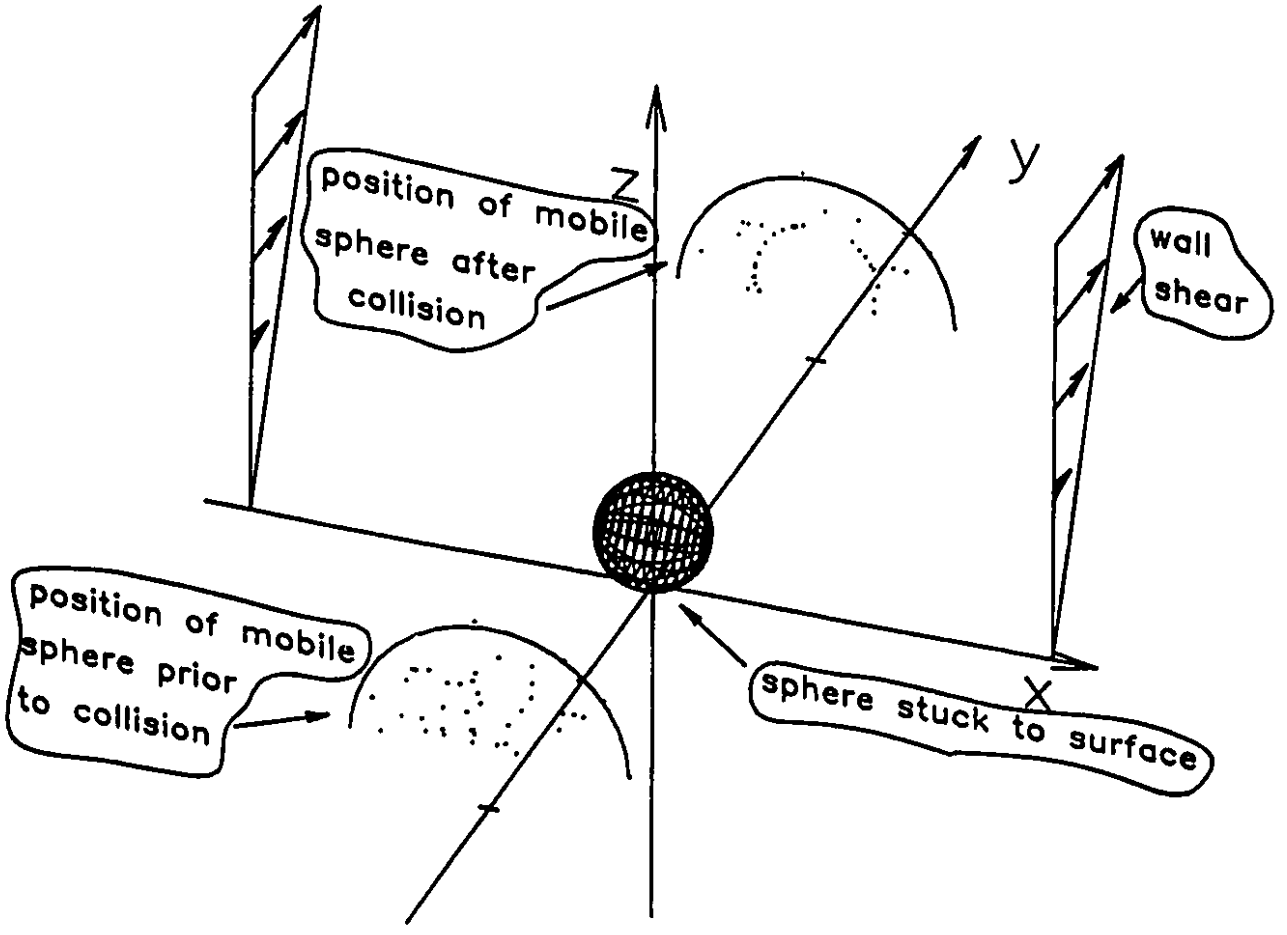

Fig. 2.2 Illustration of the basic principles of the CPS method. The initial and final positions of a moving particle (cf. Fig. 2.1) for many collisions are plotted in a "scattering diagram". Different interaction force vs. interparticle distance profiles will lead to different scattering patterns. From an experimentally determined scattering pattern, it is possible to calculate the force-distance profile with the trajectory inversion technique.

colloidal systems the Reynolds number based on the flow velocity, the dimensions of the particles and the viscosity of the medium is almost always much smaller than 1, one can neglect inertia effects and use the creeping flow equation instead.

Eq. [2.1] describes the evolution of the relative positions of the moving particle with time. By knowing the initial position of the particle and the interaction forces, one can predict its final position after the collision. When two particles are far apart, the moving particle follows the direction of the flow, and the x and z coordinates (cf. Fig. [2.1]) of the particle remain constant. Therefore, it is sufficient to describe the collision trajectory in terms of the initial position, (x_i , z_i), and the final position, (x_f , z_f), and the collision can be formally expressed as a transformation in the complex plane $Z_i \rightarrow Z_f$, where $Z_i = x_i + iz_i$ and $Z_f = x_f + iz_f$ $(i = \sqrt{-1})$. If we assume that the interaction force is given by some function of distance between particles, $\mathbf{F}_{int} = \mathbf{F}_{int}(r, A_1, \ldots, A_N)$, where A_i are parameters, we can calculate the theoretical final positions of the moving particle from the experimentally given initial positions and adjust the set of parameters A_i to match them to the experimental final positions.

The fitting procedure is accomplished by minimizing the χ^2- function defined as:

$$\chi^2 = \sum_{i=0}^{J} \frac{(Z_f^{th} - Z_f^{exp})_i \cdot (Z_f^{th} - Z_f^{exp})_i^*}{(\Delta Z_f^{exp})_i \cdot (\Delta Z_f^{exp})_i^*} \qquad [2.2]$$

where J is the number of experimental trajectories, Z_f^{exp} is the experimental final position of the moving particle expressed as a complex number, Z_f^{th} is the theoretical final position calculated from the initial position Z_i by solving the trajectory equation, ΔZ_f^{exp} is the error of the final position which consists of the experimental error in measuring the particle position

and possible displacements due to Brownian motion during the collision. The asterisk indicates the complex conjugate. A standard procedure like the Marquart-Levenberg algorithm (24) is used for the minimization.

The set of parameters A_i for which χ^2 attains a minimum describes the interaction force profile. The goodness-of-fit is characterized by the value of χ^2 for J-N-1 degrees of freedom, where N is the number of parameters. The confidence intervals for the parameters can be calculated in the usual way using a covariance matrix.

For traveling microtube experiments (22,23), the basic principle is the same except that the wall shear flow is replaced by a simple shear flow and the stationary particle is replaced by a freely rotating particle.

2. Error Analysis

Since the position of a particle is measured with some experimental errors, it is necessary to analyze how the errors affect the resulting interaction force profile. This was done by a Monte Carlo simulation method. To speed up the calculation, only collisions in a simple shear flow (observed with the traveling microtube) were simulated. In such a system the trajectory equation of the moving particle (cf. Eq. [2.1']) can be simplified considerably. For equal-sized spheres the trajectory equation can be expressed in spherical coordinates as (25),

$$\frac{dr}{dt} = GA(r)\sin^2\theta\sin 2\phi + \frac{kTC(r)\bar{F}_{int}(r)}{3\pi\mu a^2}$$

$$\frac{d\theta}{dt} = \frac{1}{4}GB(r)\sin 2\theta\sin 2\phi \qquad [2.3]$$

$$\frac{d\phi}{dt} = \frac{1}{2}G(1 + B(r)\cos 2\phi)$$

where r is the dimensionless distance between particles scaled by the particle radius a, G is the shear rate, μ is the viscosity, A(r), B(r) and C(r) are known functions of r (25-27).

The interaction force was assumed to be of the DLVO type (28,29). In dimensionless units of kT/a (k is the Boltzmann constant and T is the temperature), it can be expressed as,

$$\bar{F}_{int}(\bar{h}) = Dl\tau\exp(-\tau\bar{h}) - \frac{Ad}{2\bar{h}^2}f(Al,\bar{h}) \qquad [2.4]$$

with

$$f(Al,\bar{h}) = \begin{cases} \dfrac{1 + 3.54p_h}{(1 + 1.77p_h)^2} & \text{for } p_h < 1 \\ \dfrac{0.98}{p_h} - \dfrac{0.434}{p_h^2} + \dfrac{0.067}{p_h^3} & \text{for } p_h \geq 1 \end{cases} \qquad [2.4a]$$

where $\bar{h}$=h/a (h being the separation distance), $\tau = \kappa a$ (κ being the reciprocal Debye length), Dl is the double-layer interaction parameter defined as, $Dl = 32\pi\gamma_0^2\epsilon akT/(ze)^2$ [ϵ being the permittivity of the medium, ze the ionic charge, $\gamma_0 = \tanh(ze\psi_0/4kT)$, ψ_0 being the surface potential of the particle], Ad = A/6kT (A is Hamaker constant), $Al = 2\pi a/\lambda$ (λ is the characteristic wavelength accounting for the effect of retardation) and $p_h = Al\bar{h}$.

A DLVO interaction force profile with a deep secondary minimum (cf. solid lines in

Figs. 2.3 and 2.4) was chosen, because the trajectories would then be very sensitive to the changes of initial positions, and the effect of position errors is pronounced. The procedure of the analysis is as follows: first, a set of initial positions of the moving particle was randomly generated and the trajectory equation with the assumed force profile was solved to obtain the final positions of the particle. Then the values of the initial and final positions were spread around the original ones according to a normal distribution with a variance equal to the square of the experimental error. Finally, a force curve was calculated from the new initial and final positions of the moving particle. This procedure was repeated several times and the resulting force profiles are represented by the dashed lines in Figs. 2.3 and 2.4. Ideally, to obtain a good reproducibility of the original force curve (solid lines in the figures), it is necessary to have at least 60 trajectories for a 6% error (relative to particle radius) or 30 trajectories for a 3% error. However, due to the limit of the computational power of the present computer (IBM 386 with a AT-super coprocessor board from YARC system corporation), fewer collisions are actually used in the fitting. Usually we consider the scattering in the fitted force profiles in Fig. 2.4(a) (with only 15 trajectories) still tolerable, so 20-25 collisions will be enough for a 6% error.

The error results from Brownian motion, misalignment and external noise. Brownian motion is the main contribution to the error. It affects both the position measurement before and after a collision and the collision trajectory itself during a collision (resulting in an error after the collision). As will be shown later, both effects can be minimized by using certain data processing procedures. The latter effect, however, remains much bigger than the former one even after the processing. Its magnitude can be evaluated from,

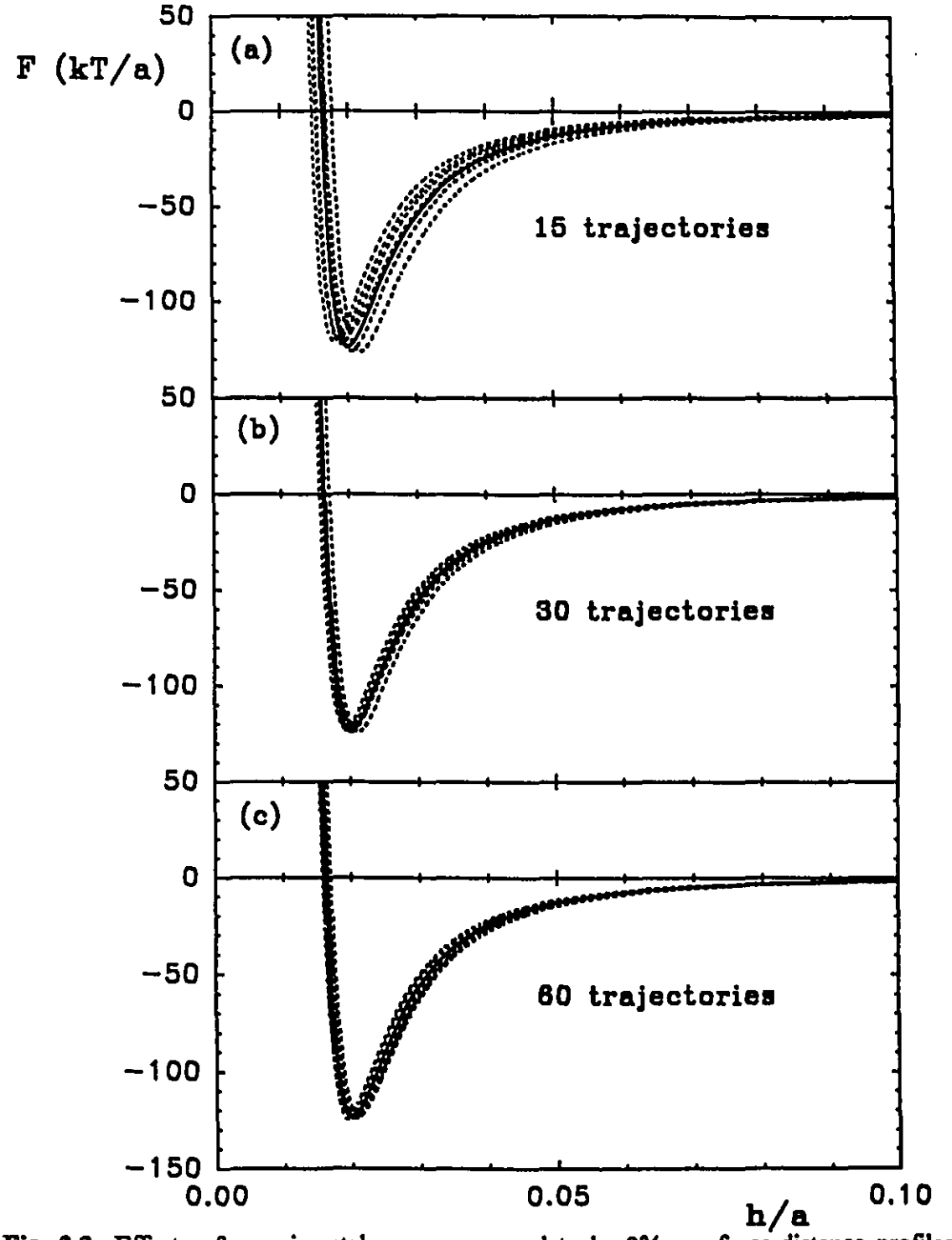

Fig. 2.3 Effects of experimental errors, assumed to be 3%, on force-distance profiles evaluated by Monte Carlo simulations. The solid curves are the force-distance profiles used in generating the trajectories, while the dotted curves are obtained by the trajectory inversion technique. The number of collision trajectories used in the fitting are (a) 15, (b) 30 and (c) 60.

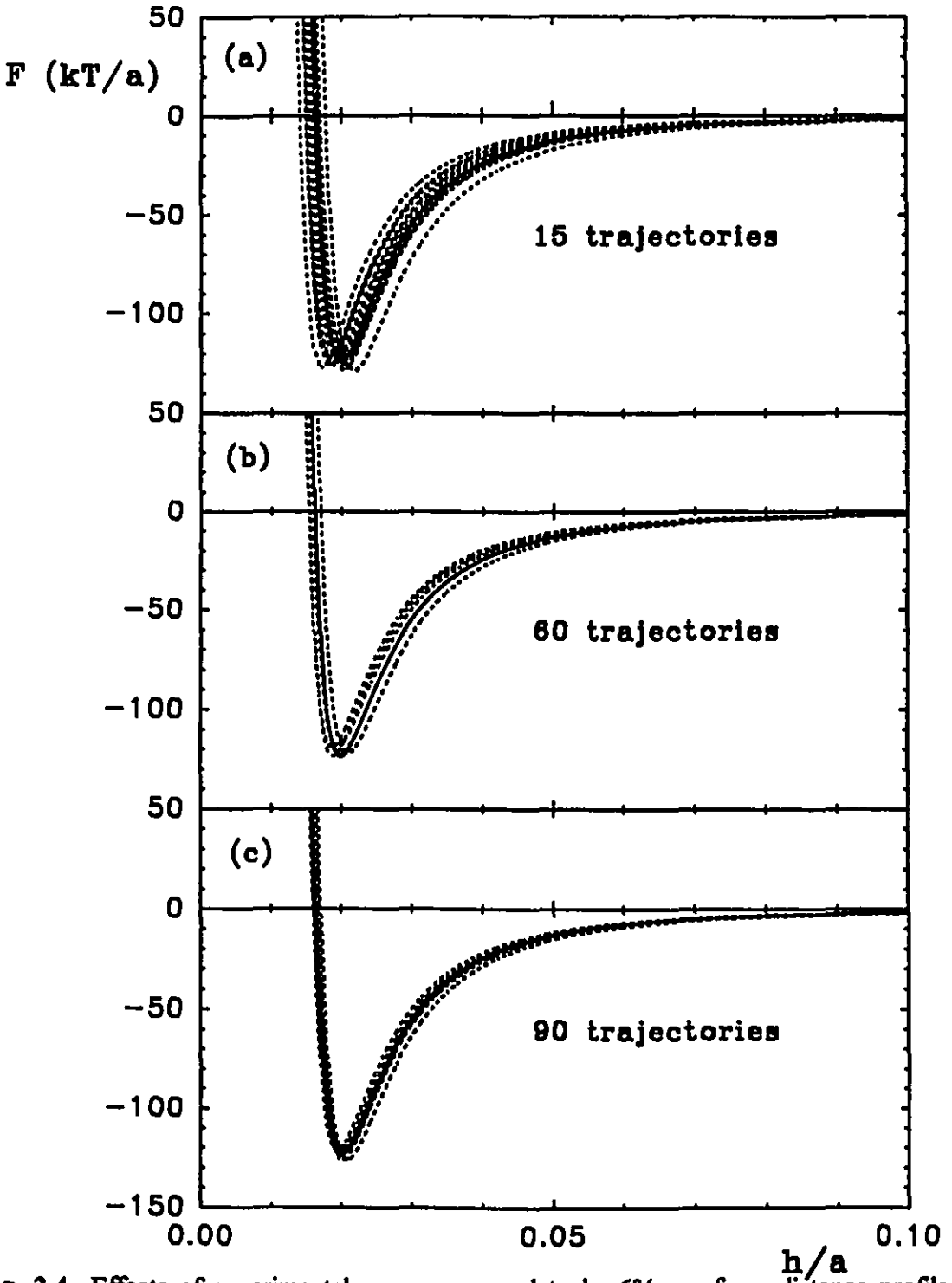

Fig. 2.4 Effects of experimental errors, assumed to be 6%, on force-distance profiles evaluated by Monte Carlo simulations. The meaning of solid and dotted curves is the same as in Fig. 2.3 The number of collision trajectories used in the fitting are (a) 15, (b) 60 and (c) 90.

$$\Delta_{x,z}^{Br} = \sqrt{\frac{2D_{x,z}a}{u}} \qquad [2.5]$$

where u is the velocity of the moving particle, $D_{x,z}$ is the diffusion coefficient of the particle in two directions perpendicular to the flow. Eq. [2.5] determines the minimum size of particles for which the collision experiment is still feasible. In aqueous solution this minimum size appears to be around 4 μm. On the other hand, using very big particles may decrease the sensitivity of detecting interaction forces since the ratio of colloidal to hydrodynamic forces decreases with increasing particle size. It has been found by trial and error that the optimal particle size in aqueous system is around 5 μm. The optimal particle size in other systems can be scaled accordingly from the relative viscosities of the systems to water, based on the Stokes-Einstein relationship between diffusion coefficient and viscosity. With the optimal particle size the error in the final position is still larger than 10% of the particle radius due to the Brownian motion effect during a collision. After certain selection procedures (to be discussed later) this error can be reduced to about 10% of the particle radius. Taking into account that the error in the initial position is much smaller (about 2%, see Experimental section for details), the average error in initial and final positions is around 6%. As mentioned above, for such an error 20-25 collisions are sufficient to fit a force profile curve.

3. Choice of the Form of F_{int}

When the shape of the function F_{int} is known from theory (e.g. DLVO theory), the most convenient choice of the parameters A_i is the one corresponding to the theoretical

parameters like Hamaker constant, double-layer thickness, etc. If the nature of the interaction is unknown, F_{int} can be chosen as a general function of interparticle distance given by a series of some orthogonal functions, e.g., a Fourier series, a Chebyshev or any other polynomial expansion, with adjustable weighting coefficients. For many colloidal systems, the form of the DLVO force is usually good enough to represent the real interaction force.

The validity of the force form given by DLVO theory has been confirmed by fitting the collision data in the simple shear flow system. The fitted force-distance profiles are shown in Fig. 2.5. Three kinds of force-distance relationships were tried. The solid curve represents the DLVO force. The dashed curve represents the polynomial form of 12th-order. The dotted curve represents a combination of an exponential term and a 10th-order polynomial term. Since the latter two forms are arbitrary, the similarity in shape between the curves given by these two force-distance relationships and the curve given by DLVO theory proves that the DLVO expression for the force is valid for systems with bare latex particles. For systems containing polymer-coated particles, a DLVO expression can still be used because its exponential repulsion term can represent either double layer repulsion or steric repulsion or both (30).

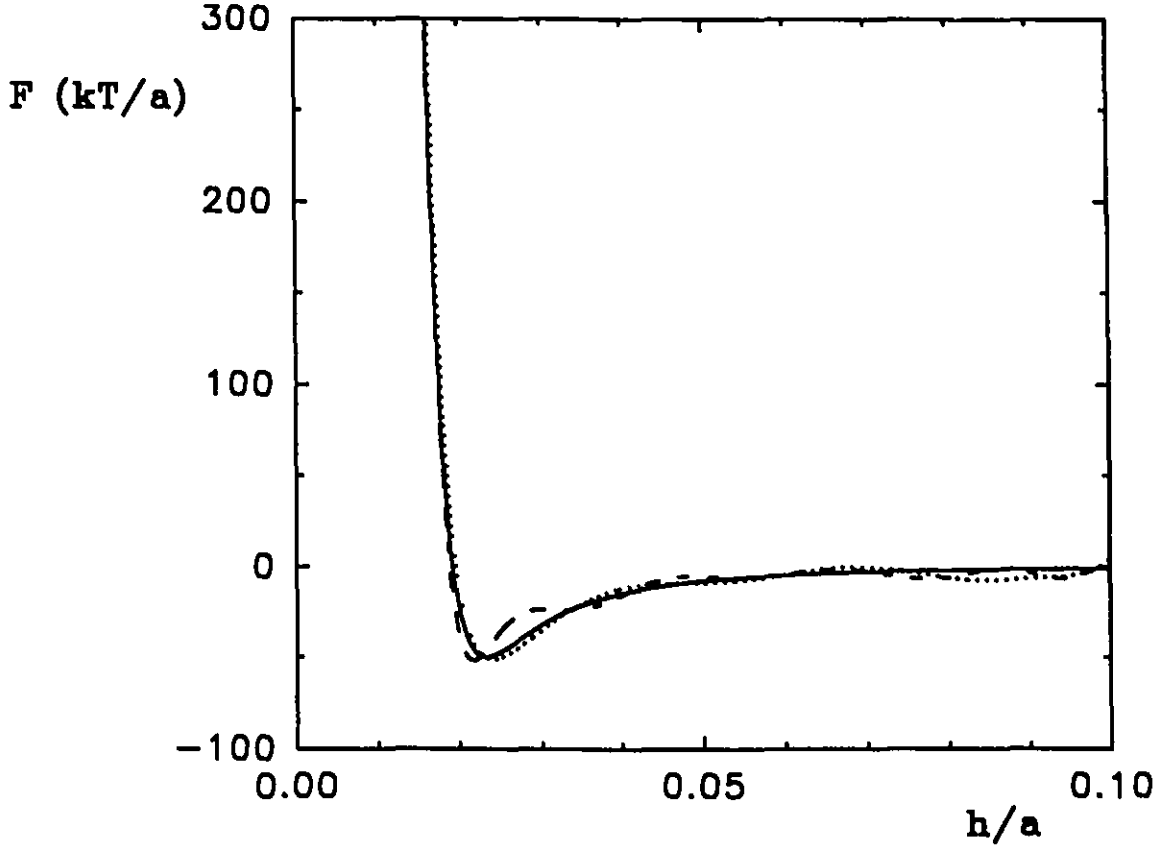

Fig. 2.5 Comparison of various force-distance curves fitted from the same set of collision data for 2.6 μm polystyrene latex particles suspended in 50% glycerol-water solution with a salt (KCl) concentration of 10^{-2} M, subjected to simple shear flow. The solid curve represents the DLVO force-distance expression. The dashed curve represents a polynomial form of 12th-order. The dotted curve represents a combination of an exponential term and a 10th-order polynomial term.

COLLISIONS IN A SIMPLE SHEAR FLOW

Experimental data of particle collision trajectories given by Takamura et al. (22,23) with the traveling microtube apparatus were reanalyzed to test our trajectory inversion technique. In these experiments collisions between 2.6 μm polystyrene latex particles were observed in a 10 mM KCl solution containing 50% glycerol to suppress the Brownian motion of the particles. A cationic polyelectrolyte "Cat-floc" was then introduced into the system, and different trajectories were observed. The description of the apparatus, the experimental procedure and the method of finding particle positions before and after a collision is given elsewhere (22,23).

Since there were not enough experimental data available (less than 10 trajectories in each experiment), we restricted ourselves to fit only two parameters, Dl and Ad (cf. Eq. [2.4]). The retardation parameter has a small influence on the shape of the force-distance curve. A value corresponding to λ = 100 nm was assumed. The value of τ was determined by the ionic strength of the suspension and was fixed in the minimization procedure. The results of the inversion of the trajectory equation for 3 systems are shown in Fig. 2.6(a, b and c). The soft wall repulsion in the absence of polyelectrolyte reflects the electric double layer interaction. A shift of the soft wall repulsion for solutions containing polyelectrolyte indicates the superposition of double-layer and steric repulsion. The fitted Hamaker constant (calculated from Ad) in Fig. 2.6(a and b) is 4.4×10^{-21} J and the fitted surface potential (calculated from Dl) is -43 mV. Takamura et al. (22) quoted a Hamaker constant of 2.7×10^{-21} J from theoretical calculations and a zeta-potential of -45 mV from electrophoresis

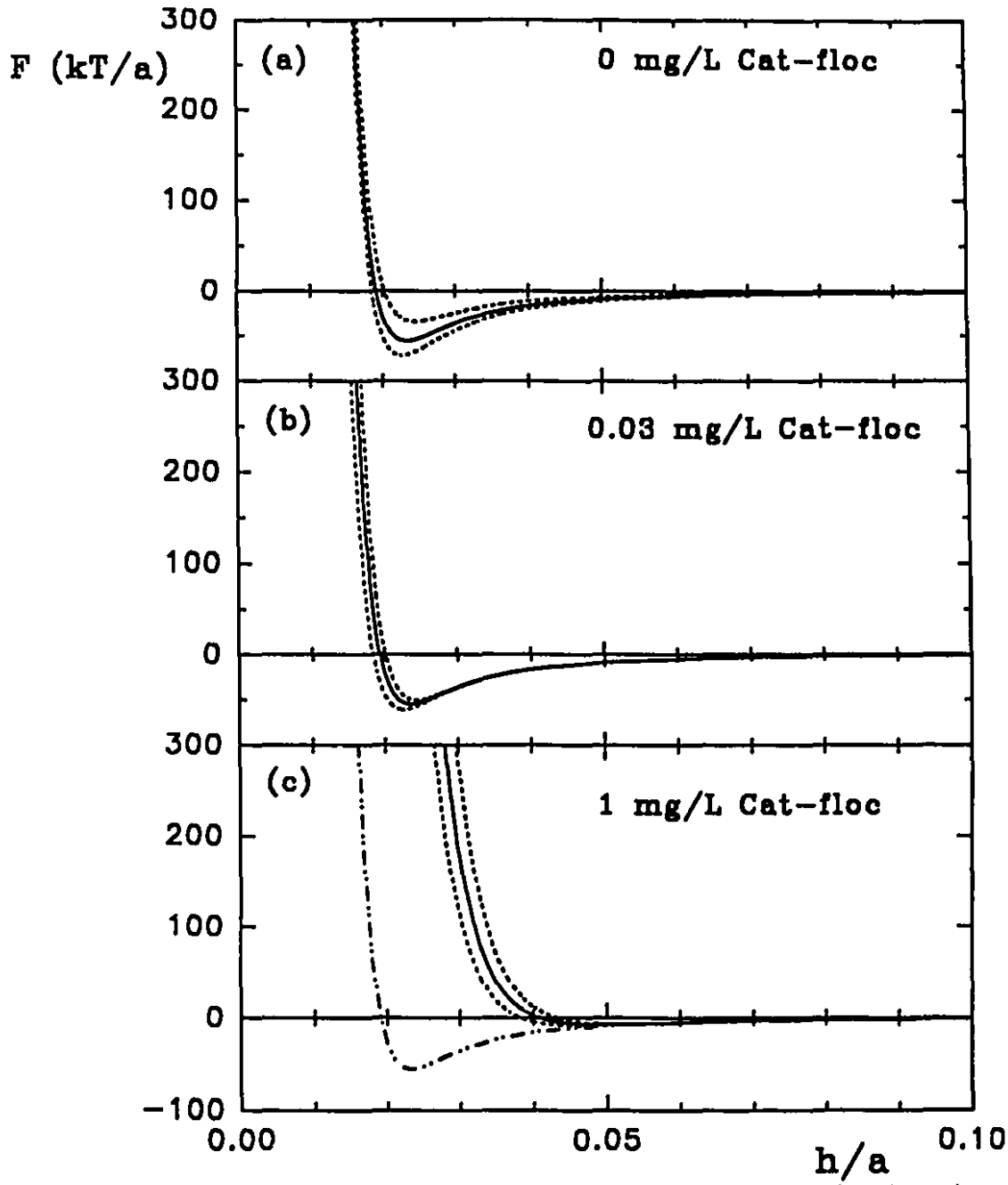

Fig. 2.6 Fitted force-distance profiles from traveling microtube data using the trajectory inversion technique. 2.6 μm polystyrene latex particles were used to study the effects of a polyelectrolyte (Cat-floc) on force-distance profiles in 50% glycerol-water solution with 10^{-2}M KCl. The dotted curves are the 90% confidence limits. (a) No Cat-floc was added. (b) 0.03 mg/L Cat-floc was added. (c) 1 mg/L Cat-floc was added. The dashed line in (c) is the result of (a) (in the absence of polyelectrolyte) used for comparison. The distance between this line and the solid line is an indication of the thickness of the adsorbed polyelectrolyte layer.

experiments. The fitted surface potential in Fig. 2.6(c) is +39 mV, and the zeta-potential from Takamura's measurement (23) is +35 mV. The agreement between our fitting results and the literature values shows that the trajectory inversion technique is really capable of extracting the interaction force profile from particle collisions.

COLLISIONS IN A WALL SHEAR FLOW

The main drawback of the traveling microtube technique is its low efficiency in generating collisions. One is unable to observe a sufficient number of collisions to satisfy the conditions of statistical significance for the inversion of the trajectory equation. In this section we propose a new experimental technique using a microcollider. It increases the efficiency by three orders of magnitude, and its trajectory measurement is far more accurate than for the traveling microtube technique since both coordinates of a particle position can be measured directly instead of being fitted (22). The microcollider creates particle collisions in a wall shear flow (cf. Fig. 2.1). Since one particle is kept stationary, one can easily control the collisions (to make a head-on collision or a grazing collision, for example). Hence, not only the number of collisions is greatly increased compared with the traveling microtube technique, but the quality of the collisions is improved as well.

The basic principles have already been discussed above. In this section a more detailed description about the trajectory equation is given.

The components of the mobility matrix in the trajectory equation (Eq. [2.1]) are found

by solving the linearized, steady-state Navier-Stokes equation and the continuity equation:

$$\begin{aligned} \mu\nabla^2\mathbf{v} &= \nabla p \\ \nabla\cdot\mathbf{v} &= 0 \end{aligned} \qquad [2.6]$$

where $\mathbf{v}(\mathbf{x})$ is the fluid velocity vector at point $\mathbf{x}$ and p is the pressure.

If we consider a system bounded by a stationary wall with an undisturbed fluid flow field given by $\mathbf{v}^0(\mathbf{x})$, the solution of Eq. [2.6] for two solid particles can be written as:

$$\mathbf{v}(\mathbf{x}) = \mathbf{v}^0(\mathbf{x}) + \sum_{i=1}^{2} \int_{S_i} \mathbf{O}(\mathbf{x},\mathbf{y})\cdot\mathbf{f}(\mathbf{y})\,dS_i(\mathbf{y}) \qquad [2.7]$$

where $\mathbf{f}(\mathbf{y})$ is the force density at a point $\mathbf{y}$ of the particle surface S. The no-slip boundary conditions at the wall can be satisfied by choosing a proper expression for the Oseen tensor $\mathbf{O}(\mathbf{x},\mathbf{y})$ (31,32).

The total force $\mathbf{F}_j$ and torque $\mathbf{T}_j$ exerted by the particle j (j=1,2) on the fluid are given by:

$$\begin{aligned} \mathbf{F}_j &= \int_{S_j} \mathbf{f}(\mathbf{y})\,dS_j(\mathbf{y}) \\ \mathbf{T}_j &= \int_{S_j} (\mathbf{y}-\mathbf{r}_j)\times\mathbf{f}(\mathbf{y})\,dS_j(\mathbf{y}) \end{aligned} \qquad [2.8]$$

where $\mathbf{r}_j$ is the vector pointing to the center of sphere j.

Eqs. [2.7] and [2.8] can be reduced to discrete form by using the Kirkwood-Riesman theory which was generalized by Dabros (33) to account for the presence of a wall. In

discrete form particle surfaces are divided into subunits and the integration in Eqs. [2.7] and [2.8] is replaced by summation over these subunits. A more detailed discussion of the subunit method is presented elsewhere (34).

The two particles in the collision are considered equal-sized spheres. One of them is free to move and rotate as a result of the external flow and forces acting on it and the other one is held stationary on the wall. The force exerted on the subunits of each particle is chosen in such a way that the appropriate boundary conditions are satisfied at the particle surface. For the freely mobile particle the force, which consists of the interaction force between particles and possible external forces, has to be balanced by the hydrodynamic force. The same applies to torques acting on this particle. The inertia effects are expected to play no significant roles.

When the number of subunits for the two spheres is equal to m, Eq. [2.7] can be replaced by 6m linear equations plus six equations for the mobile particle expressing the balance of forces and torques. When the forces acting on the particle are specified, one can find 6m force components acting on the subunits and six components of the translational and rotational velocities. A sum of proper force components acting on the stationary particle provides information on the hydrodynamic force to which the particle is subjected. In our calculations we match the numerical solutions with the analytical lubrication theory solutions (36-41) for small interparticle and/or particle-wall separations.

In the creeping flow limit the translational and rotational velocities of a particle (u_i and ω_i) are linear functions of the total forces and torques (f_i and t_i). Following Brenner's notation (35) the generalized velocity $U = \{u_1,u_2,u_3,\omega_1,\omega_2,\omega_3\}$ and force $F = \{f_1,f_2,f_3,t_1,t_2,t_3\}$ acting on

the freely mobile particle are related by:

$$\mathbf{U} = \mathbf{M} \cdot \mathbf{F} \qquad [2.9]$$

where **M** is the symmetrical, second order mobility tensor of dimension 6×6. The resistance matrix **R** is defined as the inverse of the mobility matrix: $\mathbf{R} = \mathbf{M}^{-1}$. From Eq. [2.9] it follows that $\mathbf{F} = \mathbf{R} \cdot \mathbf{U}$.

The mobility and hence the resistance matrices depend on the viscosity of the fluid and geometry of the system. For two spherical particles near a wall, the components of **M** can be calculated from the response of a particle to a unit force and torque in a quiescent fluid. For small separations expressions from lubrication theory can be used for the components of **M** (34).

With known expressions for the mobility tensor, for the hydrodynamic force acting on the moving particle at any given position and for the interaction forces between two particles and between the moving particle and the wall, the trajectory equation (Eq. [2.1]) can be solved numerically (34).

EXPERIMENTAL SECTION

In this section we discuss some experiments with the microcollider. Because of its distinctive advantages over the traveling microtube apparatus, we no longer use the latter for the observation of particle collisions.

1. Materials

Two systems were studied. In one system we used 3.4 μm polystyrene latex particles, supplied by Dow Chemicals, in a glycerol (28% by weight) - water solution. In the other system we used 5 μm polystyrene-divinylbenzene latex particles, supplied by Duke Scientific, in D_2O (60% by volume) -water mixture.

The ionic strengths of the two solutions were adjusted by the addition of KCl to 10^{-4} M and 10^{-3} M respectively. The glycerol was used to suppress the Brownian motion of the particles as well as to prevent them from sedimentation. D_2O was used only to prevent the sedimentation. The Brownian motion effect was reduced by using bigger particles (5μm).

2. Setup and Procedures

The diagram of the microcollider is shown in Fig. 2.7. The latex suspension is contained between two parallel plates placed at a distance of about 150 μm from each other. The upper plate is transparent to enable observation with an optical microscope. It is attached to an x-y-z manual manipulator for accurate positioning. The lower plate is the bottom of a sample cell in which the suspension is contained. It is mounted on the platform of an electronic x-y manipulator which can be either driven by an IBM 386 computer or controlled manually with a joystick. The movement of the bottom plate creates a wall shear flow in the gap between the two plates. Since the ratio of the gap and the size of the plate is of the order of 0.001, at the center of the plate the edge effects which could disturb the flow pattern can be neglected.

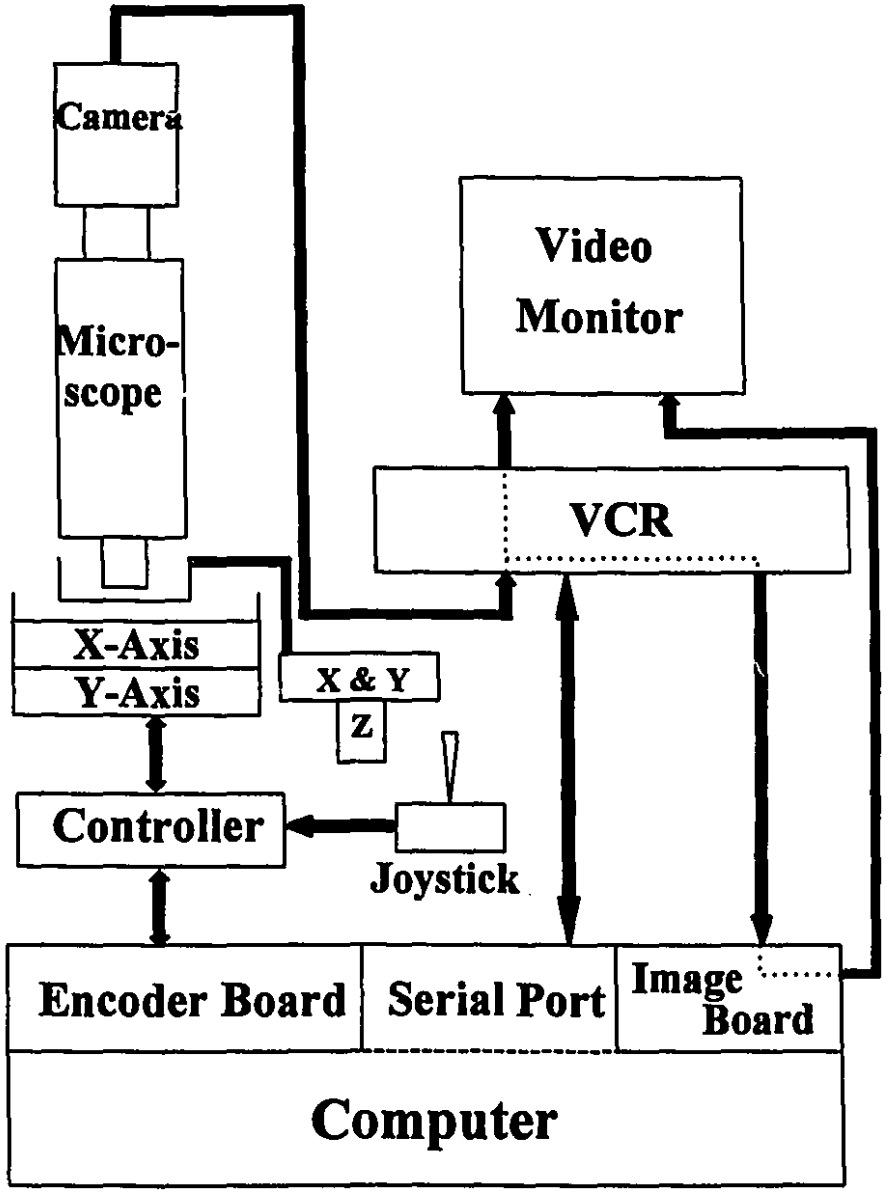

Fig. 2.7 Setup of a microcollider. A wall shear flow is generated by moving the x and y-axes of an electric micromanipulator (or encoder stage). The particle collisions occurring in the flow are observed under the microscope and recorded with the video camera and VCR. The collision trajectories are analyzed by the image processing board plugged in the computer. The solid arrows indicate the directions of controlling and feedback data signals.The shaded arrows indicate the directions of video signals.

The first step of the experiment is to find a stationary particle stuck to the upper plate due to random collisions between the particle and the plate. Then the bottom plate is moved with a joystick to bring any mobile particle in close vicinity of the stationary particle. After positioning the mobile particle, we set the movement speed of the electronic manipulator to obtain the desired value of the shear rate and let these two particles collide (cf. Fig. 2.8). The collision can be monitored and recorded with a video monitor, a VCR and a video camera mounted on an optical microscope (Zeiss Axioplan). The same procedure is repeated to obtain a sufficient number of collisions required to invert the trajectory equation.

A typical picture of a collision is shown in Fig. 2.9. Subsequent parts of the figure represent three stages of a particle trajectory: before, during and after collision. For the purpose of the numerical analysis presented in the previous sections we are only interested in the initial and final parts of the trajectory, i.e., when the distance between the two particles exceed 6 radii. At such a separation distance the particle moves along a straight line in the direction of the flow since its motion is not influenced by the presence of the stationary particle. From the analysis of the motion of the moving particle we can find two coordinates x and z perpendicular to the direction of shear (cf. Fig. 2.1). This is done by analyzing the recording of the collision using an image processing technique. The video signal containing the process of a collision is digitized by a PC Vision Plus video analyzing board (Imaging Technology) plugged in the computer. From each video frame the positions of the particles are extracted. Proper calibration of the image enables us to express the distance between particles in micrometers. Since the VCR (JVC BR-S605U) is computer-driven, frame analysis proceeds automatically from the moment the moving particle enters the monitor screen till the

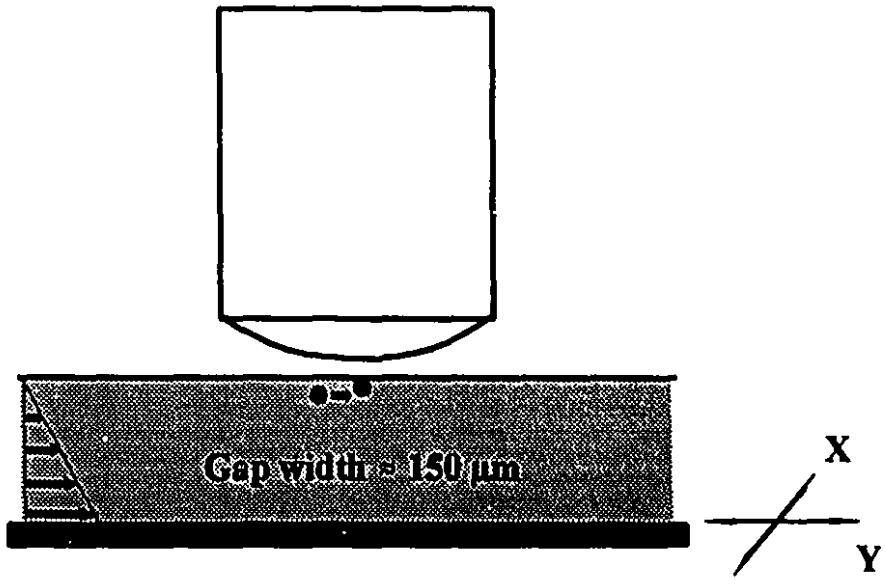

Fig. 2.8 Particle collision in the sample cell. The upper plate remains stationary during a collision. The lower plate, which is mounted on the platform of the electric manipulator, moves at a velocity set by the computer. The gap width, h, is usually adjusted to be approximately 150 μm. A wall shear flow with certain shear rate is thus generated. The mobile particle moves in the shear flow and collides with the stationary particle stuck to the upper plate. Its initial position can be accurately controlled by moving the x-y manipulator with a joystick.

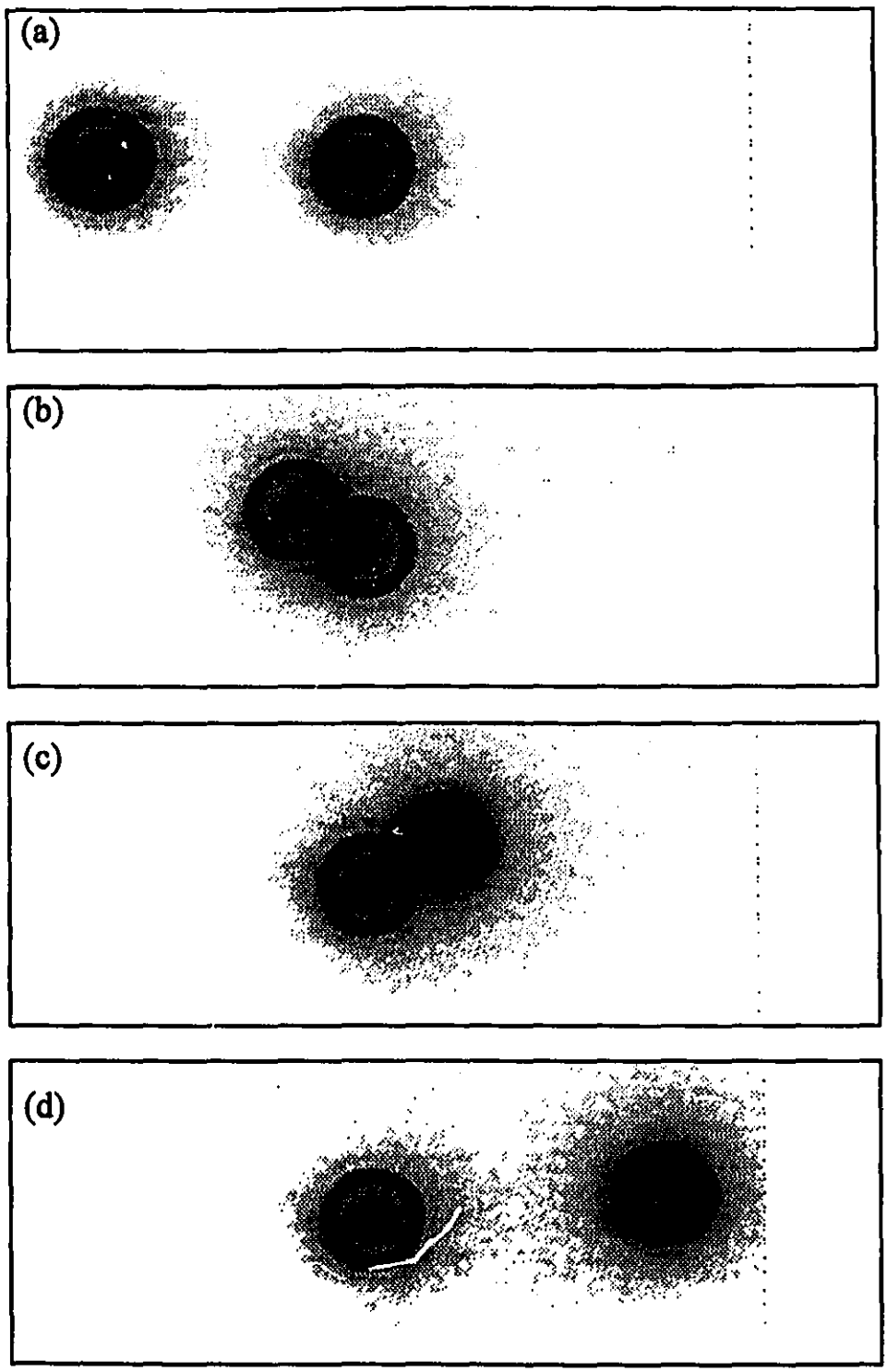

Fig. 2.9 Snapshots of different stages of a particle collision: (a) the first stage: before collision; (b) the second stage: during collision, approaching part; (c) the second stage: during collision, receding part; (d) the third stage: after collision.

moment when the distance between the moving particle and the stationary particle is equal to 6 particle radii. This procedure yields the required information about the position of the moving particle prior to the collision (initial position). The video frame analysis is then interrupted during the moment of collision and resumed after the collision when the distance between particles exceeds, again, 6 particle radii. The analysis is continued until the moving particle leaves the monitor screen, yielding the information about the position after the collision (final position). A typical graph illustrating the changes of the moving particle positions before and after the collision is shown in Fig. 2.10. Since the particle moves in the direction of shear, the x-coordinate perpendicular to shear remains unchanged, and the y-coordinate along shear changes linearly with time yielding the particle velocity. The scattering of the particle positions around the straight lines is the result of Brownian motion and external noise (even though the whole setup is placed on a vibration-free table to minimize the influence of external noise).

It is evident from Fig. 2.10 that the x-coordinate before and after the collision can be measured directly. In principle the distance of a particle to a wall (z-coordinate) can be determined either by hydrodynamics (17) or by total internal reflection microscopy (TIRM) (18) or by reflection interference contrast microscopy (RICM) (19). The hydrodynamic method is the simplest one for obtaining the distance between a particle and a wall since it only needs measurements of the particle velocity and the shear rate. The former has already been given by the analysis of the y-coordinate varing with time. The shear rate can be simply calculated by dividing the manipulator speed by the gap width between the two parallel plates. Hence, we chose the hydrodynamic method to determine the z-coordinate in the CPS method.

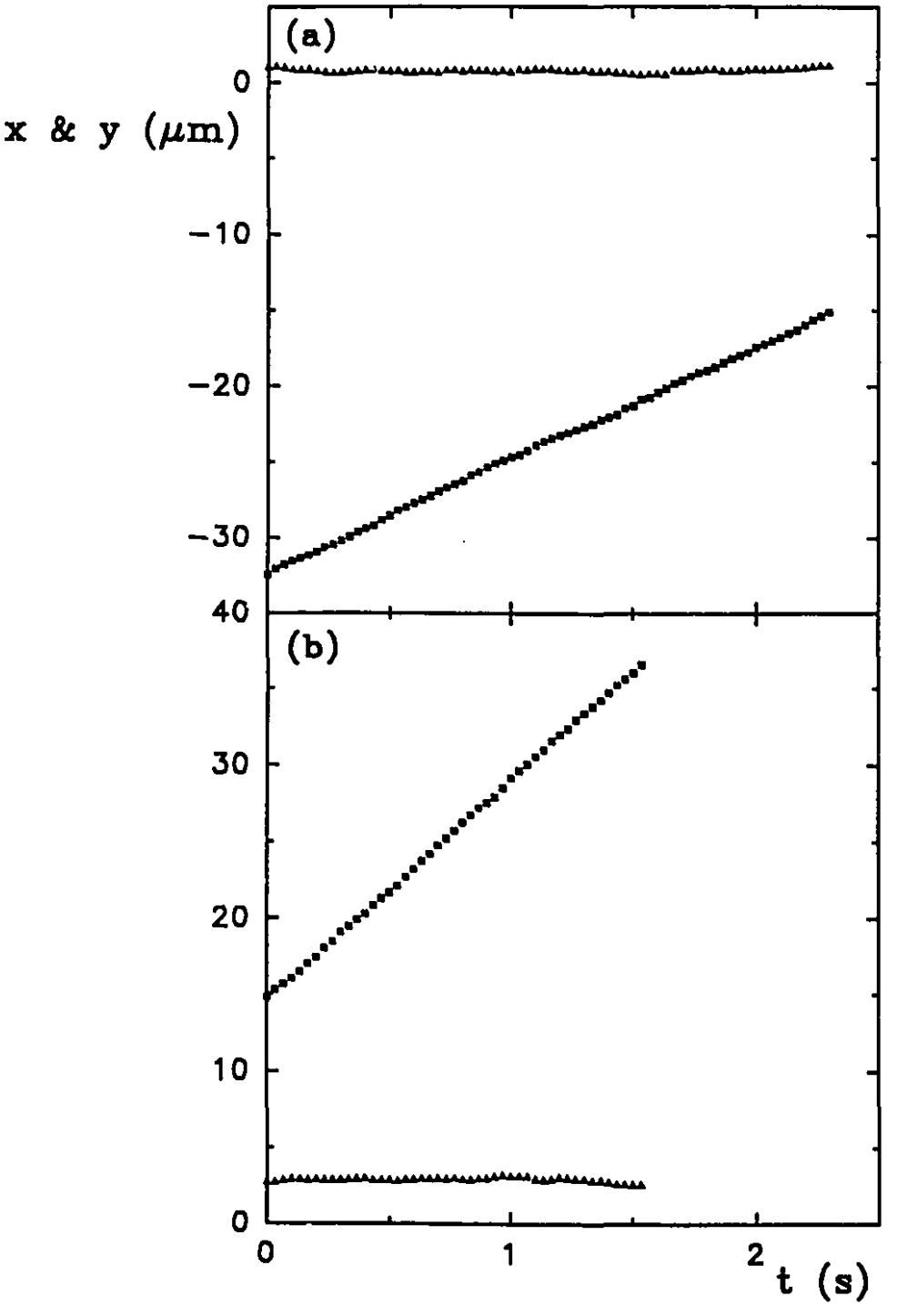

Fig. 2.10 Position changes of the moving particle during a collision. The triangles stand for the x-coordinate and the squares stand for the y-coordinate. The stationary particle is at position (0,0). (a) The position of the moving particle as a function of time before a collision. (b) The position of the moving particle as a function of time after a collision.

The procedure is as follows. The velocity, u, of a sphere moving in the vicinity of the wall in a shear flow is given by:

$$u = f_3(H)Gz \qquad [2.10]$$

where $H = (z - a)/a$, and $f_3(H)$ is a correction function accounting for the influence of the wall on the motion of the particle given by refs. (37,42-44). We have tabulated $f_3(H)$ according to the expressions given by O'Neil and coworkers (42-44) at 60 distances (note that a factor of 0.5 is missing in Eq. [4.24] in ref. (44)). At other distances $f_3(H)$ can be calculated by cubic spline interpolation. After the velocity of the moving particle has been found, we can invert Eq. [2.10] to find the distances between the particle and the wall (z-coordinate) before and after the collision. The z-coordinate determined in this way is very accurate. The error is usually around 3% of the particle radius. The x-coordinate is even more accurate because it can be directly measured. After the initial and final positions of the moving particle for all collisions have been found, we plot them in a "scattering diagram" (cf. Figs. 2.2 and 2.11). This diagram is a convenient way of presenting experimental data and also provides information about the properties of a system even before the parameter fitting is performed.

Finally, we proceed with the trajectory inversion calculation presented above to obtain the interaction force-distance profile.

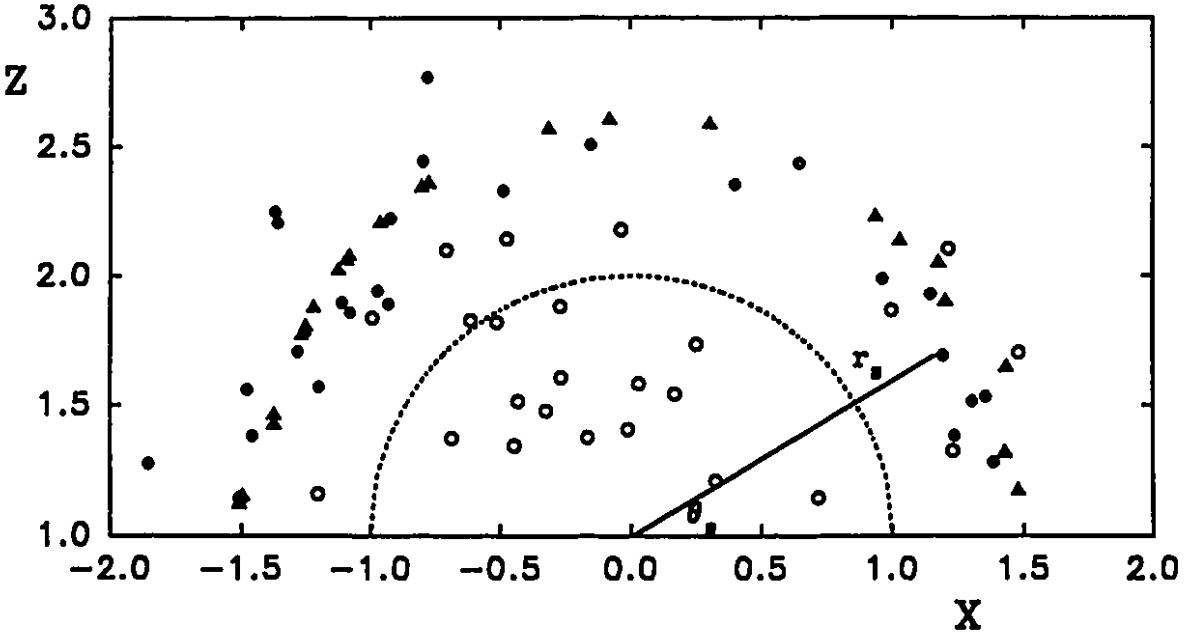

Fig. 2.11 A scattering diagram of 3.4 μm latex particle collisions in 28% glycerol-water solution with 10^{-4} M KCl. The coordinates are scaled by the particle radius. The open circles represent the initial positions of the moving particles. The filled circles represent the experimentally determined final positions of the particles. The filled triangles stand for the theoretically calculated final positions of the particles. The semicircle in the middle is the projection shadow of the stationary particle.

RESULTS AND DISCUSSION

Fig. 2.11 shows the scattering pattern obtained for 25 collisions in the glycerol-water system. The open circles stand for the initial positions of the moving particle and the filled circles are the final positions of the particle. The semi-circle in the middle is the projection "shadow" of the stationary particle. It can be seen that all trajectories that start within the semi-circle or close to it end up much further away from it. This indicates that there is a strong repulsive force acting between two particles, which was confirmed when we applied the minimization procedure to obtain the interaction force as a function of interparticle distance. As a test function we assumed that the force-distance relationship was given by DLVO theory (cf. Eq. [2.4]) with three adjustable parameters: the dimensionless double layer τ, the double layer interaction parameter Dl and the scaled Hamaker constant Ad. The retardation parameter Al was kept constant at a value corresponding to λ = 100 nm. The resulting force profile is shown in Fig. 2.12. The best fit gives: double-layer thickness $1/\kappa$ = 28.5 nm, Hamaker constant $A = 2.1\times10^{-20}$ J and surface potential ψ_0 = -54 mV. The surface potential is in good agreement with the zeta potential, ζ = -51 mV measured with a microelectrophoresis apparatus (Rank Brothers, Cambridge, England). The double-layer thickness also agrees with the theoretical value, 28.9 nm, calculated from the ionic strength of the solution. The fitted force profile describes a strong electrostatic repulsion with a shallow secondary minimum. The dotted lines indicate the 90% confidence intervals for the force profile. The accuracy of the procedure will be discussed in more detail below.

After the interaction force profile has been obtained, one can solve again the trajectory

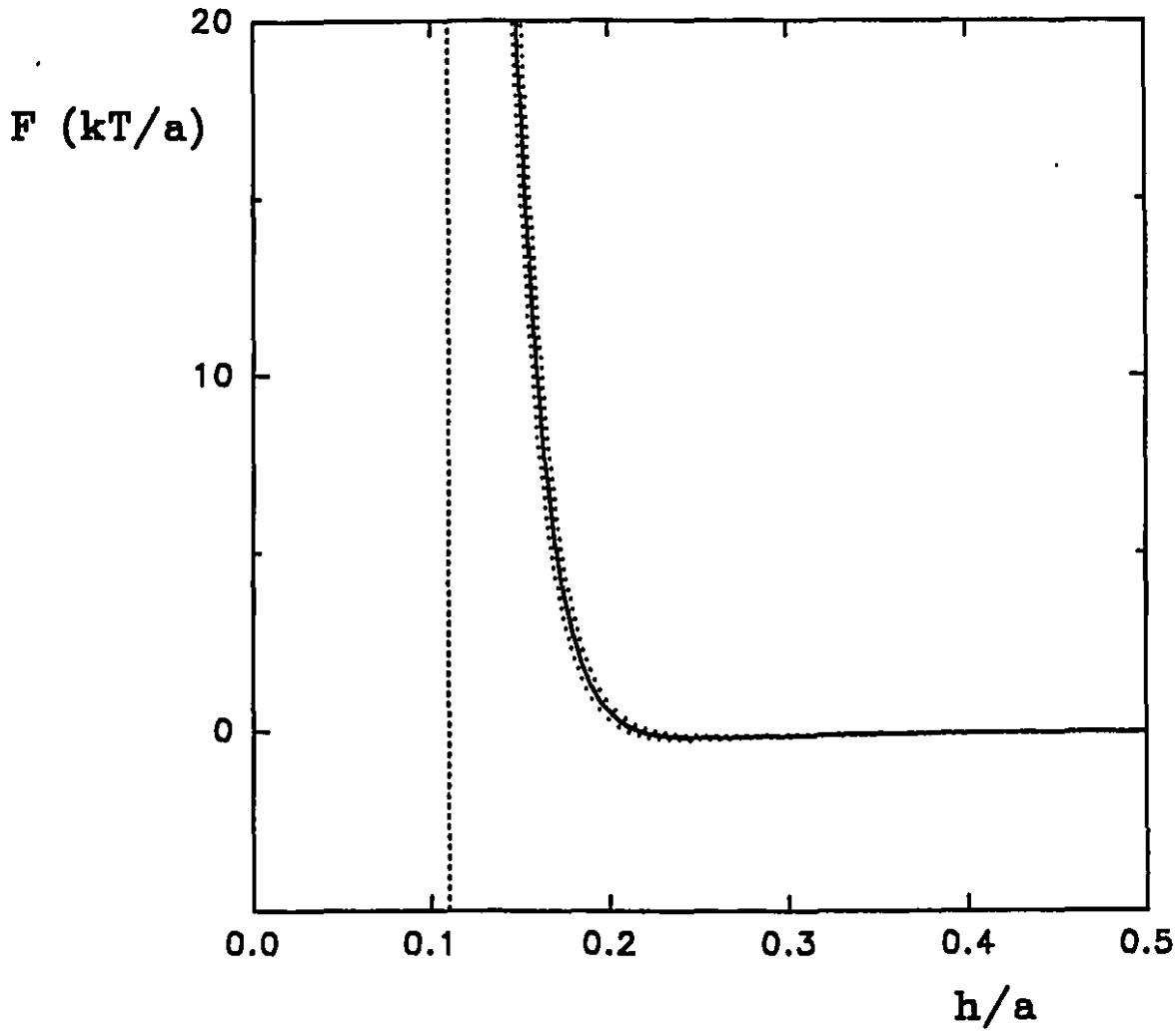

Fig. 2.12 Fitted interaction force vs. interparticle distance profile in 28% glycerol-water solution with 10^{-4} M KCl. The distance has been scaled by particle radius (a = 1.7 μm). The force has been scaled by kT/a. The solid line is the force-distance curve. The dotted lines are the confidence intervals at 90% confidence level. The dashed line on the left is the minimum separation distance between the two particles observed in the experiment. The fitted Hamaker constant, A, is 2.1×10^{-20} J and the fitted surface potential, ψ_0, is -54 mV.

equation for the experimentally given initial positions to calculate the "theoretical" final positions and then compare them with the experimental final positions. The filled triangles in Fig. 2.11 are these theoretical positions. The differences between them and experimental final positions can be attributed to the influence of Brownian motion, the instrumental error in measuring particle positions, misalignment and slight vibration of the system. Polydispersity of the sample can also contribute to the error since all calculations are performed in dimensionless units scaled by the particle radius assumed identical for both particles. Among all of these errors, Brownian motion is the most serious one. Other errors are either small or can be eliminated under certain conditions. As mentioned earlier, there are two kinds of Brownian motion effects. The effect to the particle position measurement can be minimized by a selection criterion which discards collisions with a difference in the directions of approaching and receding trajectories greater than 1°. The effect to the collision trajectory can be minimized by selecting collisions with a scattering angle, θ_s, (see Fig. 2.11 for definition) similar to the one predicted by the hydrodynamic theory. This selection criterion does not affect the choice of force parameters because it has been found by experience that the force profile mainly changes the radial scattering distance, r_s. The scattering angle almost solely depends on the hydrodynamics. In the case of the experiments with glycerol-water system, the 25 collisions used for fitting were selected from 80 observed collisions using these criteria.

The same experiment was carried out in a D_2O-water system. The scattering pattern is shown in Fig. 2.13. The meaning of symbols is the same as in Fig. 2.11. Before we started the Marquart-Levenberg fitting, we studied the topology of χ^2 of this system using bicubic spline interpolation from 54 grid points. The resulting contour map of χ^2 (cf. Fig. 2.14)

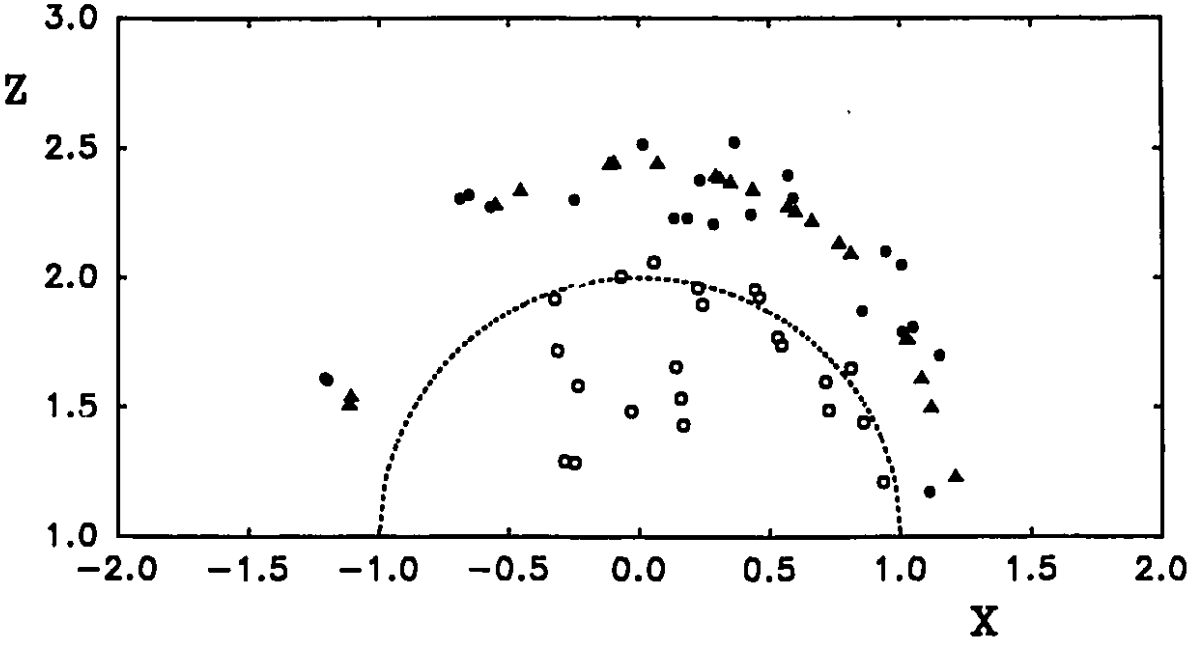

Fig. 2.13 A scattering diagram of 5 μm latex particle collisions in 60% D_2O-water mixture with 10^{-3} M KCl. The coordinates are scaled by particle radius. The meaning of the symbols is the same as in Fig. 2.10.

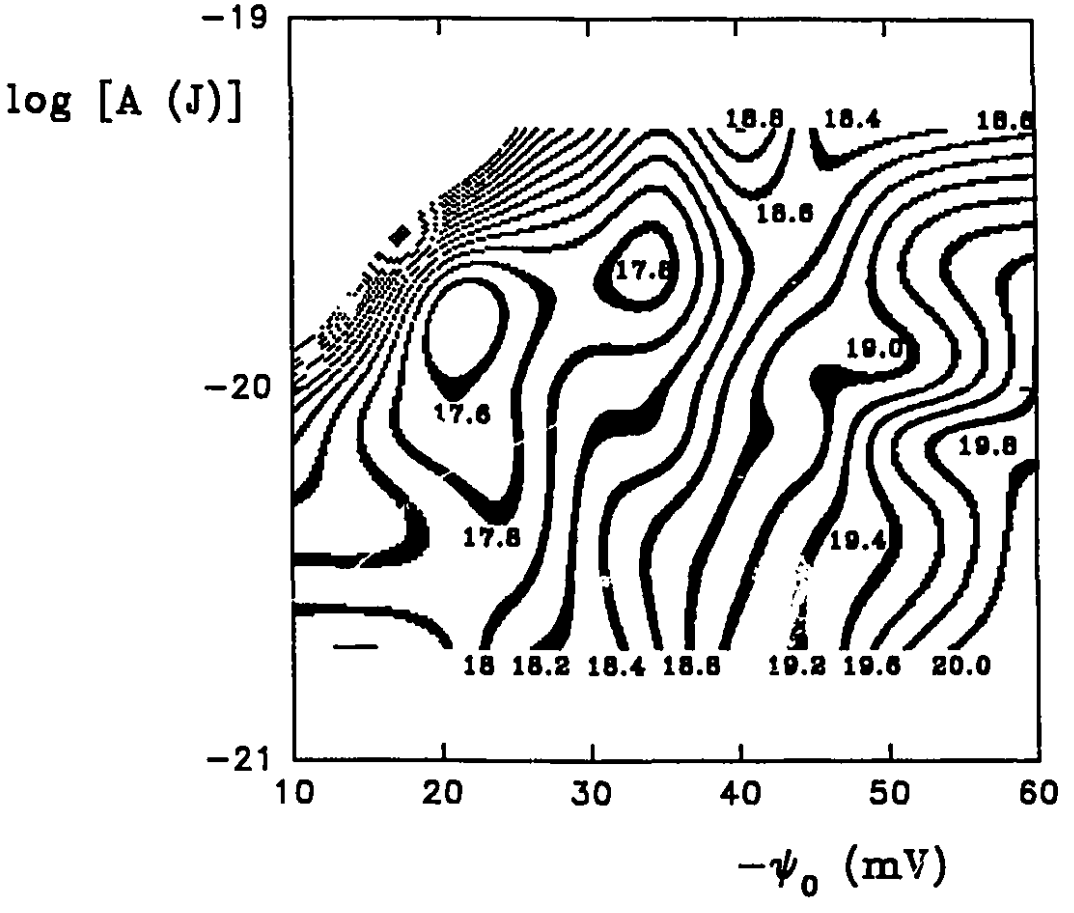

Fig. 2.14 χ^2 contour map of the fitting of 5 μm latex particle collisions in 60% D_2O-water mixture with 10^{-3} M KCl. The numbers on the graph are χ^2 values. The double-layer thickness $1/\kappa$ is fixed according to the calculated value, 30 nm. ψ_0 is the surface potential and A is the Hamaker constant.

shows two minima (near χ^2 = 17.6 and 17.8) and one flat valley around ψ_0 = -40 mV and A = 2×10^{-20} J. The minimum surrounded by the 17.6 contour circle (ψ_0 = -22 mV and A = 1.4×10^{-20} J) is too far away from the experimental zeta potential, ζ = -42 mV. The flat valley was not chosen because the value of χ^2 (18.4) is relatively large. Hence, the minimum surrounded by 17.8 contour circle (ψ_0 = -32 mV and A = 2×10^{-20} J) is the only one which provides a good fit to the data. The starting point of the Marquart-Levenberg fitting was thus chosen within the circle to prevent trapping in other inappropriate local minima.

The values of the best fit parameters are: Hamaker constant A = 2.0×10^{-20} J and surface potential ψ_0 = -33 mV. The corresponding force profile is shown in Fig. 2.15(a). Both of the two parameters agree reasonably well with the theoretical Hamaker constant A = 9.5×10^{-21} J calculated from spectroscopic data (45) and the zeta potential ζ = -42 mV measured by microelectrophoresis.

The slightly bigger value of the measured Hamaker constant can be explained by the experimental error and the influence of the surface roughness of the particles which increases the apparent van der Waals attraction (46).

It is of interest to compare the experimental Hamaker constant with the theoretical Hamaker constant A = 9.5×10^{-21} J since one hypothesis (47) suggests that there is a long range hydrophobic interaction force between hydrophobic bodies (like two latex spheres). If hydrophobic forces were operating, the apparent Hamaker constant should be at least an order of magnitude larger than the theoretical one. The experimental Hamaker constant determined here with CPS together with the results of Figs. 2.6 and 2.12 does not show the existence of such a hydrophobic force between two latex spheres, at least not for distances

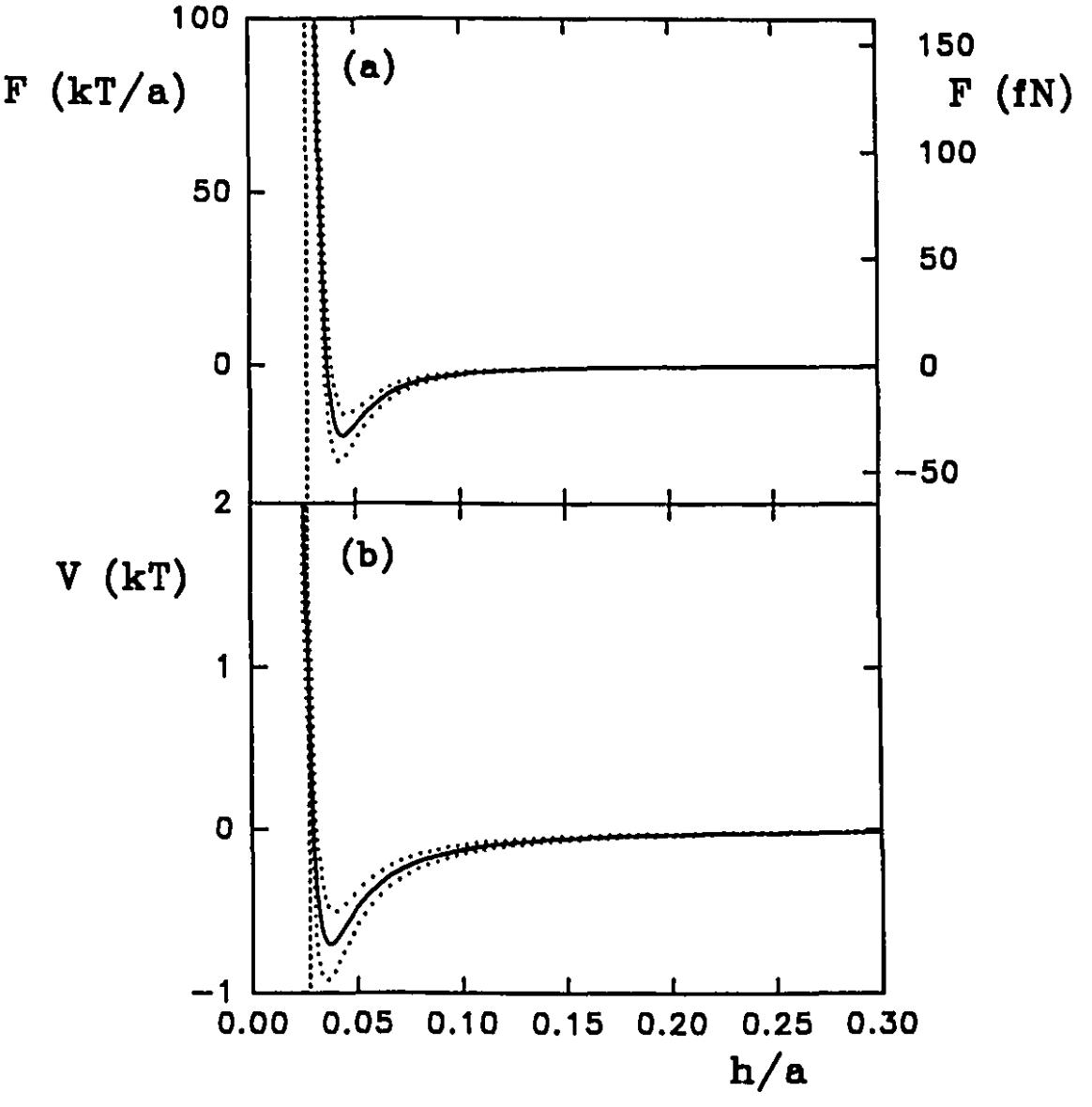

Fig. 2.15 (a) Fitted interaction force vs. interparticle distance profile in 60% D_2O-water mixture with 10^{-3} M KCl. The distance has been scaled by particle radius (a = 2.5 μm). The force is presented in both dimensionless form scaled by kT/a and in dimensional units, fN (10^{-15} N). The solid line is the force-distance curve. The dotted lines are the confidence intervals at 90% confidence level. The dashed line on the left is the minimum separation distance (about 75 nm) between the two particles observed in the experiment. The fitted Hamaker constant, A, is 2.0×10^{-20} J and the fitted surface potential, ψ_0, is -33 mV. (b) Fitted interaction energy vs. interparticle distance profile integrated from the above force profile. The energy has been scaled by kT. The meaning of curves and lines is the same as above.

larger than about 75 nm.

It is worth noting that, when we express the interaction force profile in dimensional units [cf. Fig. 2.15(a)], the magnitude of the force measured with our method is on the order of 10^{-14} N, which is 3 - 4 orders of magnitude smaller than the minimum force that can be detected by a SFA or an AFM. If we transform this force into a corresponding interaction energy, we obtain an energy of the order of kT [cf. Fig. 2.15(b)], which is a typical depth of the secondary energy minimum in a stable colloidal system. With this sensitive force detection ability, some useful properties of a colloidal system can thus be predicted from the force measurement.

CONCLUSION

In this paper we presented a new method to determine interaction forces between colloidal particles. The advantage of this method over other force measurement methods is that it determines the forces acting between two colloidal particles during a collision — a dynamic process taking place repeatedly in a real colloidal system and playing a key role in its stability as well as its rheological behavior. The forces determined in such a way can thus be used to predict the properties of a colloidal system. The method is based on the inversion of the trajectory equation that governs the relative motion of particles in a shear flow. From the experimentally determined positions of two particles before and after a collision, we can find the parameters describing the dependence of the interaction force upon distance between

these two particles. This is achieved by minimizing the differences between the experimentally determined final positions of particles and the final positions calculated from respective experimental initial positions by solving the trajectory equation.

The Monte Carlo simulations show that approximately 25 collisions are required to obtain a reliable force-distance curve. The traveling microtube technique, which was used previously to study collisions of colloidal particles, fails to offer such a number of collisions in a single experiment. Nevertheless, some meaningful results can be obtained by applying our minimization technique to the existing traveling microtube data.

A new experimental technique, the surface collision apparatus, has been developed to replace the traveling microtube technique. It is based on the observation of collisions between two particles in a wall shear flow. Although the theoretical analysis of the hydrodynamic problem in this case is much more complicated than that in a simple shear flow (the system of the traveling microtube), the experimental technique has proven to be far more efficient than that of the traveling microtube. With the aid of a fast computer, the problem of the theoretical analysis can also be solved.

Preliminary results of the interaction forces between polystyrene latex particles in mixtures of glycerol-water and D_2O-water prove the usefulness of the technique. Furthermore, they indicate that the method is much more sensitive than SFA and AFM methods. It is capable of determining a force corresponding to an interaction energy of several kT.

REFERENCES

1. Israelachvili, J. N., and Adams, G. E., *J. Chem. Soc., Faraday Trans. 1* **74,** 975 (1978).
2. Israelachvili, J. N., "Intermolecular and Surface Forces." 2nd Ed., Academic Press, San Diego 1992, p.169.
3. Marra, J., and Hair, M. L., *J. Colloid Interface Sci.* **125,** 552 (1988).
4. Israelachvili, J. N., and Kott, S. J., *J. Polym. Sci.*, Part B: *Polym. Phys.* **27,** 489 (1989).
5. Binnig, G., Quate, C. F., and Gerber, Ch., *Phys. Rev. Lett.* **56,** 930 (1986).
6. Hartmann, U., *Phys. Rev. B* **43,** 2404 (1991).
7. Weisenhorn, A. L., Hansma, P. K., Albrecht, T. R., and Quate, C. F. *Appl. Phys. Lett.* **54,** 2651 (1989).
8. Ducker, W. A., Senden, T. J., and Pashley, R. M. *Nature* **353,** 239 (1991).
9. Butt, H.-J., *Biophys. J.* **60,** 1438 (1991).
10. Li, Y. Q., Tao, N. J., Garcia, A. A., and Lindsay, S. M. *Langmuir* **9,** 637 (1993).
11. Evans, E., *Biophys. J.* **31,** 425 (1980).
12. Parsegian, V. A., Rand, R. P., and Fuller, N. L., *J. Phys. Chem.* **95,** 4777 (1991).
13. Rohrsetzer, S., Kovács, P., and Nagy, M., *Colloid Polym. Sci.* **264,** 812 (1986).
14. Dabros, T., and van de Ven, T. G. M., *Colloid Polym. Sci.* **261,** 694 (1983).
15. Adamczyk, Z., Dabros, T., Czarnecki, J., and van de Ven, T. G. M., *Adv. Colloid Interface Sci.* **19,** 183 (1983).

16. Schumacher, G. A., and van de Ven, T. G. M., *Langmuir* **7**, 2028 (1991).

17. Alexander, B. A., and Prieve, D. C., *Langmuir* **3**, 778 (1987).

18. Prieve, D. C., and Frej, N. A., *Langmuir* **6**, 396 (1990).

19. Rädler, J., and Sackmann, E., *Langmuir* **8**, 848 (1992).

20. Hunter, R. J., "Foundations of Colloid Science." Vol.2, Clarendon Press, Oxford 1989, p.692.

21. Hirtzel, C. S., and Rajagopalan, R. "Colloidal Phenomena - Advanced Topics." Noyes Publications, Park Ridge, p.219.

22. Takamura, K., Goldsmith, H. L., and Mason, S. G., *J. Colloid Interface Sci.* **82**, 175 (1981).

23. Takamura, K.; Goldsmith, H. L.; Mason, S. G., *J. Colloid Interface Sci.* **82**, 190 (1981).

24. Press, W. H., Flannery, B. P., Teukolsky, S. A., and Vetterling, W. T., "Numerical Recipes - The Art of Scientific Computing." Cambridge Univ. Press, Cambridge 1989, p.574.

25. van de Ven, T. G. M., and Mason, S. G., *J. Colloid Interface Sci.* **57**, 505 (1976).

26. Arp, P. A., and Mason, S. G., *J. Colloid Interface Sci.* **61**, 21 (1977).

27. Batchelor, G. K., and Green, J. T., *J. Fluid Mech.* **56**, 375 (1972).

28. Vervey, E. J., and Overbeek, J. Th. G., "Theory of Stability of Lyophobic Colloids." Elsevier, Amstredam 1948, p.135.

29. Schenkel, J. H., and Kitchener, J. A., *Trans. Faraday Soc.* **56**, 161 (1960).

30. Napper, D. H., "Polymeric Stabilization of Colloidal Dispersions." Academic Press,

London 1983, p.260.

31. Blake, J. R., *Proc. Cambridge Philos. Soc.* **70,** 303 (1971).

32. Dabros, T., *J. Fluid Mech.* **156,** 1 (1985).

33. Dabros, T., *Colloids Surf.* **39,** 127 (1989).

34. Dabros, T., van de Ven, T. G. M., *J. Colloid Interface Sci.* **149,** 493 (1992).

35. Brenner, H., *Adv. Chem. Eng.* **6,** 287 (1966).

36. Goldman, A. J., Cox, R. G., and Brenner, H., *Chem. Eng. Sci.* **22,** 637 (1967).

37. Goldman, A. J., Cox, R. G., and Brenner, H., *Chem. Eng. Sci.* **22,** 653 (1967).

38. Jeffrey, D. J., and Angew, Z., *Math. Phys.* **35,** 634 (1984).

39. O'Neill, M. E., and Stewardson, K., *J. Fluid Mech.* **27,** 705 (1967).

40. Jeffrey, D. J., and Onishi, Y., *J. Fluid Mech.* **139,** 261 (1984).

41. Cox, R. G., and Brenner, H., *Chem. Eng. Sci.* **22,** 1753 (1967).

42. Dean, W. R., and O'Neill, M. E., *Mathematika* **10,** 13 (1953).

43. O'Neill, M.E., *Mathematika* **11,** 67 (1964).

44. Goren, S. L., and O'Neill, M. E., *Chem. Eng. Sci.* **26,** 325 (1971).

45. Hunter, R. J., "Foundations of Colloid Science." Vol.1, Clarendon Press, Oxford 1989, p.222.

46. Czarnecki, J., *Adv. Colloid Interface Sci.* **24,** 283 (1986).

47. Ninham, B. W., *Plenary Lecture at 67th Colloid and Surface Science Symposium,* Toronto 1993.

CHAPTER 3

CHARACTERIZATION OF HAIRY LATEX PARTICLES WITH COLLOIDAL PARTICLE SCATTERING

OBJECTIVES

In the previous chapter, we have introduced a new method (colloidal particle scattering) to determine colloidal forces. The objective of this chapter is to demonstrate its application in characterizing surface structures of latex spheres which are widely applied in both industry and academe. It will be shown that some surface properties, such as "hairy layer" thickness, on large latex beads can be almost exclusively determined with the colloidal particle scattering method.

ABSTRACT

Many experiments in the literature suggest that the surfaces of colloidal latex particles suspended in water are not smooth. The surface roughness is often referred to as being "hairy". We determined the thickness of the hairy layer on two 5 μm latex particles by colloidal particle scattering, a new method recently developed by us to measure surface forces. The results are consistent with electrophoretic mobility measurements. The thickness can be determined with an error of 1 nm. Besides the layer thickness, qualitative information about the evenness of the hairy layer can also be obtained. According to our calculations, the stabilizing mechanism under our experimental conditions is related to the hairy layer but cannot be ascribed to steric repulsion. Instead, a layer of immobilized water in the hairy layer effectively lowers the van der Waals interactions, thus increasing the relative importance of electrostatic repulsion. Hamaker constant measurements on the same latex samples indicate that there is no hydrophobic force acting between latex surfaces at separations larger than 28 nm.

INTRODUCTION

Latex particles are widely used in industry as paints, coatings, adhesives, sealants, latex foams, surface sizing agents, etc. and also in biomedical fields for immunoassays, biological cell-labelling and drug-delivery (1). In colloid science, latex spheres are treated as model colloids because of their regular shape and relatively well-characterized surface (2). To stabilize the suspension, latex particles are usually charged by either incorporating the initiator's charge groups on the surface, e.g. sulfate latexes, or by grafting other charge groups onto the surface, e.g. carboxylic latexes. Charge groups and their supporting polymer chains make the surface of the latex particles "hairy" (3-5), which provides an additional stabilizing mechanism when the ionic strength is high enough to screen the charges on the surface. However, this "hair" increases the surface roughness and limits the use of latex particles as model colloids.

Experimental methods to characterize the hairiness are scarce. Photon correlation spectroscopy (PCS) is a very useful technique to measure the hydrodynamic radius of latex spheres in suspension where the hair is extended. The measured radius equals the sum of the latex core radius, a, and the hairy layer thickness, L_h. The core radius can be determined by transmission electron microscopy (TEM) on dried samples for which the hairy layer is collapsed onto the core surface. However, for polydisperse dispersions, the particle radius determined by PCS is not equal to the mean radius (6). Corrections can be made if the full distribution is known, but usually a Gaussian distribution is assumed which may not be true

in a real system (5). The resulting error can easily become comparable to L_h itself if L_h is only several nanometers.

The heat treatment introduced by Chow and Takamura (4) consists of heating a latex suspension above the glass transition temperature, T_g in an autoclave. For polystyrene latexes the typical temperature of the treatment is 115°C or higher. The treatment causes some of the hairs on the polystyrene latex particle to collapse, thus smoothing the surface. The difference in particle size between heat-treated and untreated particles has been determined with PCS (5) and electrophoretic mobility measurement (4). However, heat treatment does not eliminate all the hair on the latex surface (7). Neither of these two techniques can measure the hairiness of heat-treated latex spheres due to the unavailability of a perfectly smooth sphere (without hair) required for a reference.

An alternative way to determine the hairy layer thickness is to measure the force acting between two latex spheres. The layer thickness is obtained by interpreting the force-distance profile with the aid of a theoretical model. With a surface force apparatus (SFA) introduced by Israelachvili *et al.* (8) one cannot measure the forces between latex spheres directly. An atomic force microscope (AFM) has been used to determine the interaction forces between two 2 μm latex spheres (9). However, in addition to its low accuracy to directly measure the colloidal forces, it is very hard to determine the exact position of the latex core surface because the hairy layers may prevent two core surfaces from touching each other. When the "zero" position is not on the core surface, the result of L_h could be significantly underestimated. A new method, scanning probe microscopy, developed by Evans *et al.*(10) is able to determine surface forces 3 orders of magnitude smaller than a SFA or an

AFM. It has been used to measure the thickness of a "fuzzy" polymer layer grafted on a latex surface (11). They used rather thick layers (42 ± 3 nm), and if the thickness of the hairy layer on latex particles can be measured with the same relative errors (7%), this method might also be a promising one.

In this paper we present another ultrasensitive force measurement method, colloidal particle scattering (CPS), developed recently by us (12), to probe the latex hairy structure. It is 4 to 5 orders of magnitude more sensitive than SFA or AFM and is capable of accurately measuring any parameters, including L_h, that determine the colloidal forces between two latex particles.

THEORY

1. Principles of CPS

The method is based on the analysis of particle collision trajectories between an immobile particle stuck to a wall and a freely mobile particle subjected to a wall shear flow of known shear rate, a schematic example of which is shown in Fig. 3.1. The direction of observation is through the transparent glass wall on which the immobile sphere is attached. Initial positions of mobile spheres can be controlled by a micromanipulator and collisions can be generated at will at a rate of several hundred per day. These collision trajectories are recorded and analyzed with an image processing board. Collision trajectories can also be calculated by solving the trajectory equations (12). These theoretical trajectories are fitted to the experimentally observed ones by varying the parameters in the colloidal force equations

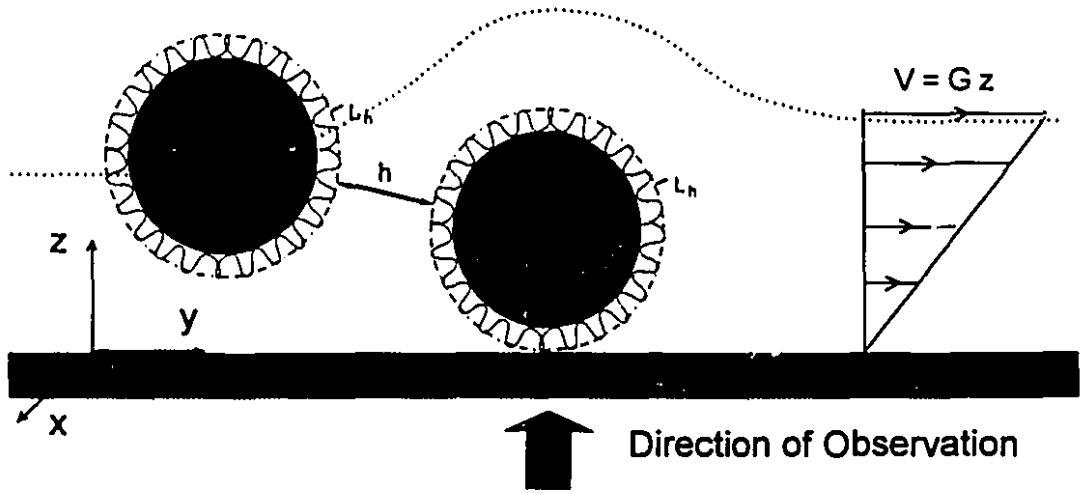

Fig. 3.1 Schematics of two colliding latex particles. One particle is attached to a glass surface, while the other one moves in a wall shear flow. G is the shear rate and V is the flow velocity. L_h is the thickness of the hairy layer, a is the radius of the particle and h is the separation gap width used in hydrodynamic calculations. In the van der Waals force equation, the distance between two surfaces is taken as $h_c = h + 2L_h$. The dotted line represents the trajectory of the mobile sphere.

which enter in the trajectory equation. The best fit yields the optimum parameters with which the force-distance profile can be calculated. Usually collision trajectories of approach are different from those of recession, and thus the mobile particle is "scattered" by the immobile particle, similar as in, for example, elementary particle scattering. The technique is discussed in detail in ref. (12), in which we measured the surface potential and Hamaker constant of polystyrene latex particles assuming the force-distance profile follows the classical DLVO theory of colloid stability. The results agree with zeta-potential measurements and the theoretical prediction of the Hamaker constant between polystyrene and polystyrene in water.

An important factor in CPS experiments is the minimum distance of approach, h_{min}, between two particle surfaces during a collision. No surface forces can be determined beyond this minimum range. Since different types of forces have different active ranges, we can vary the salt concentration, which, in turn, can change h_{min} by typically an order of magnitude, and then selectively measure different forces. The electrostatic force between two spheres can be expressed, according to the Gouy-Chapman theory and the Derjaguin approximation, as (13):

$$F_{elec} = 32\pi\epsilon\kappa a \tanh^2\left(\frac{ze\psi_0}{4kT}\right)\left(\frac{kT}{ze}\right)^2 e^{-\kappa h} \quad , \qquad [3.1]$$

where ϵ is the permittivity of the medium, κ is the reciprocal Debye length, ψ_0 is defined in this thesis as the surface potential of the shear plane on a particle and h is the gap width between two electrically charged surfaces. It decays exponentially with h and is the longest-range force at low salt concentrations. The van der Waals force calculated by Hamaker and modified by Schenkel and Kitchener (13,14) can be expressed as:

$$F_{vdw} = \frac{Aa}{12h_c^2} f(p_h)$$

$$\text{where} \quad f(p_h) = \frac{1+3.54p_h}{(1+1.77p_h)^2} \quad \text{when } p_h<1; \qquad [3.2]$$

$$\text{and} \quad f(p_h) = \frac{0.98}{p_h} - \frac{0.434}{p_h^2} + \frac{0.067}{p_h^3} \quad \text{when } p_h>1.$$

where A is the Hamaker constant, h_c is the gap width between latex cores (to be discussed) and $p_h = 2\pi h_c/\lambda$ (λ being the retardation wavelength). It is also a long-range force which decays at large distances as h_c^{-3} because of the retardation effect. The steric force has an active range equal to the sum of the thicknesses of two stabilizing layers (usually polymeric) and is a short-range force. Table I gives a list of different measurable force parameters at different salt concentrations. Only a parameter with high sensitivity to a force can be determined accurately by CPS.

Table I. Relationship between salt concentration and measurable parameters*

Case	Salt concentration (M)	h_{min} (nm)	Sensitivity of parameters to different forces
1	10^{-4}	175	electrostatic: κ and ψ_0 (high); van der Waals: A and λ (low), L_h (none)
2	10^{-3}	75	electrostatic: κ and ψ_0 (high); van der Waals: A and λ (high), L_h (low)
3	10^{-2}	28	electrostatic: κ (high) and ψ_0 (low); van der Waals: A, L_h and λ (high)
4	≥1	hairy layers overlap	steric: many parameters (high); other forces: all parameters (low)

* Results based on the calculation of collisions between two 4.7 μm latex particles having a zeta-potential of -70 mV.

2. Hairy Latex Model

In a previous study (12) we assumed that the latex particle is a smooth sphere. In that study, the salt concentration was 10^{-3} M, as in case 2 of Table I, and h_{min} is large compared with the hairy layer thickness, so the assumption of a smooth sphere causes negligible errors. However in the present study, we have increased the salt concentration to 10^{-2} M (as in case 3) and the hairy layer starts to affect the force measurement. Hence we model the latex particle as a solid spherical core of radius a, coated evenly with a hairy layer of a thickness L_h (cf. Fig. 3.1). When the particle moves in water, we assume that the water trapped in the hairy layer is immobile and the shear plane is on the outer surface of the hairy layer, so the particle radius in hydrodynamic calculations is considered to be $a+L_h$ instead of a. The model can be justified by PCS observations on PEO-coated latex particles which show that the hydrodynamic radius of the particle includes 90% of the hairy polymer layer (15).

At a salt concentration of 10^{-2} M (case 3), the two hairy surface layers do not overlap during a collision, and thus no steric repulsion occurs. We can assume that the colloidal forces in our system are solely composed of electrostatic and van der Waals forces expressed as Eqs. [3.1] and [3.2]. For the calculation of the electrostatic force, the gap width is taken as h, i.e. the distance between the two outer surfaces of the hairy layers (cf. Fig. 3.1); ψ_0 thus becomes the potential on that surface. Since at salt concentration of 10^{-2} M, collision trajectories are not very sensitive to the variation of ψ_0, we keep the parameter constant at the measured zeta-potential value, ζ, i.e. $\psi_0 \approx \zeta$ (16).

The hairy layer is mostly composed of water. The polymer in it contributes very little to the van der Waals force. In our model this contribution is neglected completely. For this reason the gap width in the calculation of van der Waals force is taken as $h_c=h+2L_h$.

If the salt concentration becomes very high, i.e. larger than 1 M, as in case 4 of Table I, this model is not valid because the two hairy layers start to overlap during the collision. Water is forced out of the layer and the no-slip boundary condition no longer applies on the outer surface of the layer. Such systems require a steric repulsive force term to be included in the calculation, which will be discussed in a future publication (17).

3. Choice of Parameters to be Fitted

Because of the long computation time in CPS, fitting more than two parameters at the same time is cumbersome. For case 3 of Table I, there are four parameters sensitive to the colloidal forces: κ, A, L_h and λ. κ depends on the salt concentration and can be accurately calculated. We thus keep it constant at the theoretical value. The other three parameters come from the van der Waals force (cf. Eq. [3.2]). λ can be fixed at 100 nm according to literature data (14) and our previous analysis (12,18). Therefore, the two parameters to be fitted are the Hamaker constant, A, and the hairy layer thickness, L_h.

EXPERIMENTAL

1. Materials

Two latex samples were used in the experiments: 5 μm divinylbenzene-crosslinked polystyrene latex supplied by Duke Scientific Corp. (denoted as Duke latex) and 4.7 μm surfactant-free polystyrene latex supplied by Interfacial Dynamics Corp. (denoted as IDC latex). The stabilizing charge groups are sulfate groups in both cases. The samples have undergone heat treatment (mentioned above) to smooth their surfaces. Before each experiment the latex sample was washed for several times by centrifuging and supernatant removal, and then dispersed in a 0.01 M KCl solution consisting of 60% D_2O and 40% H_2O which matches the density of polystyrene and thus eliminates sedimentation during a collision. Both D_2O and H_2O were double-distilled to minimize contamination. The same water was also used in the cleaning of the latex spheres before each experiment.

2. Experimental Techniques

In the sample cell, we kept the gap width between two glass plates around 130 μm and the shear rate around 4 s^{-1}. Typically 2 or 3 pairs of latex spheres were used in each experiment to create more than 100 collisions. These collisions were recorded on video cassettes and subsequently analyzed with an image analysis board in the computer (12). A data processing program was then used to convert the screen x-y coordinates to particle x-y coordinates (scaled by the particle radius) and calculate the z-coordinate (cf. Fig. 3.1) from the particle velocity.

3. Data Selection Procedures

A collision trajectory is characterized by the values of the coordinates (x, z) (cf. Fig. 3.1) before and after the collision. The values of x can be obtained directly from the video image, while the values of z can be obtained from the particle velocity. The collision trajectories can be presented in a scattering diagram (cf. Fig. 3.2) where the open circles represent the positions of the moving particle before the collision and the filled circles represent the positions after the collision. All of these collisions are affected by Brownian motion. Some of them are also subjected to deviations caused by surface roughness and, apparently, by some long strings on the latex surface resulting in anomalous collisions. These long strings could be similar to those observed previously on the same Duke latex particles (19). Because of the relatively fast approach-velocity of the two surfaces during a collision, typically 10 μm/s, such a string has very little time to deform and can create a large long-range repulsive force. On other occasions, a long string may entangle with the hair on the second particle, resulting in a large attractive force during the receding period of a collision. Some of these anomalous collisions from the Duke latex experiment are plotted in Fig. 3.3 where filled triangles represent the theoretical final positions of the moving particle. Collisions 1-4 show anomalous large repulsion, while collisions 5-6 represent anomalous large attraction. Since they can be easily differentiated from normal collisions, which form a semicircular ring around the center (cf. Fig. 3.2), they are not used to calculate the force. However, by analyzing the scattering pattern of these collisions, we can obtain the qualitative information about these anomalies. For example, Fig. 3.2 (a) and (b) give the scattering diagrams of all analyzed collisions in experiments with the Duke and IDC latexes. The final

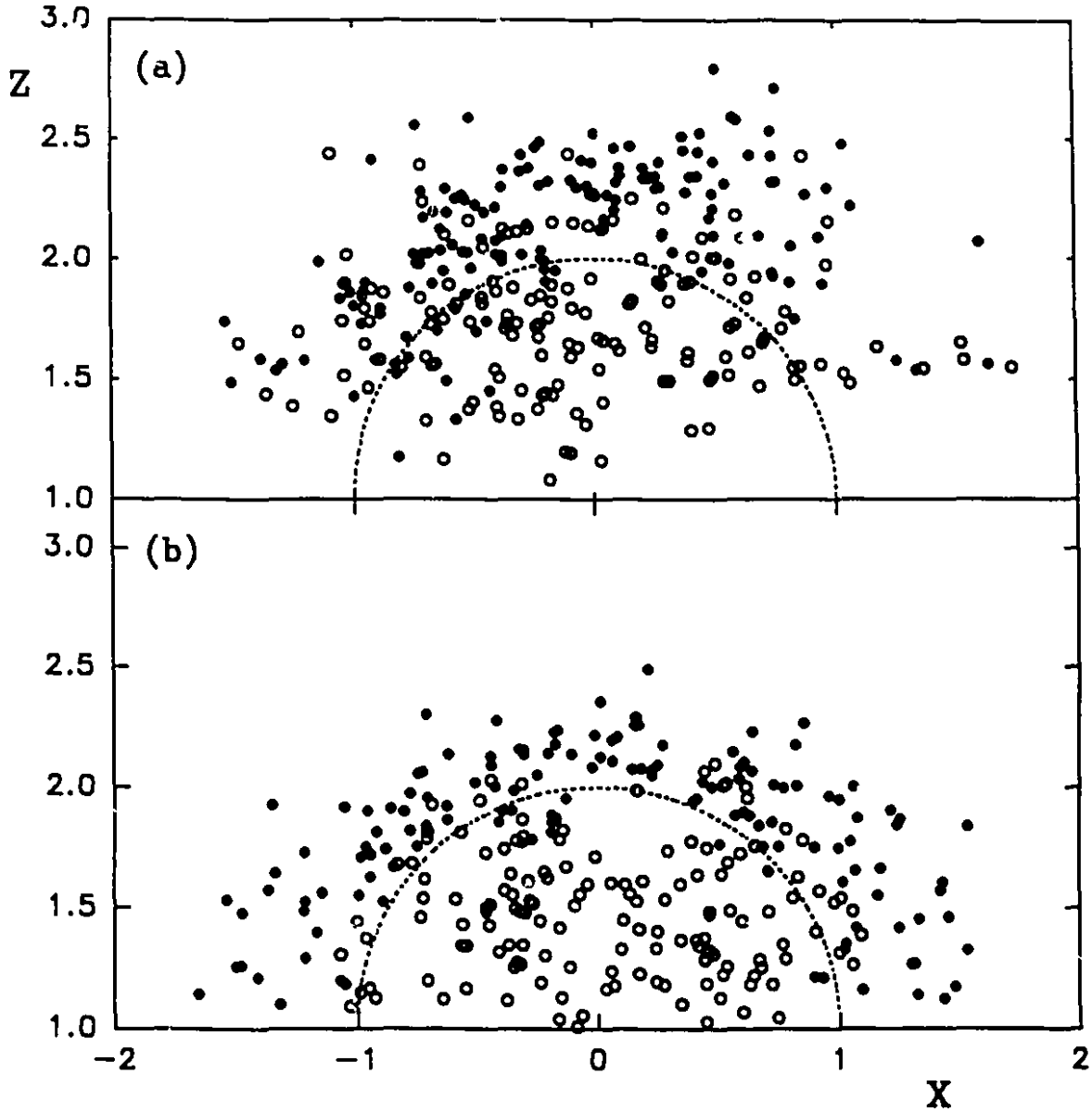

Fig. 3.2 Scattering diagrams of collision experiments with (a) Duke latex (152 collisions) and (b) IDC latex (142 collisions). The coordinates are scaled by the particle radius. The open circles represent the initial positions of the moving particle, the filled circles stand for the experimentally determined final positions of the particles. Same symbols will be adopted in the following scattering diagrams. Most of the final positions form a ring outside the projection of the stationary particle (dotted semicircle). Those filled circles which are very close to or very far from the center represent the collisions subjected to an anomalously large attractive or repulsive force possibly originating from long strings on the latex surface. The degree of scattering in such a diagram indicates the number of these strings.

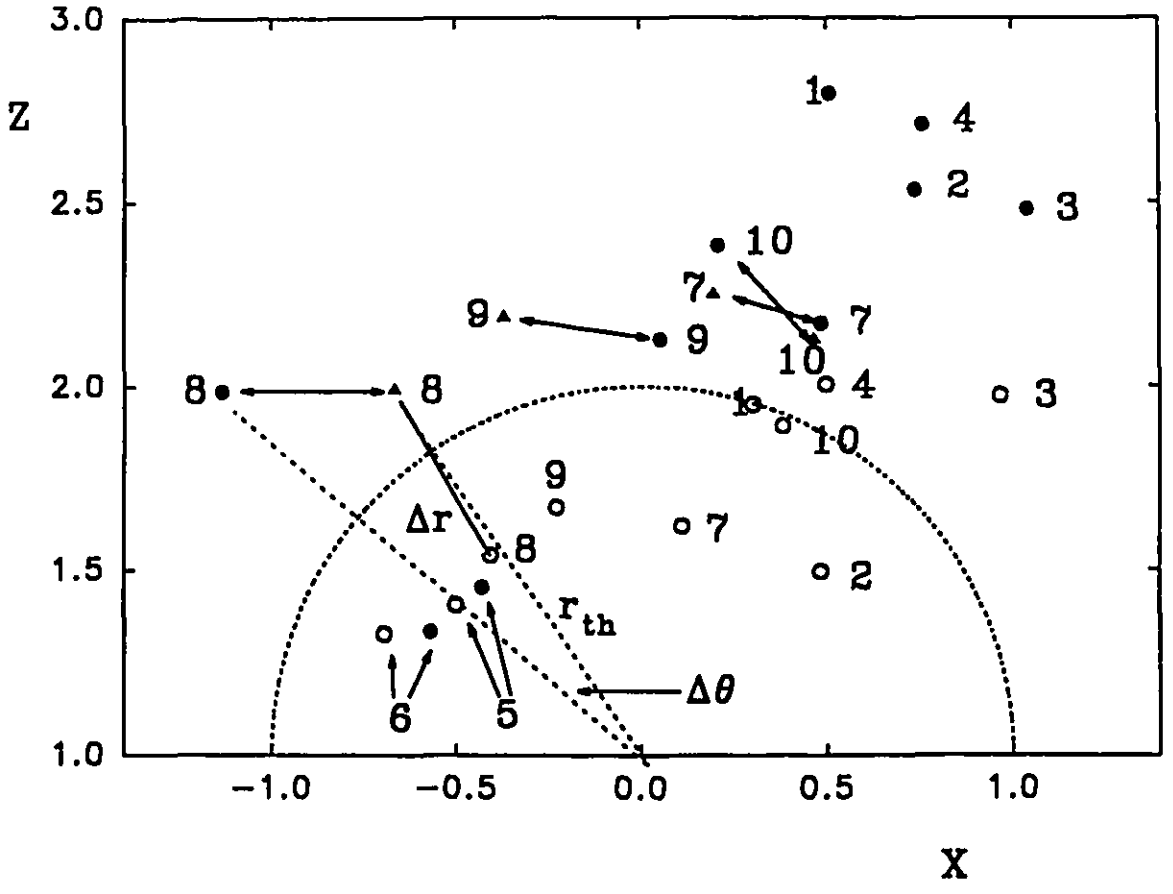

Fig. 3.3 Scattering diagram of some anomalous collisions. The filled triangles are the theoretically calculated final positions of the particles using the best-fit parameters in the force equation. r_{th} represents the distance from the origin to a theoretical final position, $\Delta\theta$ is the difference in scattering angle between the experimental and theoretical final positions, and Δr is the distance from the initial position to the theoretical final position. The values of Δr and $\Delta\theta$ are indicated for collision 8; thus r_{th} is the distance between the origin and filled triangle 8, Δr between circle 8 and triangle 8,and $\Delta\theta$ the angle between the two dotted lines.

positions (filled circles) in Fig. 3.2 (a) (Duke latex) appear to be more scattered than those in Fig. 3.2 (b) (IDC latex). This indicates that the surface of Duke latex is rougher and contains more long strings, a result which can be understood from our quantitative analysis presented below showing that the hairy layer thickness of the Duke latex is three times larger than that of the IDC latex.

Most of the collisions are "disqualified" because of surface roughness and larger-than-average Brownian motion. The surface roughness may cause a different flow pattern from that around a smooth sphere. This effect is not very prominent at large h_{min}, as in cases 1 and 2 of Table I, but becomes more and more serious at small h_{min}, as in cases 3 and 4. It can cause large tangential deviations as shown by the values of $\Delta\theta$ of collisions 7-10 in Fig. 3.3. Since the relative orientations of the spheres are different in different collisions, the effect is random. If we define a deviation factor $f_\perp = r_{th}\Delta\theta/\Delta r$ (cf. Fig. 3.3 for definitions of r_{th}, $\Delta\theta$ and Δr), which is a rough measure of the anomalous tangential displacement normalized by the radial displacement, and plot the histogram of $f_\perp$, we should obtain a normal distribution of $f_\perp$ centered at $f_\perp = 0$. Fig. 3.4 gives such a histogram from the data of the IDC latex experiment. It is obvious that the central peak region represents the collisions with the least errors. 25 collisions were thus selected from this region (cf. Fig. 3.5).

If the stationary particle would move slightly (up to 100 nm) under the impact of the colliding particle, it could cause an error in the final position of that particle. Since this motion is beyond the detection capability of an image processing board, we cannot eliminate the possibility of its occurrance. However, this error would probably be a systematic one. According to our error analysis in Fig. 3.4, the experimental errors tend to be random which

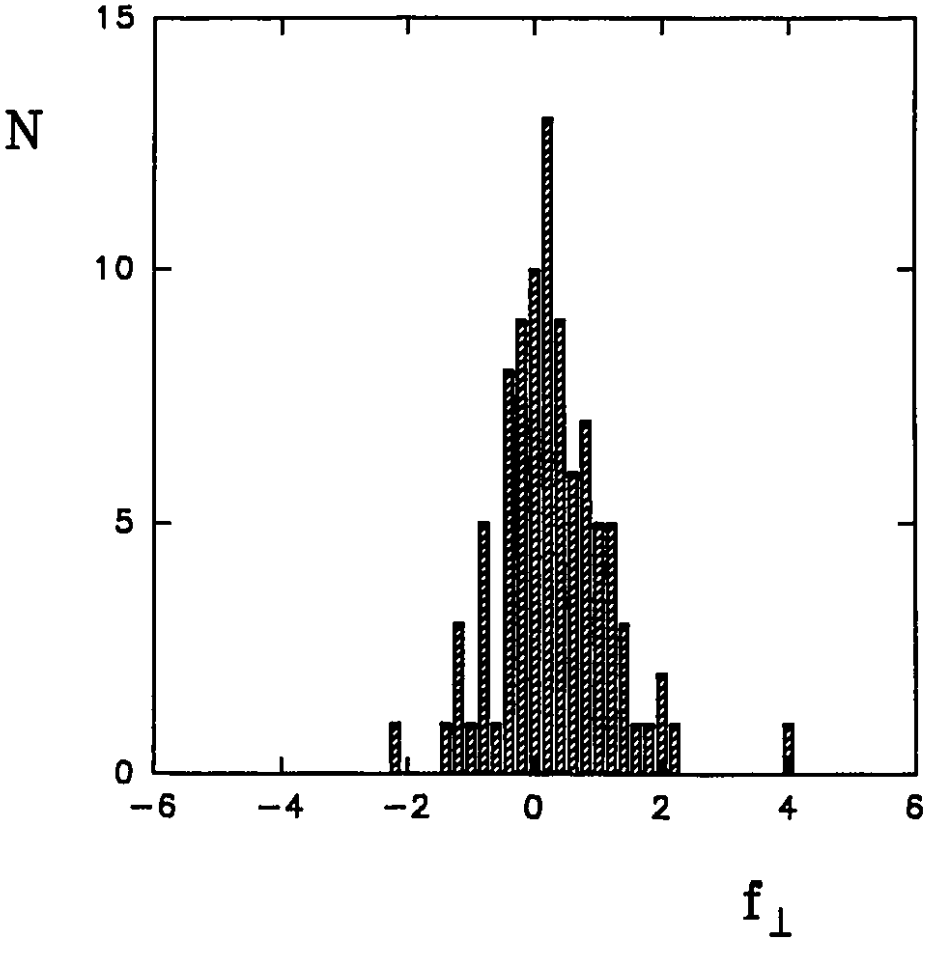

Fig. 3.4 Histogram of the deviation factor, $f_{\perp}$, calculated from the data on IDC latex [cf. Fig. 3.2 (a)]. N is the number of collisions.

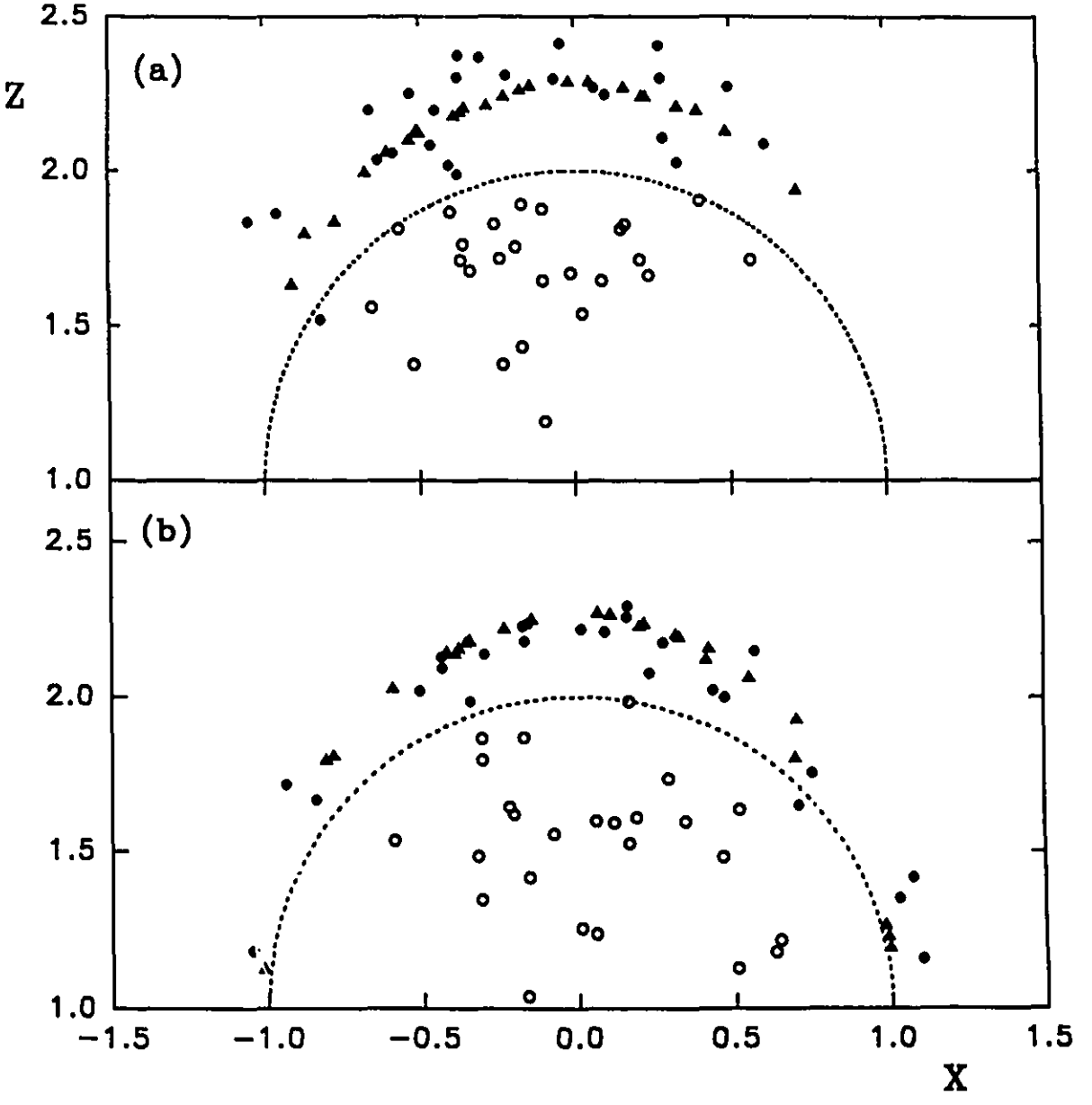

Fig. 3.5 Scattering diagrams of 25 selected collisions from the experiments of: (a) Duke latex, zeta-potential -50 mV and (b) IDC latex, zeta-potential -70 mV.

disfavors the existence of such an error. Also different stationary particles if slightly displaced would have resulted in different scattering patterns since the adhesion of the particle to the glass surface depends on the number of anchoring chains which is unlikely to be identical for different particles. This difference has not been observed in our experiments.

4. Results

From the experimental data (selected 25 collisions) we can obtain the colloidal forces by finding the values of A and L_h which give the best fit between theoretical and experimental trajectories. The other force parameters are kept constant. The fitting is carried out by plotting a contour map of χ^2, which indicates the goodness-of-fit (12), at different values of A and L_h (cf. Fig. 3.6). The minimum value of χ^2 on the map gives the optimum values of A and L_h. The trends of contour lines in Fig. 3.6 show the expected dependency, i.e., an increase in L_h requires an increase in A to compensate for the effect of hairiness and thus most of the minima and contour lines are aligned diagonally from bottom left to up right. In Fig. 3.6 (a) the global minimum is at (L_h=11 nm, A=1.1×10^{-20} J) and thus the hairy layer thickness of Duke latex is 11 nm and the measured Hamaker constant is 1.1×10^{-20} J. Fig. 3.6 (b) shows a minimum at (L_h=3 nm, A=8×10^{-21} J). The hairy layer thickness of IDC latex is thus 3 nm and the measured Hamaker constant is 8×10^{-21} J.

After the optimum parameters are obtained, the force-distance profile can be plotted according to the DLVO theory (cf. Fig. 3.7). The imaginary force curve between smooth latex spheres (L_h = 0) is also plotted for comparison, all the parameters being kept the same.

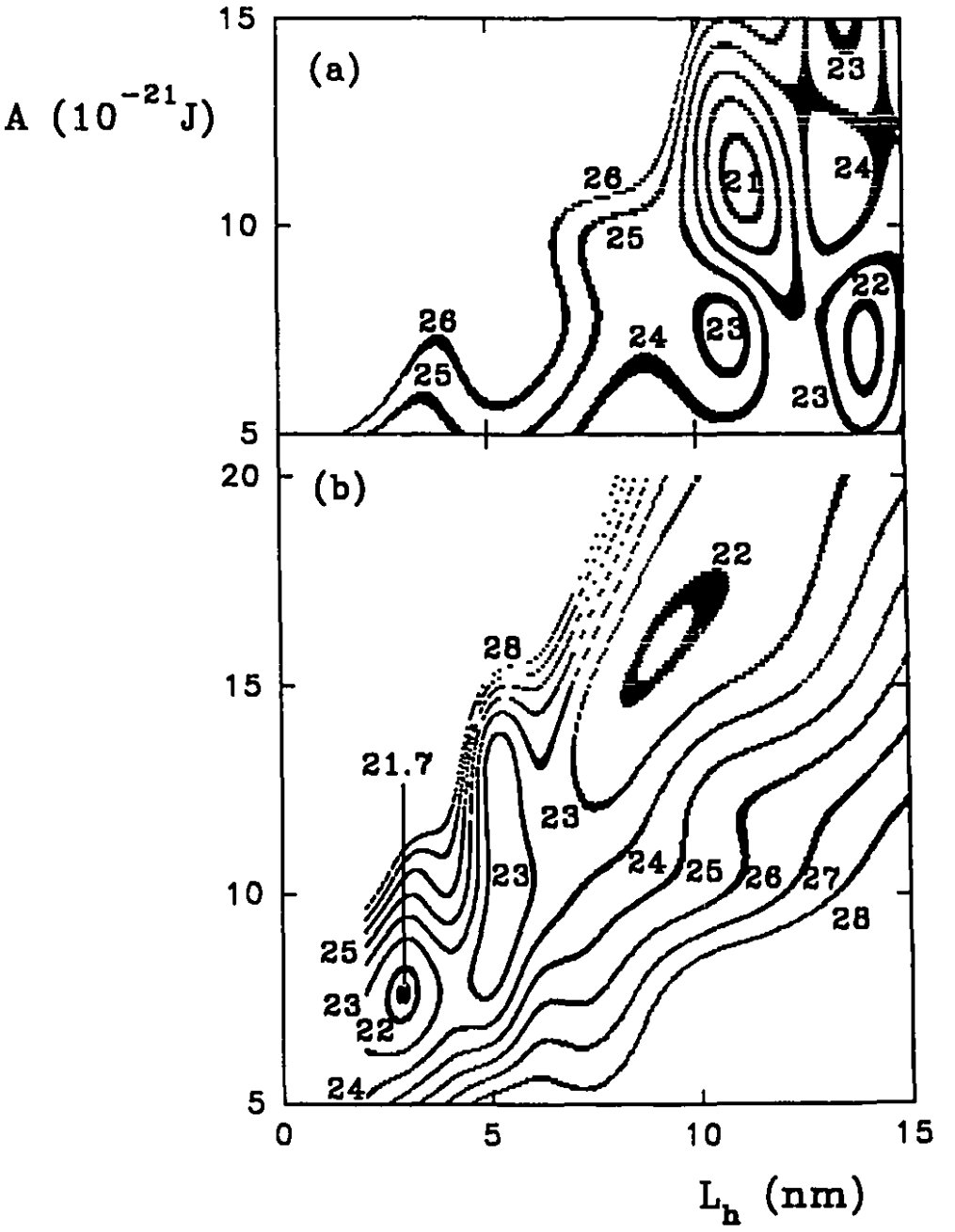

Fig. 3.6 Contour maps of least-squares fitting parameter χ^2 of two experiments: (a) Duke latex, minimum at (L_h = 11 nm, A = 1.1×10^{-20} J); (b) IDC latex, minimum at (L_h = 3 nm, A = 8×10^{-21} J). The χ^2 values of contour lines are indicated by the numbers in the figure.

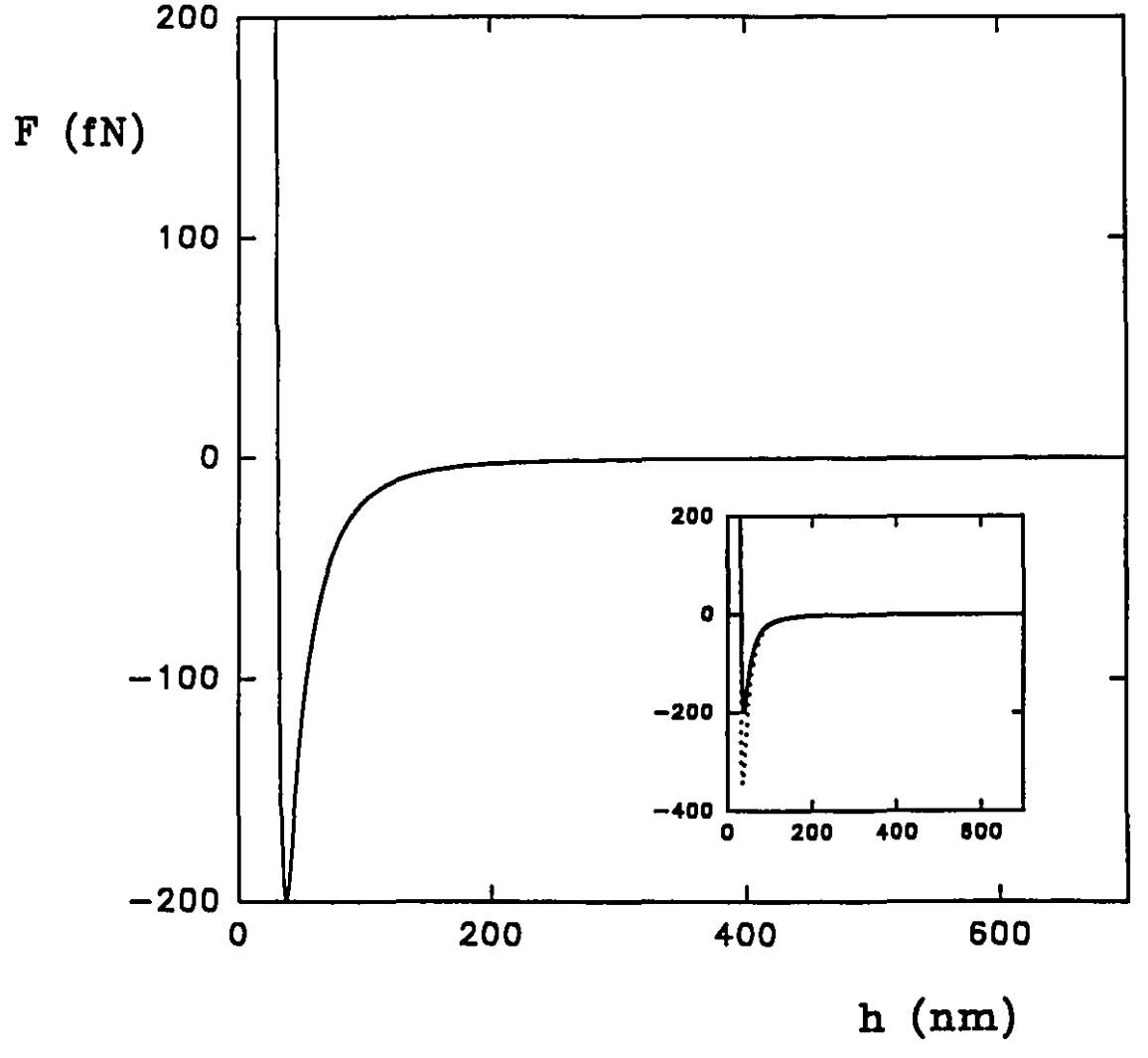

Fig. 3.7 A fitted DLVO-type force vs. separation gap width (solid curve). The force parameters are taken from the measurement of IDC latex experiment, i.e. L_h = 3 nm, $A = 8\times10^{-21}$ J and λ = 100 nm. The unit of force is femtonewton (10^{-15} N). Imaginary force between perfectly smooth latex spheres (L_h = 0) with the same A, λ, κ and ψ_0 is also plotted for comparison (dotted curve). Note the large effect of hairiness on the force curve.

DISCUSSION

1. Latex Hairy Layer

The results show that L_h of the Duke latex particles is larger than that of the IDC latex particles, indicating that the Duke latex is more hairy than IDC latex. This may be due to the different procedures of the synthesis. The surfactant used during the process of synthesizing Duke latex may somehow increase the hairiness. Another reason may be that the heat treatment works well on pure polystyrene spheres (like IDC latex) but not so well on divinylbenzene-crosslinked polystyrene spheres (like Duke latex) (20). We verified this possibility by performing zeta-potential measurements.

The electrophoretic mobilities of IDC and Duke latexes were measured at two salt concentrations before and after the heat treatment and their zeta-potentials were calculated according to the Dukhin-Semenikhin theory (21) (cf. Table II). At both salt concentrations, we found a significant increase in the zeta potentials (about 8 mV) of the IDC latex particles after the heat treatment. The zeta potentials of Duke latex, on the other hand, remained unchanged or even decreased somewhat. The zeta-potential is known to decrease with increasing hairy layer thickness (4,22). Hence our data indicate that the IDC latex becomes smoother after the heat treatment while the Duke latex remains as hairy. The small decrease in zeta-potentials of the Duke latex could be due to the desorption of some charge groups on the latex surface during heat treatment (7).

Table II. Zeta-potentials of IDC and Duke latexes before and after heat treatment

Latex	Salt concentration (M)	Zeta-potential before heat treatment (mV)	Zeta-potential after heat treatment (mV)
IDC	10^{-4}	-93	-101
	10^{-3}	-94	-102
Duke	10^{-4}	-93	-92
	10^{-3}	-85	-80

It is of interest to note that although no forces can be determined when $h < h_{min}$ (28 nm in this case), a hairy layer thickness smaller than this value can be measured, as it alters the force which has an active range longer than h_{min}. Another interesting finding is that at low shear rates (~4 s^{-1}) and medium high salt concentrations (~0.01 M) the stabilizing mechanism for our latex particles is related to the hairy layers but not due to steric repulsion because the layers do not overlap. The hairy layers give rise to another stabilizing mechanism: by providing a surface layer with almost the same Hamaker constant as water, they decrease the van der Waals attraction, making the electrostatic repulsion relatively stronger, and thus prevent the particles from coagulating. The same mechanism applies to some surfactant-coated latex suspensions for which the adsorption layer thickness is several nanometers, similar to that of the hairy layer (18). This mechanism can be demonstrated by comparing the depths of secondary energy minima of hairy and smooth latex particles at different salt concentrations (cf. Tables III and IV).

Table III. Depth of secondary energy minimum at various salt concentrations for large latexes*

KCl Concentration (M)		0.005	0.006	0.01	0.1
Hairy Latex	Energy (kT)	-0.81	-0.97	-1.58	-8.79
L_h = 3 nm	h_m** (nm)	48	41	32	8.7
Smooth Latex	Energy (kT)	-1.07	-1.32	-2.36	-24.5
L_h = 0 nm	h_m (nm)	46	41	30	6.9

* The measured Hamaker constant and surface potential of IDC latex (size: 4.7 μm) were used in the calculation. They are 8×10^{-21} J and -70 mV respectively.

** h_m is the separation distance at the secondary energy minimum.

Table IV. Depth of secondary energy minimum at various salt concentrations for small latexes*

KCl Concentration (M)		0.01	0.1	1	2
Hairy Latex	Energy (kT)	-0.07	-0.38	-0.91	-1.06
L_h = 3 nm	h_m (nm)	31	8.7	2.7	1.9
Smooth Latex	Energy (kT)	-0.10	-1.07	-6.77	-11.2
L_h = 0 nm	h_m (nm)	29	7.0	1.6	1.0

* The calculation was based on 200 nm latexes with the same Hamaker constant and surface potential as in Table III.

For hairy latexes, there is usually an energy barrier at h=0 because the van der Waals force has a finite value at h=0 which is normally smaller than electrostatic force at zero separation distance provided that the hairy layer is sufficiently thick (e.g. 3 nm), therefore the secondary minimum becomes the only energy minimum in the energy-distance profile. We define that when this minimum is larger than 1 kT, the system is considered unstable. Table III shows that this critical coagulation concentration (CCC) for hairy latex is 0.006 M and the CCC for smooth latex is 0.005 M. The small difference of CCC is due to the large separation distance at the energy minimum (h_m) , typically 40 nm. Under our experimental conditions: 0.01 M salt and 4 s^{-1} shear, however, the hairy latex suspension was found stable while the smooth latexes are expected to coagulate according to our hydrodynamic calculation. The stabilizing mechanism of hairy layers can be more clearly shown in Table IV where a more frequently encountered latex size, 200 nm, was used in the calculation. The CCC for the hairy latex is 2 M, 20 times higher than that of the smooth latex which is 0.1 M. However, one should be cautious to interpret the data at a salt concentration higher than 1 M. At salt concentration 1 M, h_m is smaller than L_h (3 nm). At this distance the assumption of taking the zeta-potential as the surface potential on the outer surface of the hairy layer is not valid because the charge groups are actually randomly dispersed in the layer. Therefore, this treatment overestimates the electrostatic repulsion at small separations. At a salt concentration higher than 1 M, the hairy layers are expected to overlap during a collision and the stabilizing mechanism is steric repulsion.

The surface roughness of the layer can be analyzed by studying the tangential deviation in the histogram of $f_\perp$ (cf. Fig. 3.4). In ref. (12) we show that it is possible to take

an arbitrary form of force-distance relationship instead of the DLVO-type force to fit the collision trajectories. Thus, in principle, we can use some force which includes both normal (center-to-center) and tangential components to fit the data. The fitted force will then reveal the actual magnitude of the tangential contribution. Unfortunately this treatment involves many force parameters which makes the procedure difficult to implement. However, we can estimate the tangential force by studying the tangential displacements on a scattering diagram. Since the magnitude of the tangential displacement is similar to the normal one, we conclude that the forces are probably of the same magnitude as well. This suggests that the effect of surface roughness of large latex spheres on the colloidal force is quite significant. As far as surface properties are concerned, they cannot be considered as ideal model colloids

2. Error analysis

After the optimum values of the parameters are obtained, we can plot the theoretical prediction of the particle's final positions (cf. triangles in Fig. 3.5). The discrepancy between experimental and theoretical positions, which is about one-tenth of the particle radius (0.1a), is due to Brownian motion and measurement errors. How these errors affect our experimental results can be analyzed by a Monte Carlo method. We varied all of the Duke latex experimental final positions randomly within 0.1a and constructed another contour map. The same procedure was repeated ten times. The shifts in the minima on these ten contour maps were found to be within 1 nm for L_h and 1×10^{-21} J for A. These are thus the estimated errors for the determined parameters. The systematic error caused by Schenkel and Kitchener's approximation of retarded van der Waals forces is around 10% (23) which is roughly of the

same order of magnitude as the random errors provided that L_h is small. When L_h becomes larger 15 nm, the systematic errors are expected to increase as our latex model breaks down because of the overlap of two hairy layers.

3. Absence of hydrophobic force

The nature of the so-called hydrophobic force is a pertinent issue in colloid and surface science. Various experimental studies indicate that a long-range attractive hydrophobic force is acting between hydrophobic surfaces (like two polystyrene latex particle surfaces) (24-29), roughly equivalent to increasing the apparent Hamaker constant by at least an order of magnitude. This force was not detected in our experiments since both measurements of the Hamaker constant are close to the theoretical value calculated from spectroscopic data for the interaction between polystyrene and polystyrene in water (30): $A = 9.5\times10^{-21}$ J. This can be explained by the fact that the hydrophobic force is usually too weak to be observed at a separation distance larger than 20 nm (24-26), which is the case in our experiments with $h_{min} = 28$ nm. However, some studies do indicate that the hydrophobic force between a polystyrene latex surface and a polystyrene flat surface in water operates up to 29 nm (27) and the force between fluorocarbon surfaces in water is significant up to 80-90 nm (28). In those studies the surfaces were not charged. According to Israelachvili's observation (24), charged groups on hydrophobic surfaces greatly diminish the hydrophobic force. Since our latex spheres are stabilized by sulfate charge groups, it is maybe not surprising that no hydrophobic force was detected.

CONCLUSION

We have shown that CPS is capable of determining the hairy layer thickness of latex particles quantitatively and the evenness of the layer qualitatively (by analysis of the scattering diagram and the f_1-histogram). The magnitude of tangential force caused by the latex hair during a collision can also be analyzed and was found comparable to the force acting along sphere centers. The small experimental errors, about 1 nm for the layer thickness, enable us to characterize the hairy layers on large latex spheres accurately. The data interpretation using the hairy latex model indicates that under our experimental conditions the stabilizing mechanism of latex suspensions is the reduction of van der Waals attraction caused by hairy layers rather than steric repulsion. The measured Hamaker constant for polystyrene-water-polystyrene interactions closely agrees with theory. It shows that CPS is capable of measuring Hamaker constant with 10% accuracy. According to our experimental results, no hydrophobic force was detected between latex spheres down to a separation distance of 28 nm.

ACKNOWLEDGMENTS

The authors wish to thank Dr. Piotr Warszynski (Institute of Catalysis and Surface Chemistry, Krakow, Poland) for helpful discussion and advice. We would also like to acknowledge Paprican for providing a scholarship to X. Wu and NSERC for partial support of the project.

REFERENCES

1. Daniel, E. S., Sudol, E. D., and El-Aasser, M. S., "Polymer Latexes - Preparation, Characterization, and Applications." American Chemical Society, Washington DC 1992, p.1.
2. Hearn, J., Wilkinson, M. C., and Goodall, A. R., *Adv. Colloid Interface Sci.* **14,** 173 (1981).
3. Lyklema, J., *Adv. Colloid Interface Sci.* **17,** 307 (1982).
4. Chow, R. S., and Takamura, K., *J. Colloid Interface Sci.* **125,** 226 (1988).
5. Polverari, M., and van de Ven, T. G. M., *Colloids Surfaces A: Physicochem. Eng. Aspects* **86,** 209 (1994).
6. Czarnecki, J., and van de Ven, T. G. M., *J. Colloid Interface Sci.* **145,** 298 (1991).
7. Varennes, S., and van de Ven, T. G. M., *PhysicoChemical Hydrodynamics* **9,** 537 (1987).
8. Israelachvili, J. N., and Adams, G. E., *J. Chem. Soc., Faraday Trans. 1* **74,** 975 (1978).
9. Li, Y. Q., Tao, N. J., Pan, J., Garcia, A. A., and Lindsay, S. M., *Langmuir* **9,** 637 (1993).
10. Evans, E., Ritchie, K., and Merkel, R., *Biophys. J.* **68,** 2580 (1995).
11. Evans, E., private communication.
12. van de Ven, T. G. M., Warszynski, P., Wu, X., and Dabros, T., *Langmuir* **10,** 3046 (1994).

13. van de Ven, T. G. M., "Colloidal Hydrodynamics." Academic Press, London 1989, p.24 and 37.

14. Schenkel, J. H., and Kitchener, J. A., *Trans. Faraday Soc.* **56,** 161 (1960).

15. Napper, D. H., "Polymer Stabilization of Colloidal Dispersions." Academic Press, London 1983, p.250.

16. Hunter, R. J., "Zeta Potential in Colloid Science - Principles and Applications." Academic Press, London 1981, p.5.

17. Wu, X., and van de Ven, T. G. M., to appear (Chapter 5 of this thesis).

18. Wu, X., and van de Ven, T. G. M., to appear (Chapter 4 of this thesis).

19. Dabros, T., Warszynski, P., and van de Ven, T. G. M., *J. Colloid Interface Sci.* **162,** 254 (1994).

20. Takamura, K., private communication.

21. Dukhin, S. S., Semenikhin, N. M., *Colloid Journal* (English version of *Kolloidn. Zh.*) **32,** 298 (1970).

22. Ohshima, H., Makino, K., and Kondo, T., *J. Colloid Interface Sci.* **113,** 369 (1986).

23. Clayfield, E. J., Lumb, E. C., and Mackey, P. H., *J. Colloid Interface Sci.* **37,** 382 (1971).

24. Israelachvili, J. N., and Pashley, R. M., *J. Colloid Interface Sci.* **98,** 500 (1984).

25. Pashley, R. M., McGuiggan, P. M., Ninham, B. W., and Evans, D. F., *Science* **229,** 1088 (1985).

26. Christenson, H. K., and Claesson, P. M., *Science* **239,** 390 (1988).

27. Karaman, M. E., Meagher, L., and Pashley, R. M., *Langmuir* **9,** 1220 (1993).

28. Claesson, P. M., and Christenson, H. K., *J. Phys. Chem.* **92,** 1650 (1988).

29. Yaminsky, V. V., and Ninham, B. W., *Langmuir* **9,** 3618 (1993).

30. Hunter, R. J., "Foundations of Colloid Science." Vol.1, Clarendon Press, Oxford 1989, p.222.

CHAPTER 4

RETARDED VAN DER WAALS FORCES BETWEEN TRIBLOCK-COATED LATEX SPHERES

OBJECTIVES

In Chapters 2 and 3, we have described colloidal particle scattering as a new technique to measure colloidal forces between latex spheres. Since the "hairy structure" on latex surface is very similar to a surfactant adsorption layer, it will be the objective of this chapter to extend the application of the colloidal particle scattering to a triblock copolymeric surfactant-coated latex system. With abundant literature data of the same material to compare, it can be proven that this application is a success.

ABSTRACT

Retarded van der Waals forces between colloidal particles play a major role in colloid and surface science, but no direct measurement of these forces has been reported. A new experimental technique has been developed to accurately determine these forces between two 4.7 μm latex spheres coated by triblock copolymers. The retardation wavelength has been found to be 110 ± 10 nm, and the Hamaker constant $(1.0 \pm 0.1) \times 10^{-20}$ J. Both of them agree well with theoretical predictions. In addition, the experiments allow the measurement of the layer thickness of adsorbed triblock copolymers. The results are consistent with the data from field-flow fractionation and photon correlation spectroscopy.

INTRODUCTION

Van der Waals forces are of great interest in colloid and surface science because they play an important role in many physical and chemical phenomena, such as colloid stability, physical adsorption, adhesion, surface tension, wetting, foam stability, strength of clay minerals and micellar structure (1,2). The forces are known to be retarded at large separation distances (about 5 nm for two molecules in free space) (2), because of the finite time it takes for an electromagnetic signal to travel forth and back between two molecules. This retardation effect was first studied by Casimir and Polder (3) and later implicitly incorporated in the full Lifshitz treatment (4). However, adequate data for accurate Lifshitz calculations are lacking except for a few systems; so for practical purposes the Casimir and Polder approach is usually applied to calculate retarded van der Waals forces (5). Another approach, widely used because of its simplicity, was introduced by Hamaker (2). Unlike the Lifshitz treatment, it does not take retardation into account, but modifications have been carried out to include this effect (6,7) which yield similar results as exact calculations (5,7). Since the van der Waals forces that determine colloid stability are almost always retarded, it is of interest to measure these forces between colloidal particles experimentally. The commonly used surface force apparatus (SFA) (8) or atomic force microscopy (AFM) (9) are unfortunately not sensitive enough to detect these colloidal forces, although the retarded van der Waals forces between two macroscopic mica surfaces in aqueous solutions, which are five orders of magnitude larger than the colloidal forces, were measured with SFA by Israelachvili *et al.* (8). Recently a new method, Colloidal Particle Scattering (CPS), was developed by us to

measure surface forces (10). The forces detected by CPS are at least four orders of magnitude smaller than those detected by SFA or AFM. In this paper we determine the retarded van der Waals forces between latex spheres coated with triblock copolymers which are widely used as stabilizers for colloidal particles. As an additional advantage, the thickness of adsorbed polymer layers on latexes can also be determined.

THEORY

The CPS method is based on the analysis of particle collision trajectories between an immobile particle stuck to a wall and a freely mobile particle subjected to a wall shear flow of known shear rate (cf. Fig. 4.1). Usually collision trajectories of approach are different from those of recession, and thus the mobile particle is "scattered" by the immobile particle, similar as in elementary particle scattering. Initial positions of mobile spheres can be controlled by a micromanipulator and collisions can be generated at will at a rate of several hundred per day. These collision trajectories are recorded and analyzed with an image processing board. The fitting of the theoretically calculated trajectories to the experimentally observed ones, by varying the parameters in the colloidal force equations, yields the optimum parameters which then gives the force-distance profile. The technique is discussed in detail in ref. (10), in which we measured the surface potential and Hamaker constant of polystyrene latex particles assuming the force-distance profile follows the classical DLVO theory of colloid stability. The results agree with zeta-potential measurements and the theoretical prediction of the Hamaker

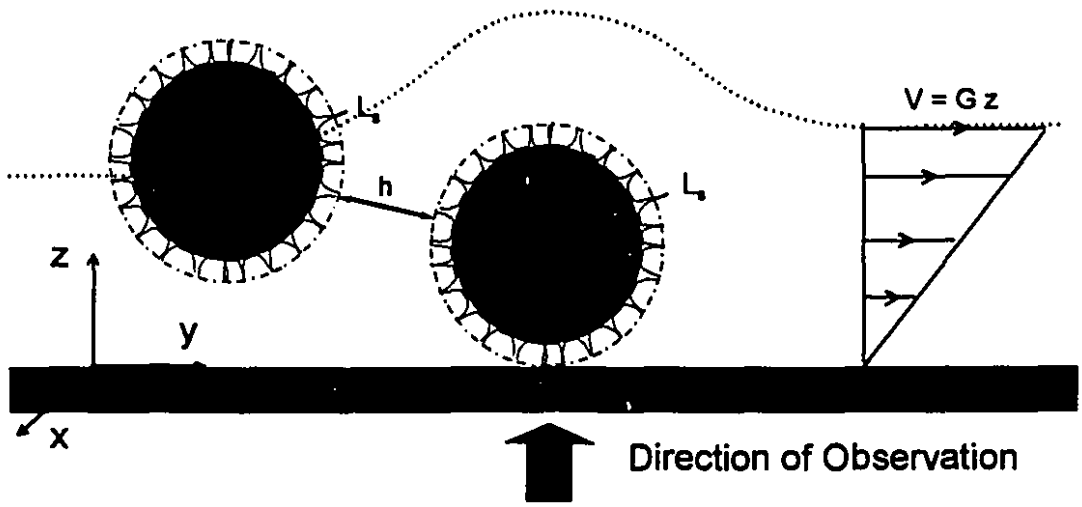

Fig. 4.1 Schematics of two colliding latex particles. One particle is attached to a glass surface, while the other one moves in a wall shear flow. G is the shear rate and V is the flow velocity. L_s is the thickness of the adsorption layer on the latex surface, a is the radius of the particle and h is the separation gap width used in hydrodynamic calculations. In the van der Waals force equation, the distance between the two surfaces is taken as $h_c = h + 2L_s$. The dotted line shows the trajectory of the mobile particle. The trajectory of approach is characterized by two coordinates: x and z prior to the hydrodynamic and colloidal interactions, while the trajectory of recession is characterized by another set of x and z after the collision.

constant between polystyrene and polystyrene in water. Since then the data processing technique has been improved to yield even more reliable results and the original smooth latex model has been replaced with a more realistic hairy latex model (11) to account for various observations with dynamic light scattering (12) and electrophoresis (13).

A similar model can be applied to triblock-coated latex spheres. The polymer is assumed to be evenly coated on the latex surface and form a layer of thickness L_s (cf. Fig. 4.1). When the particle moves in water, we assume that the water trapped in the adsorption layer is immobile, so the particle radius in hydrodynamic calculations is taken as $a + L_s$ instead of a. Since the adsorption layer is mostly composed of water, the triblocks contribute very little to the van der Waals force. In our model this contribution is neglected completely and the gap width in the equation of the van der Waals force is taken as $h + 2L_s$. This model is valid only when two adsorption layers do not overlap during a collision. For our system we know from literature data (14,15) that the layer thickness is about 10 nm. If we control the salt (KCl) concentration at 0.01 M, the minimum gap width between two particle surfaces during a collision (about 30 nm) will be larger than the sum of the two layers. This ensures that the layers do not overlap.

According to this model, no steric repulsive force is involved and the classical DLVO theory which considers two colloidal forces, i.e. electrostatic and van der Waals forces, describes the system reasonably well. Two parameters enter in the electrostatic force: the Debye length, κ^{-1}, and the surface potential, ψ_0; κ^{-1} can be accurately calculated from the known salt concentration, while ψ_0 is not very sensitive to collision trajectories at the experimental conditions (0.01 M KCl) and can be kept constant at the measured zeta-

potential. Hence the parameters to be fitted come solely from the retarded van der Waals force and the accuracy of this force measurement is maximized. Because the total number of parameters to be fitted is limited (usually two), we need simple expressions for the van der Waals force. The Hamaker expression modified by Schenkel and Kitchener's retardation term (6) is adequate in this case. It is determined by two parameters: the Hamaker constant, A, and the retardation wavelength, λ, usually of the order of 100 nm (2,6,16). It further depends on the geometry of the colliding particles, i.e. the particle radius a (a constant value given by the manufacturer) and the adsorption layer thickness L_s. According to our previous results (10), the choice of λ = 100 nm is a reasonable one. A more detailed discussion will be given below. A and L_s are thus the two parameters to be fitted by experimental data.

EXPERIMENTAL

The latex spheres used in the experiments are 4.7 μm surfactant-free polystyrene latexes supplied by Interfacial Dynamics Corp. The sample has undergone heat-treatment above the glass transition temperature, T_g, to smooth the surface (13). The polymers used for adsorption are Pluronic F88 and Pluronic F108 supplied by BASF Corp. They are PEO-PPO-PEO [PEO being poly(ethylene oxide) and PPO being poly(propylene oxide)] triblock copolymers with different sizes of blocks (104/39/104 repeat units for F88 and 129/56/129 repeat units for F108). The coated samples were made by dropping the bare latex suspension into a 50 mg/L Pluronic F108 or F88 surfactant solution and leaving it over night on a rotary

machine to prevent sedimentation. The samples were then separated from the solutions by centrifuging and supernatant removal. Before each experiment the polymer-coated latex spheres were dispersed in a 0.01 M KCl solution consisting of 60% D_2O and 40% H_2O, a mixture in which the latex spheres are density matched. Both D_2O and H_2O were double-distilled to minimize contamination. In aqueous solution PPO is the anchor-block on the surface of latex particles due to its higher hydrophobicity and PEO is the buoy-block extending into solution (17). The adsorption layer thickness, L_s, is thus the thickness of this PEO layer.

In each experimental run, more than 100 collision trajectories were analyzed. From these collisions, 25 were selected according to a criterion discussed in ref. (11), in essence rejecting collisions for which the tangential deviation is not small compared with the radial displacement (11); this procedure minimizes the error caused by surface roughness. These selected collisions are plotted in a scattering diagram (cf. Fig. 4.2) where the open circles represent the positions of the moving particle before the collision, the filled circles represent the positions after the collision and the filled triangles are the theoretical final positions (to be discussed shortly). The x-coordinates can be obtained directly from the video images, while the z-coordinates are obtained from the measured particle velocities (10).

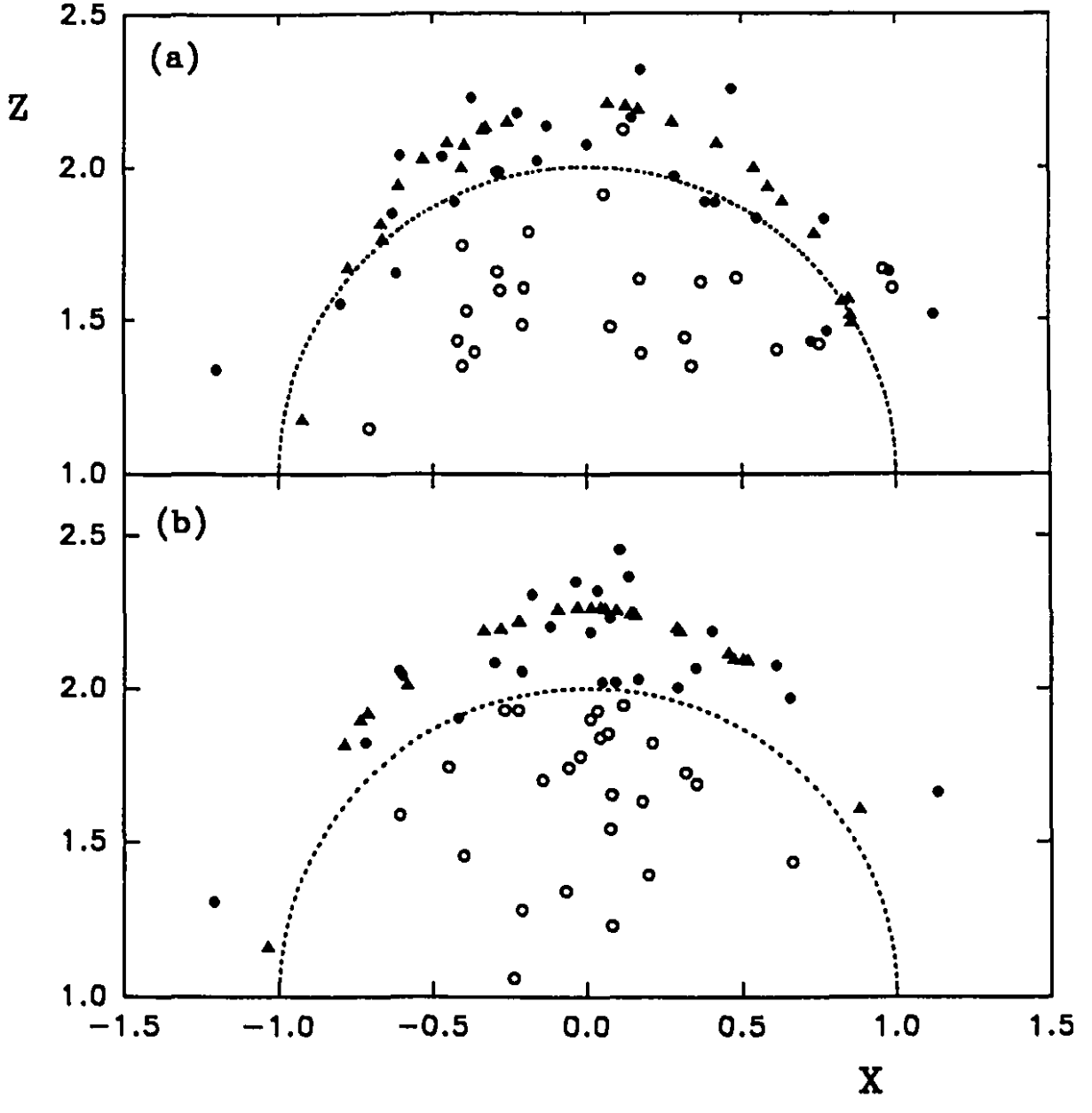

Fig. 4.2 Scattering diagrams of 25 selected collisions from two Pluronic triblock-coated latex experiments: (a) F88-coated latex, zeta-potential -23 mV; (b) F108-coated latex, zeta-potential -20 mV. The coordinates are scaled by the particle radius. The open circles represent the initial positions of the moving particle (one set of x and z), the filled circles stand for the experimentally observed final positions of the particle (another set of x and z), and the filled triangles are the theoretically calculated final positions using the best-fit parameters in the force equations. The dotted semicircle is the projection of the stationary particle.

RESULTS AND DISCUSSION

From these selected collisions we can obtain the van der Waals force by finding the values of A and L_s which give the best fit between observed and theoretical collision trajectories. The fitting is carried out by plotting a contour map of χ^2, which indicates the goodness-of-fit (10), at different values of A and L_s (cf. Fig. 4.3). The minimum value of χ^2 on the map gives the optimum values of A and L_s. The trends in the of contour lines in Fig. 4.3 show the expected dependency, i.e. an increase in L_s requires an increase in A to compensate for the effect of a thicker adsorption layer. For this reason, most of the minima and contour lines are aligned diagonally from bottom left to up right. The global minima for F88 and F108-coated latexes are at (L_s = 7 nm, A = 1.0×10^{-20} J) and (L_s = 11 nm, A = 1.0×10^{-20} J), respectively (cf. Fig. 4.3).

The adsorption layer thicknesses of these two triblocks have been measured with field-flow fractionation (FFF) (14). For F88 and F108 adsorbed on 272 nm latex particles the results are 9 nm and 14 nm. Despite the particle size difference between 272 nm latex and our 4.7 μm IDC latex, the curvature effects on the adsorption are very small due to the relatively thin layers (18). Hence the results are comparable. The adsorption layer thicknesses determined by our method are slightly smaller than FFF results. This is due to the lower equilibrium polymer concentration of F88 and F108 (50 mg/L) in our experiments, which is at the beginning of the plateau in the adsorption isotherms (15,19). Maximum adsorption occurs at 200 mg/L and the maximum adsorption layer thickness (13 nm for F108 adsorption) occurs at 500 mg/L measured by photon correlation spectroscopy (PCS) on 56 nm latex

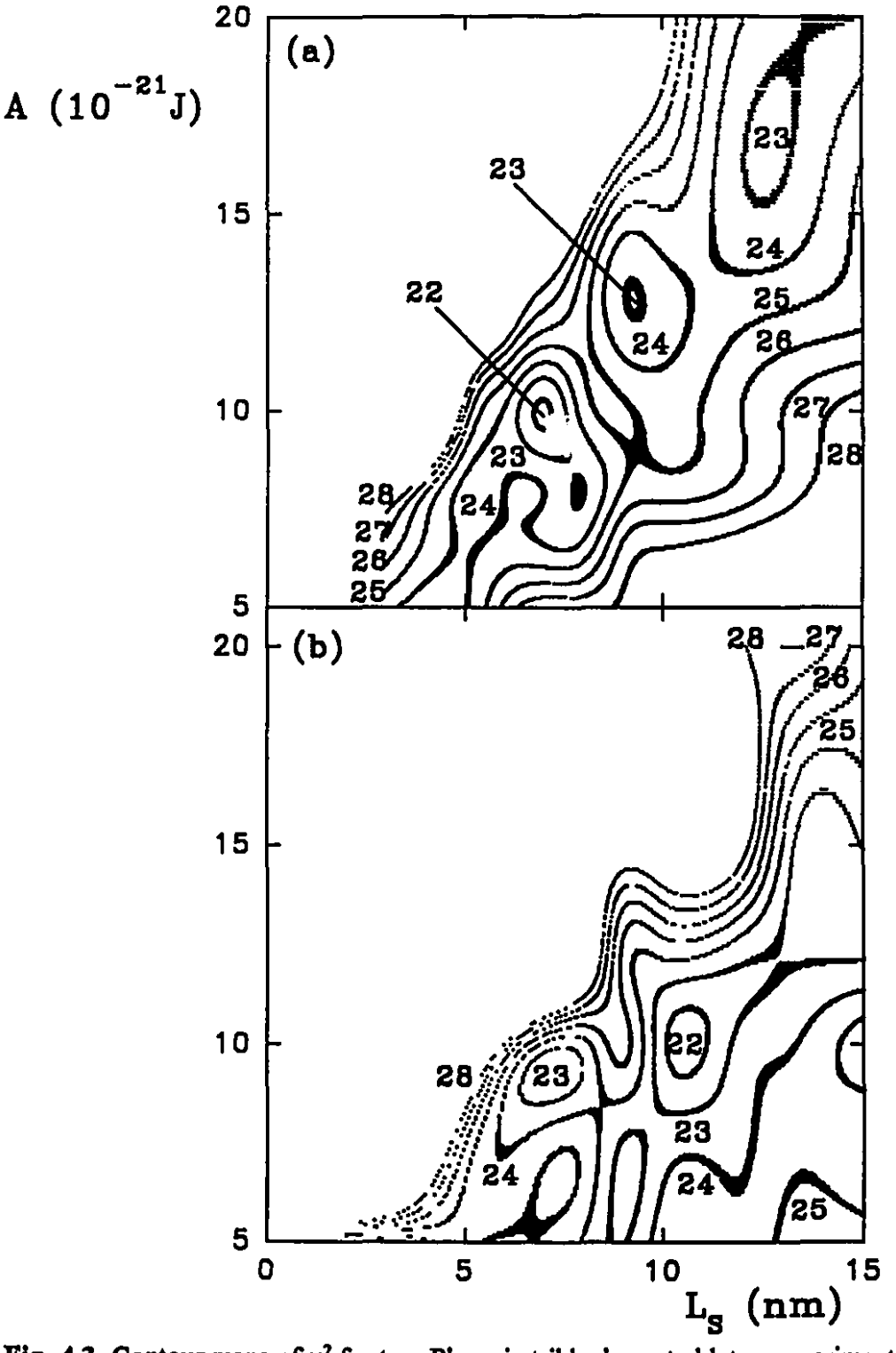

Fig. 4.3 Contour maps of χ^2 for two Pluronic triblock-coated latex experiments: (a) F88-coated latex, minimum at (L_s = 7 nm, A = 1.0×10^{-20} J); (b) F108-coated latex, minimum at (L_s = 11 nm, A = 1.0×10^{-20} J). The χ^2 values of contour lines are indicated by the numbers.

particles (15). At 50 mg/L polymer concentration, the layer thickness of F108 is determined to be 10 nm (15) which corresponds to about 11.5 nm for the same adsorption layer on a 4.7 μm sphere after correcting for curvature (18). This result agrees very well with our measurement (11 nm) at the same conditions. CPS actually has some advantages over both FFF and PCS. To obtain an accurate result of particle size with FFF, it is necessary to know the exact value of particle density (including the adlayer) which could be difficult to obtain when the particle is coated with a polymer layer whose thickness is to be determined. PCS is thus used frequently to calibrate FFF results (20,21). However, PCS requires "perfectly smooth" bare latex spheres and the layer thickness is obtained by subtracting the bare radius from the polymer-coated sphere radius. The presence of a hairy layer on bare latex spheres thus causes a problem for PCS measurements. This limitation does not apply to CPS as long as the hairy layer of the uncoated particles is thinner than the adsorption layer.

The coil diameters of the freely dissolved F88 and F108 Pluronic surfactants have been determined by Lee *et al.* (17). They are 5.8 nm and 8.1 nm, respectively. Both of them are smaller than the measured layer thicknesses: 7 nm and 11 nm. This indicates that the buoy-block (PEO) is in the form of more extended "brushes" rather than coils or "mushrooms". As predicted by de Gennes (22) and Alexander (23), an increase in polymer adsorption or anchored (or grafted) chain density will change the configuration of the buoy-block from a "mushroom" to a "brush". A further increase in adsorption up to the plateau region will make the "brushes" even more extended. This explains the 2-3 nm increase in the adsorption layer thicknesses of F88 and F108 triblocks when their equilibrium concentrations increase from 50 mg/L to 500 mg/L.

The retardation wavelength λ is a measure of how and where the transition from non-retarded to retarded van der Waals forces occurs. All of the obtained results are based on the assumption that λ = 100 nm. The validity of this assumption can be tested by fixing the Hamaker constant at the theoretical value, 9.5×10^{-21} J, calculated from spectroscopic data (1) and constructing a χ^2 contour map of λ vs. L_s. For F108-coated latexes the result is shown in Fig. 4.4. The best fit yields $\lambda = 110 \pm 10$ nm which is consistent with our previous assumption that λ = 100 nm.

After obtaining the optimum values of the parameters, we can plot the theoretical predictions of the particle's final positions in scattering diagrams (cf. triangles in Fig. 4.2). The discrepancy between experimental and theoretical positions is caused by surface roughness (of the two colliding particles) and Brownian motion (of the moving particle). According to our error analysis with a Monte Carlo method (11), these errors result in deviations of 1 nm and 1×10^{-21} J for L_s and A respectively.

The force-distance profile can be plotted according to the DLVO theory once the force parameters are known (cf. Fig. 4.5). The profile with the non-retarded van der Waals force ($\lambda \rightarrow \infty$) is also plotted for comparison.

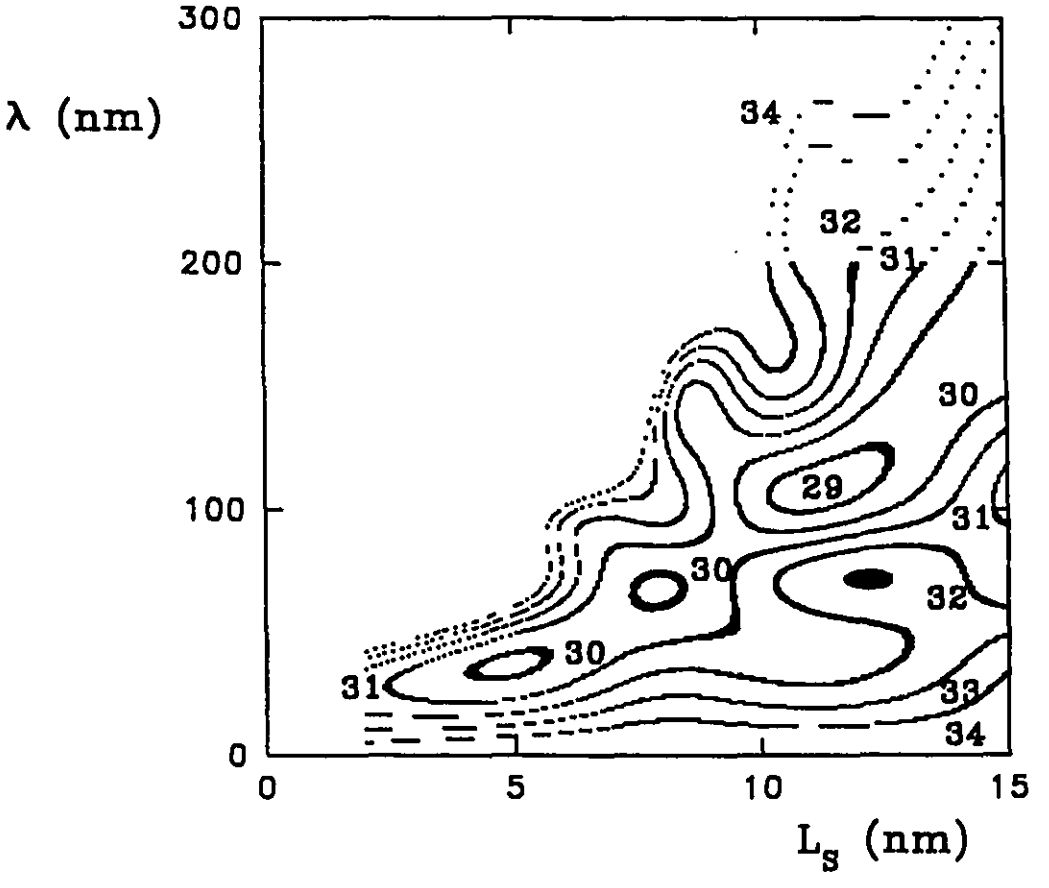

Fig. 4.4 χ^2 contour map of λ vs. L_s. The Hamaker constant, A, is fixed at the theoretical value, 9.5×10^{-21} J. The minimum gives $\lambda = 110 \pm 10$ nm.

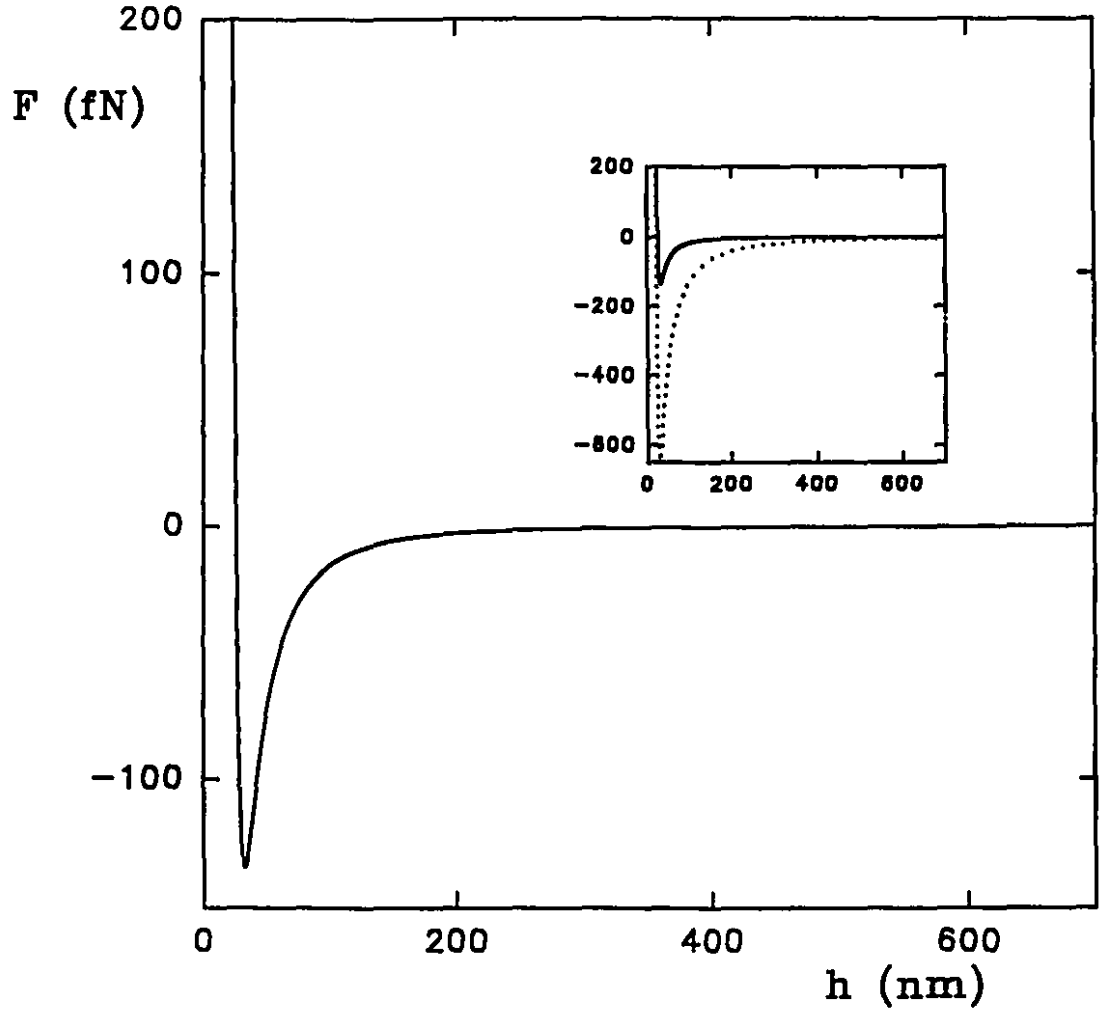

Fig. 4.5 A fitted DLVO-type force with a retarded van der Waals force term vs. separation gap width (solid curve) for two triblock-coated latex spheres. The force parameters are taken from the measurement of the Pluronic F108-coated latex experiment, i.e. L_s = 11 nm, $A = 1.0\times10^{-20}$ J and λ = 100 nm. The force unit is femtonewton (10^{-15} N). The interaction force with the same L_s and A but neglecting the retardation effect is also plotted (dotted curve) for comparison. Note the large effect of retardation on the force.

CONCLUSION

We have shown that CPS is capable of determining accurately the retarded van der Waals force between two latex spheres, while at the same time providing the thickness of polymer adsorption layers. The results for Pluronic triblock-coated latexes are: $A = (1.0 \pm 0.1) \times 10^{-20}$ J, $\lambda = 110 \pm 10$ nm and $L_s = 7$ and 11 nm ($\pm$ 1 nm) for F88 and F108, respectively. Because the model only applies when the adsorption layers do not overlap, it is limited to particles with thin layers. However, since most surfactant coatings are within 10 nm, it can actually be applied to a large number of systems.

REFERENCES

1. Hunter, R. J., "Foundations of Colloid Science." Vol.1, Clarendon Press, Oxford 1989, p.620.
2. Israelachvili, J. N., "Intermolecular and Surface Forces." Academic Press, London 1985, p.152.
3. Casimir, H. B. G., and Polder, D., *Phys. Rev.* **73**, 360 (1948).
4. Lifshitz, E. M., *Sov. Phys. JETP* **2**, 73 (1956).
5. Clayfield, E. J., Lumb, E. C., and Mackey, P. H., *J. Colloid Interface Sci.* **37**, 382 (1971).
6. Schenkel, J. H., and Kitchener, J. A., *Trans. Faraday Soc.* **56**, 161 (1960).
7. Gregory, J., *J. Colloid Interface Sci.* **83**, 138 (1981).
8. Israelachvili, J. N., and Adams, G. E., *J. Chem. Soc., Faraday Trans. 1* **74**, 975 (1978).
9. Ducker, W. A., Senden, T. J., and Pashley, R. M., *Nature* **353**, 239 (1991).
10. van de Ven, T. G. M., Warszynski, P., Wu, X., and Dabros, T., *Langmuir* **10**, 3046 (1994) (Chapter 2 of this thesis).
11. Wu, X., and van de Ven, T. G. M., to appear (Chapter 3 of this thesis).
12. Polverari, M., and van de Ven, T. G. M., *Colloids Surfaces A: Physicochem. Eng. Aspects* **86**, 209 (1994).
13. Chow, R. S., and Takamura, K., *J. Colloid Interface Sci.* **125**, 226 (1988).
14. Li, J.-T., Caldwell, K. D., and Rapoport, N., *Langmuir* **10**, 4475 (1994).

15. Baker, J. A., and Berg, J. C., *Langmuir* **4**, 1055 (1988).

16. van de Ven, T. G. M., "Colloidal Hydrodynamics." Academic Press, London 1989, p.24.

17. Lee, J., Martic, P. A., and Tan, J. S., *J. Colloid Interface Sci.* **131**, 252 (1989).

18. Garvey, M. J., Tadros, Th. F., and Vincent, B., *J. Colloid Interface Sci.* **55**, 440 (1976).

19. Kayes, J. B., and Rawlins, D. A., *Colloid Polym. Sci.* **257**, 622 (1979).

20. Caldwell, K. D., Jones, H. K., and Giddings, J. C., *Colloids Surfaces* **18**, 123 (1986).

21. Caldwell, K. D., and Li, J., *J. Colloid Interface Sci.* **132**, 256 (1989).

22. de Gennes, P. G., *Adv. Colloid Interface Sci.* **27**, 189 (1987).

23. Alexander, S., *J. Physique* **38**, 983 (1977).

CHAPTER 5

DYNAMIC INTERACTIONS BETWEEN POLYETHYLENE OXIDE LAYERS ADSORBED ON LATEX BEADS

OBJECTIVES

In the previous chapters, we have presented colloidal particle scattering as a new technique to determine colloidal forces and its applications in non-overlapping thin layer structures on latex surface. The objective of this chapter is to study steric interactions between thick polymer layers which overlap during particle collisions. A elastic layer model has been taken to describe this dynamic interaction force and interesting results have been obtained.

ABSTRACT

Dynamic interactions between two polyethylene oxide layers adsorbed on polystyrene latex spheres have been studied by colloidal particle scattering, a method developed by us to measure surface forces. The adsorption layers were modeled as an elastic gel characterized by its elastic modulus and thickness. Both of them were determined experimentally and the results agree with literature data. Furthermore, these two parameters provide us with information about polymer conformations on a latex surface at different adsorption concentrations, which is also consistent with previous theoretical and experimental findings.

INTRODUCTION

Polyethylene oxide (PEO) has been widely applied in papermaking, printing, lubrication and cleaning (1) mainly because it is a water-soluble macromolecule. In many applications, PEO is adsorbed on an interface and therefore it is of importance to study the properties of adsorbed PEO such as chain conformation and adsorption layer thickness. Adsorbed polymer conformations have been studied both theoretically and experimentally. The successful theories describing the structure of the adsorption layer are the self-consistent quasi-crystalline lattice theory by Scheutjens and Fleer (2,3) and the scaling theory by de Gennes (4,5). The former gives a clear picture of the segment distributions of trains, loops and tails. The experimental techniques to measure segment density distributions are small angle neutron scattering (SANS) (6), nuclear magnetic resonance (NMR) (7) and evanescent wave induced fluorescence (EWIF) (8). Based on these experimental and theoretical findings, some pragmatic theories of steric interactions between two polymer layers with an assumed constant or Gaussian segment density distribution were developed by Fischer (9) and Napper (10) using the model of interpenetration (or mixing) of polymer chains during a Brownian collision. Another approach to steric interactions is self-consistent field theory using a lattice mean-field model (11) to calculate the free energy change in the mixing process. Unlike the pragmatic theories, it predicts the conformational properties and the steric interactions at the same time, and does not require an assumed segment density distribution to start with. However, this analysis requires a correction because it overlooks a nonuniform pressure distribution. A modified theory developed by Evans (12) results in a longer range interaction

between polymer-coated surfaces. De Gennes (13) has also improved the mean-field analysis by introducing scaling exponents into the form of free energy. All of these theories assume the mixing of two polymer layers.

The adsorption layer thickness is also an important parameter determining the effectiveness of an adsorbed stabilizer. The thickness determined by sedimentation (14), centrifugation (15) or photon correlation spectroscopy (PCS) (16) is called the hydrodynamic thickness which is often much larger than the thickness determined by ellipsometry (17) or neutron scattering (6,18). In the former cases, water is immobilized by the long polymer tails which were found to be the main contribution to the larger value of hydrodynamic thickness (16).

All the studies mentioned above were performed under either static or pseudo-equilibrium conditions with slow approach between two surfaces. Under dynamic conditions, e.g. a pulp suspension in the head box of a paper machine, where the shear rate is usually over 1000 s^{-1}, the above arguments may not hold. For example, when a single particle coated with polymer moves in a high-shear flow, the solvent molecules can still be considered trapped in the tail region, however as soon as it is engaged in a collision with another particle, solvent molecules are drained out of the polymer layer, and thus the conventional hydrodynamic layer thickness cannot be used any more. Similarly, the polymer conformation on a single particle traveling in a high-shear flow may be described by the same train-loop-tail structure as under static conditions, but during a collision, the mixing of tails may not occur if the rearrangement time of the tails is longer than the time of surface contact. So far these dynamic aspects of steric interactions have not been fully investigated. Some hysteresis (19) and time-dependent

effects (20) on interactions between two PEO layers adsorbed on mica surfaces were observed with a surface force apparatus (SFA). These effects are caused by the momentarily higher-than-equilibrium value of polymer volume fraction (20) or transient dynamic effects. Because of the slow approach velocity (an indicator of local shear rate), about 10 nm/min, and absence of the tangential (or sliding) motion of two mica surfaces, equilibrium mixing of two polymer layers will eventually occur. Later studies (21,22) with a SFA operating at a 200 Hz vibration frequency, which generates an approach velocity of about 10 μm/s, equivalent to the approach velocity for a pair of 200 nm particles colliding in a 100 s^{-1} shear flow, successfully observed dynamic interactions between two layers of polymer melts. The viscosity of the polybutadiene melts was found to become non-Newtonian at high frequency and this was thought to arise from the driving frequency exceeding some characteristic relaxation time (21), a criterion determining an interaction to be static or dynamic.

Recently we developed a new experimental technique, colloidal particle scattering (CPS), to measure surface forces (23). It is based on the measurement of collision trajectories between two latex spheres of about 5 μm in size in a wall shear flow. The large size of the latex beads makes it possible to have a high approach velocity, e.g. 10 μm/s, at a relatively low shear rate, usually 4 s^{-1}. More importantly, because of the unique positioning of the two colliding particles, one being mobile while the other is stuck to the wall, the stationary particle cannot adhere to the mobile particle and rotate with it like a transient doublet, which frequently occurs during a collision between two freely mobile particles. Instead, it creates a sliding motion between the two surfaces and the mixing of two polymer layers on the surface will not occur. This simulates the dynamic collision process under very high shear

rates ($G>1000\ s^{-1}$) for which the polymer-polymer contact time is extremely short or the rotation of particles is hindered by attachment or entanglement.

In this paper, we first introduce some theoretical models describing the drainage of water in a polymer layer and steric interaction forces under dynamic conditions. Next, we present our data and data analysis techniques and finally compare our experimental results with some literature findings.

THEORY

1. Principles of CPS

The method is based on the analysis of particle collision trajectories between an immobile particle stuck to a wall and a freely mobile particle subjected to a wall shear flow of known shear rate (cf. Fig. 5.1). Initial positions of mobile spheres can be controlled by a micromanipulator and collisions can be generated at will at a rate of several hundred per day. These collision trajectories are recorded and analyzed with an image processing board. Collision trajectories can also be calculated by solving the trajectory equation. These theoretical trajectories are fitted to the experimentally observed ones by varying the parameters in the colloidal force equations which enter in the trajectory equations. The best fit yields the optimum parameters. With these parameters, the force-distance profile can be determined. A graph containing the mobile particle's positions before and after the collision is called a scattering diagram. It is a useful way to present and analyze collision data. The technique was discussed in detail in ref. (23).

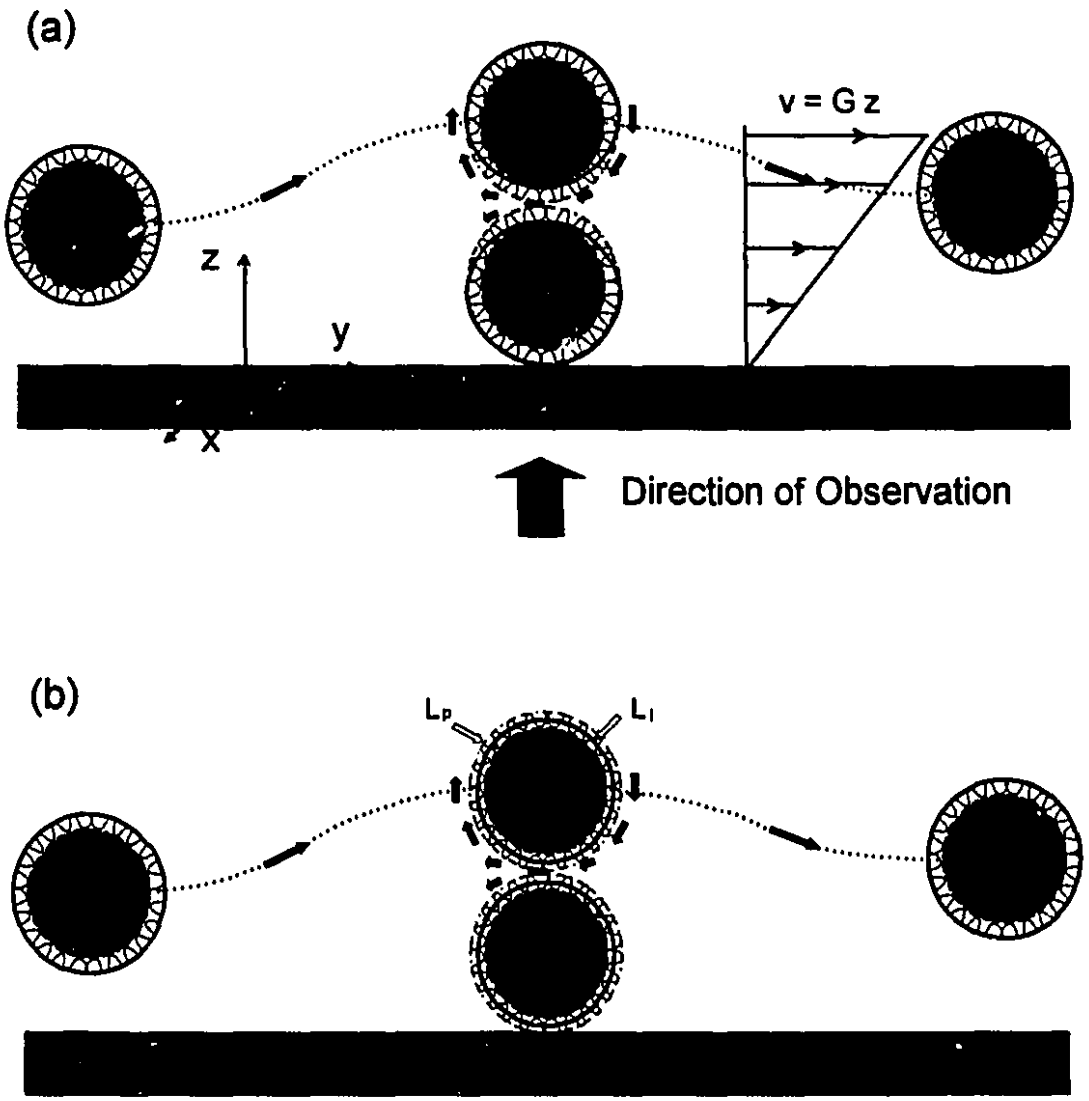

Fig. 5.1 Geometry of particle-particle collision system. G is the shear rate and v is the fluid velocity. The thick lines on top of the wall and around the spheres indicate the location of shear planes. (a) real system where the shear planes outside particles are not spherical during a collision; (b) model system where the shear planes are assumed spherical and divide the polymer adsorption layers into penetrable and impenetrable layers. Their thicknesses are denoted by L_p and L_l respectively.

2. Trajectory equation for polymer-coated spheres

The trajectory equation for bare spheres in the vicinity of a solid wall was solved by Dabros and van de Ven (24). It is based on the construction of the mobility tensor, **M**, by solving the Stokes equation for creeping flow:

$$\mu\nabla^2\mathbf{v} = \nabla p \qquad [5.1]$$

where μ is the viscosity of the fluid, **v** is the fluid velocity vector and p is the pressure. The particle position, **r**, as a function of time, t, can then be calculated by the trajectory equation:

$$\frac{d\mathbf{r}}{dt} = \mathbf{M}\cdot(\mathbf{F}_{hydr} + \mathbf{F}_{int}) \qquad [5.2]$$

where $\mathbf{F}_{hydr}$ and $\mathbf{F}_{int}$ are the hydrodynamic and colloidal interaction forces between two particles.

However, for collisions between two spheres coated with thick polymer layers, the problem becomes more complicated. Before or after a collision, the shear (or no-slip) plane stays on the outer surface of polymer layer as for a single particle moving in a fluid. During the collision, however, the shear plane transforms from a perfect spherical shape with a radius $a+L_s$ (a being the radius of the particle and L_s the total layer thickness) to a "dented" spherical shape as water is forced to pass through the layer [cf. Fig. 5.1 (a)]. This asymmetrical geometry makes the trajectory equation extremely difficult to solve. For this reason, an approximate model has been adopted to facilitate the analysis. The shear plane is assumed to be spherical even during the collision, but with a smaller radius, $a+L_i$, where L_i is the thickness of the impenetrable layer (the part of the polymer layer inaccessible to water

flow). We call the remaining part of the polymer layer penetrable layer with a thickness L_p. Obviously, $L_s = L_p + L_i$. The penetrable layer is considered "water" for hydrodynamic calculations, i.e. exerting no resistance to the flow, but it contributes to the steric interactions in the same way as the impenetrable layer. This treatment may appear to be an oversimplification. However, regarding the complexity of the problem, it could be a reasonable approximation to interpret the trajectory data, at least as a first step.

According to this model, the shear plane gradually shifts from the outer surface of the penetrable layer before the collision to the outer surface of the impenetrable layer during the collision and shifts back after the collision. In other words, the "hydrodynamic" layer thickness varies from L_p+L_i to L_i and finally back to L_p+L_i. This process cannot be described exactly by theory since the definition of penetrable or impenetrable layer itself is an approximation. However, a careful analysis of the collision trajectory reveals that the final position of the moving particle, which is used for force fitting (23), strongly depends on its position during the collision and is not very sensitive to the changing process of the shear plane before and after the collision. For this reason, we use an empirical expression to simulate the process:

$$L_d = L_p e^{-f_{perm} h_w} \qquad [5.3]$$

where L_d is the drainage layer thickness varying from 0 (non-penetration) to L_p (full penetration), h_w is the dimensionless separation distance (scaled by particle radius) between two polymer surfaces (width of "water gap") and f_{perm} is an arbitrary factor related to the permeability of the polymer layer. When $f_{perm} = 0$, water penetrates the polymer layer even

before the collision and the shear plane remains in the same position during the collision; when $f_{perm} \rightarrow \infty$, water never penetrates the layer, similar to the case when particles are coated with thin hairy or polymer layers (25,26) and never approach to the distance where these layers overlap. Neither of these two extreme cases can be applied to the present system. By trial and error, we found that the intermediate values between 10 and 100 are the optimum and, not surprisingly, the resulting trajectories are not very sensitive to the change in f_{perm} within this range for the reason mentioned above. Hence, we used a median value of $f_{perm} = 50$ in all calculations.

The choice of the exponential function in Eq. [5.3] can be justified by the literature data on the drag force exerting on fluid passing through a polymer-coated flat channel (27). The drag in a channel evenly filled with polymer ($h_w = 0$) is an order of magnitude higher than that in a water-filled channel with only two thin polymer layers on both walls ($h_w \approx$ channel width) assuming a typical adsorption amount of PEO (0.5 mg/m^2). It implies that most of the water will pass through the gap between two polymer layers even when this gap becomes very narrow. Little amount of water flowing through the polymer layer results in a small value of L_d. When $h_w \rightarrow 0$, L_d "jumps" from a small value to L_p and this trend can be accurately described by an exponential function.

3. Dynamic steric interactions

In a CPS experiment, as the stationary particle is incapable of rotating, a sliding motion occurs on the surfaces of the two colliding particles. This tangential velocity is in the same order of magnitude as the approach velocity (10 μm/s), so the time of contact between

two polymer chains can be calculated as the dimension of a chain's cross-section (about 1 nm) divided by the tangential velocity, which gives 10^{-4} s. The terminal relaxation time for polystyrene of $M_w = 5\times10^4$ is known to be 2×10^{-4} s (28) and for PEO of $M_w = 6\times10^5$ which was used in our experiments, this relaxation time is probably much longer. Without time to change its configuration, polymer chains from two layers will not mix. This makes the polymer layer behave like an elastic gel. The theory to describe the interaction between two solid spheres covered by elastic gel layers was developed by Jäckel (29) on the basis of the earlier work of Hertz (30):

$$V_{elas} = \frac{8\sqrt{2}}{15} E h_d^{\frac{5}{2}} (a+L_s)^{\frac{1}{2}} \qquad [5.4]$$

where V_{elas} is the elastic interaction energy, E is the elastic modulus of the polymer layer, h_d is the "denting" thickness (cf. Fig. 5.2). A similar relationship for the interaction energy between two elastic spheres was found by Landau and Lifshitz (31). The interaction force can be obtained by taking the derivative with respect to h_d in Eq. [5.4]:

$$F_{elas} = \frac{4\sqrt{2}}{3} E h_d^{\frac{3}{2}} (a+L_s)^{\frac{1}{2}} \qquad [5.5]$$

Incorporating this equation into our drainage model could result in a small deviation of the spherical shape of the shear plane, but since under our experimental conditions h_d is always smaller than the penetrable layer thickness L_p and this layer, as defined, is always outside the shear plane, the error is indeed negligible. In Eq. [5.5], L_s is usually two orders

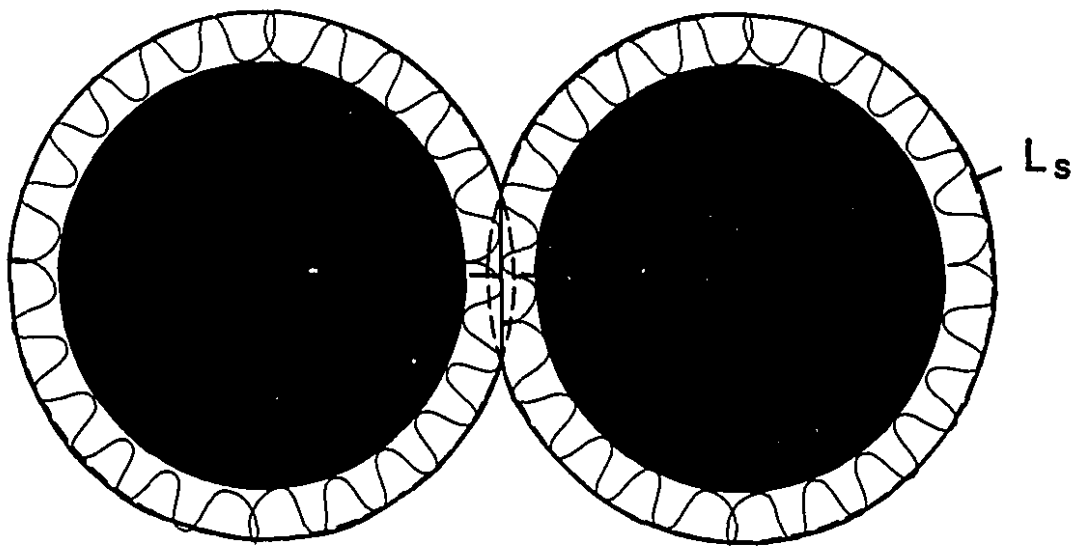

Fig. 5.2 "Denting" in polymer layers during a collision. L_s represents the total layer thickness, a is the particle radius and h_d is the "denting" thickness.

of magnitude smaller than a, and thus contributes very little to the force. Therefore, at a given separation distance, the elastic force solely depends on the elastic modulus.

In a transient network, the polymer chains are linked with entanglement points instead of permanent cross-linking points. These points determine the size of blobs, the fundamental units in a network. The elastic modulus is related to the number of blobs per unit volume, C_b, and the average interval between entanglement or attachment points, N_e (32):

$$E \propto \frac{C_b}{N_e} \qquad [5.6]$$

We can, therefore, gain information about the gel structure through measuring the elastic modulus, E.

Another theory describing the non-mixing steric force is Bagchi's "denting" theory (33,34). It calculates the free energy change due to the "volume restriction effect". This theory, however, cannot be applied in a dynamic system because the lattice model which is used implies a gentle approach of the polymer layers which may not be true in a dynamic system where squeezing and stretching of polymer chains are commonplace.

When the impact force is not very strong or the polymer chain is very rigid, we can use a hard-wall approximation to give a quick analysis of the collision data. This approximation assumes that the repulsive force becomes infinite at a separation of $2L_t$. Thus the polymer layers never dent or mix and no unknown parameters have to be determined to calculate the force. However, no information about the polymer layers can be obtained either. As will be shown later, we only use this model to fit the insensitive parameter, L_t, which does

not affect the trajectory very much and is almost completely insensitive to the interaction models used in the calculation.

EXPERIMENTAL

1. Materials and experimental conditions

The latex sample used in the experiments consists of 4.7 μm surfactant-free polystyrene latex spheres supplied by Interfacial Dynamics Corp. The stabilizing charge groups are sulfate groups. Before the experiments, the latex spheres were heated in an autoclave at 115~120°C for 16 hours to smooth their surfaces (35) and were subsequently washed several times with deionized water to minimize contamination.

The PEO sample with a viscosity molecular weight of 600,000 was supplied by Aldrich Chemical Co. Its polydispersity was measured as 2.86 (36). A 250 mg/L solution was prepared and filtered through a 0.2 μm filter supplied by Chromatographic Inc.

A 0.005% latex suspension was dropped into the PEO solution and the dispersion was left to stand for one hour. Two samples were prepared afterwards: one with the solution diluted to a final 50 mg/L PEO content and the other still containing 250 mg/L PEO. Both solutions contain 60% D_2O and 0.01 M KCl. Two sets of experiments were then performed with these two solutions (set A: 50 mg/L PEO and set B: 250 mg/L PEO). The added PEO amounts correspond to 900 mg/m^2 latex surface for set A and 4500 mg/m^2 for set B.

2. Procedures

The detailed experimental procedures were described in ref. (23). In the present experiments we used a relatively narrow gap width (~120 μm) between two glass plates to create a larger shear rate (~4.6 s^{-1}). Typically, 100-200 collisions were generated and analyzed. A collision trajectory is characterized by the values of the coordinates (x, z) (cf. Fig. 5.1) before and after the collision. The values of x can be obtained directly from the video image, while the values of z has to be calculated from the particle velocity. In the present experimental systems, both the glass wall and the particle were coated with PEO. In principle the velocity correction function $f_3(z/a)$ used to calculate z from the particle velocity should be modified accordingly. However, a study (37) showed that by shifting the shear plane to the outer surface of the adsorption layer, we can keep the function for bare particle-wall system without introducing much error.

The collision trajectories can be presented in a scattering diagram (cf. Fig. 5.3) where the open circles represent the positions of the moving particle before the collision and the filled circles represent the positions after the collision. Most of the collisions shown in Fig. 5.3 were, to some extent, affected by an anomalous tangential force component (25) caused by the surface roughness and larger-than-average Brownian motion. They were "disqualified" for the force fitting according to the data selection rules discussed in ref. (25). However, they can be used to analyze the surface roughness qualitatively. Usually, more scattered final positions indicate a rougher surface. After the data selection, the resulting scattering diagrams containing only "qualified" collisions are shown in Fig. 5.4, 32 collisions were selected for set A and 30 collisions for set B.

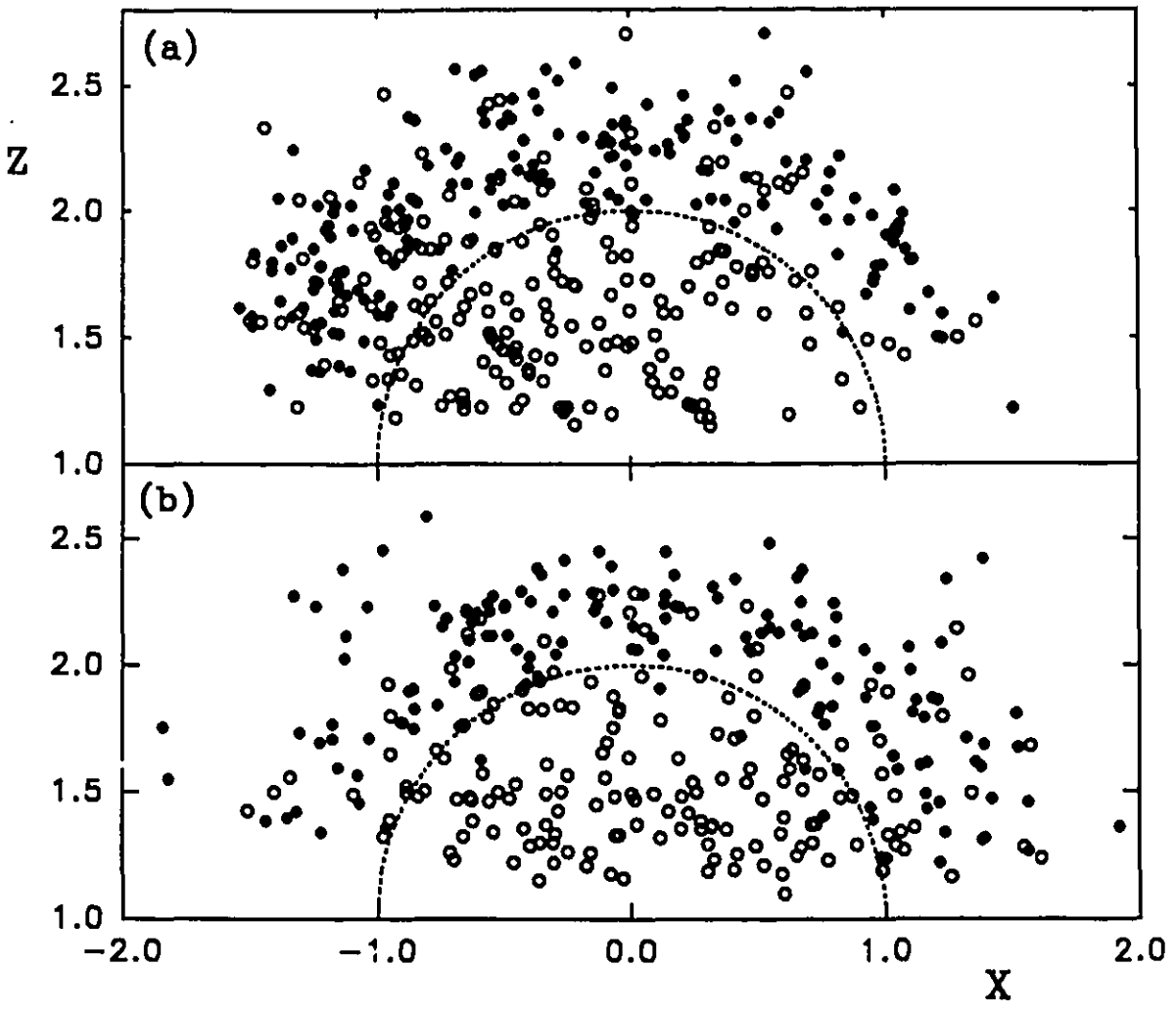

Fig. 5.3 Scattering diagrams of collision experiments with latexes coated by (a) 50 mg/L PEO, 193 collisions; and (b) 250 mg/L PEO, 160 collisions. The coordinates are scaled by the particle radius. The open circles represent the initial positions of the moving particle, the filled circles stand for the experimentally determined final positions of the same particle. The semicircle in the middle is the projection of the stationary particle. Same symbols will be adopted in the following scattering diagrams.

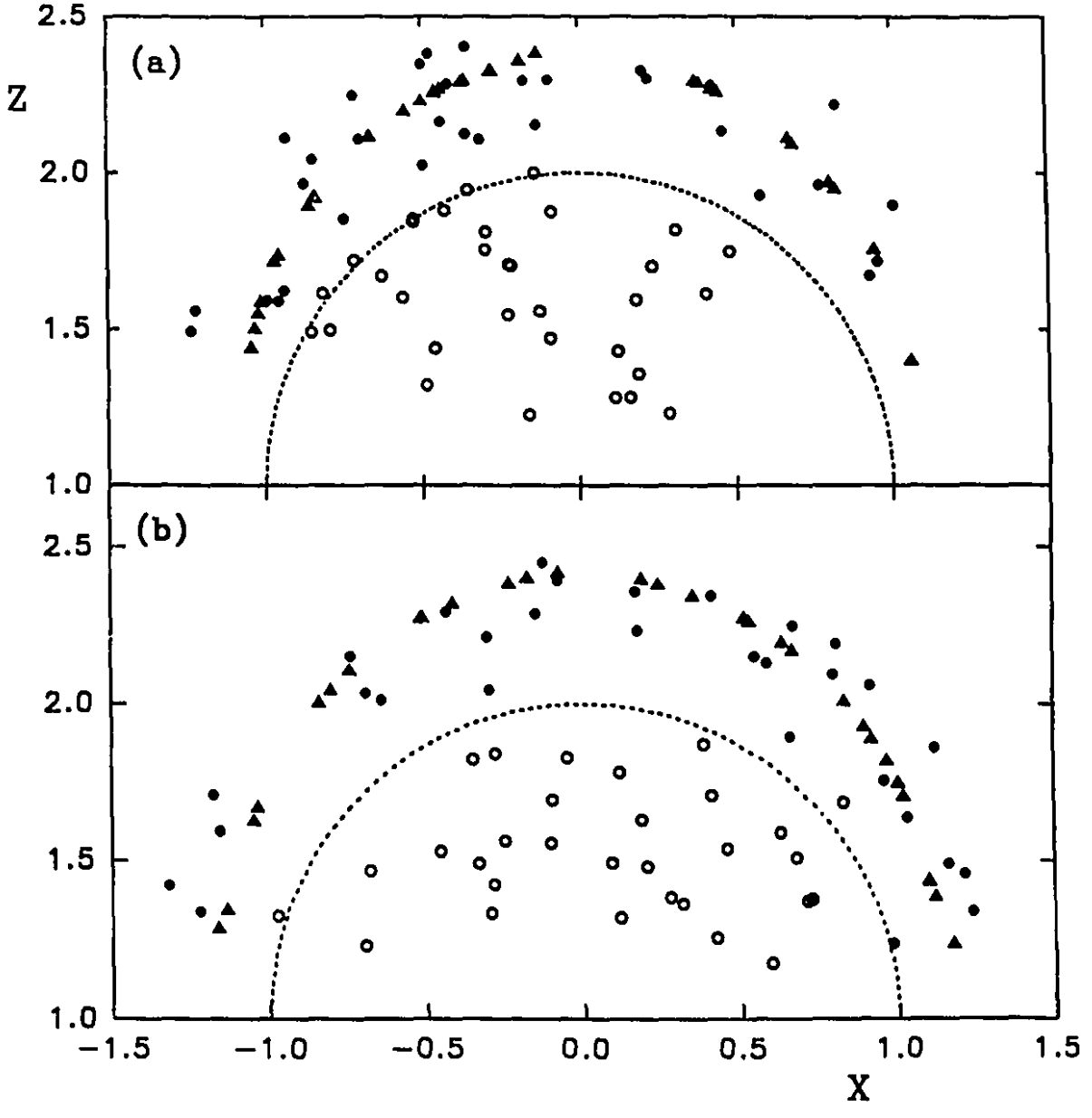

Fig. 5.4 Scattering diagrams of (a) 32 and (b) 30 selected collisions from Fig. 5.3. The filled triangles represent the theoretical final positions calculated from the best-fit parameters.

3. Data analysis

Many parameters affect the interaction forces. Some of them have been determined in our previous study (25) in which the same IDC latex sample was characterized. It shows that the measured Hamaker constant, A, and retardation wavelength, λ, of this sample are within 10% deviation from the theoretical values, 9.5×10^{-21} J (38) and 100 nm (39) respectively. These parameters are thus treated as constants. The surface potential (potential on latex core surface), ψ_0, is fixed at the zeta-potential value, -70 mV, of the bare IDC latex particles, which was also measured in ref. (25). This large surface potential value does not imply a large electrostatic force because it is almost completely screened at a separation distance of $2L_s$ (typically over 50 nm) in a 0.01 M KCl solution.

Three parameters are then left to be fitted from the collision data: L_p, L_i (from our drainage model) and E (from Eq. [5.5]). In principle, these three parameters can be fitted simultaneously by constructing a 3-D χ^2 contour map. (χ^2 represents the goodness-of-fit. A minimum value of χ^2 yields the optimum parameters.) However, this procedure requires unrealistically long computation times. By studying the sensitivity of a collision trajectory to variations in these three parameters, we found that only the change in L_p greatly affects the trajectory. Hence, we can replace the 3-D contour map with two 2-D maps to achieve the same accuracy. First, the hard-wall approximation is taken to construct a χ^2 contour map of L_p vs. L_i. The minimum value gives the optimum L_i and L_p. Since polymer layers do not dent in the hard-wall model, this "optimum" L_p is actually the real L_p less the denting thickness at the last stage of a collision. A more accurate fitting using Eq. [5.5] is then performed to plot a contour map of L_p vs. E. The minimum yields the final optimum values of L_p and E.

4. Error analysis

A Monte Carlo analysis was performed to estimate the measurement errors in L_p, L_i and E. The errors are caused by Brownian motion and surface roughness and thus affect the trajectories or particle final positions randomly (25). From Fig. 5.4, it can be seen that the distances between theoretical and experimental final positions are mostly within 0.2a. Therefore, we varied the experimental final positions randomly within this range and reconstruct the χ^2 contour maps of L_p vs. L_i and L_p vs. E which give the new set of optimum values for L_p , L_i and E. This procedure was repeated 1000 times and the variations of these parameters were evaluated.

RESULTS AND DISCUSSION

1. Adsorption layer thickness

From Figs. 5.5 and 5.6, it can be seen that for set A, L_p=27 nm, L_i =0 nm and L_s=L_p+L_i=27 nm; for set B, L_p=28 nm, L_i=29 nm and L_s=L_p+L_i=57 nm. Previous studies indicate a strong correlation between the adsorption layer thickness, L_s, and the adsorbed amount, Γ (16). At low Γ, polymer chains are in a flat conformation with very few tails. This makes L_s small and almost independent of Γ until the surface is saturated at certain threshold value of Γ. When the adsorbed amount is higher than this threshold value, loops and tails start to develop and L_s increases dramatically. Since the only difference between sets A and B is the final PEO concentration, our results of very different L_s in these two sets indicate that desorption occurred after diluting the PEO solution, though the amount of PEO desorbed

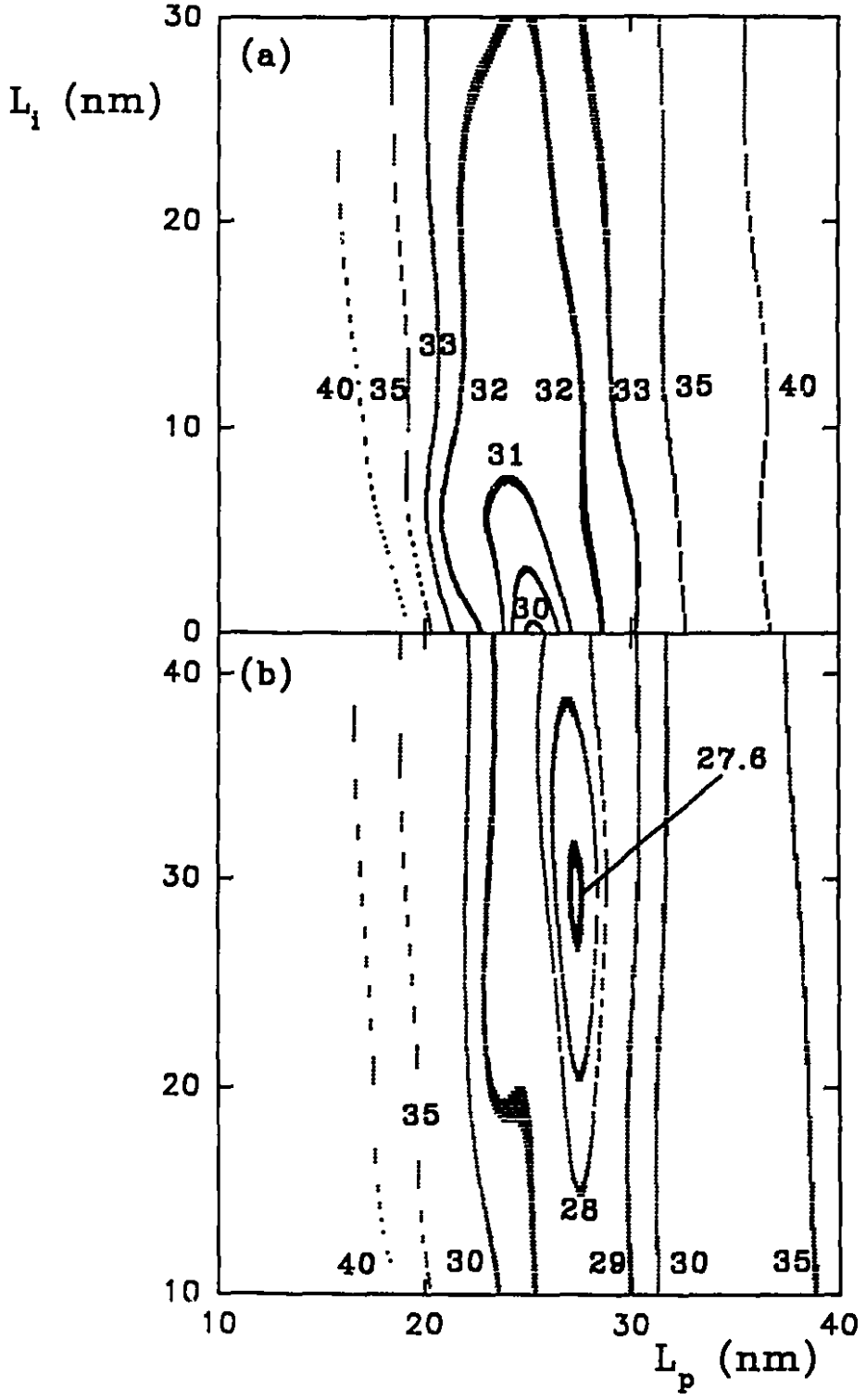

Fig. 5.5 χ^2 Contour maps of L_p and L_i under two experimental conditions: (a) 50 mg/L PEO, minimum at (L_p = 25 nm, L_i = 0 nm); (b) 250 mg/L PEO, minimum at (L_p = 27 nm, L_i = 29 nm). The parameters kept constant are $A = 9.5\times10^{-21}$ J, λ = 100 nm and ψ_0 = -70 mV.

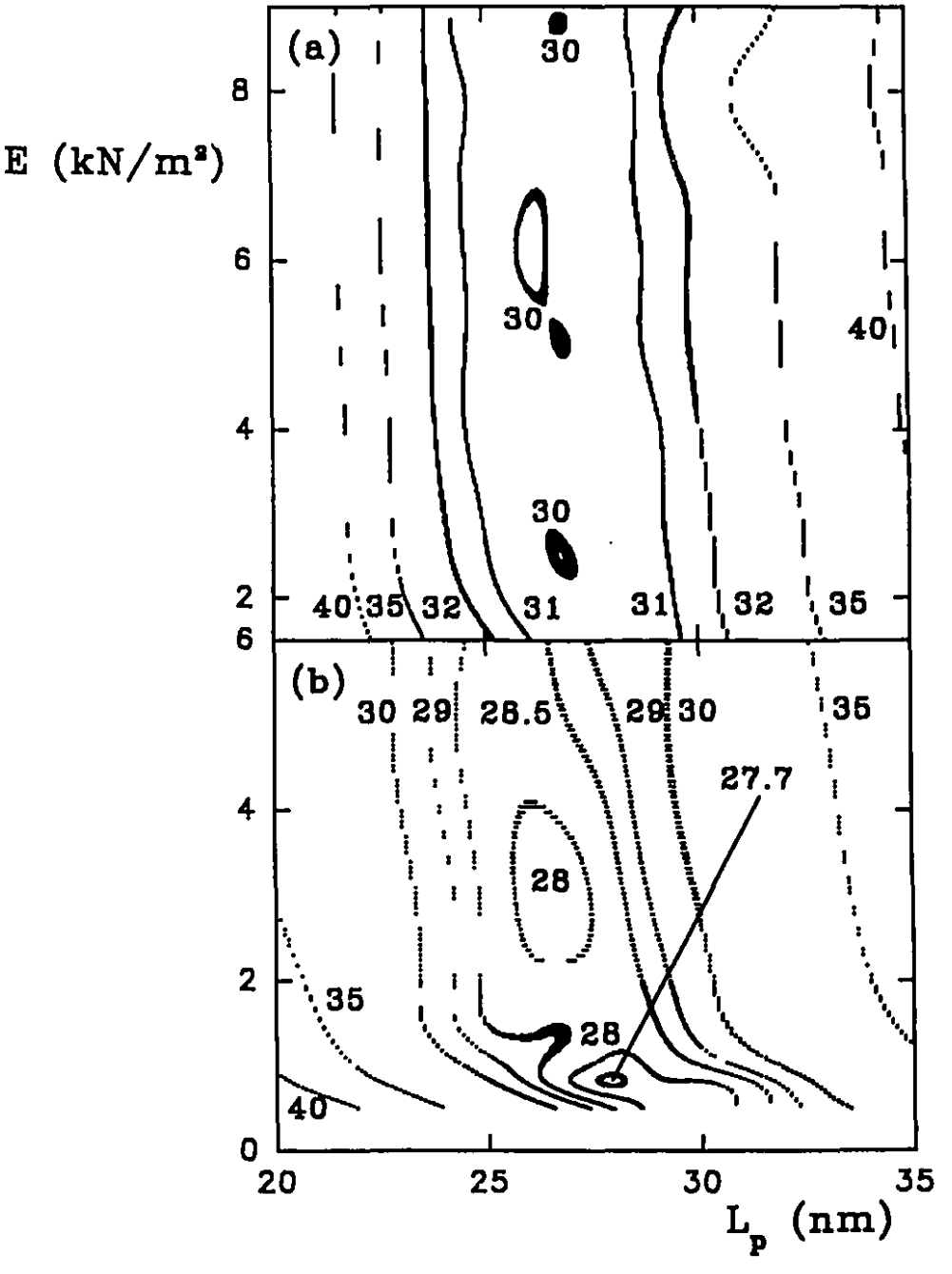

Fig. 5.6 χ^2 Contour maps of L_p and E under two experimental conditions: (a) 50 mg/L PEO, average minimum at (L_p = 27 nm, E = 5×10^3 N/m^2); (b) 250 mg/L PEO, minimum at (L_p = 28 nm, E = 8×10^2 N/m^2). The parameters kept constant are A = 9.5×10^{-21} J, λ= 100 nm, ψ_0 = -70 mV and L_1 = 0 nm (set A); L_1 = 29 nm (set B).

may not be much because L_s drops dramatically when Γ becomes slightly lower than the threshold value. The desorption was further verified with an electrophoretic mobility (E_m) measurement. E_m of set B is 0 while E_m of set A is -6.2×10^{-9} m^2/sV. The non-zero E_m indicates that some PEO molecules have left the surface making the neutral adsorption layer too thin to cover some long charged strings (25,40). The electrostatic force generated by this finite charge is, nevertheless, negligible because of the screening effect of salt.

Polymer desorption under washing or dilution was not observed in previous studies (36,41) with smaller latex particles. In our system, the "hairy" layer with a determined thickness of 3 nm on the latex particle surface (25) might sterically hinder PEO adsorption and weaken the attachment. This is probably the reason for the desorption. The steric hindrance is not so serious in small latex particle systems because the hairy layer thickness, L_h, is normally scaled down with the particle size, e.g. the L_h of a 160 nm sulfate latex sample was calculated from the electrophoretic mobility data to be 0.6 nm (36). This hypothesis is consistent with the adsorption layer thickness data obtained from the 160 nm latex particles coated by the same PEO sample with photon correlation spectroscopy (36). A graph of L_s vs the added PEO amount, C_{add}, was plotted and the onset of the plateau was found to be around 500 mg/m^2. Since the bonding of PEO with the latex surface is weaker in our system, we would expect this concentration to be higher when the plateau is reached to compensate the desorption. The L_s (27 nm) of set A (C_{add} = 900 mg/m^2) is obviously not on the plateau because the L_s (57 nm) of set B (C_{add} = 4500 mg/m^2) is higher. The latter is probably on the plateau because the measured value of L_s, 57 nm, is very close to the plateau L_s, 50 nm, determined by PCS in ref. (36). These results indicate that the onset of the plateau shifts, as

expected, from 500 mg/m^2 to the regime of 900 to 4500 mg/m^2. An adsorption isotherm may depict the effect of PEO concentration on adsorption amount more clearly, but it does not reveal much information about the adsorption layer thickness as well as the polymer conformation since, as mentioned above, the relationship between the adsorption amount and the layer thickness is not linear (16,42). Even if both polymer concentrations are found to be on the adsorption plateau, the corresponding adsorption layer thicknesses could be very different due to the dramatic change in the layer thickness around the threshold value of the adsorbed amount.

Our data also show that the penetrable layer thicknesses, L_p, for sets A and B are almost identical despite the fact that the layer thickness, L_s, for set B is twice as large as that for set A. This can be explained by the same constant shear rate in both experiments which drives the flow with a very similar velocity profile through the gap between the two spheres. In our calculation, this is modeled as the same L_p and the same position of the shear plane.

2. Surface roughness

The surface roughness can be qualitatively evaluated by the degree of scattering of experimental final positions in a scattering diagram (see Experimental part). From Fig. 5.3, it can be seen that the pattern shown in the diagram of set B [cf. Fig. 5.3 (b)] contains considerably more scatter than that in the diagram of set A [cf. Fig. 5.3 (a)]. This means that the surface of latex in a 250 mg/L PEO solution is more irregular than that in a 50 mg/L solution. This is probably caused by the polydispersity of PEO which manifests itself more clearly in a loop/tail structure than in a flatter configuration.

3. Elastic modulus of gel-like layer

Fig. 5.6 gives four minima for set A and one minimum ($E = 8\times10^2$ N/m^2) for set B. If we take the average value of the moduli in set A, the result is $E = 5\times10^3$ N/m^2. The error in the measurement will be discussed shortly. The reason for the difference of these two moduli is that the flatter conformation in set A produces many attachment points on the surface while the more extended conformation in set B relies on a few entanglement points between tails to build up a network. The average length between two attachment points is probably shorter than that between two entanglement points. In addition, more attachment points also create more blobs in a unit space. According to Eq. [5.6], both trends lead to a smaller E for set B.

When a 2-D surface gelation on an air-water interface was studied (43), similar results were obtained, i.e. an unfolded 2-D structure adopted by polymer molecules at low concentration results in a higher gel strength than that from a loop/tail structure when the polymer concentration is high.

Since most of the reported data of polymer layer properties were obtained under less dynamic conditions and PEO layers are known not to behave like an elastic gel under these conditions, it is hard to verify the elastic moduli at different PEO concentrations. However, a polyvinyl alcohol (PVA) layer displays a gel-like behavior even under "static" conditions. The elastic modulus of PVA was determined with a reflectance apparatus at a PVA concentration of 2000 mg/L (44). The result was $E = 1.2\times10^4$ N/m^2. Another measurement performed by Sonntag (45) yielded an E of 1.4×10^3 N/m^2. These results are of the same order of magnitude as those of PEO obtained in this study.

Under dynamic conditions, many other polymer layers also resemble an elastic gel provided that the contact time is shorter than chain relaxation time. Therefore, the use of an elastic modulus to describe the dynamic properties of an adsorption layer can be applied to lots of systems. Interestingly, this was foreseen by Napper (46) more than a decade ago.

4. Measurement errors

The errors in experiment set A were evaluated by a Monte Carlo analysis (see Experimental part). Fig. 5.7 shows the histograms of the three parameters: L_i, L_p and E. Fig. 5.7 (a) and (b) give $0 < L_i < 6$ nm and $L_p = 27 \pm 4$ nm at 90% confidence. Since there is no obvious peak in Fig. 5.7 (c) and no χ^2 minima are found outside the range 1 kN/m^2 < E < 9 kN/m^2, we can conclude that E = 5±4 kN/m^2. The relative error for the layer thickness of set B is expected to be similar (10%-20%). The error for elastic modulus of set B should be less than 80% because of the obvious convergence of the minimum in Fig. 5.6 (b).

CONCLUSION

We have successfully demonstrated the use of colloidal particle scattering to study dynamic interactions between two PEO layers adsorbed on polystyrene latex particles. Under dynamic conditions, the adsorption layer acquires gel-like properties, which can be described by an elastic modulus. We have determined this modulus, as well as the adsorption layer thickness. The results reveal information about polymer conformations at different adsorption concentrations, which is consistent with literature data.

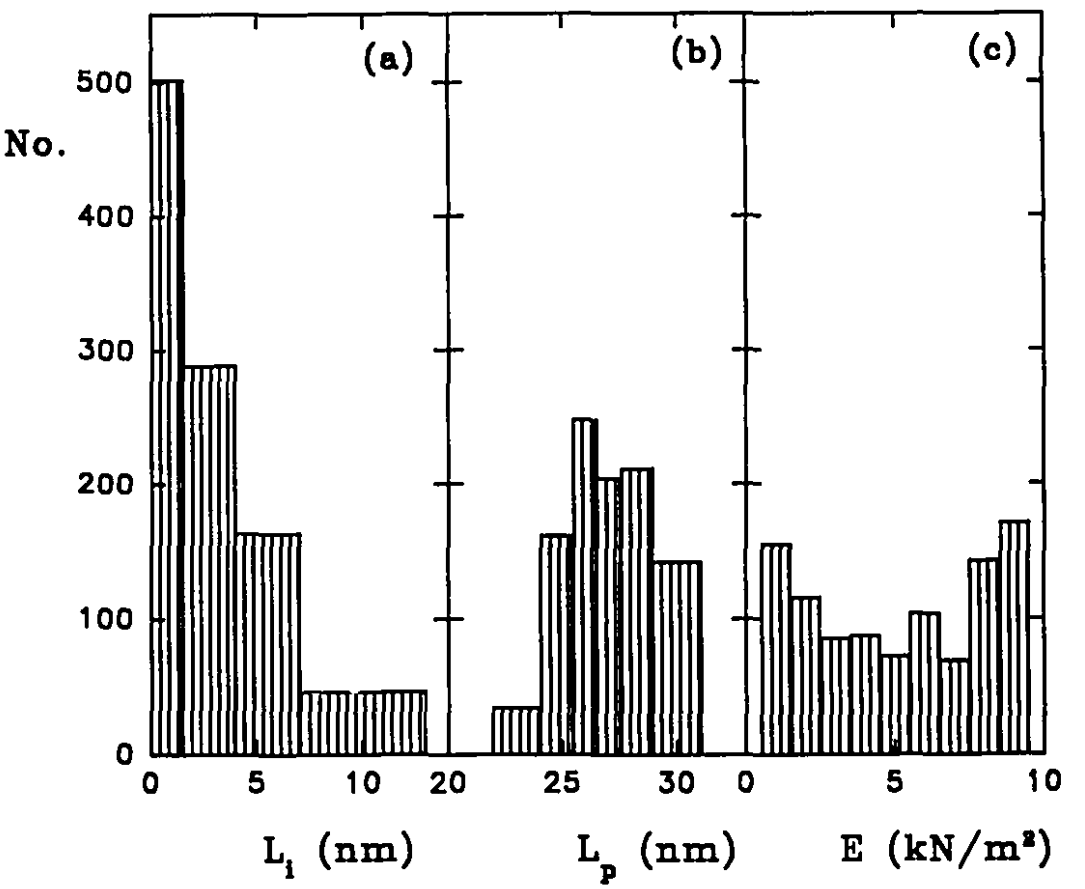

Fig. 5.7 Histograms of L_i, L_p and E. The width and the total counts of a peak region indicate the error and its confidence level respectively. The results are (a) $0 < L_i < 6$ nm and (b) $L_p = 27 \pm 4$ nm both at 90% confidence level. The even distribution in (c) gives an average value $E = 5 \pm 4$ kN/m^2.

REFERENCES

1. Meltzer, Y. L., "Water-Soluble Polymers." Noyes Data Corp., Park Ridge 1981, p.199.
2. Scheutjens, J. M. H. M., and Fleer, G. J., *J. Phys. Chem.* **83,** 1619 (1979).
3. Scheutjens, J. M. H. M., and Fleer, G. J., *J. Phys. Chem.* **84,** 178 (1980).
4. de Gennes, P. G., *J. Physique* **37,** 1445 (1976).
5. de Gennes, P. G., *Macromolecules* **14,** 1637 (1981).
6. Cosgrove, T., Crowley, T. L., Ryan K., and Webster, J. R. P., *Colloids Surf.* **51,** 255 (1990).
7. Cosgrove, T., and Ryan, K., *Langmuir* **6,** 136 (1990).
8. Caucheteux, L., Hervet, H., Jerome, R., and Rondelez, F., *J. Chem. Soc. Faraday Trans.* **86,** 1369 (1990).
9. Fischer, E. W., *Kolloid Z.* **160,** 120 (1958).
10. Napper, D. H., *J. Colloid Interface Sci.* **58,** 390 (1977).
11. Edwards, S. F., *Proc. Phys. Soc.* **85,** 613 (1965).
12. Evans, E., *Macromolecules* **22,** 2277 (1989).
13. de Gennes, P. G., *Macromolecules* **15,** 492 (1982).
14. Ottewill, R. H., and Walker, T., *Kolloid Z. Z. Polym.* **227,** 108 (1968).
15. Coll, H., Oppenheimer, L. E., and Searles, C. G., *J. Colloid Interface Sci.* **104,** 193 (1985).
16. Cohen-Stuart, M. A., Waajen, F. H. W. H., Cosgrove, T., Vincent, B., and Crowley,

T. L., *Macromolecules* **17,** 1825 (1984).

17. Stromberg, R. R., Smith, L. E., and McCrackin, F. L., *Symp. Faraday Soc.* **4,** 192 (1970).

18. Barnett, K. G., Cosgrove, T., Vincent, B., Burgess, A. N., Crowley, T. L., King, T., Turner, J. D., and Tadros, Th. F., *Polymer* **22,** 283 (1981).

19. Israelachvili, J. N., Tandon, R. K., and White, L. R., *J. Colloid Interface Sci.* **78,** 430 (1980).

20. Klein, J., and Luckham, P. F., *Macromolecules* **17,** 1041 (1984).

21. Israelachvili, J. N., Kott, S. J., and Fetters, L. J., *J. Polym. Sci.: Part B: Polym. Phys.* **27,** 489 (1989).

22. Montfort, J. P., and Hadziioannou, G., *J. Chem. Phys.* **88,** 7187 (1988).

23. van de Ven, T. G. M., Warszynski, P., Wu, X., and Dabros, T., *Langmuir* **10,** 3046 (1994) (Chapter 2 of this thesis).

24. Dabros, T., and van de Ven, T. G. M., *J. Colloid Interface Sci.* **149,** 493 (1992).

25. Wu, X., and van de Ven, T. G. M., to appear (Chapter 3 of this thesis).

26. Wu, X., and van de Ven, T. G. M., to appear (Chapter 4 of this thesis).

27. de Witt, J. A., and van de Ven, T. G. M., *J. Colloid Interface Sci.* **151,** 118 (1992).

28. Hesselink, F. Th., *J. Phys. Chem.* **75,** 65 (1971).

29. Jäckel, K., *Kolloid Z. Z. Polym.* **197,** 143 (1964).

30. Hertz, H., *Mathematik* **92,** 155 (1888).

31. Landau, L. D., and Lifshitz, E. M., "Course of Theoretical Physics, Vol. 7: Theory of Elasticity." 3rd Edition, Pergamon Press, Oxford 1986, p.26.

32. de Gennes, P. G., "Scaling Concept in Polymer Physics." Cornell University Press, London 1979, p.221.

33. Bagchi, P., *J. Colloid Interface Sci.* **47**, 86 (1974).

34. Bagchi, P., *J. Colloid Interface Sci.* **47**, 100 (1974).

35. Chow, R. S., and Takamura, K., *J. Colloid Interface Sci.* **125**, 226 (1988).

36. Polverari, M., and van de Ven, T. G. M., *Colloids Surf.* **86**, 209 (1994).

37. Warszynski, P., *Colloids Surf.* **39**, 79 (1989).

38. Hunter, R. J., "Foundations of Colloid Science." Vol.1, Clarendon Press, Oxford 1989, p.222.

39. Schenkel, J. H., and Kitchener, J. A., *Trans. Faraday Soc.* **56**, 161 (1960).

40. Dabros, T., Warszynski, P., and van de Ven, T.G.M., *J. Colloid Interface Sci.* **162**, 254 (1994).

41. de Gennes, P.G., *Adv. Colloid Interface Sci.* **27**, 189 (1987).

42. de Witt, J. A., and van de Ven, T. G. M., *Langmuir* **8**, 788 (1992).

43. Cohen-Stuart, M.A., Keurentjes, J.T.F., Bonekamp, B.C., and Fraaye, J.G.E.M., *Colloids Surf.* **17**, 91 (1986).

44. Cain, F.W., Ottewill, R.H., and Smitham, J.B., *Faraday Disc. Chem. Soc.* **65**, 33 (1978).

45. Sonntag, H., *Abh. AdW. DDR Klasse Chemie NI* **2**, 517 (1974).

46. Napper, D.H., "Polymeric Stabilization of Colloidal Dispersions." Academic Press, London 1983, p.215.

CHAPTER 6

ELECTROKINETIC LIFT:

OBSERVATIONS AND COMPARISONS

WITH THEORIES

OBJECTIVES

In the previous chapters, a new force apparatus, the microcollider, and its applications in determining various colloidal forces between two bare or coated latex spheres have been presented. It has been realized that this apparatus will be an equally accurate instrument to measure particle-wall interactions. Therefore in this chapter, the objective is to reconfigure the microcollider to determine a very weak force called electrokinetic lift force. The experimental results not only prove that the reconfigured microcollider is capable of accurately determining weak particle-wall interactions, but point out the incorrectness of several electrokinetic theories which has been later confirmed.

ABSTRACT

A new experimental technique has been developed to study the electrokinetic lift force, acting on an electrically charged particle moving parallel to a surface in a polar liquid. It is based on the observation of the normal movement of a particle close to a wall in a wall shear flow. Our experimental results show that the force increases with increasing shear rate and decreasing solution conductivity. These findings are consistent with previously reported data and confirm the existence of an electrokinetic lift force which is difficult to detect because of its small magnitude. The experimental results are compared with various theoretical predictions. The comparisons show that the lift force calculated by most electrokinetic theories is not correct. Two new recently developed theories were applied to interpret the data and reasonably good agreement with experimental results was found.

INTRODUCTION

Electrokinetic lift is caused by the sliding motion of two charged surfaces in a polar fluid (1-4). This interesting phenomenon was first observed by Alexander and Prieve (5) who studied the change in depth of a 9 μm latex particle moving along a glass wall at a speed of 50 μm/s in their slit-like flow cell apparatus containing a glycerol-water solution. Under conditions of low conductivity and high relative tangential velocity of the two surfaces, this lift force becomes a dominant force in particle-wall interactions which govern particle deposition and detachment (6), hydrodynamic chromatography (7), mineral flotation, various biological phenomena (8), etc. For this reason, it is of importance to understand the cause of the force and its magnitude. Various theories (1-4) used the non-zero normal Maxwell stress tensor to explain the lift force. They predict the force to increase with increasing particle velocity parallel to the wall and to decrease with increasing conductivity of the system. These predictions are consistent with Alexander *et al.* (5) and Bike (9)'s experimental results. Despite this qualitative agreement, the predicted force is at least two orders of magnitude smaller than the experimentally observed one.

To better understand the exact magnitude of the lift force as well as its mechanism, we performed a systematic study of this force with our "microcollider" (10) which is capable of accurately controlling the shear rate and measuring the changes in particle depth as a function of time. We also developed a new theory (later denoted as Warszynski-van de Ven theory or W-V theory) emphasizing the non-zero normal hydrodynamic stress which was found to be orders of magnitude larger than the Maxwell stress and is the main contribution

to the lift force. The theory will be discussed in detail in a future publication (11). Recently another theory was developed independently by Cox to calculate the lift force (12,13). It also treats the hydrodynamic stress term as the dominant term. In this paper we first give a brief review of all the theories concerning electrokinetic lift, including the W-V theory and Cox's theory, then we present our experimental technique and data, and finally we compare these data with various theoretical results and discuss their validity.

THEORY

The electrokinetic lift force is generally a repulsive force (13) between two charged surfaces which are undergoing a sliding motion. The Stokes equation predicts no hydrodynamic force acting normal to the surfaces and, therefore, the lift is caused solely by the distortion of the counterion clouds resulting from the sliding motion. The two charged surfaces can be of any shape, however, since the most common experimental system consists of a planar glass wall and a several-micron large latex sphere (cf. Fig. 6.1), the lift force theories are developed for similar geometries.

Most of the existing theories are valid in one of the following two regions:

$$(a)\ \kappa^{-1} \ll h \ll a;\ \ (b)\ h \geq a,$$

where κ is the reciprocal Debye length, h is the separation distance between the particle and the wall (or particle depth), and a is the particle radius.

The first theory, developed by Bike and Prieve (1), applies to region (a). Within this

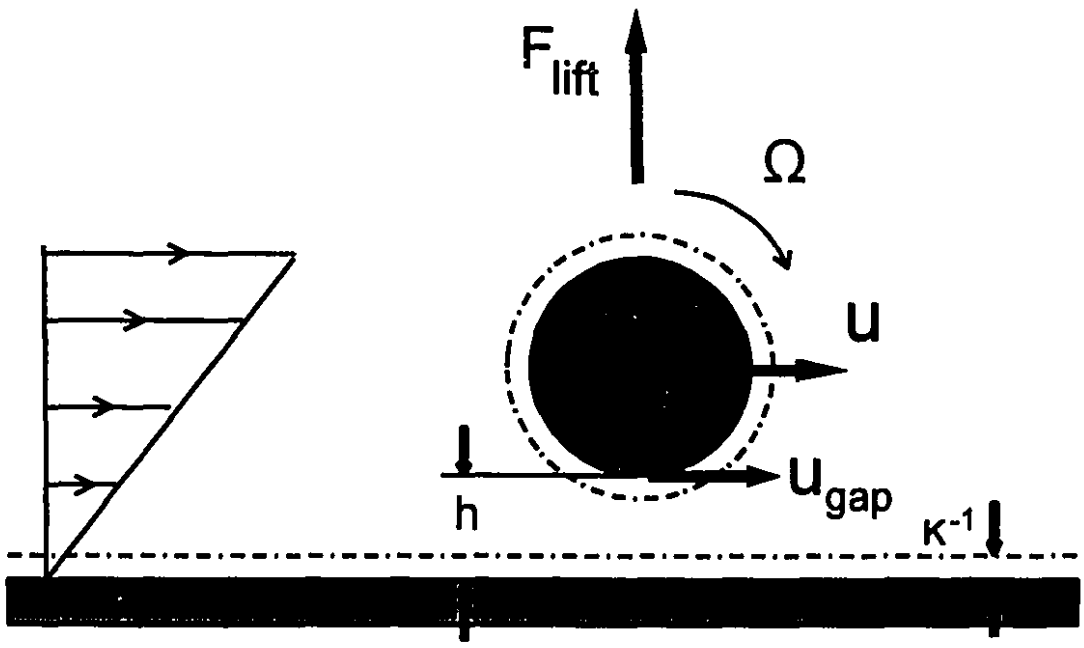

Fig. 6.1. Schematic illustration of the electrokinetic lift force and a typical experimental system. The dashed lines indicate the locations of the electric double layers of the particle and the wall with a thickness of κ^{-1} (not drawn to scale). h is the separation distance, a is the particle radius, u is the particle velocity, Ω is the angular velocity and u_{gap} is the translational velocity of the bottom of the particle ($u_{gap} = u - \Omega a$). The same symbols may be applied to a cylinder-wall system as in the W-V and Cox's theories.

region, the electric double layers of the particle and the wall do not overlap and, moreover the lubrication theory can be used to solve the Stokes equation. The theory yields the following result:

$$F_{lift} = 0.3840\pi\epsilon^3 \left(\frac{u\zeta}{K}\right)^2 \frac{a}{h^3} \qquad [6.1]$$

in which ϵ is the permittivity of the media, u is the particle velocity parallel to the wall, ζ is the zeta potential of the particle or the wall (considered equal) and K is the conductivity of the solution.

Another theory, developed by van de Ven *et al.* (3), used the technique of dipole mirror images. It assumes that the hydrodynamic flow field is undisturbed and the lift force is caused by the symmetry breaking of the electric field. Since this assumption becomes invalid when the separation distance is smaller than the particle radius, the applicability of the theory is restricted to region (b). The lift force given by this theory is

$$F_{lift} = \frac{27}{16}\pi\epsilon^3 \left(\frac{u\zeta_s}{K}\right)^2 \frac{a^2}{(a + h)^4} \qquad [6.2]$$

where ζ_s is the zeta potential of the particle. The zeta potential of the wall, ζ_w, is zero for that specific system.

Bike and Prieve developed a new theory (2) using the thin double layer approximation, i.e. they solved the Laplace equation, which governs the streaming potential outside the double layer, with the boundary condition of charge conservation at the outer

edge of the double layer. Like van de Ven and colleagues' theory, it is valid only in region (b). The lift force can be expressed as

$$F_{lift} = \frac{27}{16}\pi\epsilon^3\left(\frac{u}{K}\right)^2(\zeta_s + 2\zeta_w)\zeta_s\frac{a^2}{h^4} \qquad [6.3]$$

Eq. [6.3] reduces to Eq. [6.2] if we take $\zeta_w = 0$ and $h \gg a$.

All of the theories discussed above assume that the Peclet number, defined as $Pe = ua/D_s$ (D_s being the average diffusion coefficient of different ions in the system), is much smaller than unity. This assumption is not valid in most experimental systems which consist of over 95% glycerol. The Peclet number for those systems varies from 10 to 50. Besides, all of these theories have other serious problems. The Maxwell stress term used to calculate the lift force does not seem to be the dominant one. A complete analysis was carried out independently by Warszynski and van de Ven (11) and Cox (12,13). They concluded that the main contribution to the lift force comes from the non-zero normal hydrodynamic stress in the gap caused by the tangential flow of ions in the double-layer as a result of streaming potential built up outside the double layer. For the sake of simplicity they restricted their considerations to interactions between a cylinder and a wall. As will be shown later, these two theories give very similar results and the lift force they predict is at least two orders of magnitude larger than previous predictions referred to as Bike-Prieve (B-P) theory (1).

The Warszynski-van de Ven (W-V) theory is valid for arbitrary-Peclet numbers. It applies as long as $\kappa^{-1} \ll h \ll a$, which is usually satisfied in most experiments. The lift force can be determined only numerically. It is calculated by integration of the stress tensor:

$$\sigma = - pI + \mu(\nabla v + \nabla v^{t}) - \frac{\epsilon}{2} E^{2}I + \epsilon EE \quad , \qquad [6.4]$$

(p being the pressure, μ the viscosity of the medium, v the fluid velocity, E the electric field and I the unit tensor), over the particle surface. The parameters in Eq. [6.4] were obtained from the numerical solution of the convective diffusion equation, Poisson equation, Stokes equation and continuity equation with the usual boundary conditions (14). The resulting lift force is a function of G (shear rate), h, ζ, a, κ and D_∞. The first four parameters can be determined experimentally; κ can be calculated from the solution conductivity and D_∞ from the fluid viscosity.

The W-V theory cannot be applied directly to an experimental sphere-wall system. Developing a theory for sphere-wall systems is very difficult due to the complexity of the problem and the extremely long computation time. For this reason we used an approximation method to convert the calculated lift force of a cylinder-wall system to a sphere-wall system. This method is based on the fact that the electrostatic forces in both systems can be calculated by applying the Derjaguin approximation (14). We can assume that the ratio of these two forces is roughly the same as that of the lift forces. Since the electrostatic force is not a function of particle velocity, this "scaling" method does not take the translational or rotational velocities into account. To obtain the right lift force for a sphere, the translational velocity of the cylinder must be treated as being the same as that of a sphere with the same radius moving at the same depth. The velocity of a sphere moving at a given depth in a wall shear flow can be readily calculated by,

$$u = f_3(h/a)\, G\, (a + h) \quad , \qquad [6.5]$$

where $f_3(h/a)$ is a correction function of the particle velocity accounting for the influence of a wall, originally provided by refs. (15-17). However, in these references there are not enough points for accurate interpolation of the data at an arbitrary distance. We recalculated and tabulated $f_3(h/a)$ according to O'Neill's expression at 60 distances. At other distances the function can then be calculated by cubic spline interpolation. With this "scaling" treatment, the force-distance profiles under typical experimental conditions can be calculated. Results are shown in Fig. 6.2 (solid curves).

Cox's theory is in essence a singular perturbation expression of the equations mentioned above. An analytical solution for low Pe has been obtained assuming $\kappa^{-1} \ll h \ll a$ and only one symmetrical electrolyte is present in the system (13):

$$F_{lift} = \frac{\sqrt{2}\pi}{8} \frac{\epsilon^2 k^3 T^3 a^{1.5}}{(ze)^4 n_\infty h^{2.5}} \left[u_{gap}^2 \left(\frac{(9G_s + G_w)(G_s + G_w)}{D_1^2} \right.\right.$$

$$\left. + \frac{2(9G_sH_s + 5G_sH_w + 5G_wH_s + G_wH_w)}{D_1 D_2} + \frac{(9H_s + H_w)(H_s + H_w)}{D_2^2} \right)$$

$$+ 4u_{gap} a\Omega \left(\frac{(4G_s + 3G_w)(G_s + G_w)}{D_1^2} + \frac{(8G_sH_s + 7G_sH_w + 7G_wH_s + 6G_wH_w)}{D_1 D_2} \right. \qquad [6.6]$$

$$\left.\left. + \frac{(4H_s + 3H_w)(H_s + H_w)}{D_2^2} \right) + 8a^2\Omega^2 \left(\frac{(G_s + G_w)}{D_1} + \frac{(H_s + H_w)}{D_2} \right)^2 \right] \quad ,$$

where k is the Boltzmann constant, T is the temperature, ze is the ionic charge, n_∞ is the ion

concentration in the bulk, D_1 and D_2 are diffusion coefficients of the two ion species, Ω is angular velocity of the cylinder rotating as shown in Fig. 6.1, u_{gap} is translation velocity of the bottom of the cylinder ($u_{gap} = u - \Omega a$), and

$$G_s = \ln\left(\frac{1 + e^{-\frac{ze\zeta_s}{2kT}}}{2}\right) \quad , \quad G_w = \ln\left(\frac{1 + e^{-\frac{ze\zeta_w}{2kT}}}{2}\right) \quad , \qquad [6.7]$$

$$H_s = \ln\left(\frac{1 + e^{\frac{ze\zeta_s}{2kT}}}{2}\right) \quad , \quad H_w = \ln\left(\frac{1 + e^{\frac{ze\zeta_w}{2kT}}}{2}\right) \quad . \qquad [6.8]$$

Two force-distance profiles have been calculated from Eq. [6.6] using the "scaling" method discussed above to transform the cylinder-wall interaction into a sphere-wall interaction. They are plotted in Fig. 6.2 (dashed curves). Ω was assumed zero in both cases. Note that Eq. [6.6] is only valid at low Pe. The extension of the solution to a high Pe system (Pe~20) in Fig. 6.2 can be justified by the fact that according to the theoretical analysis by Cox (12), the lift force originates from the gap between two surfaces, and a physically more realistic Peclet number should be defined as $Pe^* = u_{gap}h/D_s$. u_{gap} is smaller than u and h is usually one-tenth of a, hence Pe^* is around unity which is not too far from $Pe^* \ll 1$ where Eq. [6.6] applies exactly. In Fig. 6.2 it can be seen that the difference in the lift forces calculated from the W-V theory and Eq. [6.6] at both low and high Pe is less than one order of magnitude. Despite the similarity of these two theories, they both have advantages and weaknesses. One advantage of Cox's theory is that it takes rotation into account, which was neglected in the W-V theory. We compared the lift forces with or without rotation at low and high Pe (cf. Fig. 6.3) and found

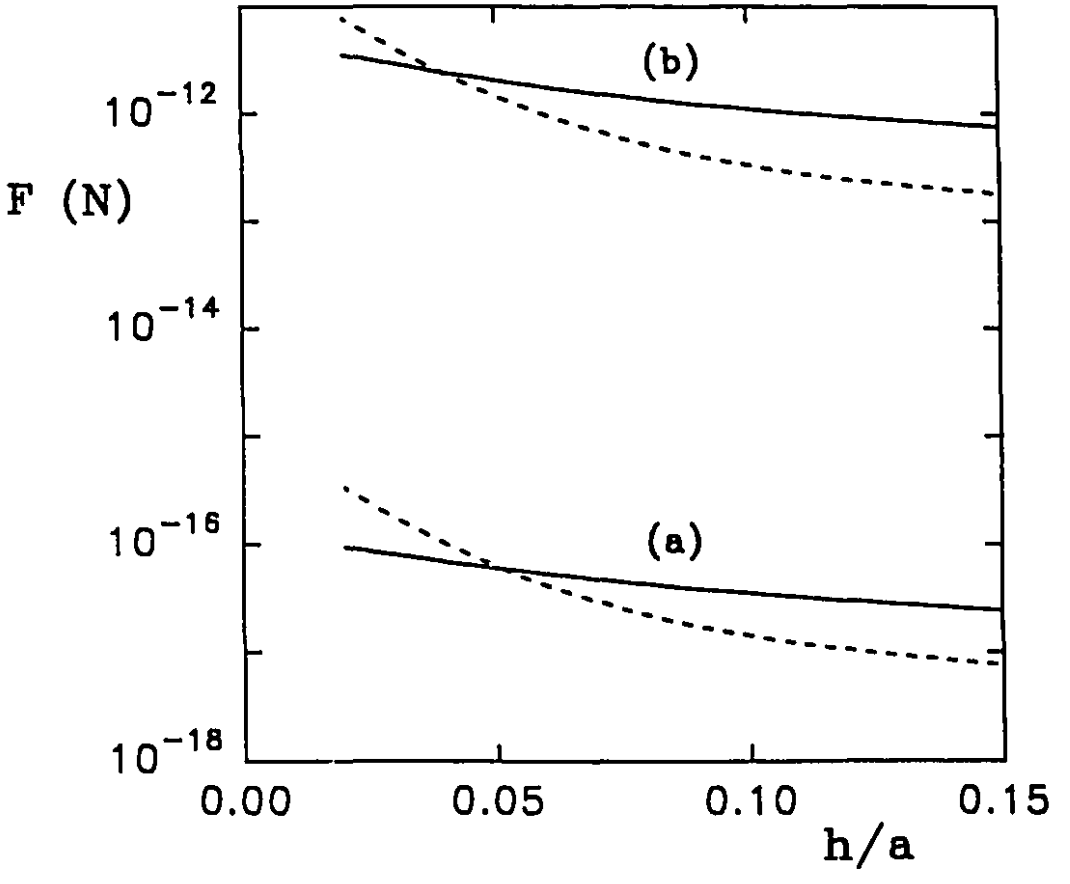

Fig. 6.2 Lift force-separation distance profiles for a sphere moving along a wall calculated from both the W-V theory (solid curves) and Cox's theory (dashed curves) in 100% water [set (a), Pe~0.05] and 96% glycerol-water solution [set (b), Pe~20]. The theories were modified by the "scaling" method. The flow is a wall shear flow with a fixed shear rate of 20 s^{-1}. The sphere radius is 2.6 μm. The surface potentials of the sphere and the wall are both -45 mV. The ionic strength is 10^{-4} M. The rotational velocity is assumed to be zero.

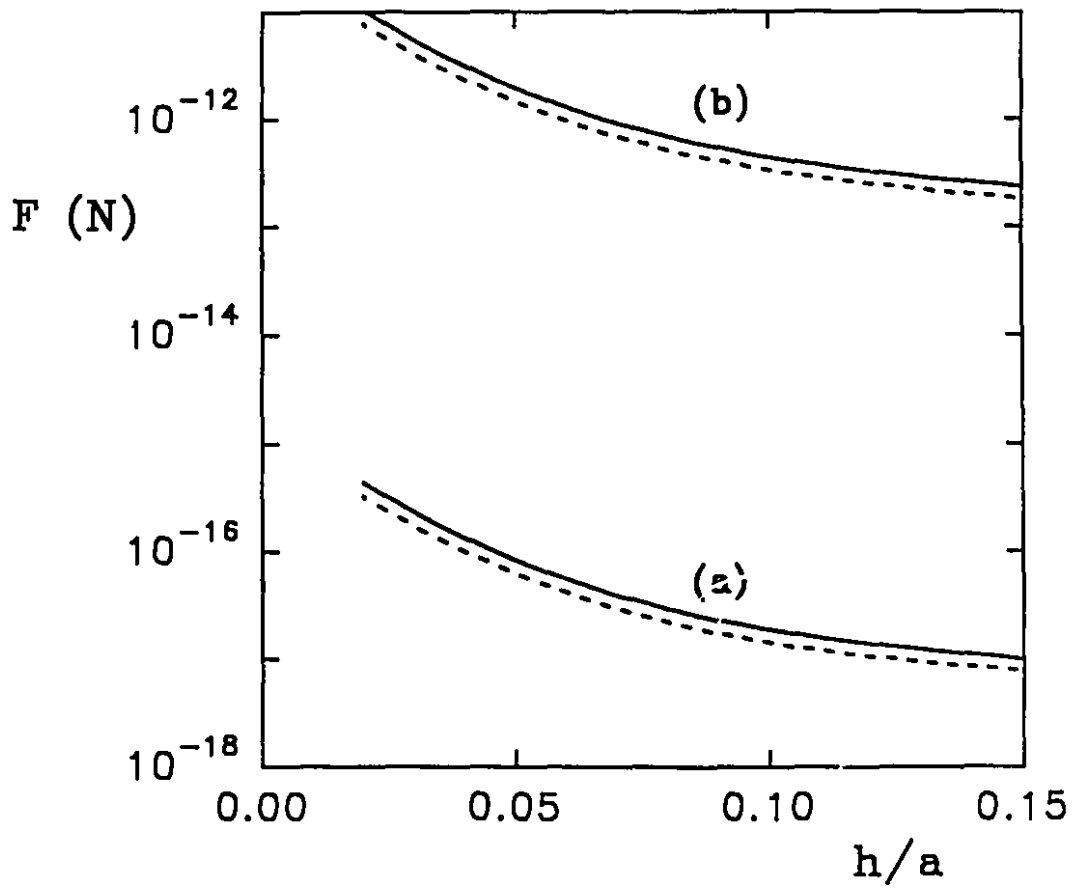

Fig. 6.3 Effect of rotation on lift force. The results are calculated from Eq. [6.6] for the same systems and under the same conditions as in Fig. 6.2. The solid curves represent the forces acting on the rotating sphere while the dashed curves are the forces on the non-rotating sphere.

that the sphere rotation only slightly increases the lift force. Therefore, it can be neglected without introducing much error. The weakness of the current Cox's theory is the extension of Eq. [6.6] to high Pe systems which may create some error, though less serious than it appears owing to the relatively small value of Pe^*.

EXPERIMENTAL

1. Materials

5.1 μm polystyrene - DVB latex particles ($a \approx 2.6$ μm), supplied by SPI Supplies, were used in a 96% (by weight) glycerol-water solution. Samples with different conductivities ranging from 5 - 20 μS/m were prepared by addition of KCl. The ionic strengths of the samples calculated from conductivities are between 1×10^{-4} - 4×10^{-4} M.

The particle zeta potential, ζ_p, can, in principle, be determined directly by microelectrophoresis. However, due to the high viscosity of the system, electrophoretic movement is difficult to observe. An extrapolation of zeta potentials measured at lower concentrations of glycerol was carried out to determine the zeta potential at 96% glycerol concentration (cf. Fig. 6.4). The result is $\zeta_p \approx -45$ mV. The zeta potential of the glass wall is assumed to be the same.

2. Experimental Techniques

The experiments were carried cut in a "microcollider" (cf. Fig. 6.5). The apparatus is discussed in detail in ref. (10). It was designed mainly for the study of interaction forces

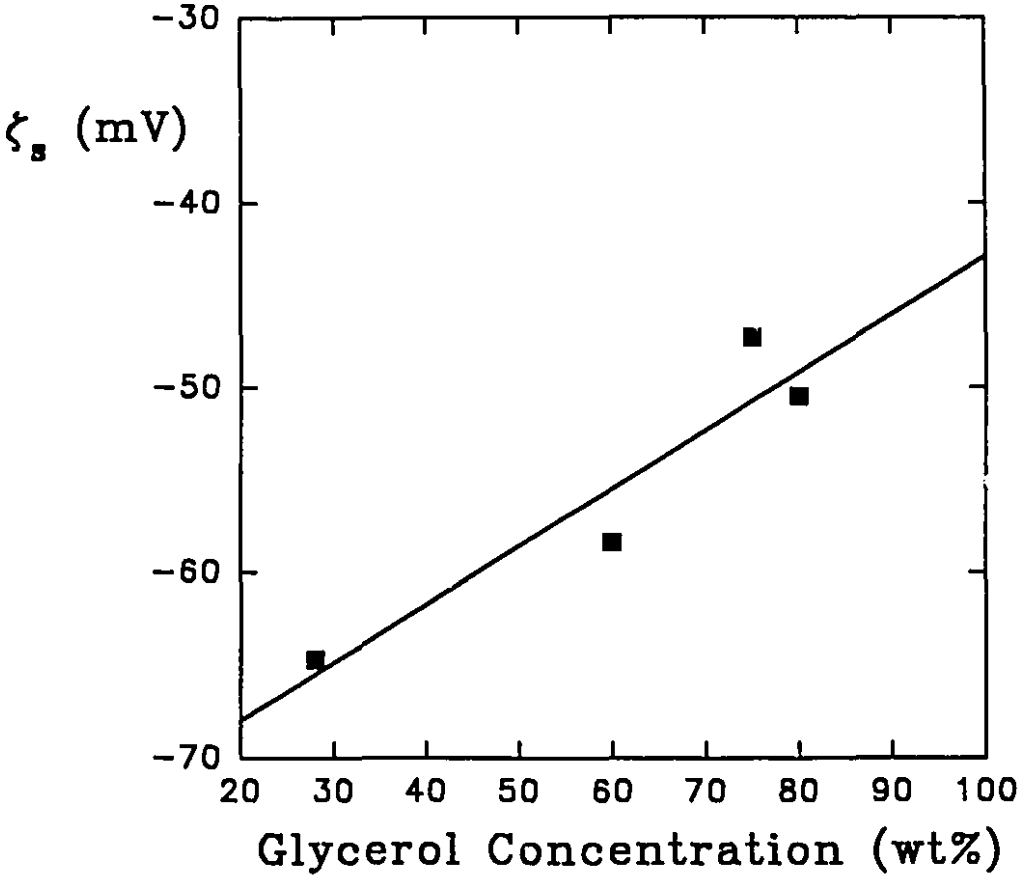

Fig. 6.4 Zeta potential of latex beads in various glycerol-water solutions. The extrapolated value for 96% glycerol is $\zeta_s \approx$ -45 mV.

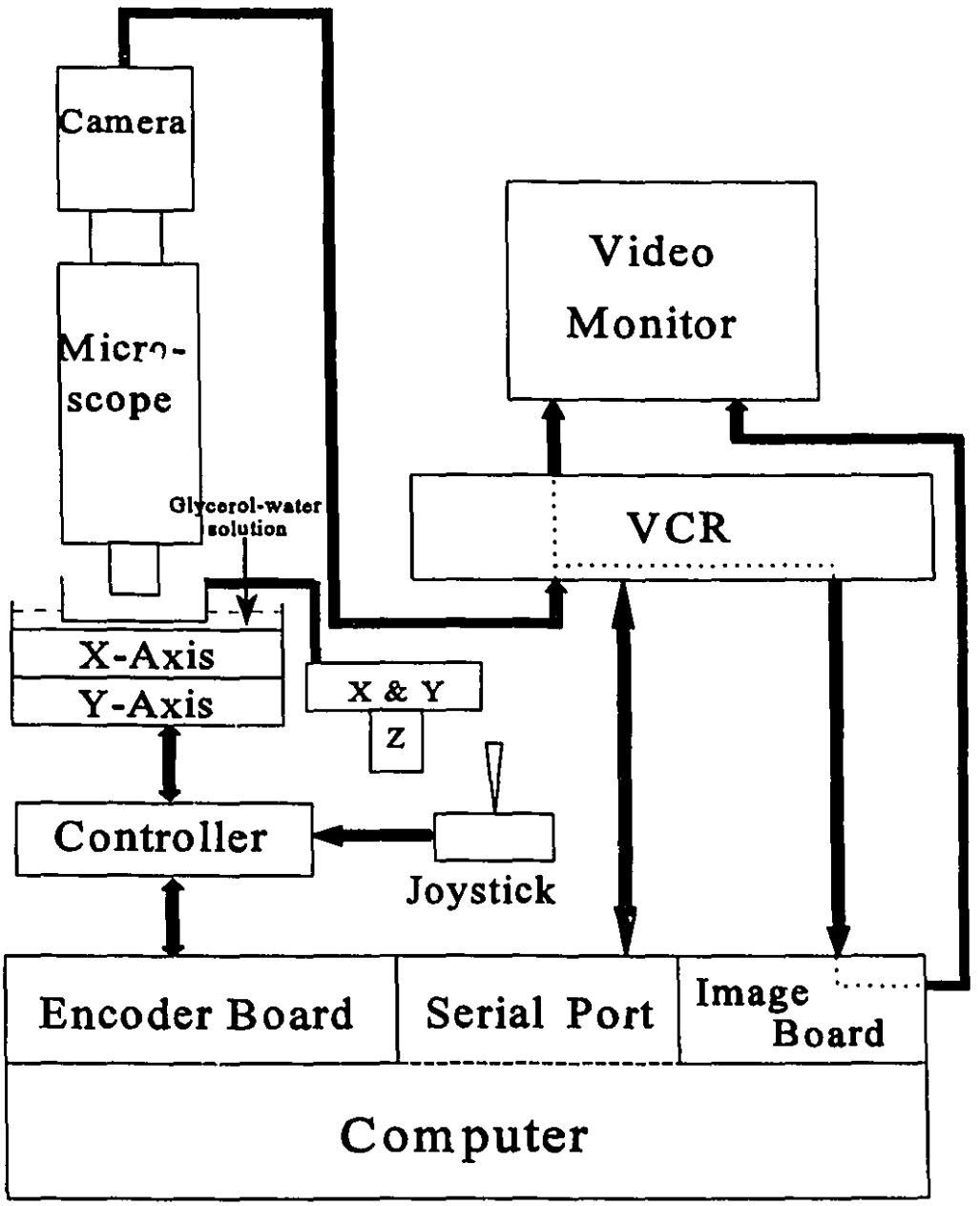

Fig. 6.5 General setup of a microcollider. A wall shear flow is generated by moving the x and y-axes of an electric micromanipulator (encoder stages). The particle movement in the flow is observed with a microscope and recorded with a video camera and VCR. The depth of the particle is determined from the particle velocity measured on the monitor.

between two colloidal particles in the vicinity of a glass wall. However it is equally effective for studying the interactions between a particle and a wall.

The flow geometry is illustrated in Fig. 6.6. Surface A is a 0.1 mm-thick microscopic cover slip with its cylindrical base held by a tilting device containing x and y-micrometers. Surface B is the bottom of the sample cell containing a 96% glycerol-water solution. Before each experiment, surface A is aligned to be parallel to surface B separated by a gap width around 200 μm. The alignment procedures are as follows. First, surface A is tilted by turning the x-micrometer to touch surface B. When contact is made, the sensitive micromanipulator stage underneath surface B will report a slight shock due to the touch. The angular value of the x-micrometer is recorded. Surface A is then tilted towards the other direction and another angular value is obtained. Turning the x-micrometer to the average value of these two will make the surface stay in the parallel position in the x-direction. The same procedure is repeated for the y-micrometer. Finally, the alignment is checked by moving a particle along the surface in a wall shear flow. If the two surfaces are parallel, the particle should move in exactly the same direction as that of the micromanipulator stage which has been marked as a "track" on the monitor. Otherwise it moves out of the "track" due to a lateral flow caused by the misalignment. In this case, fine adjustment of the micrometers is necessary to bring the particle back on the "track".

The sample cell is mounted on a X-Y micromanipulator stage. The stage can be either controlled by a joystick to bring a particle into the field of vision or driven by an IBM compatible computer to move the stage at a constant speed. When the sample cell (or surface B) moves with the manipulator stage and surface A is held stationary, a wall shear flow is

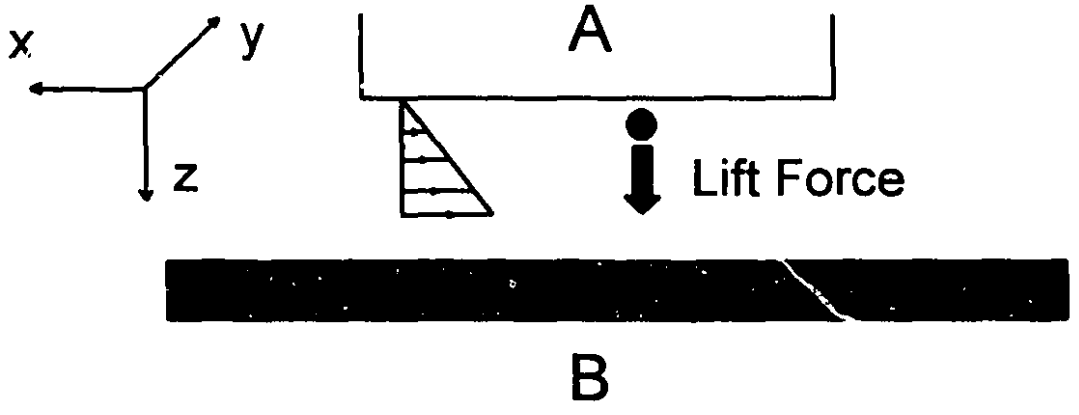

Fig. 6.6 Schematic illustration of the flow geometry and the sample cell.

generated in the gap. The shear rate can be easily controlled by setting different manipulator speeds through a computer interfacing program.

Because of the buoyancy force, latex particles tend to float towards the top surface (surface A) until this force is balanced by the electrostatic repulsion between the negatively charged glass surface and the latex particle. Therefore the first step of the experiment is to find a particle in the equilibrium layer where the buoyancy force is balanced by the electrostatic force. To verify if the particle is really in this layer, we move it back and forth in a flow with the same low shear rate and a constant particle velocity should be observed. Then, to create a lift force, a high-shear flow is generated and the flow direction is reversed immediately after the translational limit of the manipulator is reached. To minimize the oscillating wave of the fluid and non-steady-state effects (to be discussed later) caused by the flow reversal, a gradual start and stop of the manipulator was included in the controlling program (cf. Fig. 6.7). During the gradual start and stop, the shear rate is lower than that of constant shear regime. The lift force during this period was neglected in data interpretation. Thus, the efficiency of shearing can be defined as $r_{eff} = t_{eff}/t_{shear}$ where $t_{eff} = \sum_i t_i$ (cf. Fig. 6.7). In our experiments, r_{eff} varied from 58% to 80% depending on the shear rate which varied from 19 s^{-1} to 6 s^{-1}. The detailed data interpretation will be discussed shortly.

The particle movement was recorded on a S-VHS video cassette with the aid of a computer-controlled VCR (JVC BR-S605U) and a video camera (Panasonic WV-D5100) mounted on the top of an optical microscope (Zeiss Axioplan). The particle velocity was determined by analyzing the tape. Ideally, the image processing board built in the microcollider could be used to analyze the particle movement (10). However, because of the

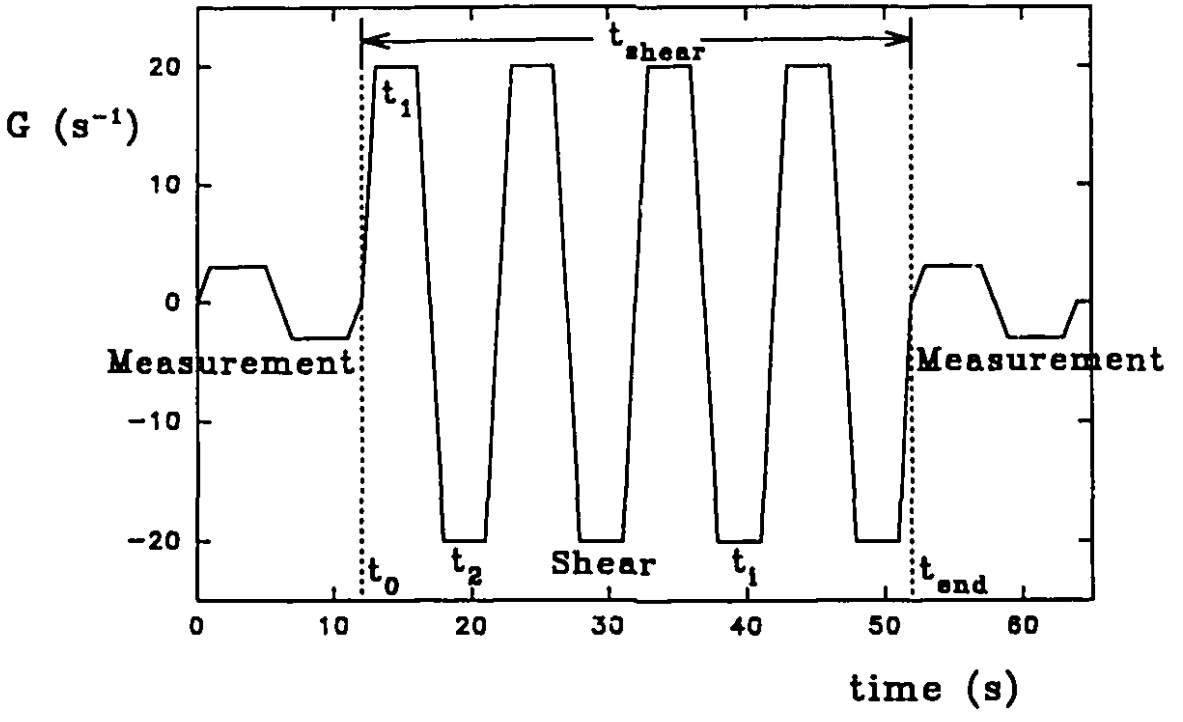

Fig. 6.7 A typical shear rate profile. Negative shear rate indicates the reversal of flow. t_i is the "effective" time for a single cycle, i.e. the time of high shear rate which generates a noticeable lift force; t_{shear} is the total shearing time and t_0 and t_{end} are the starting and ending time of the high shear regime ($t_{shear} = t_{end} - t_0$).

similarity of refractive indexes of polystyrene and glycerol, the contrast of the particle image was not good enough for the image board analysis. Another equally accurate method was developed to measure the particle velocity. First, two lines were marked on the monitor screen, and the distance between them, L_m, was measured by the image board. Then the tape was replayed and set to the shuttle forward mode when the particle was close to the first line. The time of the VCR counter was saved when the center of the particle was right on the line. The same procedure was applied when the particle moved to the second line. The difference between the two VCR counters, t_m, was the time the particle spent traveling between the two lines. The particle velocity was thus given by $u = L_m/t_m$. After the particle velocity has been determined, the separation distance, h, can be calculated from the particle velocity by solving Eq. [6.5].

Since L_m can be very accurately determined, the error in the particle velocity, Δu, can be simply estimated by $\Delta u = (u^2/L_m)\cdot\Delta t$ where Δt is the time measurement error which is typically 1 or 2 video frames (1 frame = 1/30 second) and is independent of u or G. Since $h = f(u, G, a)$ (cf. Eq. [6.5]), the error of particle depth, Δh, comes from Δu and ΔG. ΔG results from the measurement error of the gap width between surfaces A and B, and is independent of G. Δu, on the other hand, is related to u^2 and thus strongly depends on G. At high shear rates ($G > 10\ s^{-1}$), Δu is the dominant error which usually results in a Δh around 10% of the particle radius. It seriously affects the measurement of the lift force which changes the particle depth with a similar magnitude. Thus a procedure was adopted to measure the particle velocity at a low shear rate ($G = 3\ s^{-1}$) before and after shearing the particle at a high shear rate for a predetermined time period (cf. Fig. 6.7). Each measurement yields the initial

equilibrium depth of the particle and one experimental point in Fig. 6.8 or 6.9. During the measurement at low shear rate, the lift force disappears and the particle tends to float back to the surface due to the buoyancy force. The error caused by this motion, however, is negligible because the measurement takes about 15 seconds, while floating back to the initial equilibrium depth typically takes 15 minutes. For the same reason, we wait 20 minutes (without shear) before the procedure is repeated with a different shearing time to ensure that for each data point the particle starts at the same depth (equilibrium depth). By following this procedure of measurement, the error Δh can be controlled to around 1% of the particle radius.

3. Data Interpretation

The electrokinetic lift forces can be calculated from the raw data in Figs. 6.8 and 6.9 by doing a simple analysis as follows:

The force balance on the particle requires that

$$F_{net} = \frac{6\pi\mu a u_{\perp}}{f_1(h/a)} \quad , \qquad [6.9]$$

where μ is the fluid viscosity, $u_{\perp}$ is the particle velocity normal to the wall which can also be denoted as u_{lift} when the lift force is dominant and u_{gr} without the lift force, and $f_1(h/a)$ is a correction function for the diffusion coefficient normal to the wall, which has been calculated by O'Neill *et al.* (15-17). In principle $f_1(h/a)$ requires modification due to electroviscous effects. The effect on a similar function for spheres approaching each other has been

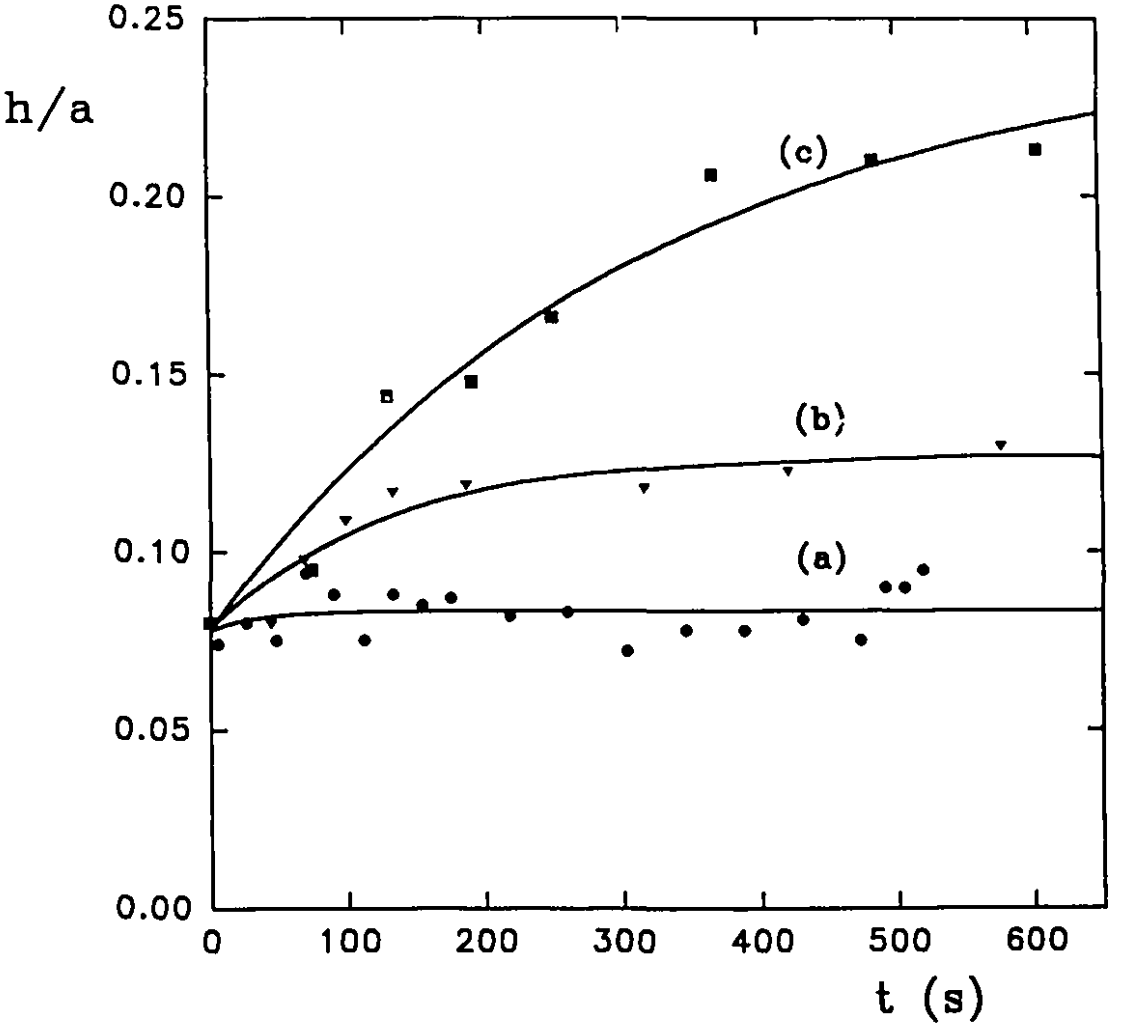

Fig. 6.8 Changes in particle depth with time for various shear rates: (a) 6.1 s^{-1}, (b) 14.0 s^{-1}, (c) 19.1 s^{-1}. Other conditions are a = 2.6 μm, ζ = -45 mV, $\epsilon = 43.5\epsilon_0$ (ϵ_0 being the permittivity of the vacuum) and K = 5 μS/m. The symbols are experimental points and the solid curves are best fits to Eq. [6.13]. The optimum parameters for these curves are c'=0.078; (a) p'=0.00538, b=0.0293; (b) p'=0.0493, b=0.00803; (c) p'=0.167, b=0.00315. The time scale here represents the time period from t_0 to t_{end} in Fig. 6.7.

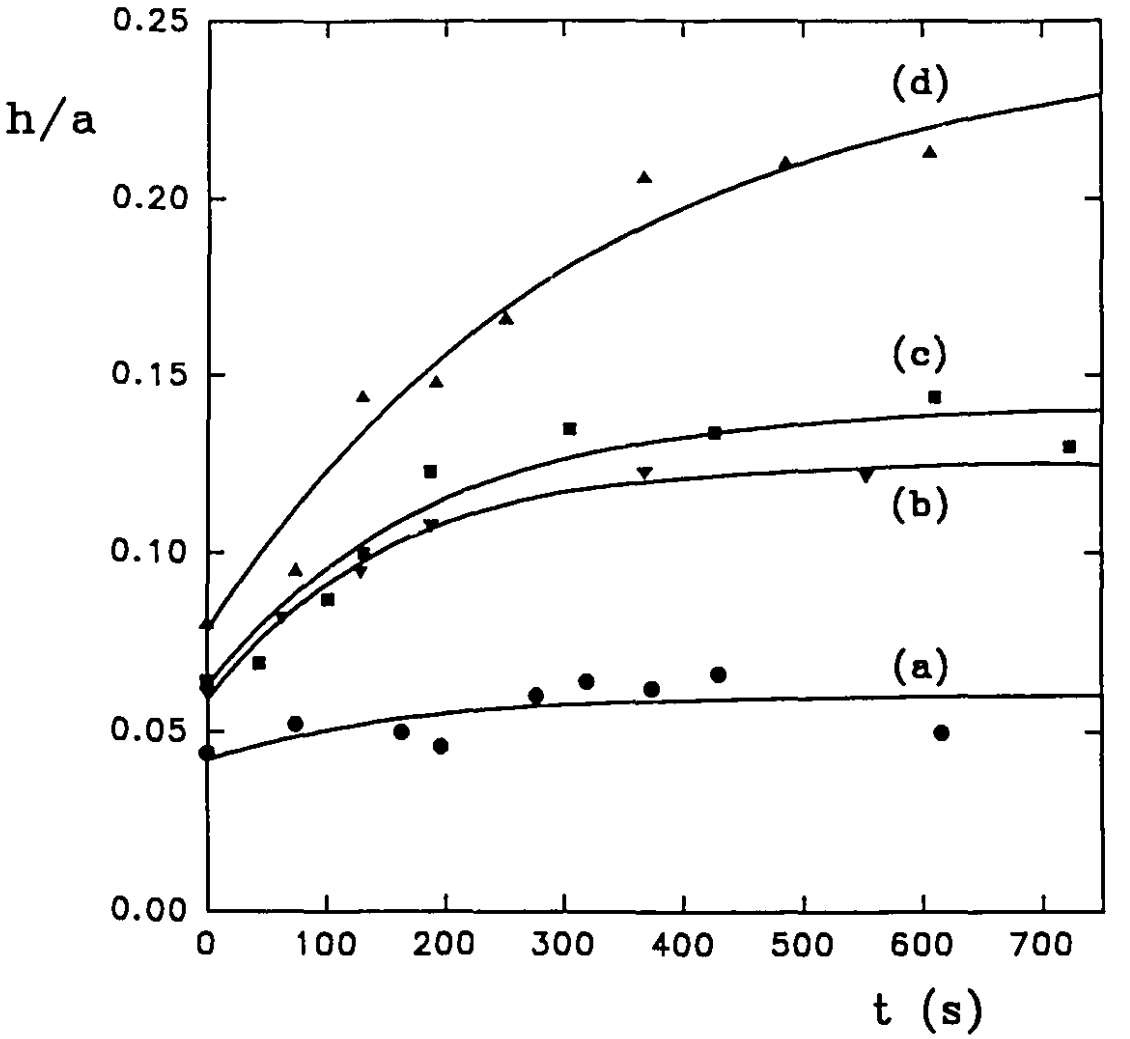

Fig. 6.9 Changes in particle depth with time for various conductivities: (a) 20 μS/m, (b) 10 μS/m, (c) 8.5 μS/m, (d) 5 μS/m. Other conditions are a = 2.6 μm, ζ = -45 mV, $\epsilon = 43.5\epsilon_0$ and G = 19.1 s^{-1}. The optimum parameters for these curves are (a) p'=0.0183, b=0.00632, c'=0.042; (b) p'=0.0678, b=0.00680, c'=0.058; (c) p'=0.0797, b=0.00552, c'=0.062; (d) p'=0.167, b=0.00315, c'=0.078.

calculated by Warszynski and van de Ven (6,18), from which it follows that the correction to the original function (without the electroviscous effect) is about 10% for our experimental conditions ($h \gg \kappa^{-1}$). Hence we can take the unmodified $f_1(h/a)$ without making a significant error. Similarly $f_3(h/a)$ in Eq. [6.5] is also affected by the electroviscous effect. So far no analysis has been done on this function. Since the wall effect on tangential motion is less pronounced than on normal motion, i.e., f_3 converges to 1 at smaller h than f_1 (14), we assume that the electroviscous effect for f_3 is also weaker and can be safely neglected.

F_{net} is composed of the buoyancy force and the electrical forces which includes equilibrium (double-layer force) and non-equilibrium (lift force) contributions during t_{eff} and only buoyancy force and double-layer force during $t_{shear} - t_{eff}$. The van der Waals force can be neglected because the calculated Hamaker constant between polystyrene (latex particle) and silica (glass) in a medium of 96% glycerol - 4% water solution is, $A = 1.3 \times 10^{-21}$ J (19,20), which represents a force three orders of magnitude smaller than the lift force at typical separation distances, e.g., h = 0.1a. Therefore, during shearing period:

$$F_{lift} + \frac{2\pi aB}{\kappa} e^{-\kappa h} - \frac{4}{3}\pi a^3(\rho_f - \rho_p)g = \frac{6\pi\mu a u_{lift}}{f_1(h/a)} \qquad [6.10a]$$

while during a non-shearing period:

$$\frac{4}{3}\pi a^3(\rho_f - \rho_p)g - \frac{2\pi aB}{\kappa} e^{-\kappa h} = \frac{6\pi\mu a u_{gr}}{f_1(h/a)} \qquad [6.10b]$$

where ρ_f is the fluid density, ρ_p is the particle density, g is gravitational acceleration constant

and B can be expressed as

$$B = 32\tanh^2\left(\frac{ze\zeta}{4kT}\right)\epsilon\kappa^2\left(\frac{kT}{ze}\right)^2 \quad . \qquad [6.11]$$

Since each cycle of the forward or backward movement of the manipulator is very short compared with the total shearing time, i.e. $t_i / t_{shear} \ll 1$, the time periods of t_{eff} and $t_{shear} - t_{eff}$ can be considered evenly "dispersed" with weighting factors r_{eff} and $1-r_{eff}$, respectively. Hence, the separation distance varies with time according to:

$$h(t) = r_{eff}\int_{t_0}^{t} u_{lift}dt - (1 - r_{eff})\int_{t_0}^{t} u_{gr}dt \quad , \qquad [6.12]$$

where $t \gg t_i$ and $t_0 \le t \le t_{end}$, t_0 and t_{end} being the starting and ending times of the high shear regime (cf. Fig. 6.7).

Experimentally observed variations in sphere-wall separation distances with time were fitted to an empirical expression:

$$h/a = p'(1 - e^{-bt}) + c' \quad , \qquad [6.13]$$

where p', b and c' are three adjustable parameters determined from the best fit.

Taking derivatives with respect of time of both sides of Eqs. [6.12] and [6.13] and combining them with Eq. [6.10] yields

$$F_{lift} = \frac{1}{r_{eff}}\left[\frac{6\pi\mu a^2 b(p' + c' - h/a)}{f_1(h/a)} - \frac{2\pi aB}{\kappa}e^{-\kappa h} + \frac{4}{3}\pi a^3(\rho_f - \rho_p)g\right] \quad . \qquad [6.14]$$

RESULTS AND DISCUSSION

We performed two sets of experiments. In the first set, the conductivities of the samples were kept constant and the shear rates were varied. The changes in particle depths with time were observed and plotted (cf. Fig. 6.8). In the second set, the shear rates were kept constant and samples with different conductivities were used (cf. Fig. 6.9). The lift force determined from these data are plotted in Figs. 6.10 and 6.11. They show the same trends as reported earlier by Alexander *et al.* (5) and Bike (9), i.e., the force increases with increasing shear rate or particle velocity and decreases with increasing solution conductivity.

The lift forces predicted by the W-V and Cox's theories modified for sphere-wall interactions are also plotted in Figs. 6.10 and 6.11 with dashed and dotted curves, respectively. There is roughly a factor-of-two difference between them. This discrepancy is probably caused by the errors in the numerical calculations in the W-V theory and the "inappropriate" extension of Cox's solution of lift force in high Pe systems. All the experimental curves fall midway between these two theoretical curves. Except for curve (c) in Fig. 6.10 and curve (d) in Fig. 6.11, experimental forces tend to decay somewhat faster than theoretical predictions. This trend may be caused by the error introduced in the data interpretation which tends to increase in the plateau regions of particle depth vs. time plots (cf. Figs. 6.8 and 6.9) where the slope, dh/dt, becomes zero. Despite the discrepancies between these two theories and between theory and experiment, the differences never exceed a factor of two. Regarding the complexity of the problem and the various approximations used, such as the transformation of a cylinder-wall system to a sphere-wall system, the

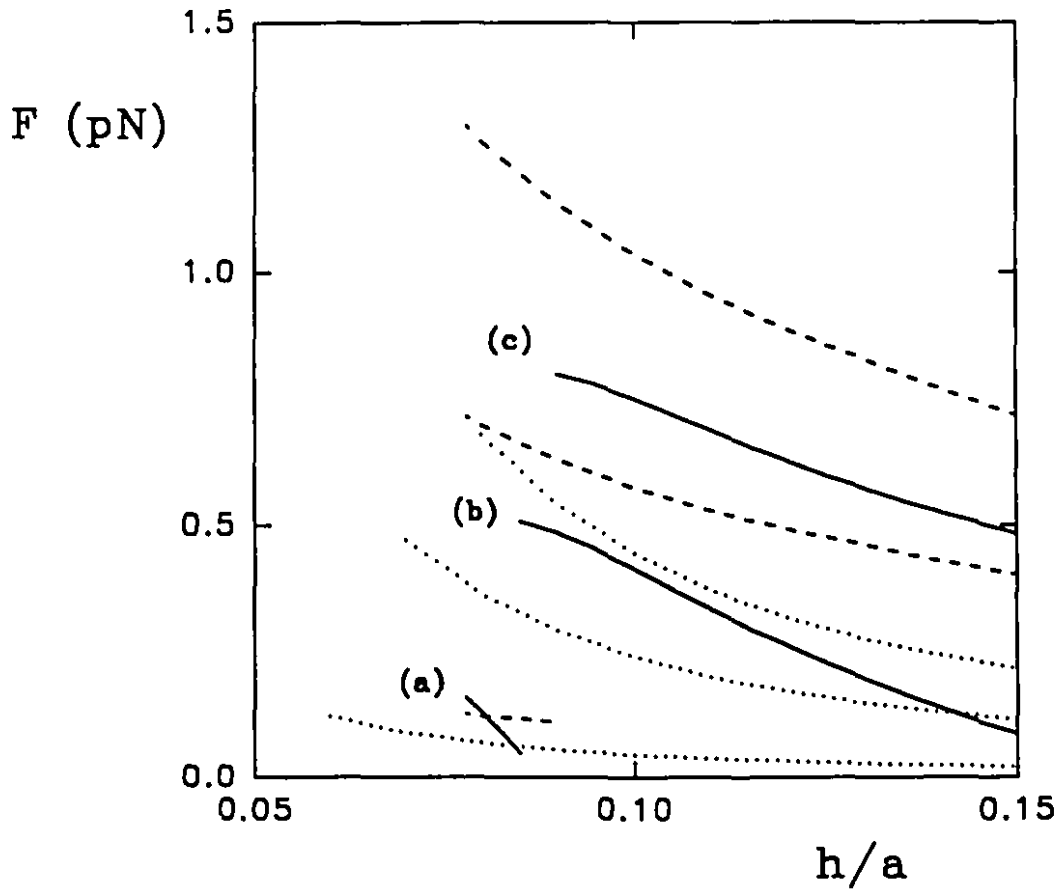

Fig. 6.10 Lift force profiles at various shear rates for a fixed conductivity (K=5 μS/m). The solid curves represent the experimental forces calculated from the data in Fig. 6.8. The dashed and dotted curves represent the theoretical forces calculated from the W-V and Cox's theories respectively, modified to sphere-wall systems by the "scaling" method. Particle rotation is taken into account in Cox's theory. The three sets, a, b and c, refer to the corresponding systems in Fig. 6.8. The unit of force is pN (10^{-12} N).

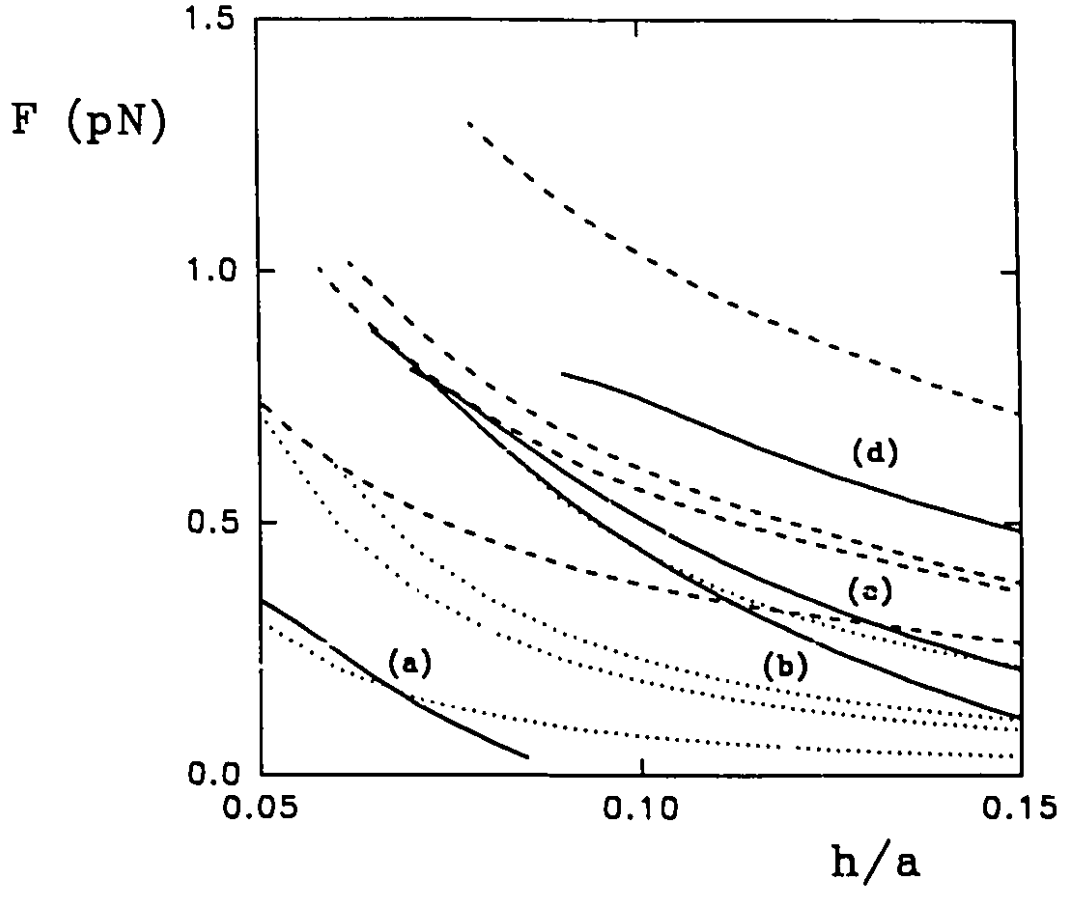

Fig. 6.11 Lift force profiles at various conductivities for a fixed shear rate (G=19.1 s^{-1}). The solid curves represent the experimental forces calculated from the data in Fig. 6.9. The dashed and dotted curves represent the theoretical forces calculated from the W-V and Cox's theories respectively. The theoretical treatment is the same as in Fig. 6.10. The four sets, a, b, c and d, refer to the corresponding systems in Fig. 6.9.

agreement between theoretical results and experimental data is considered reasonably good.

Fig. 6.12 gives a comparison of different theoretical predictions (dashed curves) with the experimental results (solid curve) under the conditions of K = 5 μS/m and G = 19.1 s^{-1}. It is quite obvious that the B-P theory (curve c) underestimates the lift force by two orders of magnitude while the W-V and Cox's theories (curves a and b) are consistent with the experimental results.

Moreover, the W-V theory also agrees qualitatively with Alexander and Prieve's data (cf. Table I). Although the predicted particle depth at G = 9.32 s^{-1} is smaller than the experimental value, it at least shows the right trend. By contrast, the B-P theory does not predict any changes in particle depth in both cases. The discrepancy between Alexander's data and the predictions of the W-V theory may result from imperfections in the theory and experimental errors. The experimental error may include non-steady-state effects on the lift force, which occurs at the moment when the direction of the flow is suddenly reversed. A

Table I. Comparison between Alexander's data (5) and theoretical results*.

Shear rate (s^{-1})	Final depth (μm) (experimental)	Final depth (μm) (B-P theory)	Final depth (μm) (W-V theory)
5.58	0.2	0.19	0.35
9.32	1.2	0.19	0.7

* The calculation was based on a = 4.6 μm, K = 4.6 μS/m, T = 298 K, κ^{-1} = 25 nm and glycerol concentration = 98.1%. The surface potentials of the particle and the wall were both assumed to be -50 mV. Equilibrium depth h_{eq} = 0.19 μm. Flow reversal was assumed to be instantaneous.

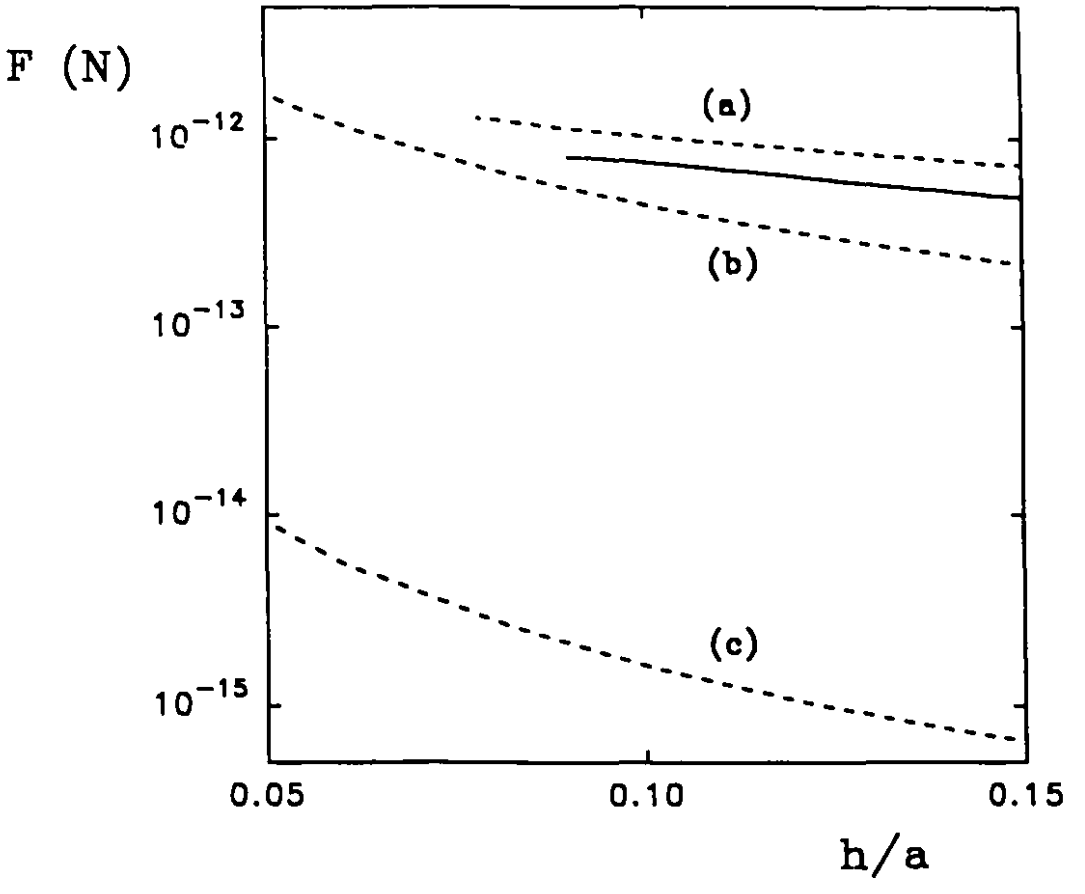

Fig. 6.12 Comparison of theoretical lift forces (dashed curves) with the experimentally observed one (solid curve). The conditions are: $a = 2.6\ \mu m$, $\zeta = -45$ mV, $\epsilon = 43.5\epsilon_0$, $G = 19.1\ s^{-1}$ and $K = 5\ \mu S/m$. The theories involved are: (a) W-V theory; (b) Cox's theory; (c) B-P theory. Curves (a) and (b) have been modified to sphere-wall systems by "scaling" method.

preliminary analysis we performed suggests that the lift force is probably larger in a non-steady-state system, which may explain the large normal displacement observed by Alexander *et al.* In our experiments, the procedure of gradually stopping and starting the manipulator in the opposite direction was adopted to minimize this effect.

Fig. 6.2 set (a) shows that in low Pe systems, e.g. an aqueous solution sheared at a moderately high shear rate, the lift force is extremely small and likely to be overwhelmed by the Brownian motion of the particles. This conclusion is consistent with Bike's (9) and our experimental findings, that no lift force effect was observed in water. However, at extremely high shear rates ($G>1000\ s^{-1}$), the lift force becomes significant even in water and has actually been observed by Hollingsworth and Silebi who studied the transport of latex particles through microcapillary tubes (21).

It is of interest to note that the lift force in 96% glycerol is of the order of 10^{-12} N (cf. Figs. 6.10 and 6.11) which is beyond the detection capability of most force measuring techniques. This shows how sensitive our technique is in determining particle-wall interaction forces. This sensitivity enables it to be further applied to measure other interactions, e.g. steric interactions between a polymer-coated particle and a wall.

CONCLUDING REMARKS

A new experimental technique has been applied to study the electrokinetic lift force. The results are consistent with literature data which indicate that the lift force increases with

increasing shear rate or decreasing solution conductivity. In addition, our data shows the kinetics of the particle motion, i.e., how fast a particle moves away from the wall under the influence of a lift force. The results prove conclusively the existence of the lift force which is too small to be detected by most force measurement techniques. A comparison between the experimentally determined lift forces and various theoretical predictions was also made. It shows that most of the existing electrokinetic theories of the lift force are not correct. The recently developed W-V and Cox theories are in reasonably good agreement with experiments. The sensitive force detection capability of our technique shows the potential of determining other interaction forces between particles and walls.

ACKNOWLEDGMENTS

The authors would like to thank Prof. R. G. Cox for providing results of his cylinder-wall calculations and for many stimulating discussions. We are saddened by his recent death. The notes on electrokinetic lift force he left behind are to be submitted for publications (12,13) in the near future. The authors also acknowledge Paprican for providing a scholarship to X. Wu and NSERC for partial support of the project.

REFERENCES

1. Bike, S. G., and Prieve, D. C., *J. Colloid Interface Sci.* **136**, 95 (1990).
2. Bike, S. G., and Prieve, D. C., *J. Colloid Interface Sci.* **154**, 87 (1992).
3. van de Ven, T. G. M., Warszynski, P., and Dukhin, S. S., *J. Colloid Interface Sci.* **157**, 328 (1993).
4. Prieve, D. C., and Bike, S. G., *Chem. Eng. Comm.* **55**, 149 (1987).
5. Alexander, B. M., and Prieve, D. C., *Langmuir* **3**, 788 (1987).
6. Warszynski, P., and van de Ven, T. G. M., *Adv. Colloid Interface Sci.* **36**, 33 (1991).
7. Small, H, *J. Colloid Interface Sci.* **48**, 147 (1974).
8. Parsegian, V. A., *Annu. Rev. Biophys. Bioeng.* **2**, 221 (1973).
9. Bike, S. G., Ph.D. Dissertation, Carnegie Mellon University, 1988.
10. van de Ven, T. G. M., Warszynski, P., Wu, X., and Dabros, T., *Langmuir* **10**, 3046 (1994) (Chapter 2 of this thesis).
11. Warszynski, P., and van de Ven, T.G.M., to appear.
12. Cox, R. G., to appear.
13. Cox, R. G., to appear.
14. van de Ven, T. G. M., "Colloidal Hydrodynamics." Academic Press, London 1989, p.448.
15. Dean, W. R., and O'Neill, M. E., *Mathematika* **10**, 13 (1963).
16. O'Neill, M. E., *Mathematika* **11**, 67 (1964).
17. Goren, S. L., and O'Neill, M. E., *Chem. Eng. Sci.* **26**, 325 (1971).

18. Warszynski, P., and van de Ven, T. G. M., *Faraday Discuss Chem. Soc.* **90**, 313 (1990).

19. Visser, J., *Adv. Colloid Interface Sci.* **3**, 331 (1972).

20. Vincent, B., *J. Colloid Interface Sci.* **42**, 270 (1973).

21. Hollingsworth, A., and Silebi, C., to appear.

CHAPTER 7

GENERAL CONCLUSIONS

CONCLUDING REMARKS

Chapters 2-6 have demonstrated various applications of the CPS method. The major achievement with this method is that real colloidal forces have been determined. These forces are typically 3-4 orders of magnitude smaller than the surface forces measured by a commercial force apparatus, such as a surface force apparatus (SFA) or an atomic force microscope (AFM) (1). Although an AFM can be reconfigured to determine colloidal forces (2), the modification does not improve its detection sensitivity, so the measured force is mainly the large electrostatic force on its rising part before the energy barrier. This part of the force-distance curve is not as important as that around the secondary energy minimum, which determines various properties of a colloidal system.

Depending on experimental conditions, we can investigate different interaction forces between bare or polymer-coated latex particles or their surface properties (cf. Fig. 7.1). The first variable condition is the shear rate, G. We chose $G \approx 4\ s^{-1}$ for all experiments because this shear rate offers us a compromise between large Brownian motion effects and serious system vibration which can be aggravated by lower and higher shear rates respectively. However, different shear rates help us study different aspects of particle-particle interactions (to be elaborated later). Therefore, it is worthwhile to investigate these conditions as a part of further research.

The second variable condition is the salt concentration, C. Low salt concentrations relatively increase electrostatic forces compared to van der Waals forces. When $C \leq 0.0001$ M, van der Waals forces are completely overwhelmed by electrostatic forces.

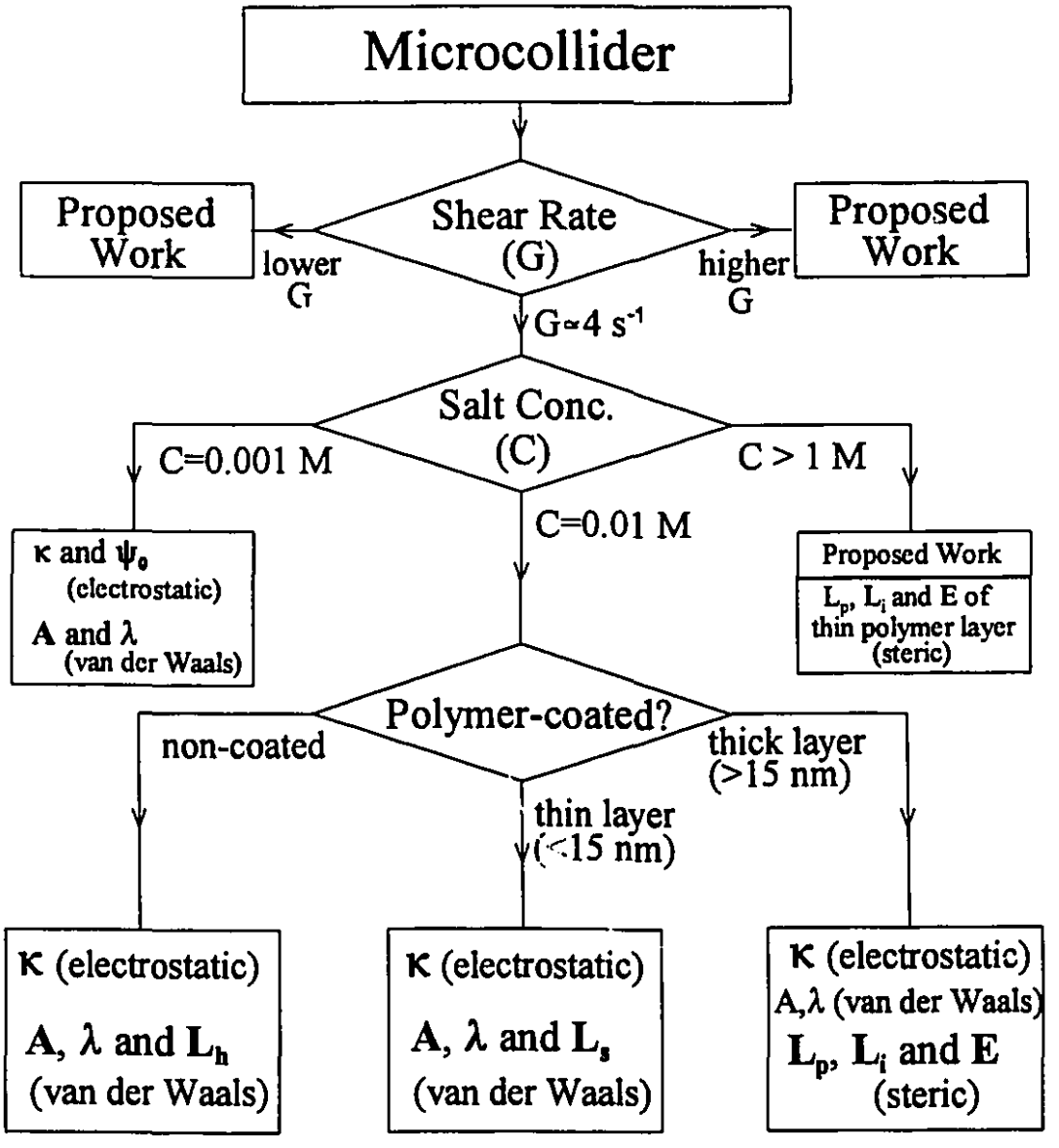

Fig. 7.1 Illustration of measurable force parameters by CPS. The parameters printed in bold have been determined in the thesis. Some of the proposed future research areas are also indicated.

When C = 0.001 M, both of them can be determined. According to Eqs. [1.2], [1.3] and [1.6], electrostatic and van der Waals forces can be characterized by κ (reciprocal Debye length), ψ_0 (surface potential), A (Hamaker constant) and λ (retardation wavelength). κ can be accurately calculated from the salt concentration and is usually kept constant. In Chapter 2, λ was fixed at the theoretical value (3), 100 nm, and we determined ψ_0 and A to be -32 mV and 2.0×10^{-20} J. The result of ψ_0 agrees with the zeta-potential value, -42 mV, of the same sample measured at the same salt concentration. The determined Hamaker constant, A, is twice as large as the theoretical prediction. This is probably due to the fact that when C = 0.001 M, van der Waals forces are still much smaller than electrostatic forces. Accurate determination of van der Waals forces is only possible at higher salt concentrations.

When C = 0.01 M, van der Waals forces are, in general, larger than electrostatic forces in the region accessible to particles during a collision. κ remains to be a sensitive parameter because of the exponential relationship, but it is usually treated as a constant. Since the separation distance between two particles during a collision is comparable to the latex hairy layer thickness, L_h, this parameter (L_h) will affect the magnitude of van der Waals forces significantly and is included in Eqs. [1.3] and [1.6] in addition to A and λ. In Chapter 3, we fixed the λ at 100 nm and determined A and L_h. The Hamaker constant, A, was found to be within 10% deviation from the theoretical value for polystyrene in water. Compared with the literature data of experimentally determined Hamaker constants which usually scatter within an order of magnitude (4), this result proves that CPS is a highly sensitive and accurate method to measure colloidal forces.

When latex particles are coated with thin surfactant layers, the same model can be

applied by replacing L_h with L_s (adsorption layer thickness). In Chapter 4, we first fixed λ at 100 nm and determined A and L_s. The results agree very well with theoretical predictions and literature data. We then fixed A at the theoretical value (5), 9.5×10^{-21} J, and determined λ and L_h. The λ was found to be 110±10 nm which agrees with our first assumption.

When the polymer layers become thicker than 15 nm (subject to change if C ≠ 0.01 M or a ≠ 2.3 μm), they start to compress each other during a collision provided that the contact time is less than the time of polymer chain relaxation. These dynamic steric interactions were studied in Chapter 5 in which we modeled the adsorption layer as two sublayers: (outer) penetrable layer where water can flow through without any resistance and (inner) impenetrable layer where water cannot penetrate. The thicknesses of these two layers are denoted as L_p and L_i respectively. This model greatly simplifies the theoretical analysis of the trajectory equation in a polymer-coated latex system. The steric force - distance relationship can be expressed as in Eq. [1.8] assuming two layers behave like elastic gels during a collision. Following these treatments, we determined the parameters L_p, L_i and E (elastic modulus of the layer) which are related to the dynamic steric interactions and the layer structures. The results are consistent with literature data. Since electrostatic and van der Waals forces are less significant in magnitude compared with steric forces, the parameters κ, A and λ are usually kept constant in these cases.

As mentioned above, the criterion of the layer thickness 15 nm varies with the salt concentration. When C > 1 M, this criterion may become less than 1 nm, thus the dynamic interactions between two thin polymer layers can be studied (to be discussed later).

In addition, the microcollider can be reconfigured to measure particle-wall

interactions. An electrokinetic lift force was determined in Chapter 6. The results disagree with previous theoretical predictions and support a new electrokinetic theory which describes the lift force more precisely.

For more than a decade, research on colloidal and surface forces has been a very active field (2, 6-12). Most of the force measurement techniques were developed during this period. The current focus moves towards biological and bilayer systems (11,12). In either case, accurate force determination is essential for the successful interpretation of the structures and properties of the material being studied. Being an ultrasensitive and accurate force measurement technique, CPS has great potential both in traditional colloid science and in new biotechnological research.

CLAIMS FOR ORIGINAL RESEARCH

This thesis introduces a new experimental method and its applications. Almost all of the research work described in the previous chapters is original. The most important ones are listed as follows:

1. Development of a useful technique to measure surface forces down to the scale of tens of femto-newtons with particle collisions.

2. Offering a way to characterize large hairy latex particles.

3. Having discovered a new stabilizing mechanism for hairy latex suspensions. It indicates that under moderately high salt concentration (0.01 M), hairy latexes are stabilized due to the

decease of van der Waals attraction, rather than the steric repulsion, although both effects are caused by the hairy layer.

4. Measurement of retarded van der Waals forces between two polystyrene latexes with an accuracy of about 10%.

5. Determination of the thicknesses of triblock copolymer and high-molecular-weight PEO layers on large latex spheres with particle collision experiments.

6. Investigation of the dynamic interactions between two PEO layers on latex spheres through the measurement of elastic moduli of the layers.

7. Offering a more accurate way to determine the electrokinetic lift force.

SUGGESTIONS FOR FURTHER RESEARCH

Further research might be carried out in three directions: improving the precision of current apparatus, investigating new experimental conditions and exploring new polymeric and biological systems.

1. Improving the Precision of the Current Apparatus

The main problem of the current microcollider is the making of the top glass surface (see Appendix for detailed procedures). This surface should be smooth and perfectly flat. The thickness of the glass piece is also a crucial factor. If it is too thin, it may not be rigid enough to withstand the hydrodynamic pressure which tends to deform the surface to a concave

shape. If it is too thick, the objective with only a limited focal length may fail to focus on the image under this surface. So far, it is an art rather than a science to make a perfect surface. We use a 120 μm-thick 40x45 cm microscopic cover slip as the material and this thickness is almost the maximum limit for the objective currently being used. Deformation up to 5 μm in the center has been observed occasionally. This deformation seems to increase with the age of the surface. Brand-new surfaces have to be made frequently to replace the aged ones. A long-distance (LD) objective will enable us to use thicker glass surfaces which may hopefully reduce the deformation. Thick glass surfaces, however, complicate the processing procedures. An experienced glassblower may be required to cut the glass.

2. Investigating New Experimental Conditions

As shown in Fig. 7.1, the variable conditions are shear rate and salt concentration. Lower shear rate may change the nature of the steric interaction from a dynamic one to a "static" one or a force in the transitional state. The problems which might be encountered when using a lower shear rate are the increase of the Brownian motion effects on slow moving particles and possible particle coagulation caused by the entanglement between two rough polymer layers which cannot be overcome by the reduced hydrodynamic force. Both problems can be solved by using larger latex particles. Higher shear rate helps investigate thick polymer layers more thoroughly and accurately. In Chapter 5, it has been shown that the thickness of the penetrable layer, L_p, can be more accurately determined than that of the impenetrable layer, L_i. Higher shear rate increases the flow through the polymer layer and enlarges the penetrable part in the layer. In addition, it results in a larger hydrodynamic force

which generates more layer-layer compression and increases the "sampling" range in the layer. Hence, a higher shear rate increases the overall measurement accuracy in a thick-polymer layer system. The current obstacles to achieve higher shear rates are large system vibration and the slow video system. The former can be overcome by using a new microscope with a "stageless" design. The microscope is fixed on a stand leaving more space below the objective, so it becomes possible to replace the stage supported only at one end on a track with a heavyset vertical translator screwed on the tilting base. The latter can be solved by a high-speed video system which can increase the current video speed (30 frames/second) by at least ten times.

Higher salt concentration can be used to investigate thin polymer or surfactant layer (1~15 nm) systems. At 0.01 M, we can only determine the layer thickness of a thin layer. At a higher concentration, e.g. 1 M, thin layers start to compress each other creating a dynamic steric force. By studying this force, we can, therefore, determine both the layer thickness and the elastic modulus of the layer which give us more information about the structure of the layer than a single layer thickness.

3. Exploring New Polymeric and Biological Systems

It has been shown that CPS is a powerful tool to determine colloidal forces and the related surface properties. Served as an introduction of CPS, this thesis only presents rather classical systems such as bare and PEO-coated latexes. It would be an exciting experience to explore various new polymeric or biological systems used frequently in industry or advanced biotech research. For example, latex spheres grafted with biotin are used as a carrier for many

diagnostic tests. The same latex sample may find its application in CPS when interactions between enzyme-protein or antibody-antigen are to be determined.

REFERENCES

1. van de Ven, T. G. M., Warszynski, P., X. Wu, and Dabros, T., *Langmuir* **10,** 3046 (1994) (Chapter 2 of this thesis).
2. Li, Y. Q., Tao, N. J., Garcia, A. A., and Lindsay, S. M., *Langmuir* **9,** 637 (1993).
3. Schenkel, J. H., and Kitchener, J. A., *Trans. Faraday Soc.* **56,** 161 (1960).
4. Visser, J., *Adv. Colloid Interface Sci.* **3,** 331 (1972).
5. Hunter, R. J., "Foundations of Colloid Science." Vol.1, Clarendon Press, Oxford 1989, p.222.
6. Israelachvili. J. N., and Adams, G. E., *J. Chem. Soc. Faraday Trans. 1* **74,** 975 (1978).
7. Pashley, R. M., *J. Colloid Interface Sci.* **102,** 23 (1984).
8. Ninham, B. W., and Evans, D. F., *Faraday Discuss. Chem. Soc.* **81,** 1 (1986).
9. Butt, H. -J., *Biophys. J.* **60,** 1438 (1991).
10. Shubin, V. E., and Kekicheff, P., *J. Colloid Interface Sci.* **155,** 108 (1993).
11. Florin, E. -L., Moy, V. T., and Gaub, H. E., *Science* **264,** 415 (1994).
12. Chen, Y. L., Chen, S., Frank, C., and Israelachvili, J. N., *J. Colloid Interface Sci.* **153,** 244 (1992).

APPENDIX

AN OPERATIONAL MANUAL

OF THE MICROCOLLIDER

PART I SETUP

The microcollider is designed to measure surface forces between two spherical particles based on the principles of colloidal particle scattering. The whole setup is shown in Fig. A.1. Its main components include,

a. Top glass surface/cylindrical holder (cf. Fig. A.2)

b. Sample cell (cf. Fig. A.2)

c. Microscope (Zeiss Axioplan) (cf. Fig. A.3)

d. Slimline Gimbal mount (Oriel 19295) (cf. Fig. A.3)

e. Horizontal and vertical translators (Oriel 16131 and 16611) (cf. Fig. A.3)

f. Tilting base (cf. Fig. A.3)

g. Encoder stages (Burleigh TSE-75) (cf. Fig. A.3)

h. Inchworm motor controller (Burleigh 6200-2-2) (cf. Fig. A.4)

I. Joystick (Burleigh 6003) (cf. Fig. A.4)

j. Video camera (Panasonic WV-D5100) (cf. Fig. A.4)

k. VCR (formerly JVC BR-S605U and presently Panasonic AG-7350) (cf. Fig. A.4)

l. Video monitor (JVC TM-1400SU) (cf. Fig. A.4)

m. IBM-compatible 386 computer (cf. Fig. A.4)

n. Vibration-free workbench

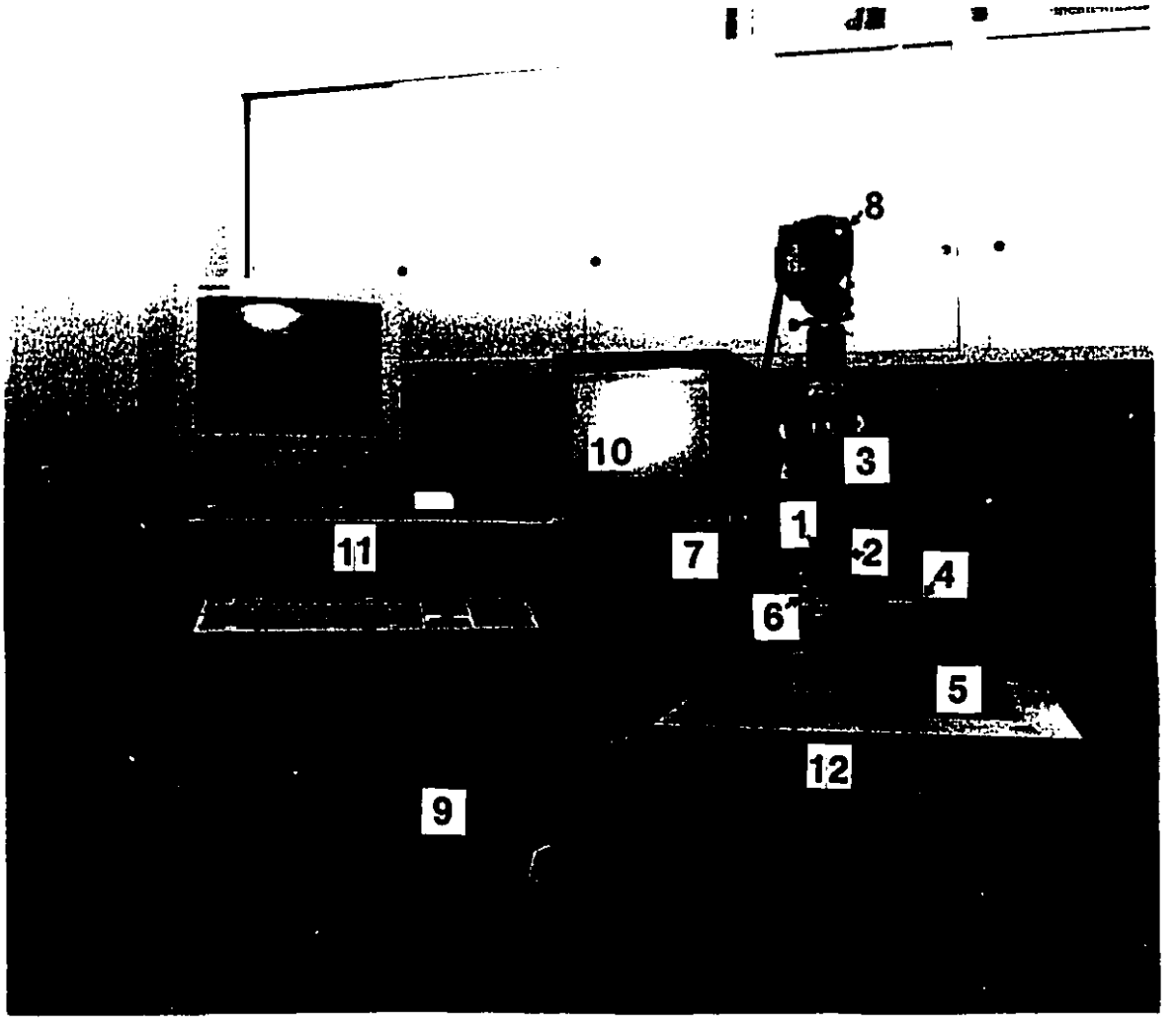

Fig. A.1 Main components of a microcollider. 1. top glass surface/cylindrical holder; 2. sample cell; 3. microscope; 4. horizontal and vertical translators; 5. tilting base; 6. encoder stages; 7. inchworm motor controller; 8. video camera; 9. VCR; 10. video monitor; 11. IBM-compatible 386 computer; 12. vibration-free workbench.

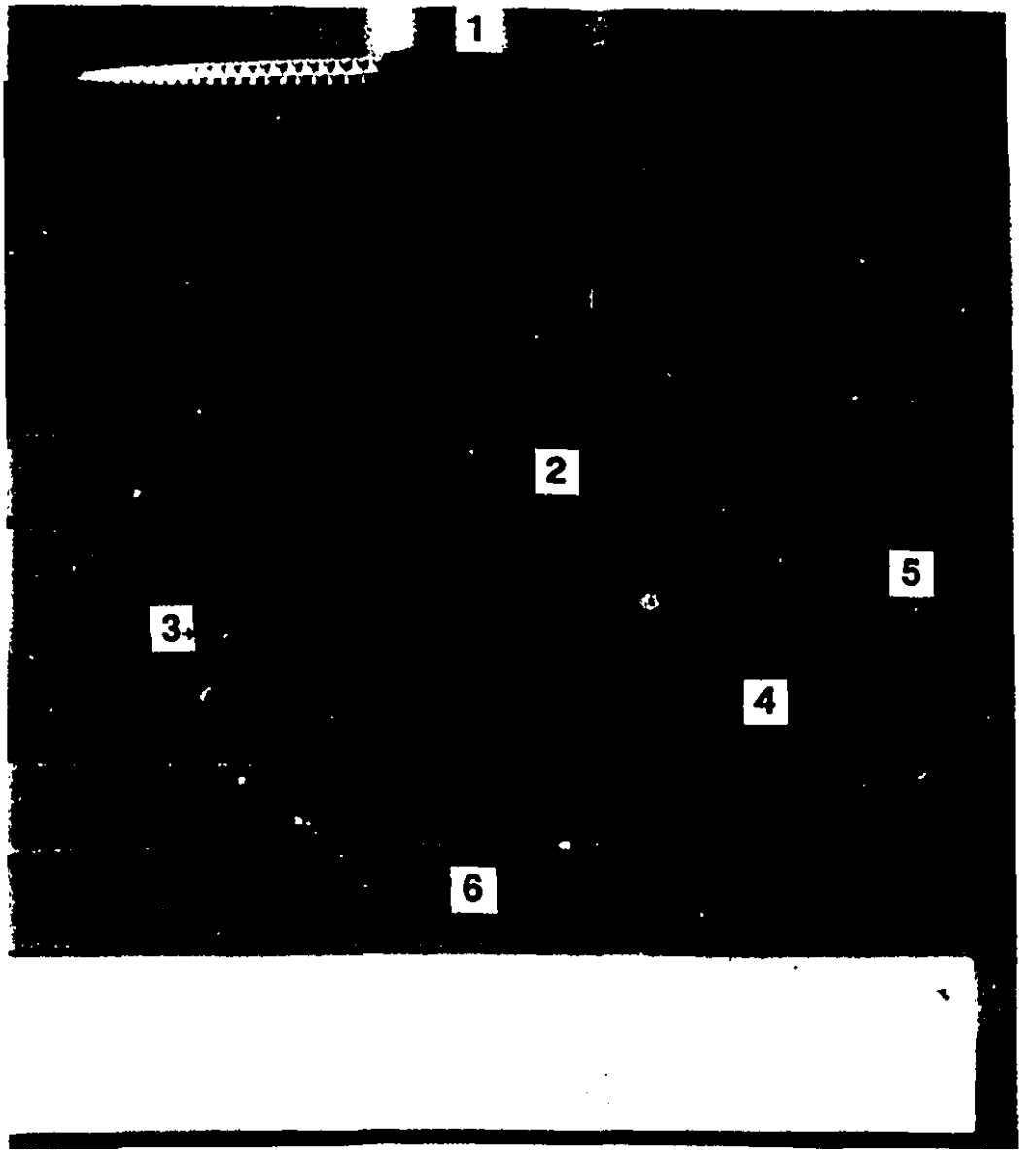

Fig. A.2 Close-up view of the top glass surface and its cylindrical holder. 1. microscope objective (Zeiss Epiplan-Neofluar 50x HD); 2. cylindrical holder; 3. top glass surface (glued to the end of the cylindrical holder); 4. sample cell (the thick dark glass base also served as the bottom surface); 5. latex suspension; 6. aluminum block (precisely cut to enable the sample cell being mounted snugly on the top).

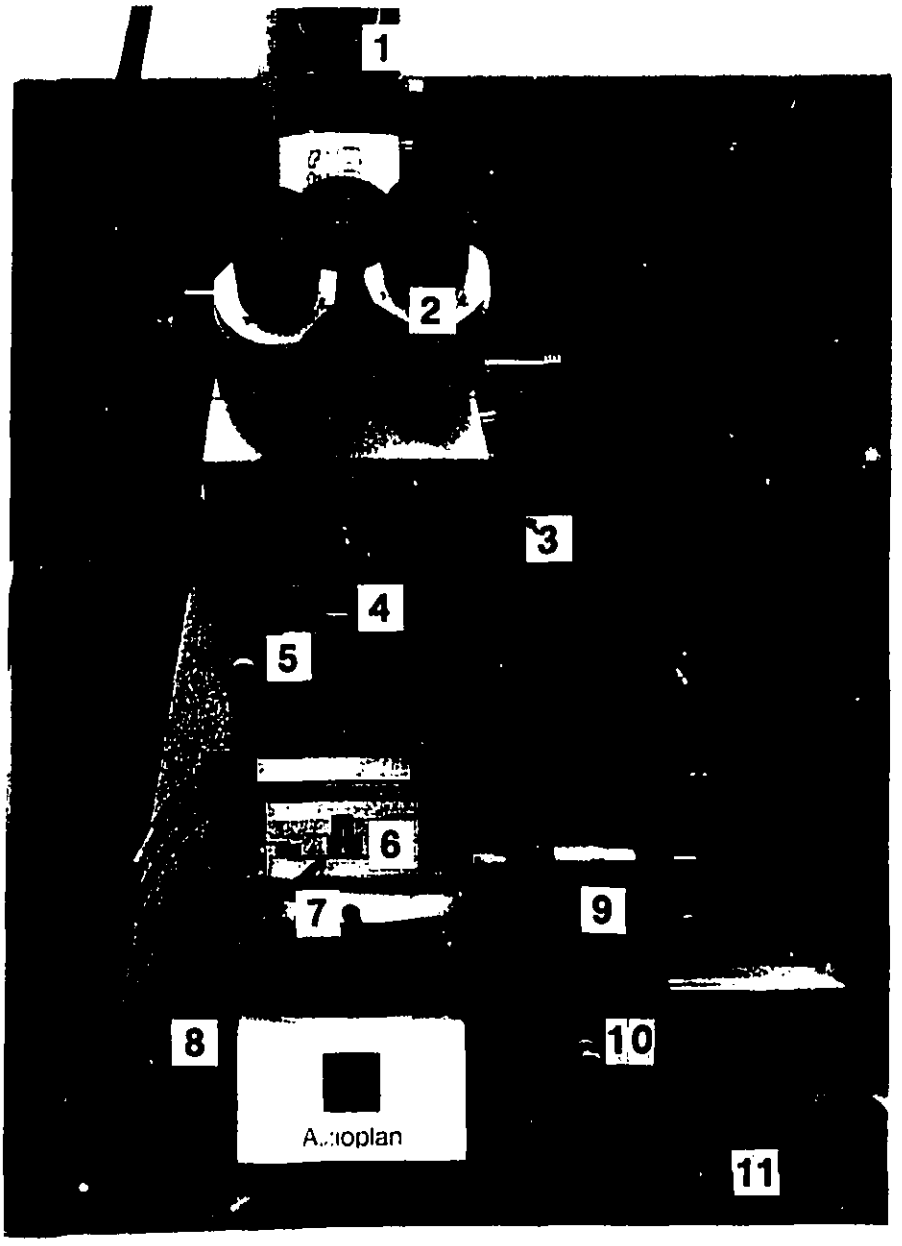

Fig. A.3 Close-up view of the mechanical and optical parts. 1. eye-piece for video camera focusing (high magnification); 2. eye-pieces for searching (low magnification); 3. dark field/bright field switch; 4. microscope objective; 5. Slimline Gimbal mount; 6. encoder stages; 7. microscope stage; 8. knob for height adjustment of the stage; 9. horizontal translators (x-y); 10. vertical translator (z); 11. tilting base with three screws to adjust the alignment.

Fig. A.4 Close-up view of the controlling parts. 1. inchworm motor controller; 2. joystick; 3. video camera; 4. VCR; 5. video monitor; 6. IBM-compatible computer.

In the mechanical part, the goal of the design is to generate a precise movement of the stage with the least vibration. The precise movement is guaranteed by the Inchworm motor designed by Burleigh Instruments which is accurate to 0.1 μm. To minimize the vibration caused both internally and externally, all mechanical parts are screwed tightly to each other and the whole setup including the microscope sits firmly on a tilting base made of cast iron. This base is placed on the table of a vibration-free workbench which is suspended by nitrogen gas at a pressure of 1000 kPa. Positioning and alignment of the top glass surface is also crucial for a successful experiment. For this reason, manual translators for x, y and z directions equipped with micrometers accurate to 1 μm are installed. The position of the microscope stage can be read from the knob which moves the stage up and down. Presently, a more precise Starrett spring-loaded displacement meter accurate to 2.5 μm is used to replace the knob reading. A Slimline Gimbal mount is installed to align the top glass surface. The maximum tilting angle is ±2.5 degrees and the accuracy is 0.01 degree. The cast-iron tilting base is only capable of coarse adjustment which is nevertheless adequate for the whole system alignment (to be discussed later).

In the optical part, a suitable light source is essential. The lamp has to be bright enough to form a clear image of a 5 μm latex sphere at a magnification of about 4000, but meanwhile to be "cold" enough not to create any undesirable convection in the suspension. For this reason, we chose an HBO 100W/2 mercury short arc lamp to replace the original halogen lamp. The result is quite satisfactory.

In the controlling part, besides controlling software which will be discussed in PART IV, it is important to choose the optimum wiring configuration for the video system.

Currently, we use the configuration shown in Fig. 2.7. It enables us to see high-quality S-VHS images directly from the camera and from S-VHS cassettes in the VCR, or to view the processed black-and-white pictures with some text remarks from the image board. The only disadvantage of this configuration is that we cannot save these texts back to the video cassette. This can be realized by temporarily reversing the wiring between image board and the VCR. Any changes of the wiring configuration should be carried out with discretion because there are no less than twenty cables behind these instruments!

PART II PREPARATION

1. Making of the top glass surface

As mentioned in Chapter 7, the top glass surface needs replacement after two or three runs. The making of this surface requires good craftsmanship. Detailed procedures are listed as follows,

a. Removing the old glass surface

Before a new surface is made, the old one should be removed from the stainless steel cylindrical holder. Safety goggles, thick rubber gloves and lab coat are mandatory since the broken glass pieces are very small, sharp and sometimes hardly visible! Take a large container for glass recycling and turn the holder to let the glass surface face the container's opening. Use a sharp utility knife to break the glass surface and clear off the glass inside the rim of the holder. When no more glass is visible, turn the holder upside down. A ring of glass glued to the rim will be seen and it has to be carefully peeled off with the knife. Note that the knife blade should be very sharp otherwise excessive force tends to be used and that will dent the rim. When the glass is removed, the residual glue should be cleared off as well. Rinse the holder to wash away any broken glass pieces. Dry it with paper towel.

b. Attaching a new glass piece

Select a piece of 40x45 cm microscopic cover slip. A good candidate should have very few specks and do not stick to other slips. Apply a thin layer of epoxy glue on the rim of the holder. Center the glass piece and put it on the rim. Once the piece is on the rim, do not move it because that will smear the surface. Turn over the holder and place the surface on a flat and

smooth glass plate. A heavy metal cylinder with a smooth end should be carefully put inside the cylindrical holder. It tightly presses the top glass surface against the bottom plate to ensure the flatness of the top surface. Wait for at least sixteen hours to let the glue reach its maximum adhesive strength.

c. Smoothing the edge

This is the most difficult step because the square glass piece has to be cut to a round shape without any sharp edges. First, place the glass surface on a layer of soft material (paper towel) and use the sharp end of the utility knife to cut away most parts of the four corners. DO NOT cut the part next to the rim since the glass tends to crack and once the crack goes inside the rim, this surface has to be removed according to step (a). Turn over the holder to let the glass surface face the experimentalist. Take a flat needle file and slide it downward to remove the jagged part of the glass piece around the rim. When proper force and motion are applied, the glass piece tends to break exactly at the outer edge of the rim. Finally, smooth the edge with the needle file and remove the glue on the outside wall of the cylindrical holder as well. Rinse both sides of the surface and the holder with distilled water and let it air dry.

2. Sample preparation

Latex suspensions should be prepared within the same day as the experiment to minimize contamination. Before preparation, the latex sample should be washed at least three times with deionized water in a centrifuge test tube. Depending on the treatment of the particle (coated or uncoated), the preparation procedures vary slightly. They are described in detail as follows,

a. Preparation of bare latex suspensions

- Example: 0.005% latex in a 0.01 M KCl solution

Weigh exactly 5.00 g 0.1 M KCl solution in a clean 50 mL volumetric flask. Dilute it with 30 mL D_2O. Take 0.25 mL 1% clean latex suspension from the centrifuge test tube and drop it into the flask. Add deionized water until the meniscus reaches the 50 mL mark.

b. Preparation of polymer-coated latex suspensions

- Example 1: 0.005% Pluronic surfactant-coated latex in a 0.01 M KCl solution (adsorption concentration: 50 mg/L)

Take 0.25 mL 1% clean latex suspension and drop it slowly into a 10 mL 50 mg/L Pluronic surfactant solution. Meanwhile, stir the mixture constantly. Wait for one hour or longer and remove the supernatant. Redisperse the coated latex spheres in 5 mL deionized water. Weigh exactly 5.00 g 0.1 M KCl solution in a clean 50 mL volumetric flask. Dilute it with 30 mL D_2O. Drop in the latex suspension. Add deionized water until the meniscus reaches the 50 mL mark.

- Example 2: 0.005% polyethylene oxide-coated latex in a 0.01 M KCl solution (adsorption concentration: 250 mg/L)

Mix 12.5 mL 1000 mg/L polyethylene oxide (PEO) solution with 30 mL D_2O in a clean 50 mL volumetric flask. Take 0.25 mL 1% clean latex suspension and drop it slowly into the flask. Meanwhile, stir the mixture constantly. Wait for one hour or longer. Weigh exactly 5.00 g 0.1 M KCl solution and drop it into the flask. Add deionized water until the meniscus reaches the 50 mL mark.

PART III EXPERIMENTAL PROCEDURES

1. Starting an experiment

The microscope lamp needs a few minutes to warm up. When it is switched on, its power supply generates a high voltage to make an arc in the lamp. The voltage of nearby power sockets may drop below tolerance limit. Be sure that all the other instruments are turned off at that moment. Once the lamp is lit, switch on the computer, the video camera, the VCR, the video monitor, two power supply boxes for the encoder stages and the inchworm motor controller. The top glass surface with its cylindrical holder should be immersed in chromic acid for five minutes and then be rinsed with deionized water and later with the latex suspension. This cleaning procedure does not cause serious corrosion on the stainless steel holder.

2. Generation of particle collisions

a. Alignment

The microcollider requires a very precise alignment of its stages and glass surfaces. There are three levels of alignment: alignment of the encoder stage to make its movement plane parallel to the sample cell surface (or called bottom glass surface), alignment of the tilting base to make the bottom glass surface perpendicular to the direction of gravity and, finally, alignment of the top glass surface to make it parallel to the bottom one. The order of these three alignments cannot be altered.

The first alignment is necessary because when misaligned, the bottom surface will

move away or towards the top surface and an undesirable normal flow will be created in the gap. The alignment can be performed with the aid of the microscope. When the dust particles on the bottom surface are always in focus wherever the encoder stages move, we can say that the bottom surface is perfectly aligned. To adjust this alignment, a tilting table should ideally be used. However, there is not enough space on the microscope stage for a tilting table, furthermore, a commercial spring-loaded tilting table does not have the mechanism to damp the vibration intensified by its turnable surface. Therefore, we attached several strips of scotch tape at different locations of the encoder stage surface to adjust its alignment. This method, seemingly rather primitive, works extremely well. Usually one "attachment" can keep a good alignment for several months.

The second alignment, i.e. making the cell surface perpendicular to the direction of gravity, ensures that the moving particle does not drift along the top surface. Before the alignment, the vibration-free workbench should be gas-lifted. We then place a level gauge in the sample cell and adjust the screws on the tilting base until the cell surface is leveled in both x and y directions. Since a very slow drifting does not affect the experimental results significantly, this alignment does not require using accurate micrometers.

The third alignment is the most important one because if the top and bottom surfaces are not parallel, a pressure gradient will build up and it will create a sideways flow which severely affects the accuracy of the measurement. Compared with the first two alignments, the third one is not so straightforward. It has been found, by accident, that the encoder stage is extremely sensitive to an impact. If we tilt the top surface until it touches the bottom one, there will be a soft "clicking" sound coming out of the stage. Meanwhile, the position of the

stage starts to fluctuate within 0.1 μm. A computer program has been written to monitor this change and send out a loud beep which enables the experimentalist to know the "touchdown". When the top surface tilts towards the opposite way, another beep will be heard. Since the Slimline Gimbal mount contains two micrometers indicating the tilting angles in both x and y directions, we can average these two values of the angles and turn the micrometer to the level position. The same procedure should be repeated alternately for both directions until no more changes in the average angles are observed. We call this technique "clicking" alignment, because we used to rely on the "clicking" sound instead of the computer beeping to perform the alignment. "Clicking" alignment can be applied in an empty cell or a cell filled with a latex suspension. When the cell is filled with the suspension, we can check this alignment by moving a mobile particle along the top surface. If the particle does not move exactly on the line of the encoder stage direction premarked on the video monitor, we can adjust the micrometers, normally within 0.02 degree, until the top surface is perfectly aligned.

b. Filling the sample cell with latex suspensions

A good filling with a latex suspension should not create air bubbles in the gap. If the suspension is poured into a cell with a prepositioned top surface which is very close to the bottom, or the cell filled with the suspension is lifted upward by turning the knob on the microscope to meet an well aligned top surface, air tends to be trapped in the gap and many bubbles are formed. The correct way is to fill the cell, mount it on the encoder stage, move the stage towards the experimentalist until it reaches the limit, turn the top surface to face the experimentalist and finally lift the stage slowly upward. The far end of the top surface will touch the curved edge of the meniscus first, and water will then move slowly upward along

the top surface to drive away the air in the gap. When the top surface is fully immersed, a "clicking" alignment can be performed to align the top surface.

c. Collision recording

Both the top and the bottom surfaces should be fixed at certain positions throughout the experiment. The former is done by constantly focusing the stationary particle stuck to the top surface. The latter is done by keeping the reading of the Starrett displacement meter constant. It is relatively easy to generate a collision. First, use a bright field of the microscope and place the stationary particle in the center of the video monitor. Then, switch to dark field and search for a mobile particle by looking through the eye-pieces. The focus needs to be adjusted by moving the manual vertical translator after the switching from camera focusing to eye-piece focusing. Usually one should select a mobile particle which is in focus meaning that it is not far from the top surface. When the particle is selected, move it to the vicinity of the stationary one with the encoder stages manipulated by a joystick. Check the camera view first through the eye-piece for camera focusing. Focus adjustment is again necessary. The image in this eye-piece has a higher magnification than that through the search eye-pieces, so the mobile particle may need to be moved even closer to the stationary one. Slowly and carefully switch the microscope back to the bright field without introducing too much vibration to the system. Both the stationary and mobile particles should now be visible on the monitor. Use the joystick to move the mobile particle to the left or right edge of the monitor. Depending on the experimentalist's need, the initial position can be right on the central horizontal line to generate a head-on collision or be slightly off the line to generate a grazing collision. Once the particle is aimed, switch the joystick to OFF so the computer can take

over. Press a Shoot/Stop button in a controlling software (to be described in PART IV) to start the collision. One will observe the encoder stage of y-direction starts to move slowly backward for a few seconds depending on the set value and then moves towards the stationary particle at a preset velocity. At the same time, the VCR starts to record the collision process automatically. When the moving particle moves out of the screen, press the same Shoot/Stop button to stop the encoder stage. Use the joystick to move the particle back to the screen. Press a Reverse Direction button and the Shoot/Stop button. The particle will start to collide with the stationary particle from the other side. To facilitate this second recording, the VCR does not automatically stop after the first collision. However, if the mobile goes out of focus (being far away from the top surface) after the first collision, it normally takes more than 10 seconds for it to float back to focus due to the small difference between the densities of polystyrene and 60%D_2O-40%H_2O. To be able to record more collisions on one tape, it is recommended to stop the VCR manually. It will be switched to recording automatically once the second collision starts. Watch the strike number printed on the computer monitor increases. Stop the experiment when this number reaches 250. Note that strike number only indicates the number of collision trials. This criterion of 250 strikes may vary depending on the number of "missing shots".

d. Measurement of gap widths

The gap width between the top and bottom surfaces can be estimated from the "clicking" alignment since we know the tilting angle and the cylinder diameter. However, the two gap widths determined from the alignments of x and y directions are not consistent, due to the different sensitivities of the upper encoder stage to axial and lateral shocks. A more

accurate method has been developed by using the focal plane of the microscope. First, record the reading of the Starrett displacement meter as a_1. Lift the top surface out of focus and move the bottom surface up to focus. Record the reading of the displacement meter as a_2. Subtracting a_1 from a_2 yields the gap width. The focal length of the objective depends on media. When a_1 is measured, the bottom part of the top surface is focused, so the light goes through air and a thin layer of glass. When a_2 is measured, the light has to go through air, the same layer of glass and air again to give the same focal position as before. Therefore, the sample cell must be completely dry to ensure an accurate measurement. For this reason, we usually determine the gap width after the experiment. The sample cell can be dismounted and dried by soft tissue. The top surface should be kept mounted and blow dried. Any attempt to wipe off the water on this surface may alter its position and cause errors in the measurement.

3. Shut-down procedures

The microscope lamp should be switched off first to avoid the flare encountered when the top surface is dismounted. The controlling software should exit before the VCR and the micromanipulator (including encoder stages, inchworm motor controller and joystick) are turned off. Other instruments can then be switched off at will. The top surface should be rinsed with deionized water and wiped with soft tissue soaked with 50% ethanol-water to eliminate the residual latexes.

PART IV SYSTEM CONTROLLING AND DATA PROCESSING

1. Integrated controlling and image analysis software - CUE and tutorial

One of the biggest challenges in developing the CPS method was to integrate encoder control, image analysis and VCR control in one software. Commercial softwares may include these functions but they are only specialized in one of the three. The encoder controlling program offered by Burleigh is not quite satisfactory because the velocity of the encoder stage is always faster than the set point. A good program should monitor the change in the positions of the stage during its movement and perform a linear regression to calculate the true velocity of the stage. Commercial image processing softwares are usually designed for still pictures. It is extremely time-consuming to use them analyzing the particle collision trajectories frame by frame manually, especially since the number of frames involved in one experimental run (~200 collisions) is in the order of 10,000. The only feasible way to complete the analysis within reasonable time is to incorporate the image analysis and VCR frame forward control in one program and use this program to automatically analyze the trajectories. Base on these ideas, we developed a 3-in-1 software called CUE. It indeed does more than a "cue" since it not only generates collisions, but records and analyzes the trajectories and finally stores the results in data files. CUE uses an overlapped menu interface which allows more space to display data information than a traditional pull-down menu without sacrificing its user-friendliness. A guided tour will be given below to explain how to use this software.

a. Getting started

When CUE is loaded from DOS, a cover page will appear as shown in Fig. A.5.

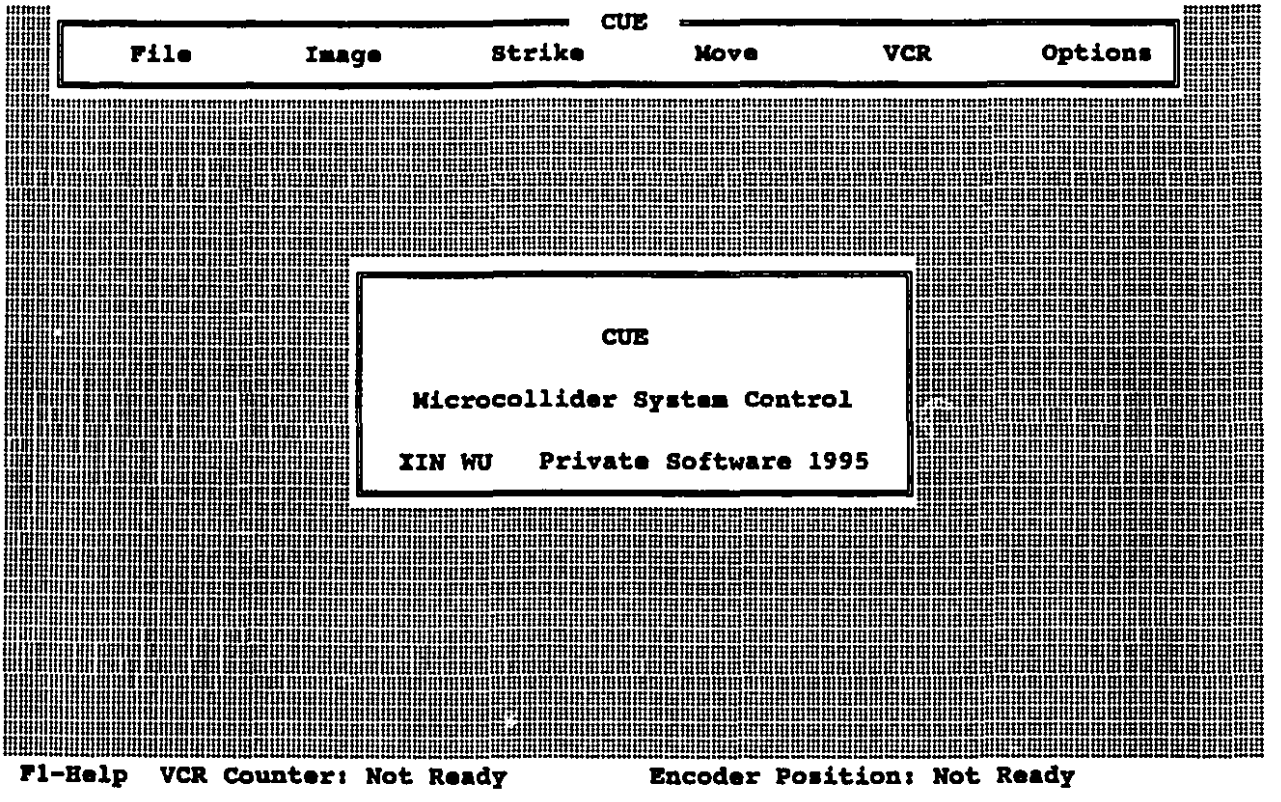

Fig. A.5 The cover page of CUE. Six basic functions are listed in the top menu bar. The bottom line is a status bar containing the real-time VCR counter (tape address) and the encoder position (both x and y).

After a key stroke, the first item **File** will be highlighted. Meanwhile, a large window titled "File - HELP" will appear in the middle. Use ←→ keys to view other help windows (rotating from **File** to **Options**). Move back to **File** and press any key. A window titled "File" will appear containing six items inside (cf. Fig. A.6). Now the first item **Data File Name** is highlighted. Use ↑↓ keys to highlight other items. The current status of one specific item is printed on the right. Try to type any name to see it replace the original name "Q.DAT". Highlight **Exit** and press <Enter> will terminate the program. Each item has a key character (printed in bright green), for example, "d" for **Data File Name** and "x" for **Exit**. Pressing this

key character is equivalent to highlighting and pressing <Enter>. The ←→ keys will take the user to the windows titled **Image**, **Strike**, etc.

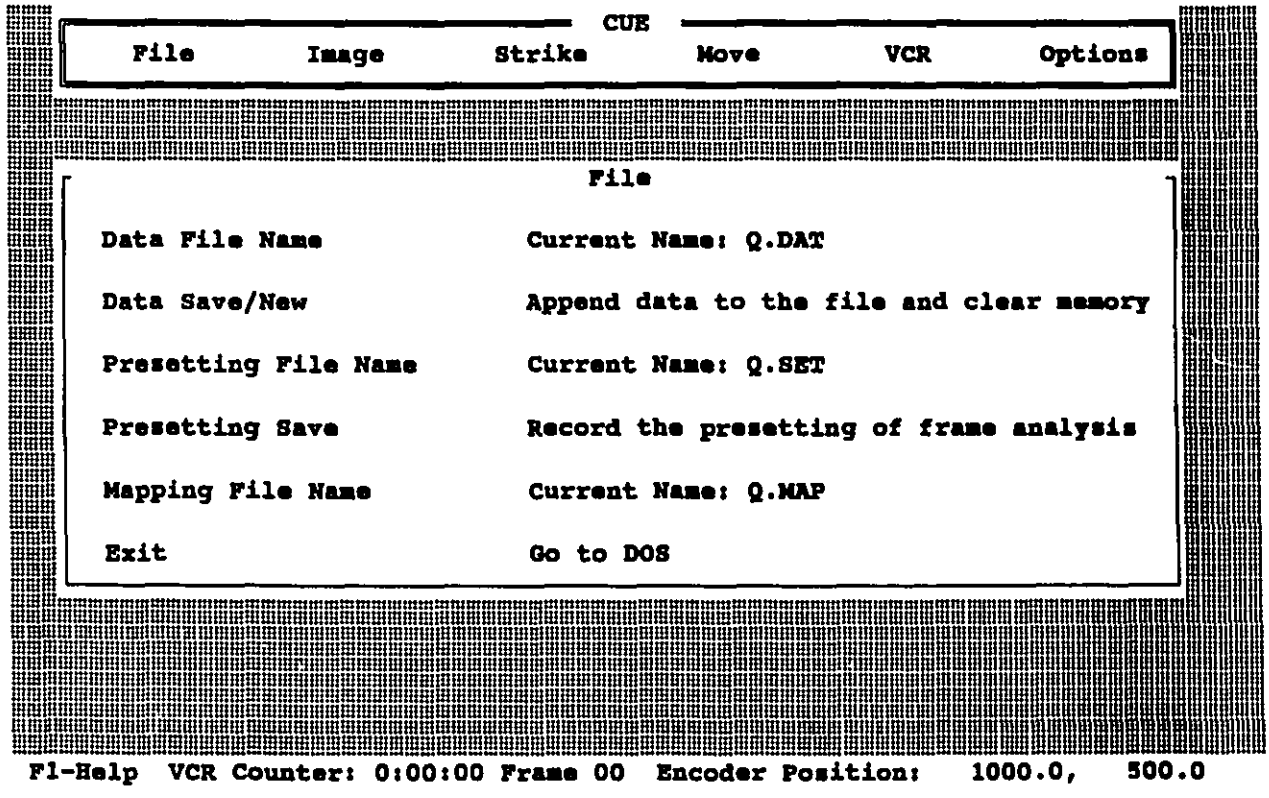

Fig. A.6 The window of **File**.

To start from the simplest function, move to **VCR**. A window shown in Fig. A.7 will appear. To play a cassette, enter the **PLAY/Shuttle Search** subwindow (cf. Fig. A.8), highlight **PLAY** and press <Enter>. The speed of normal playing is defined as x1 and the speed of FF or REW is x11, i.e. eleven times higher. To make a variable speed shuttle search, press **STILL** and then **Shuttle Forward** or **Shuttle Reverse**. Use +- buttons to increase or decrease the speed either when the cassette is in the Shuttle Forward/Reverse mode or the STILL mode. The available speeds are x1/25, x1/9, x1/5, x1/2, x1, x2, x5 and x11.

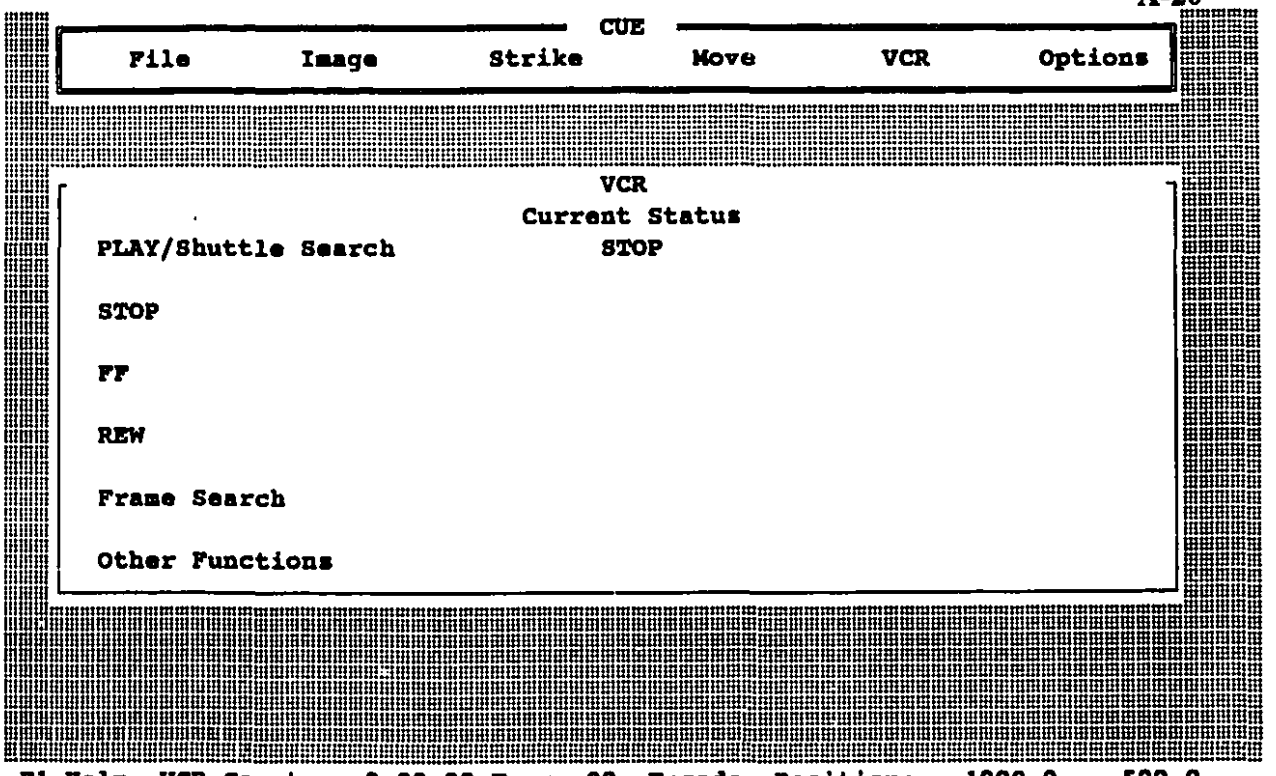

Fig. A.7 The window of VCR.

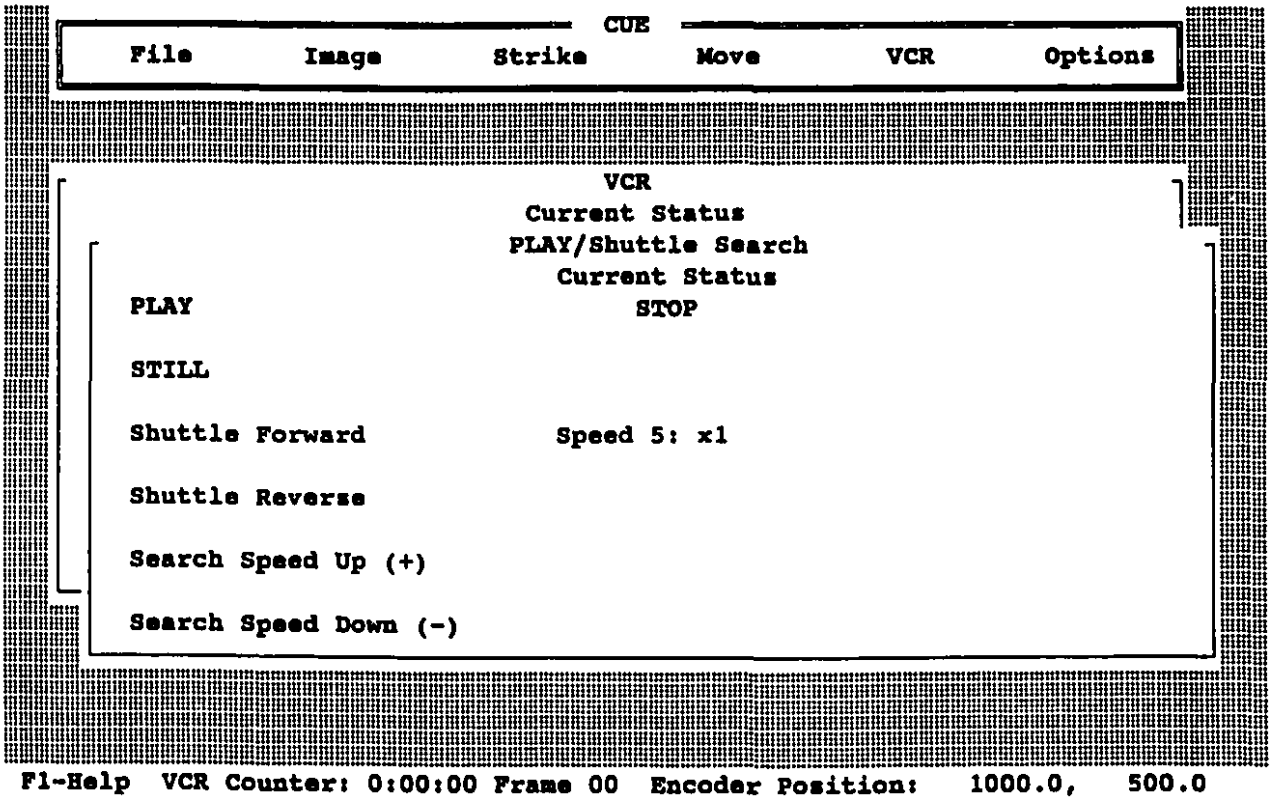

Fig. A.8 The subwindow of PLAY/Shuttle Search.

Searching in even smaller steps can be performed in the subwindow of **Frame Search** (cf. Fig. A.9). The cassette should be in the STILL mode (check Current Status to verify). When **Half Frame** is on, two strokes of **Frame Forward** or **Frame Reverse** make the cassette move a frame (1/30 s). Watch the changes in VCR Counter shown in the status bar. Another convenient searching function is **Search to Frame** designed to advance or rewind the cassette to the address specified by the user.

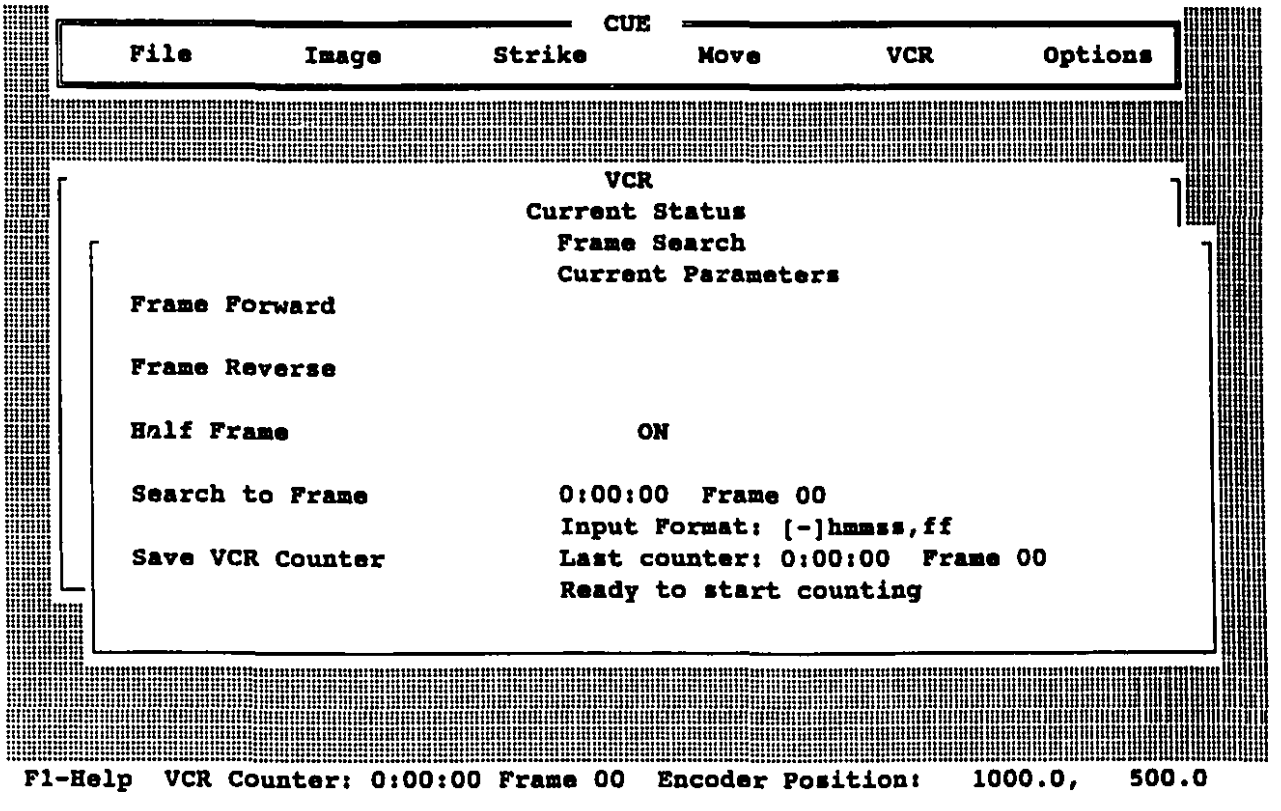

Fig. A.9 The subwindow of **Frame Search**.

The subwindow **Other Functions** (cf. Fig. A.10) in **VCR** includes **REC** (record), record **PAUSE**, **EJECT** and **Reset VCR Counter** (rezero the address). Other items are for system maintenance.

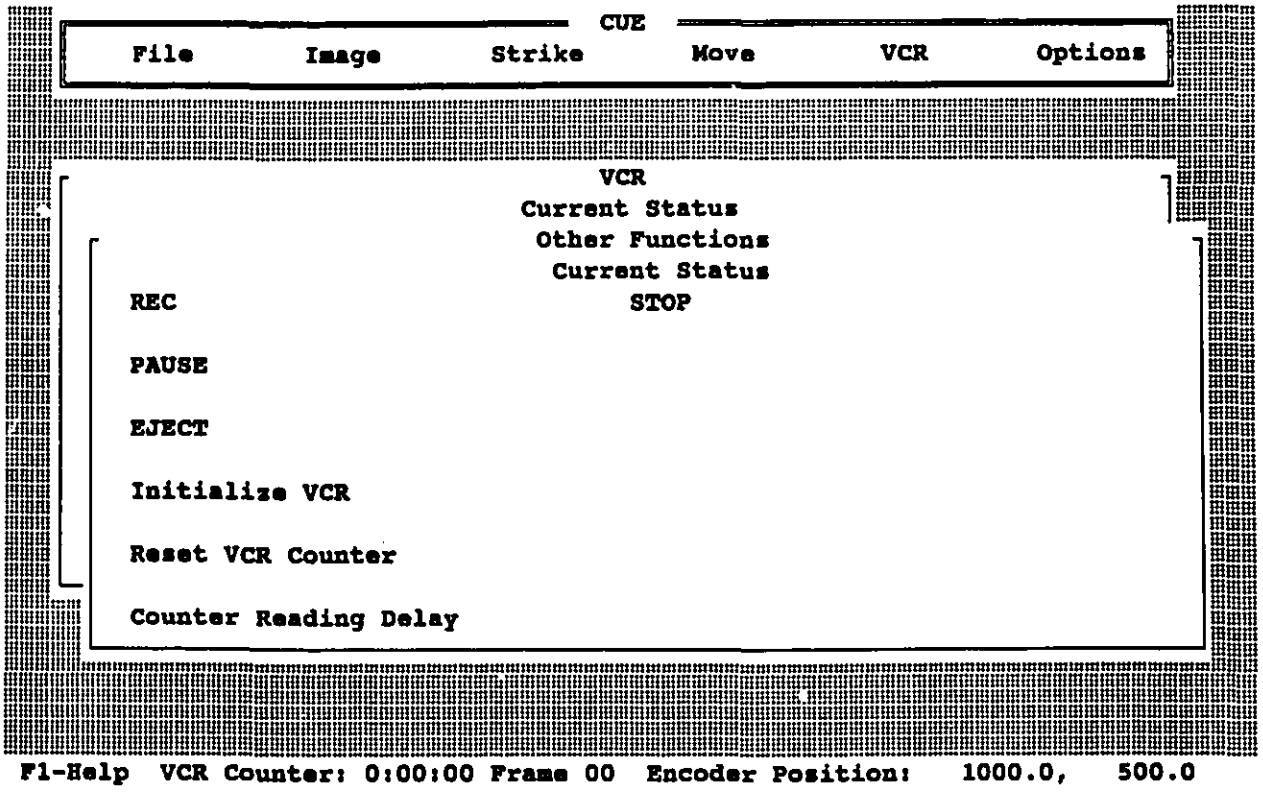

Fig. A.10 The subwindow of **Other Functions** in **VCR**.

The window of **Move** gives all of the controlling functions for the micromanipulator. It is only useful to check if the manipulator works properly. There are two running modes: moving at a set angle and moving towards a set target. They can be toggled by entering new data in either **Moving Angle** or **Target Position**. **Moving Speed** can be varied from 0 to 2000 μm/s. In the subwindow of **Other Encoder Functions**, the speed calibration part is now obsolete because it is performed automatically during an experimental run. The most important function here is the **Clicking Amplifier**. During a "click alignment", this switch should be ON, so any tiny movement of the encoder stage will trigger the computer beeper. After the alignment, toggle it off.

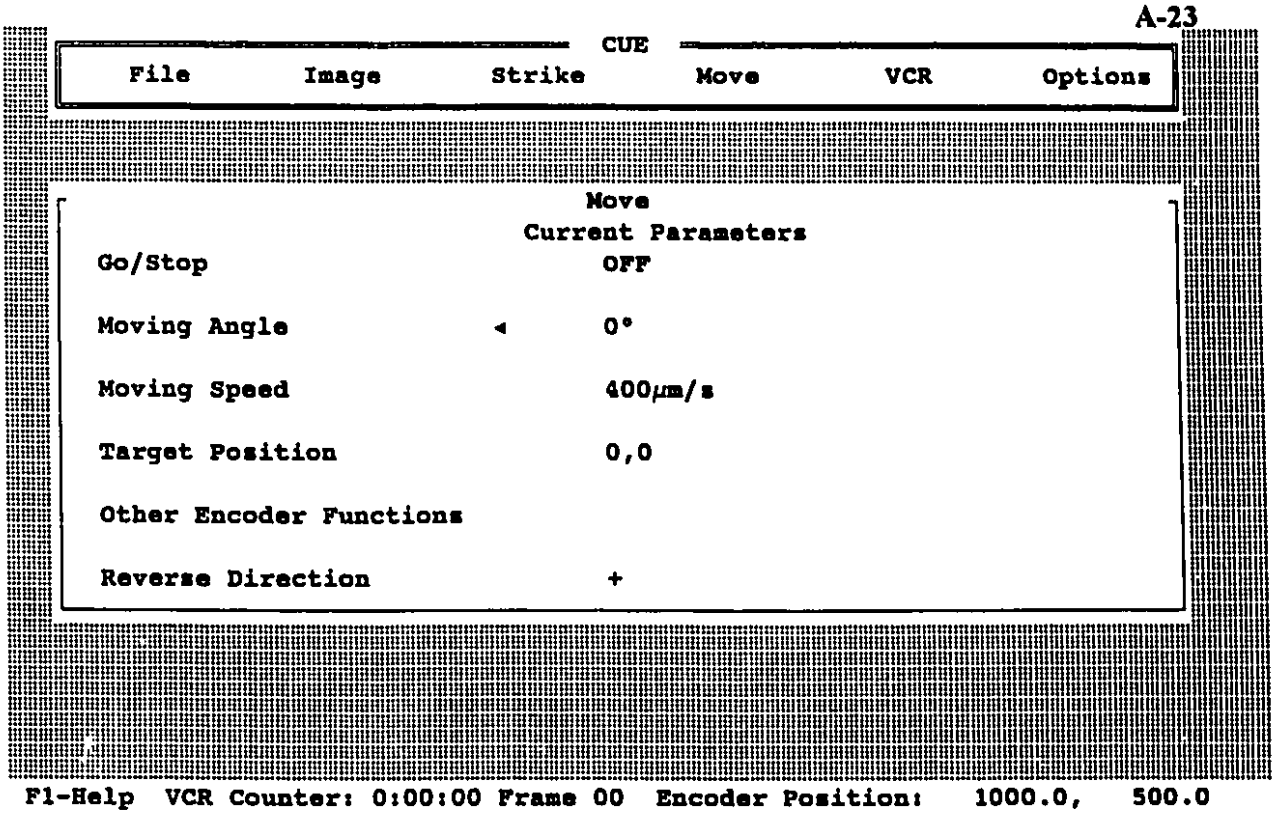

Fig. A.11 The window of **Move**.

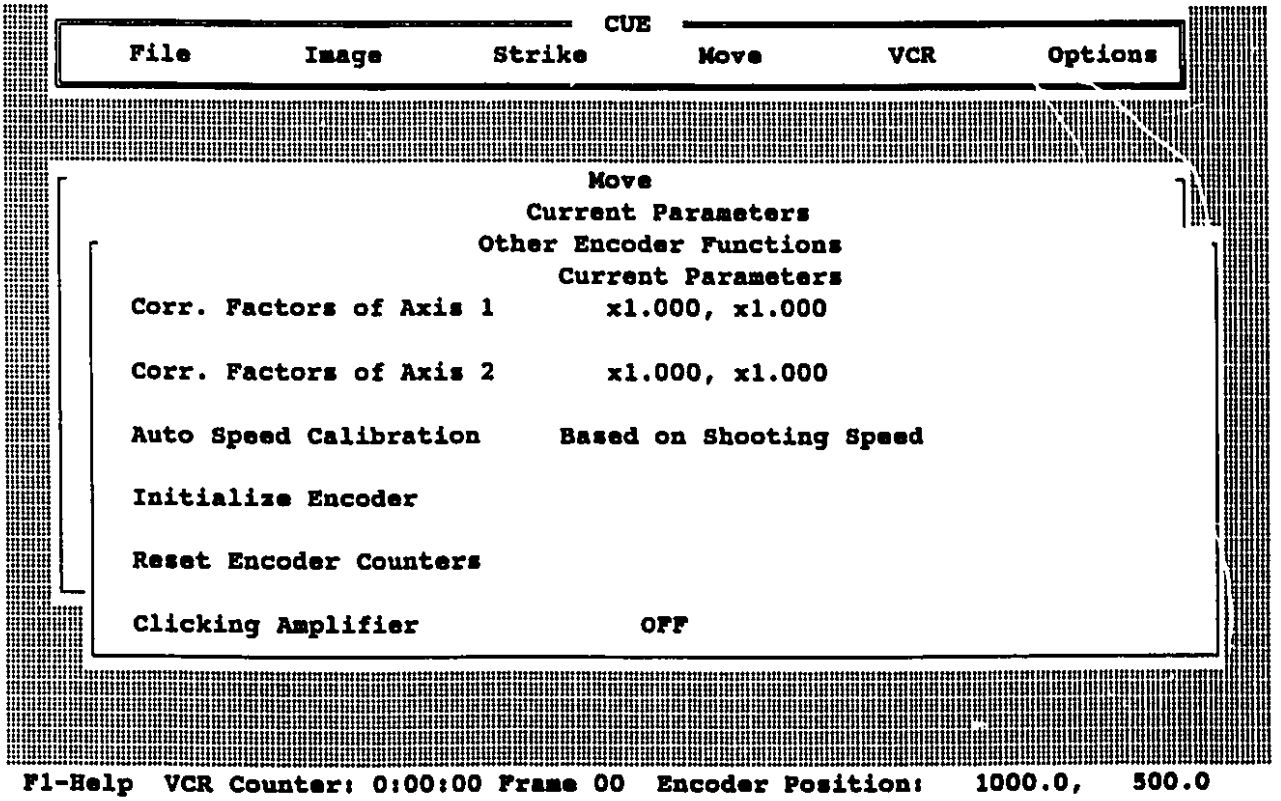

Fig. A.12 The subwindow of **Other Encoder Functions**.

b. Standard procedures for controlling operations

A configuration file is usually created to facilitate later operations. It includes **Data File Name**, **Presetting File Name**, **Mapping file Name** (in **File**), **Length Calibration** (in **Image**, cf. Fig. A.13), **Gap Width**, **Particle Radius** and **Distance Limit** (in **Options**, cf. Fig. A.14). The config. file is saved or retrieved in the window of **Options**. In that window, the first item **Surface Diameters** is used to set the limit of the manipulator to prevent the top surface holder from hitting the sample cell walls. Presently, the size of the sample cell has been designed in such a way that this contact will never occur, so we simply use a large number representing the size of the sample cell to disable this safety check. **Distance Limit** specifies the limit of image analysis (usually 3 particle radii).

Some parameters, such as **Gap Width**, are not known for the moment. They can be entered later to update the config. file. Actually, only one parameter, **Mapping File Name**, is used at this stage. A mapping file records the tape address of each collision, the direction of the encoder stage (y-axis) and the average speed of the stage (by real-time linear regression). It is saved right after one collision, so even when the computer is accidentally rebooted, it can still keep the track on recorded collisions. Before an experiment, check **Shooting Speed** in the window of **Strike** (cf. Fig. A.15). The optimum speed (with minimum vibration) was found to be 400~500 μm/s. **Prep. Time** sets the duration (in seconds) for the reverse motion after **Shot/Stop** button is pressed and the time of waiting between the reverse and the forward motions. **Reverse Direction** offers a fast way to reverse the encoder stage motion after one collision. When **Shooting Angle** is set to be 0° and **Reverse Direction** is +, latex particles will move from the left to the right on the screen. Always check the direction

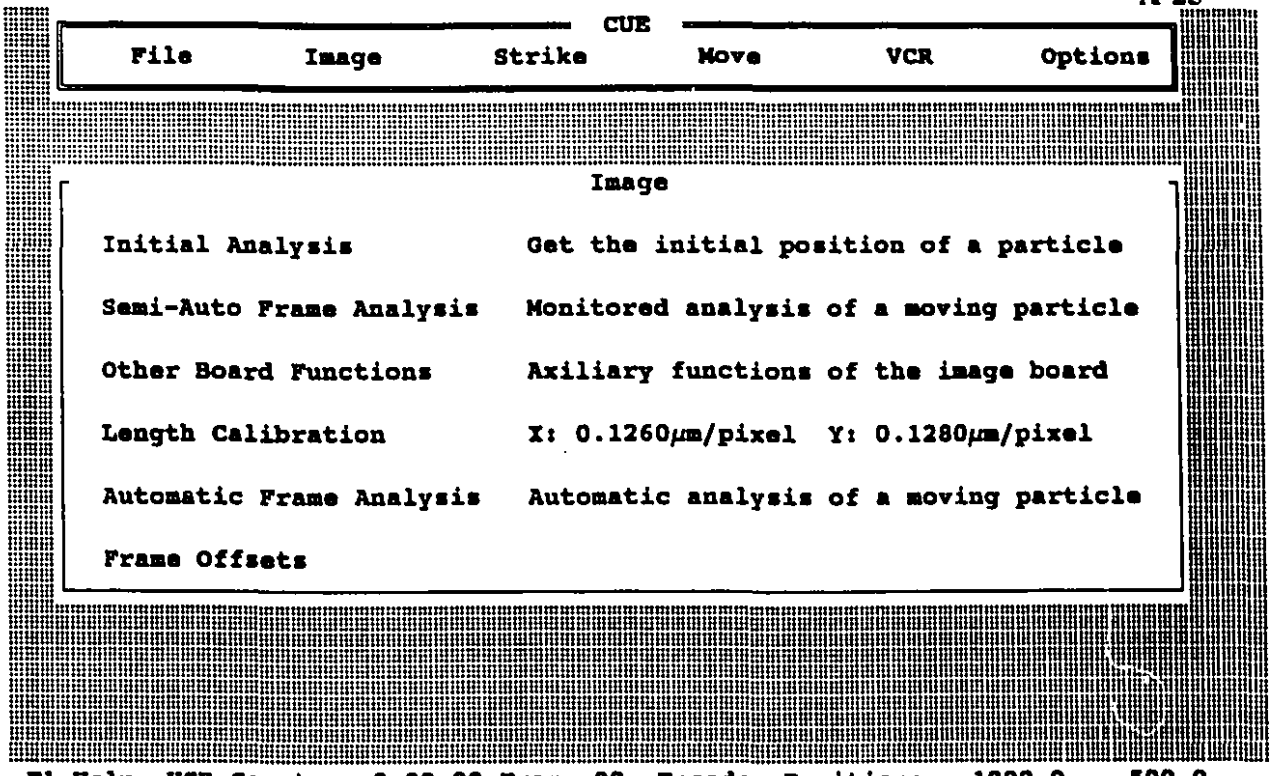

Fig. A.13 The window of **Image**.

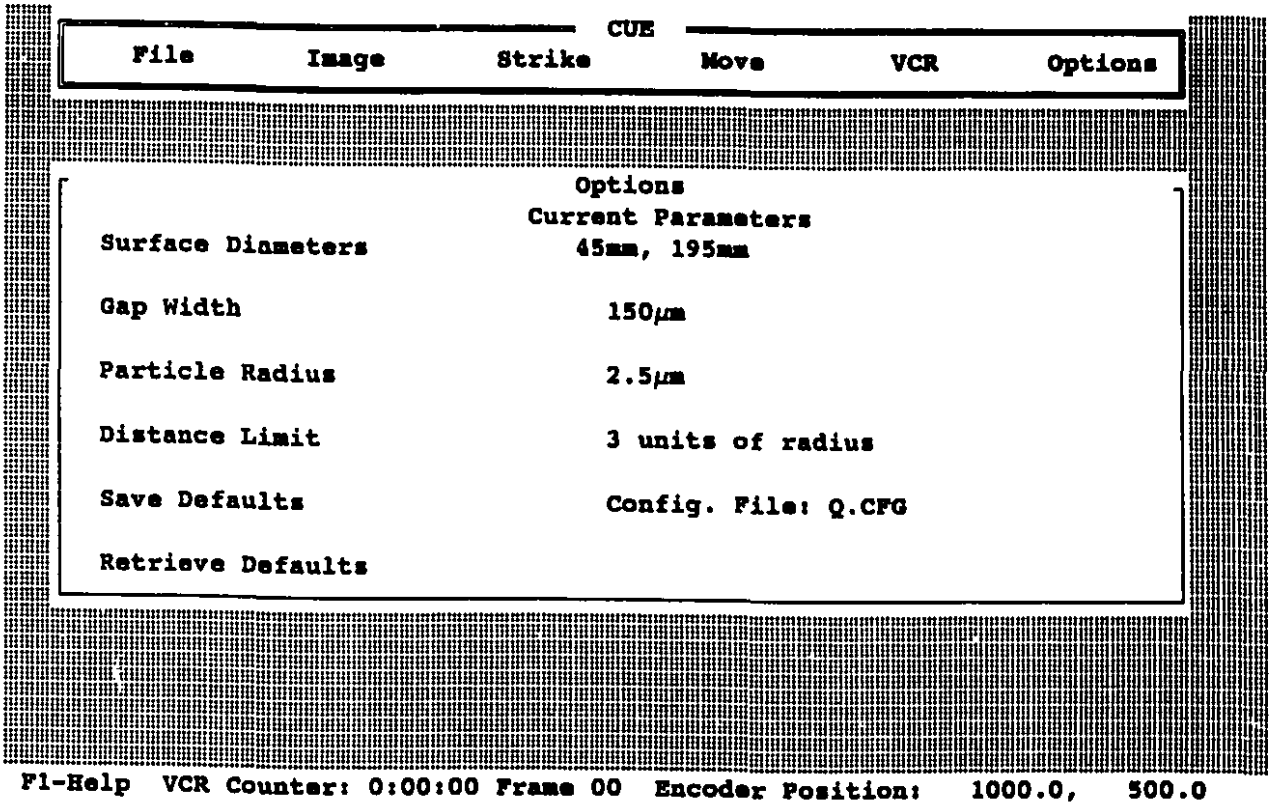

Fig. A.14 The window of **Options**.

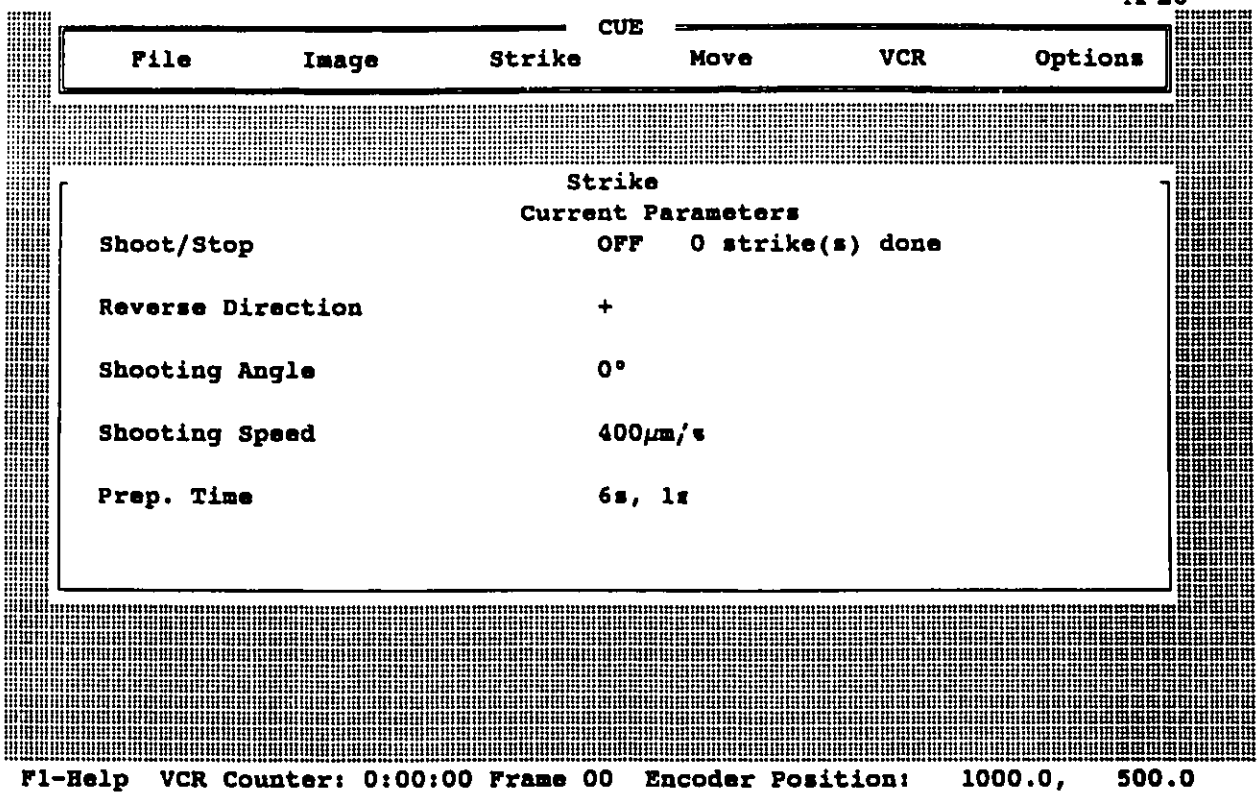

Fig. A.15 The window of **Strike**.

before every collision. When all the parameters are correct, press **Shoot/Stop** to start a collision. Note that the VCR should start to record at the same time. When the mobile particle shoots over the opposite side of the screen, press <Enter> to stop the encoder stage. Under the header "Current Parameters" there is a message "x strike(s) done" to indicate the number of collision trials. This number is only resident in the computer memory. When CUE is terminated accidentally during an experiment, the strike number is reset to zero, so the experimentalist might write down this number on his/her notebook as a guide to how far the experiment has progressed. After the experiment, enter the measured gap width and save the config. file for the next step: trajectory analysis.

c. Standard procedures for trajectory analysis

There are three steps for trajectory analysis: visual screening, threshold presetting and

image analysis. The mapping file data are first printed on a preprinted form by a program called QMAPPT.EXE. With these collision addresses, the user can replay the cassette and pick out the "missing shots". The real collisions are numbered starting from **No.0**. The collisions sharing the same **Particle Radius** (measured in **Image**, to be discussed shortly) can be grouped as one. The first group is called group "A", the second is called group "B", etc. Every time when the colliding particles are changed due to coagulation, the address of the next collision should be written down on the notebook, so the experimentalist can conveniently group the collisions between the same particles together. After screening, rewind the cassette. A non-zero address may be observed even though the cassette was reset before the playback. This is due to tape stretching and errors in counter coding. Reset the address again to 0:00:00 Frame 00.

The threshold presetting is a preparatory step for the image analysis. It requires all the parameters in a config. file except **Data File Name**. The **Presetting File Name** must include the group code. For example, a typical file name for a latex sample No.10, group "A" is QL10A.SET. Replay the cassette and use **Shuttle Search** functions to freeze the picture right after the mobile particle appears on the screen (do NOT freeze the picture before the preparatory reverse motion). Fine adjustment with **Frame Search** may be needed. Move to the window of **Image** and enter the subwindow of **Initial Analysis** (cf. Fig. A.16). Choose the first item **Set AOI** (Area of Interest) and use mouse to drag select an area around the stationary particle in the middle of the screen. Then choose the second item **Set Threshold**. A histogram of pixel gray shades will appear (cf. Fig. A.17). The typical shape of this histogram is a "camel back" with two "humps". The left "hump" indicates the counts of the

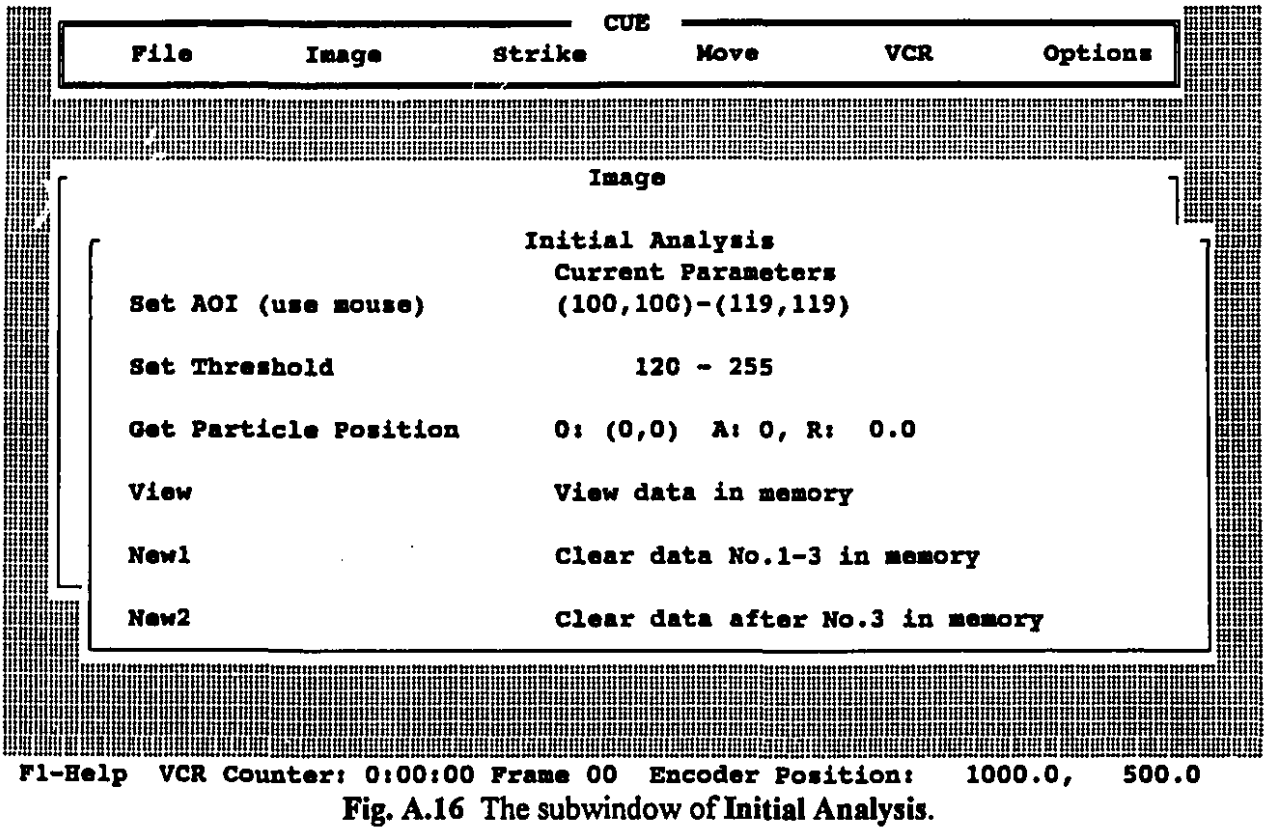

Fig. A.16 The subwindow of **Initial Analysis**.

dark background which has small gray shades and the right "hump" represents the counts of the bright ring-shaped latex image which has larger gray shades. The correct threshold setting is to sandwich the right "hump" by two thresholds. Since the noise has lower gray shades than the image, the upper threshold (threshold 2) is usually fixed at the maximum gray shade, 255. The lower threshold (threshold 1) is automatically placed between two "humps". Fine adjustment with ←→ keys may be necessary to obtain a clear image. Press <Enter> when the thresholds are set. Finally, choose the third item **Get Particle Position** to measure the particle position (x,y), image area (A:xxxx) and image radius (R:xx) in pixels. Press it twice more to get three measurements. Move to **View** and if these three positions are not consistent (deviation larger than one pixel), press **New 1** to clear the data and repeat the above procedures. If good agreement is found, repeat the procedures on the mobile particle. The

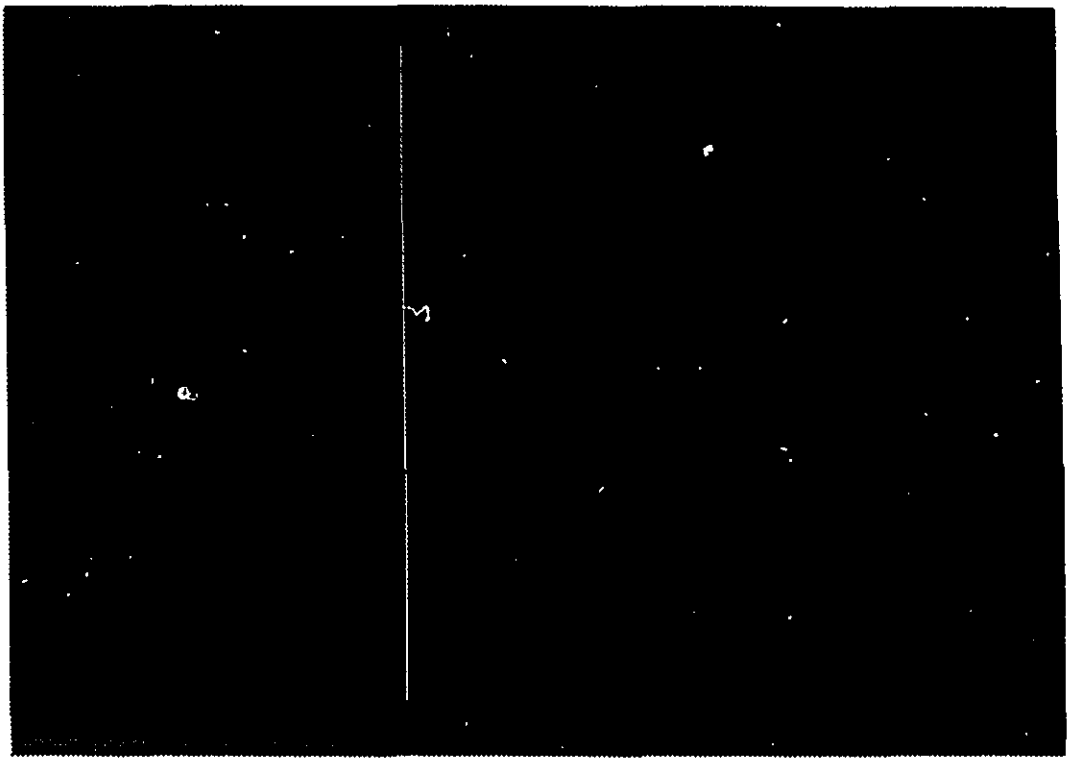

Fig. A.17 A typical histogram of pixel gray shade for a latex image.

radius measured in this way can be used to estimate the particle size. A system calibration shows that a 5 μm latex particle has an apparent radius of 24 pixels. For the measurement of the mobile particle position, the data starts from No.4. If 3 or 4 measurements do not give a consistent result, they can be eliminated by pressing **New 2**. Keep the VCR in the STILL mode and press **Presetting Save** in the window of **File**. The computer will read the current VCR counter, match it with the addresses in the mapping file and print out the collision No., the collision direction [F (forward, left to right) or B (backward, right to left)] and the speed of the encoder stage for that collision (it varies slightly in every collision and can serve as a signature of each collision) on the video monitor. Check these parameters in the mapping file form to verify if the right collision is being analyzed. Go to **Other Board Functions** (cf. Fig.

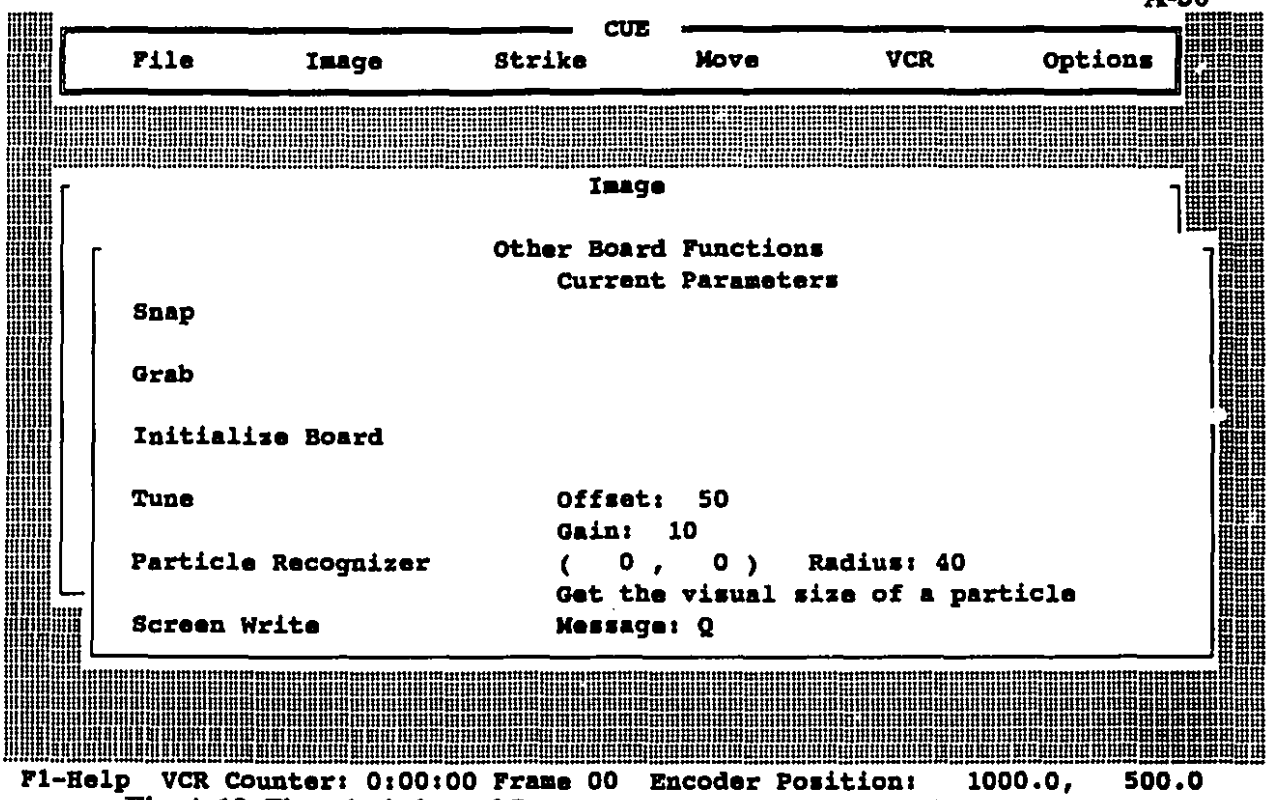

Fig. A.18 The subwindow of **Other Board Functions**. Most of the functions are designed for maintenance purposes except **Snap** and **Grab**.

A.18) and choose **Grab** to disable the **Snap** mode triggered on when **Set AOI** was selected, so when the VCR is playing, the image board will constantly grab the motion pictures and update them on the monitor. Play the cassette and freeze the picture again right after the collision (the mobile particle should be less than 3 radii away from the stationary one). Set only the AOI and thresholds of the mobile particle this time. Note that the first three positions for the stationary particle are not erased and the next determined position will be assigned as data No.4. Repeat the procedure described above for the mobile particle and then save the presetting. Activate the Grab mode again and search for the second collision. When the presetting for all of the collisions in one group is finished, rewind the cassette and reset the VCR counter before presetting the second group. This will eliminate the accumulative error

in counter coding for the first collision of the second group. The presetting directly affects the quality of the last step, automatic image analysis, because it not only saves the addresses of the collisions but gives the computer an "example" of a proper threshold (a "good" image is obvious for human eyes, but not so for a computer). However, some artificial intelligence (AI) procedures are included in CUE to search for a lost collision due to tape stretching or coding errors and to change thresholds to optimize the image (to be elaborated later).

The image analysis has been fully automated in CUE. It is performed in the subwindow of **Automatic Frame Analysis** (cf. Fig. A.19). Another subwindow **Semi-Auto Frame Analysis** (cf. Fig. A.20) gives an analysis for one set of a collision (either approaching or receding part) and now becomes out of date. However, two parameters there, **Repeat No.** and **Tolerance of Std. Deviation**, are shared by the automatic analysis. The former indicates the number of measurements for one position and the latter gives the tolerance of the standard deviation of these measurements. Before the automatic analysis, be sure that the correct presetting file and mapping file names are entered. When a group "A" presetting file is entered, the computer will search for the group "B" file and then the group "C" file... after the group "A" has been analyzed. The group names have to be adjacent to be called automatically. Therefore, in order to analyze the whole experiment, start from the group "A". To analyze just one group, enter that group name and rename the presetting file of the next group, if any, to a group "Z" for example. A **Data File Name** should also be given. Note that no group name should be included. For example, a latex sample No.10 may have a name like QL10.DAT. This is only the head of the final file names which are QL10A0, QL10A1,..., QL10B0,... QL10C0... Each file contains exactly ten collisions (or twenty sets), so QL10A0

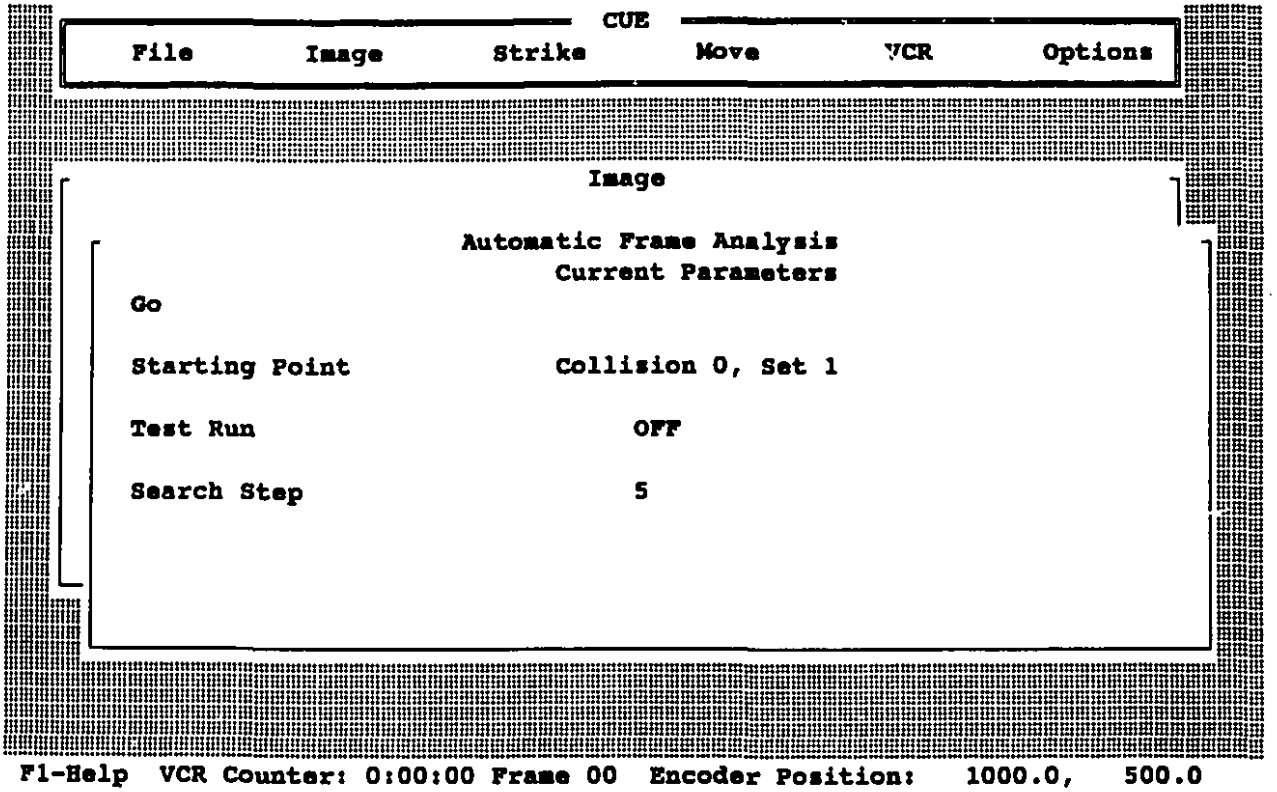

Fig. A.19 The subwindow of **Automatic Frame Analysis**.

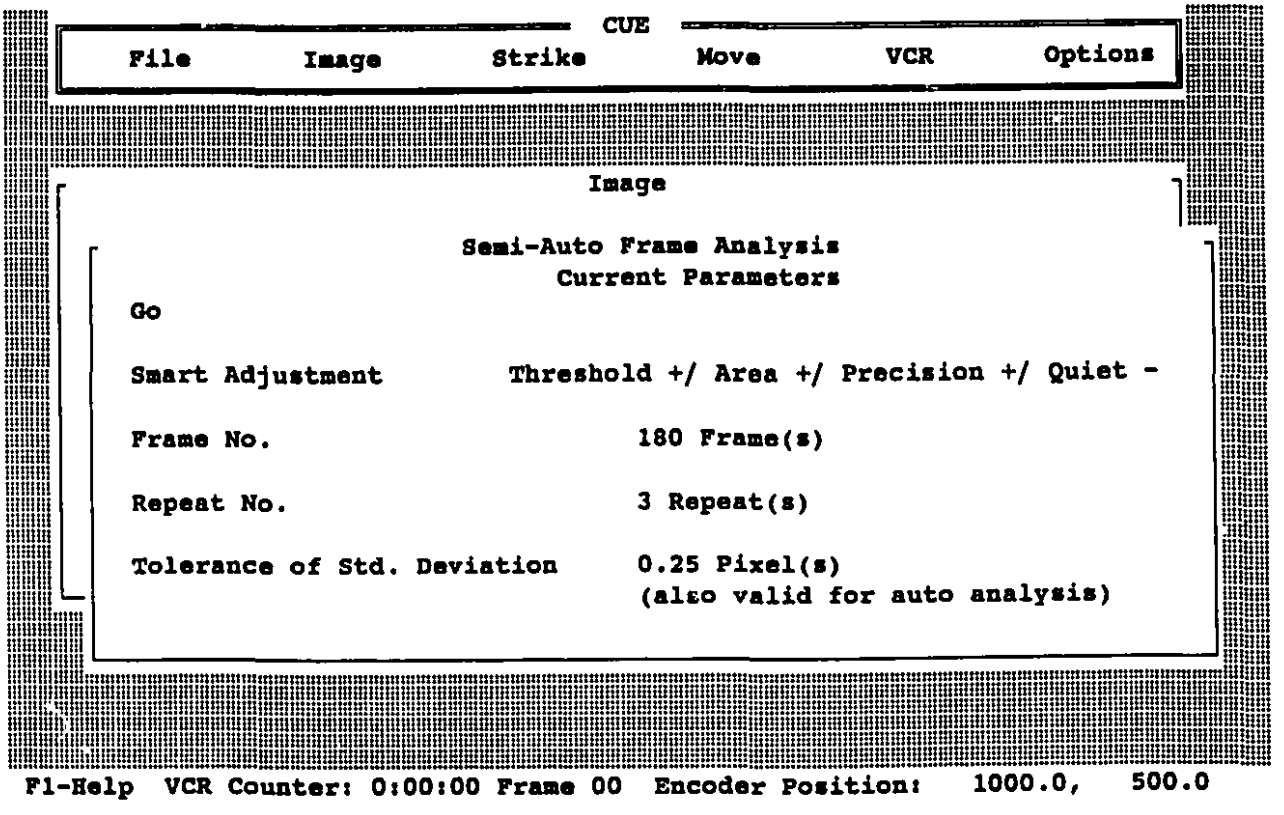

Fig. A.20 The subwindow of **Semi-Auto Frame Analysis**.

includes collisions No.0 to No.9 in group "A" and QL10B15 includes collisions No.150 to No.159 in group "B". After the file names are correctly entered, move to the subwindow of **Automatic Frame Analysis**. The No. of the first collision to be analyzed should be entered in the **Starting Point**. **Test Run** and **Search Step** are only for maintenance purposes. Press **Go** to start the analysis. The VCR will first rewind the cassette and reset the counter. Then it will advance the cassette to the address saved in the presetting for set 1 of the first collision and freeze the picture. A trial analysis will be performed at the same spot with the same thresholds as indicated in the presetting. The saved particle area (standard area) will be the indicator of the "goodness" of the image. If the measured area is too large compared with the standard area, the image is probably covered with "hairy noise signals". If the area is too small, the image ring may be broken. An automatic threshold procedure will try to keep the area close to the standard value by adjusting the lower threshold. This is a very important procedure since the background becomes brighter when the particle moves towards the center. Fixing the preset thresholds will result in fuzzy particle images in the analysis of set 1 (approaching part) and broken rings in the analysis of set 2 (receding part). When the area of an image is extremely small (<10 pixels), the computer will treat it as noise and ignore it. If no large images are found in the AOI, an automatic searching procedure will be called. First, a large AOI covering the whole area of one set is tried. This is equivalent to rewind the cassette for two seconds. If nothing has been found, the computer will assume the particle has yet to come and move 60 frames forward (two seconds). It analyzes the original AOI after every 10 frames are moved. Once part of a ring image enters the AOI, a fine adjustment is performed with a successive approximation method until the image moves to the center of the

AOI. 99% of the collisions can be found in such a way because the address of the first collision is usually quite accurate. The deviation becomes noticeable only after the analysis of a few collisions. Every time when a searching procedure is called, the computer "remembers" the frame number offset from the original address and adds it automatically to the next particle address to avoid accumulative effects. Actually, the searching procedure rarely works on an offset larger than 30 frames (one second), although the total offset after the analysis of 100 collisions can be one minute. This frame offset does not cause any significant errors in a single trajectory because it is evenly distributed in hundreds of collisions and the blank part of the cassette between collisions. It is also possible to manually offset the address of the first collision in the subwindow of **Frame Offsets** in case that really bad images are encountered. However, this is not considered a normal procedure and will not be elaborated here. The saved data give the pixel coordinates of x and y for the moving particle. The next step is to transform them to initial and final positions, (x_i, z_i) and (x_f, z_f), in order to proceed with force parameter fitting. This is done in a software called Q-ANALYZER.

2. Scientific linear regression software - Q-ANALYZER and tutorial

As we mentioned in the previous chapters, the x-coordinate is measured directly and the z-coordinate has to be calculated from the particle velocity which is determined by a linear regression of the y-coordinates. Since the data points close to the stationary particle are subject to the influence of colloidal forces and the points at the far end are sometimes affected by non-steady-state effects when the encoder stage starts to move, a proper data segment bounded by two limits should first be selected. The close bound (with a small interparticle

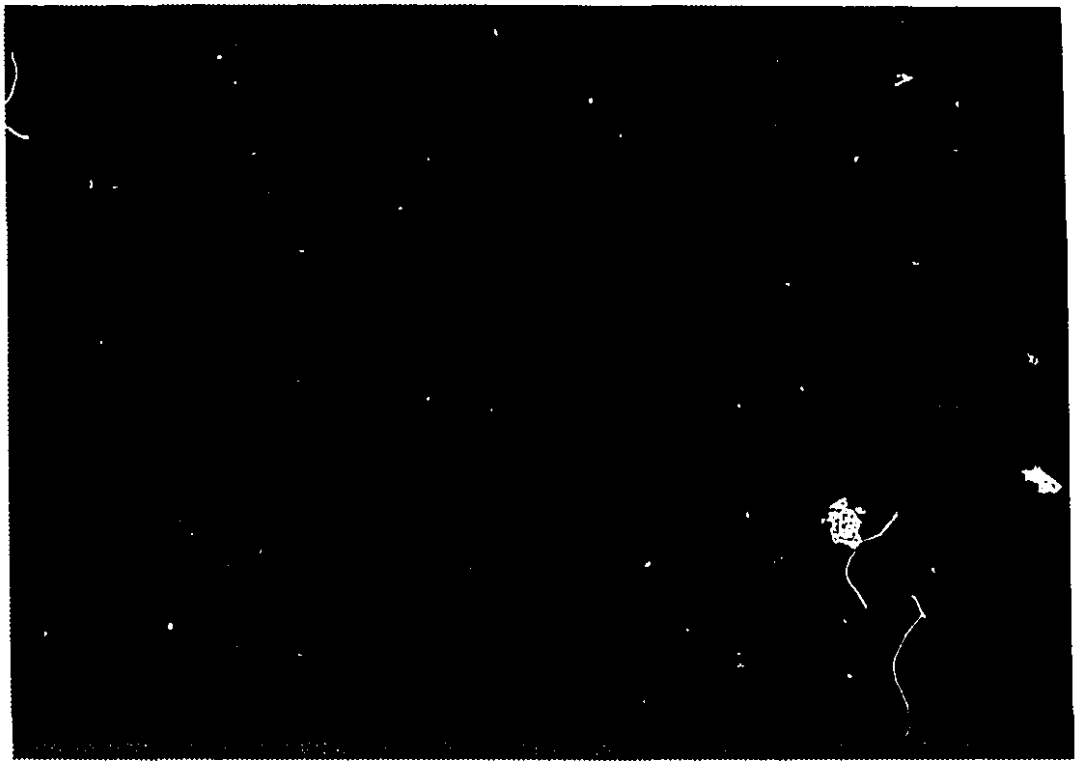

Fig. A.21 A typical data set (approaching part) in Q-ANALYZER. The horizontal line indicates the change in x-coordinate and the diagonal line from bottom left to top right indicates the change in y-coordinate (referred to the left y-axis). The diagonal line from top left to bottom right represents the interparticle distance (referred to the right y-axis).

distance, see the right vertical line in Fig. A.21) is usually fixed at an interparticle distance of six radii. The data file contains the positions up to three radii as set by **Distance Limit** in CUE in order to determine collision durations (to be discussed later). The far bound (with a large interparticle distance, see the vertical line next to the left y-axis in Fig. A.21) is automatically selected by the computer based on a routine to minimize the slope of the x-coordinate line which should be zero if the system is properly aligned. After the data selection, the relationship between x or y-coordinate vs. time is fitted to a straight line. Usually the

linearity of these two lines is very good, so the linear correlation coefficient is always close to 1. The parameter of the goodness-of-fit (1), Q, is also calculated. The linear fitting is only meaningful when Q>0.1. This Q parameter depends on experimental errors in the data points. Increasing the errors will increase the probability that the data points might follow a linear relationship, therefore, increases the value of Q. Another important parameter is the probability of the direction of the moving particle being identical to the direction of the traveling encoder stage, P_d. The latter has been calibrated to be exactly horizontal (with a zero slope). A linear regression of x and y-coordinate points yields the direction of the moving particle as x/y. P_d can be evaluated by $1-\text{erf}[2^{-1/2}(x/y)/d(x/y)]$ where erf[ ] is an error function and d(x/y) is the error of x/y (here treated as the standard deviation). When the area between x/y and 0 is less than 50% of the total area, i.e. $P_d > 0.5$, the slope x/y is statistically correct. In Q-ANALYZER, the analytical process is indeed reversed because both Q>0.1 and P_d>0.5 should be satisfied if the system is properly aligned,. However, the experimental errors which can vary these two parameters are uncertain because of multiple causes, e.g. Brownian motion and surface roughness. They are determined by computer through trial and error until the conditions for Q and P_d are finally satisfied. The resulting errors are mostly within 0.1a (a is the particle radius) and sometimes 0.2a if the latex surface is rough. These findings will be used later in Monte-Carlo error analysis. Once the errors are determined, the computer will open set 2 of the same collision and repeat the same procedure. If the difference between these two x/y's is larger than a set value (usually 0.04)or the absolute value of either of the x/y's is greater than 0.04, the collision will be discarded due to inconsistent or incorrect particle moving directions. If an agreement has been found, the computer will then calculate

the z_i or z_f from the y-slope and obtain the x_i or x_f from the intercept between the fitted line of x-coordinate and the close bound.

The above description may be a little confusing. Indeed, Q-ANALYZER is extremely user-friendly. Type AUTOQA in DOS to start the software. First, highlight **Open** (by ↑↓ keys) and press <Enter>. A dialog box will appear in the middle of the screen prompting the user to enter the name of the first data file of CUE, for example, QL10A0.DAT. The first set will be processed and displayed on the screen. Check the automatically set close and far bounds and the DATA section about **Prob.** (P_d), **Fit 1** and **Fit 2** (Q). If the bounds have to be changed, highlight **Low** or **High** and use ←→ keys to shift the bounds. Usually this is not necessary, so press **Run** to start the automatic processing. Another dialog box will appear to prompt the user to enter the result file name. An example could be QL10AC.RST if there are A, B and C three groups in the data files of latex sample No.10. Press **OK** to accept the choice of the bounds. The next set will be automatically loaded and another **OK** is needed if the setting is acceptable. After analyzing a few collisions, the user should have a rough idea about the accuracy of his/her experimental run. If everything is fine, press ALT-R to accept all the automatic settings. The computer will open files one after the other until the end of the group "A" and then open the first file of the group "B" automatically... Finally when no more files are left (at the end of the group "C"), a message box will appear to inform the user that the processing is completed. The final data will be saved in a file called QL10AC.REP which includes x_i, z_i, x_f, z_f, dx, dz, G, d_1 , d_2 and t_{exp} (dx and dz being the errors of these two coordinates, G being the shear rate, and d_1 and d_2 being the interparticle distances at the moments when the counting for the collision duration, t_{exp}, starts and ends) and another file

called QL10AC.RAD which includes $r_{s,i}$, $\theta_{s,i}$, $r_{s,f}$ and $\theta_{s,f}$ (the radial scattering distances and scattering angles before and after a collision). Further data processing will be discussed in the next section.

3. Data selection procedures

Because of the errors discussed above, only small number of the collision trajectories are suitable for the fitting of force parameters. The first screening in the Q-ANALYZER has discarded the collision trajectories affected by anomalous flows and system vibration. If we open the file QL10AC.RAD and set several tolerance limits to $r_{s,i}$ and $r_{s,f}$, we can eliminate most of the weak-force collisions for which the trajectories are almost symmetrical and the anomalous collisions affected by "long strings" on the latex surface (cf. Chapter 3). Note that it is preferable to tolerate some anomalous collisions and discard them in the following screening, so no "good" collisions would be lost. According to our experience, the suitable limits are $0 < r_{s,i} < 1.2$ and $0.9 < r_{s,f} < 1.6$. The initial positions, (x_i , z_i), of the selected collisions are inputted into a trajectory calculation program CPSFIT.EXE, written by Dr. Warszynski based on the theory described in ref. (2), to calculate the theoretical final positions, (x_{th}, z_{th}) assuming one or several typical parameter set(s). The data input file has a format as follows,

```
1       ⇦ No. of different parameter sets
7       ⇦ No. of parameters in one set
   ┌——— Parameter names (to be discussed later)
   ↓          ↓---- Parameter values (the other four columns are constants)
 AK     7.620D2    0.D-1    1      1.D0     15.D1
 DLSS   3.652D1    4.D-1    1      0.D0     100.D0
 ADSS   1.568D-3   4.D-1    1      0.D0     1.D-1
 ALSS   1.445D2    0.D-1    1      0.D0     0.D0
 LP     8.696D-3   9.D-1    1      0.D0     1.D0
 LI     0.000D0    9.D-1    1      0.D0     1.D3
 ELAS   2.272D4    5.D-1    1      0.D0     1.D0

125     ⇦ No. of collisions
0. 0. 0. 2.D-3 ⇦ Constants
2.3D-6 4.36 1.01D-3 293. ⇦ Particle radius, shear rate, viscosity and temperature (SI units)
0.1 6. 0.005 -1 0       ⇦ The 4th number has to equal the negative No. of parameter sets.
1.D-4 1.55 15 0.05 10000.   ⇦ The 2nd number is an error factor to adjust χ².

   ┌——— Append QL10AC.REP file with the selected collisions only.
   ↓     xi        zi       xf        zf       dx       dz       G       d1       d2      texp
A29  -0.5575   1.6028  -0.9316   2.1133  0.1251   0.0909   4.378   -2.970   3.221   1.167
A31   0.1602   1.2840   0.9596   1.7183  0.1047   0.0658   4.362   -2.951   3.092   1.433
A33   0.4039   1.6154   0.8266   2.2201  0.0104   0.0948   4.385   -2.974   3.049   1.033
 ...
```

where AK = τ, DLSS = Dl/Pe, ADSS = Ad/Pe, ALSS = Al (cf. Chapter 2); LP = L_p /a, LI = L_i /a and ELAS = 1.886Ea^3/(kTPe) (cf. Chapter 5). The result file will be called QL10T.TAB (the letter T indicates it is a trial set).

The goal of a final screening is to eliminate the collisions affected by larger-than-average Brownian motion and latex surface roughness. The screening is performed by evaluating a $f_\perp$ factor described in Chapter 3. It is calculated by a program called DEVHISTO.EXE which takes both the REP file and the TAB file and calculates the histogram of $f_\perp$. The results are saved in a file called QL10T.HIS which contains all the $f_\perp$ values, theoretical duration time values and a complete histogram of $f_\perp$. Usually we keep the

collisions with an absolute $f_\perp$ value less than 0.2. The duration time difference can also serve as a yardstick to check if the mobile particle has been temporarily trapped during a collision due to some entanglements. The finally selected collisions are to be used again by CPSFIT.EXE to construct a χ^2 contour map.

4. Construction of a χ^2 contour map

To make a contour map, we have to divide the map by several grids and calculate the χ^2 value of each grid point. One grid point represents a set of parameters and one contour map usually requires 60 grid point values, so a slightly modified input file will be used to calculate 60 parameter sets. The following file is an example.

```
60
7
 AK    7.620D2   0.D-1   1    1.D0    15.D1
 DLSS  3.652D1   4.D-1   1    0.D0    100.D0
 ADSS  1.568D-3  4.D-1   1    0.D0    1.D-1
 ALSS  1.445D2   0.D-1   1    0.D0    0.D0
 LP    8.696D-3  9.D-1   1    0.D0    1.D0
 LI    0.000D0   9.D-1   1    0.D0    1.D3
 ELAS  2.272D4   5.D-1   1    0.D0    1.D0
7.620D2  3.652D1  1.568D-3  1.445D2  8.696D-3  0.000D0  2.272D5
7.620D2  3.652D1  1.568D-3  1.445D2  8.696D-3  0.000D0  2.272D6
   ...

33
0. 0. 0. 2.D-3
2.3D-6 4.36 1.01D-3 293.
0.1 6. 0.005 -60 0
1.D-4 1.55 15 0.05 10000.
A29 -0.5575  1.6028 -0.9316  2.1133  0.1251  0.0909  4.378  -2.970  3.221  1.167
A31  0.1602  1.2840  0.9596  1.7183  0.1047  0.0658  4.362  -2.951  3.092  1.433
A33  0.4039  1.6154  0.8266  2.2201  0.0104  0.0948  4.385  -2.974  3.049  1.033
  ...
```

Compared with the previous input file, this one has a small collision No. (33 compared to 125) but a large parameter set No. (60 instead of 1). The results of χ^2 will be saved in a file called QL10S.RES (the letter S indicates it is a selected collision set).

5. Monte-Carlo error analysis

As mentioned above, the errors in particle positions are usually within 0.1a or 0.2a. We can use a Monte-Carlo method to analyze the errors in best-fit parameters. First, run a program called ERROR.EXE to generate 1000 error files, each containing the same set of initial positions but randomly varied final positions (the variation is within 0.1a or 0.2a from the experimental final positions). A program named MONTE.EXE will then be used to take both the error files (one at a time) and the TAB file containing the best-fit theoretical final positions and calculate the χ^2 values of the grid points for each error file. Since it is extremely time-consuming to plot these 1000 contour maps and visually determine the minimum χ^2's, another program called MONHISTO.EXE has been written to search for the minima, record the counts of different parameter values corresponding to these minima and construct histograms of the parameters being analyzed (cf. Chapter 5). We can finally evaluate the error in each parameter from these histograms.

6. Plotting a force-distance curve

The final goal of a force apparatus is to obtain a force-distance curve. With known theoretical expressions for different forces and best-fit parameters, we can plot the force-distance curve in any spreadsheet software. When the errors of these parameters are

determined, upper and lower limits of the measured force curve can also be plotted in the same graph to indicate the reliability of that measurement.

REFERENCES

1. Press, W.H., Flannery, B.P., Teukolsky, S.A., and Vetterling, W.T., "Numerical Recipes - The Art of Scientific Computing." Cambridge Univ. Press, Cambridge 1989, p.555.

2. Dabros, T., van de Ven, T.G.M., *J. Colloid Interface Sci.* **149,** 493 (1992).